STYRELSEN FÖR

# VINTERSJÖFARTSFORSKNING

WINTER NAVIGATION RESEARCH BOARD

Research Report No 51

# BALTIC EXPERIMENT FOR ERS-1 (BEERS)

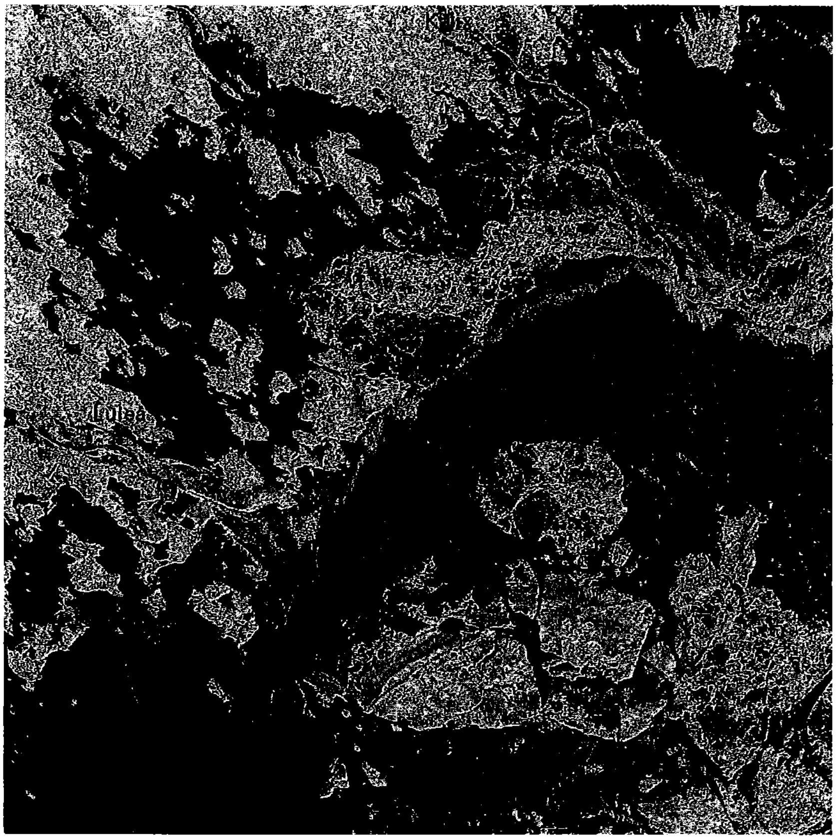

Sjöfartsstyrelsen
Finland

Finnish Board of Navigation

Sjöfartsverket
Sverige

National Maritime
Administration

STYRELSEN FÖR

# VINTERSJÖFARTSFORSKNING

WINTER NAVIGATION RESEARCH BOARD

Research Report No 51

# BALTIC EXPERIMENT FOR ERS-1 (BEERS)

Editor: Lars M. H. Ulander

Göteborg, December 1994

ISBN 91-7197-085-1
Bibliotekets Reproservice
Göteborg 1994

# PREFACE

The Winter Navigation Research Board presents its Research Report No. 51. It describes the analysis and results from the Swedish BEERS (Baltic Experiment for ERS-1) programme, a research project involving Chalmers University of Technology (CTH), the National Defense Research Establishment (FOA), the Swedish Meteorological and Hydrological Institute (SMHI), and the Swedish Space Corporation (SSC). The primary objective of BEERS is to introduce and evaluate satellite images from the synthetic-aperture radar (SAR) onboard the European Space Agency's ERS-1 satellite for the icebreaker and sea ice services. Experiments have been carried out each winter during 1992-1994 in the Bay of Bothnia. Swedish icebreakers have participated in the field experiments, and were also involved in a demonstration activity in 1994 where satellite SAR images were transferred to icebreakers involved with ship assistance and routing.

The report has been prepared by Lars M.H. Ulander (ed.), Anders Carlström, Patrik B.G. Dammert, Wolfgang Dierking, Jan O. Hagberg, CTH, Anders Gustavsson, Björn Larsson, FOA, Bertil Håkansson, Mats Moberg, SMHI, Thomas Thompson, SIOC, and Göran Liljeström, BOID. Funding and support for the BEERS project has been provided by the Swedish National Space Board, the European Space Agency, the National Maritime Administration and COLDTECH. The BEERS programme would not have been possible without the enthusiastic help from the participating ice-breakers.

The Winter Navigation Research Board expresses its thanks to all who have taken part in this research project.

Norrköping and Helsinki, December 1994

Kaj Janérus

Kyösti Vesterinen

# TABLE OF CONTENTS

# A. OVERVIEW OF THE SWEDISH BEERS EXPERIMENTS

LARS M.H. ULANDER

Department of Radio and Space Science
Chalmers University of Technology
S-412 96 Göteborg, Sweden

**Abstract.** The northern part of the Baltic Sea becomes ice covered each year and icebreakers operate in the area to assist and route the ship traffic. The Baltic Experiment for ERS-1 (BEERS) is a research programme to introduce and evaluate the use of satellite synthetic-aperture radar (SAR) images in support of winter marine traffic. Four field experiments and one operational demonstration have successfully been carried out during 1992-1994. In this chapter, we describe the Swedish BEERS experiments and summarise the main results. The present limitations for operational use of the SAR images are due to spatial coverage and temporal sampling restrictions. Daily coverage of the entire Baltic Sea area at a resolution of 100-200 m is recommended for a future operational system. Measurement results show that the SAR images mainly respond to roughness variations of the ice surface. The SAR images thus provide unique information on the ice conditions independent of daylight, clouds and fog. Models of the interaction between the radar wave and the ice surface have been used for image inversion to retrieve surface roughness. Preliminary analysis also show good correlation with ice resistance measured from ship performance data. Image interpretation is not affected by air temperature or precipitation during cold conditions, but becomes difficult as the air temperature rises above 0°C when wet snow masks the ice surface. Discrimination of open water leads and sea ice is difficult based on image tone and texture alone, but is a minor problem for a trained operator. SAR interferometry is a new technique which shows good potential for measuring small-scale motion (cm) over large areas.

## 1. Introduction

The ship traffic in the Baltic Sea (see figure 1) is of vital importance for the economy in northern Sweden. Major ports are kept open throughout the year despite difficulties caused by sea ice which forms every year. During mild winters the maximum ice extent covers the Bay of Bothnia and the Quark, whereas most of the Baltic Sea area is ice covered during severe winters (SMHI and FIMR 1982). The level ice reaches a maximum thickness in the northern archipelago of more than 70 cm, with a maximum reported of 120 cm. Level ice, however, is of less concern for winter navigation and may be penetrated by ice-strengthened ships. The major problems are instead caused by ice which has been deformed into ridges and hummocks, *i.e.* lines and hillocks of broken ice forced upwards by pressure (WMO 1989), due to actions of wind, waves and currents. Ridges have a typical thickness of 5-15 m with a maximum reported of 28 m (Palosuo 1975, Leppäranta and Hakala 1992).

Observations and forecasts of the ice conditions are provided daily by the sea ice services at the Swedish Meteorological and Hydrological Institute (SMHI) in Norrköping, Sweden. They are based on conventional *in situ* observations, helicopter reconnaissance, and optical and infra-red satellite imagery (NOAA AVHRR). Ice and weather information is available to all icebreakers through a computer network using the Nordic Mobile Telephone system NMT-450. Due to high cloud coverage (60-70%) and limited daylight conditions, however, there is often a lack of reliable data using the conventional methods. Satellite synthetic-aperture radar (SAR) is therefore needed as a complementary sensor, due to its capability of mapping the ice conditions independent of daylight, clouds and fog (Thompson 1986). An additional advantage of the SAR is that it gives information on the degree of ice deformation which is essential for support of winter navigation. Currently, SAR images are provided by the European Space Agency (ESA) ERS-1 satellite which was launched into orbit in July 1991 (Vass and Battrick 1992). It carries a SAR which operates at 5 GHz and provides 100-km wide image strips with 30-m resolution. Future satellites will also carry SAR sensors, *e.g.* the European ERS-2 and the Canadian Radarsat which are both due for launch in 1995.

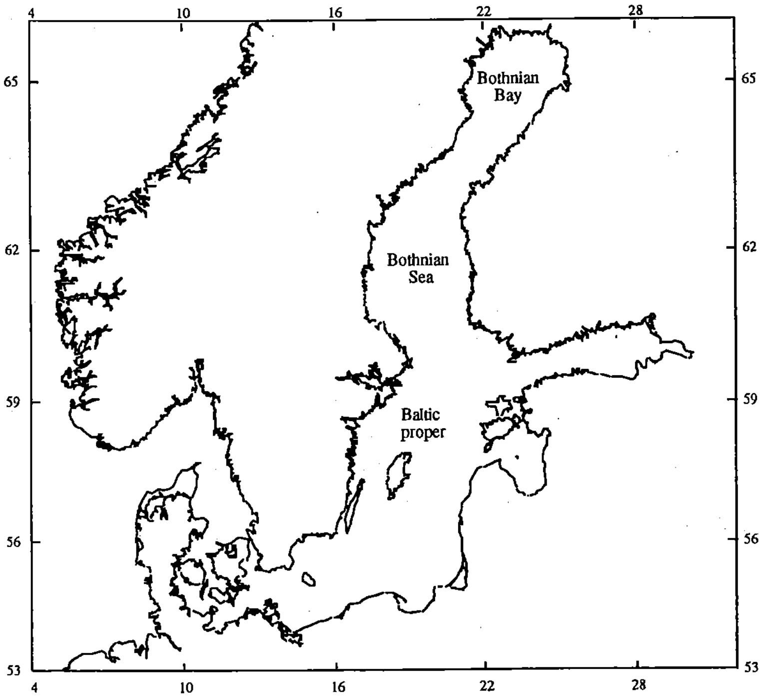

Figure 1. Map of the Baltic Sea region.

## 2. Baltic Experiment for ERS-1 (BEERS)

BEERS is a research programme to exploit the use of the ERS-1 SAR for sea ice mapping in the Baltic Sea. The programme is carried out jointly by Sweden, Finland (Herland 1994, Herland *et al.* 1994), Germany and Canada, and is also part of the Programme for International Polar Oceans Research (PIPOR 1985). It is based on a successful application in response to the ERS-1 Announcement of Opportunity resulting in the provision of ERS-1 SAR data. The Swedish BEERS group consists of scientists from Chalmers University of Technology (CTH), the National Defence Research Establishment (FOA), SMHI, and the Swedish Space Corporation (SSC).

Earlier remote sensing and sea ice experiments in the Baltic Sea have also involved imaging radars. The first experiment was SEA ICE-75 which was carried out in March 1975 and included the Dutch EMI side-looking airborne radar (SLAR) operating at 10 GHz (Blomquist *et al.* 1976). The first experiments using high-resolution airborne SAR were conducted during the Bothnian Experiment in Preparation for ERS-1 (BEPERS): BEPERS Pilot Study 1987 (Leppäranta *et al.* 1992) and BEPERS-88 (Leppäranta and Thompson 1989, Ulander 1991, Askne *et al.* 1992). The BEPERS Pilot Study involved the French VARAN-S SAR operating at 9 GHz, whereas BEPERS-88 involved the Canada Centre for Remote Sensing (CCRS) SAR operating at both 5 and 9 GHz. The main objective of these experiments was to provide simulation data in preparation for the planned ERS-1 satellite mission.

The Swedish BEERS project has included calibration and validation activities as well as application demonstrations. The original objectives included the following topics (Thompson *et al.* 1992b):

- Demonstration of the possibilities of using ERS-1 SAR data for the icebreaker services and as input to numerical forecast models.
- Evaluation of the possibilities to discriminate different ice characteristics, *i.e.* ice concentration, surface roughness, openings, and stage of development.
- Temporal and spatial investigation of the backscatter signature and mechanism at C-band and like-polarisation of low-salinity sea ice.

## 3. Field Experiments

Four extensive field experiments were carried out during the three ice seasons 1992-1994. Both the 1992 and 1993 winters were very mild and the maximum ice extent only covered the Bay of Bothnia. The mild conditions in combination with strong south-westerly winds created large areas of jammed brash barriers formed when thin ice was compacted towards the fast ice boundary. The 1994 winter, on the other hand, was normal and the maximum ice extent covered the Baltic Sea south to the northern part of the Baltic Proper. Thick level ice with large ridges were lacking in 1992 and 1993 but occurred in 1994. The maximum areal coverage each year since 1962 is shown in figure 2. Note the large annual variability, the very low values for the experiment years 1992 and 1993 and an ice area close to the median in 1994. An illustration of the difference between a mild and a normal winter is given in figure 3, which shows SAR images of the Bay of Bothnia at the time of maximum ice extent in 1992 and 1994.

The main objective of BEERS-92 (Ulander and Carlström 1993) was to characterise the major ice types at the time of the ERS-1 SAR images. The idea was to identify the ice types in the SAR images and then perform *in situ* measurements. This strategy was possible by using the icebreaker *Tor* as a mobile experiment base and by installing a computer link over NMT-450 for transmission of compressed ERS-1 SAR images from SMHI. The experiment was conducted during two periods, 15-21 February and 26-30 March 1992 resulting in 34 measurement sites. Air temperatures were generally cold (below 0°C) and ice types encountered included both fast and drift ice as well as level and deformed ice. The *in situ* measurements included snow and ice parameters relevant for the ERS-1 SAR images, *i.e.* surface roughness (mm-dm scale), ice physics (salinity, density, temperature, void size), snow physics (depth, wetness, density) and air temperature. The measurement programme also included helicopter photography, deployment of calibration radar reflectors and a land-based measurement station to collect a time series of the growing fast ice. BEERS-92 resulted in a large data set of the major ice types except thick ice and large ridges in the drift ice. The land station did not obtain any useful data due to the mild winter and lack of ice.

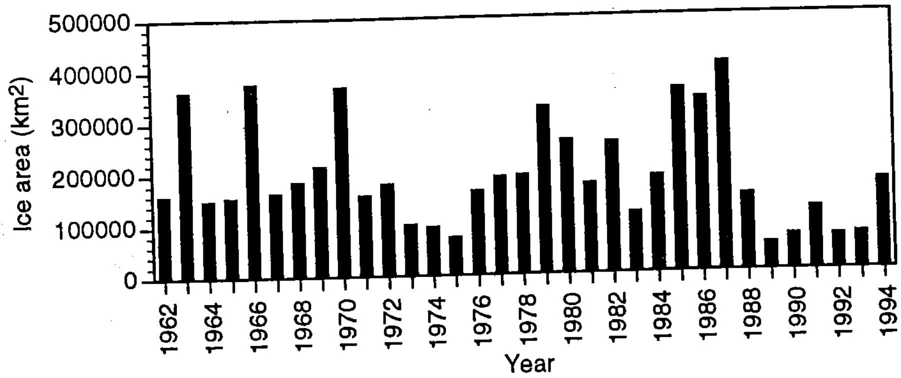

Figure 2. Maximum annual ice extent in the Baltic Sea between 1962 and 1994 (Seinä and Palosuo 1993). The data points for 1993 and 1994 have been provided by A. Seinä, Finnish Institute for Marine Research, Helsinki.

BEERS-93 (Carlström 1993) was carried out during 14-18 March 1993 and used the icebreaker *Atle* as a base. The main objective was to complement the BEERS-92 measurements by including large ridges in the drift ice, but the ice conditions turned out to be quite similar to BEERS-92. However, the air temperature varied above and below 0°C during the experiment and rain also occurred. The experiment thus provided a unique data set on the effects of temperature variations around 0°C. A total of 10 measurement sites were visited during the experiment. The measurement programme was similar to BEERS-92 with the addition of icebreaker performance measurements.

*In situ* data of large ridges and hummocks in drift ice were obtained during BEERS-94 (Carlström 1994) which was carried out during 1-10 March 1994. The experiment base was a barrack which was deployed on the ice 30 nautical miles south-east of Luleå by icebreaker *Oden* and later removed by *Atle*. Scientists were stationed in Luleå and transported out to the base each day by helicopter. Cold conditions were prevailing except during the storm when air temperatures approached 0°C. A total of 4 measurement sites were visited. The measurement programme was similar to BEERS-93 but also included airborne flights with the AeroElectroMagnetic (AEM) system operating at 3.1 kHz (Peltoniemi 1982, Hautaniemi *et al.* 1994) and the CARABAS SAR system operating at 20-90 MHz (Gustavsson *et al.* 1993). Icebreaker performance measurements were performed on *Oden* while in normal operation.

## 4. Operational Demonstrations

During BEERS-92, icebreaker *Ymer* was equipped to operationally receive and use the satellite SAR images. Due to the mild ice conditions, however, only a very limited operational demonstration was performed. The emphasis was instead on setting up a transmission link to icebreaker *Tor* in support of the field experiment as mentioned before. Nevertheless, BEERS-92 provided useful experience for streamlining the reception and processing of SAR data at SMHI. The SAR data were received at SMHI using a satellite link with a delay of 6-17 hours after the satellite overpass (Thompson *et al.* 1992a) .

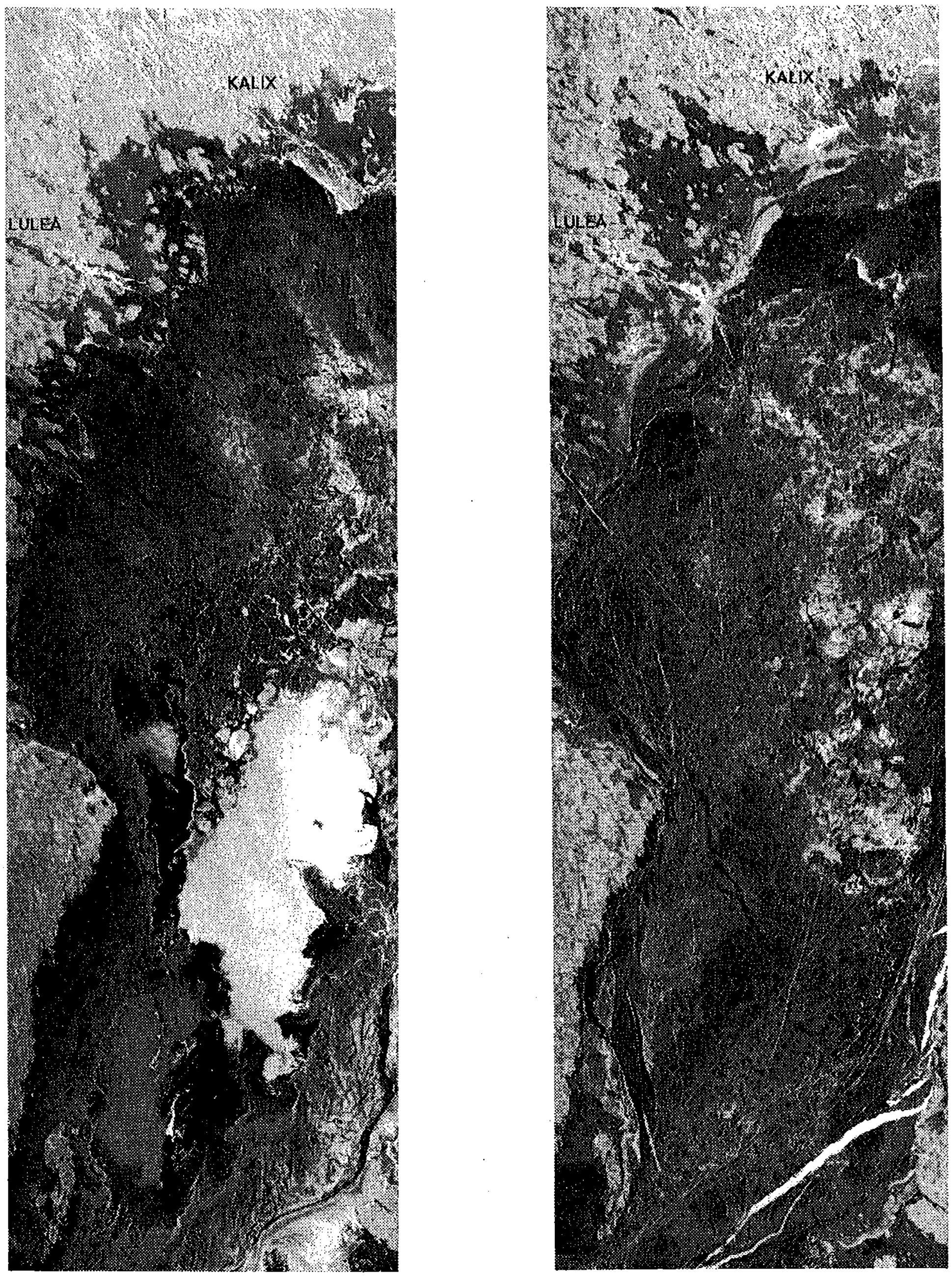

(a) 20 February 1992 © ESA 1992 (b) 5 March 1994 © ESA 1994

Figure 3. ERS-1 SAR images of the Bay of Bothnia at maximum ice extent. Level ice is dark or grey, and deformed ice is bright or very bright. Ship tracks are bright straight lines, and open water leads are very bright. Each image is 100 x 300 km.

Four icebreakers (*Atle*, *Frej*, *Oden* and *Ymer*) were equipped to receive satellite images during BEERS-93. However, since the ERS-1 orbit was in an unfavourable configuration and the winter was very mild, no operational demonstration was attempted except in support of the field experiment. A new SAR image data product was tested during BEERS-93: 100-m resolution images which were received over the *Internet* computer network. This proved to be quite successful with shorter access time after the satellite overpass. The 100-m images were received with a delay of 4 hours compared to 14-24 hours for the 30-m images via satellite link (Thompson *et al.* 1994).

The main operational demonstration was carried out during BEERS-94 between January and March 1994. Both 30-m and 100-m resolution images were transferred to SMHI over satellite and computer link, respectively. Five icebreakers (*Atle*, *Frej*, *Oden*, *Tor* and *Ymer*) were equipped with image reception equipment of the total seven icebreakers (also *Ale* and *Baltica*) in operation. Images were used for both assistance and routing of ships, and also for the ice chart production at SMHI. The 100-m images were received at SMHI about 2 hours after the satellite overpass. Users at the sea ice services and on-board the icebreakers were asked to fill out log files which were used to evaluate the use of the ERS-1 SAR images.

## 5. Summary of results

The main results from the Swedish BEERS research programme are reported in chapters B-H of this report. Results have also been presented in conference papers (Thompson *et al.* 1992a, Ulander 1992, Carlström *et al.* 1993, Askne *et al.* 1994, Carlström *et al.* 1994a, Carlström *et al.* 1994b, Thompson *et al.* 1994), journal papers (Carlström and Ulander 1994, Håkansson *et al.* 1994) and data reports (Carlström 1993, Ulander and Carlström 1993, Carlström 1994). Some research projects have not yet been completed and are deferred for future work, *e.g.* analysis of the CARABAS SAR imagery. In the following sections a brief summary of the main results is given.

### *5.1 Calibration and Validation*

Sea ice information in ERS-1 SAR images is mainly retrieved from image brightness variations. Interpretation and analysis of the images requires that sensor-induced radiometric variations are removed, *i.e.* radiometric calibration. The radar backscattering coefficient $\sigma^o$ is thus the primary observable which also is the link to electromagnetic scattering models and image inversion to retrieve geophysical information.

Radiometric calibration of different data products is described and evaluated in chapter B. ESA provides calibrated precision images (PRI) but these are available after a few weeks after the satellite overpass, which is not satisfactory for winter navigation applications. The accuracy of the PRI radiometric calibration is ±0.8 dB (max. error) corresponding to ±10% in pixel values. Special corrections may be applied which improve the accuracy a factor of two. Radiometric calibration of fast-delivery images has been developed and evaluated during BEERS. The estimated accuracy is ±1 dB (max. error) corresponding to 12% in pixel value, but is restricted to the 10-90 km image swath.

The principle mechanisms which control the image brightness is investigated by comparing backscattering coefficients with *in situ* measurements in chapter D. The conclusion is that the image brightness during cold conditions is mainly related to vertical surface height variations on the mm to dm scale. This is an important result since it shows the direct relationship to ice deformation which is the principle parameter of interest for winter navigation. A dry snow layer is essentially transparent to the radar wave, but wet snow significantly changes the backscattering due to a dramatic effect, but larger values cause the ice surface to be masked and the backscattering is completely controlled by the wet snow surface. Since the snow surface roughness is not necessarily correlated to the ice roughness, identification of deformed areas becomes difficult. For ridges and hummocks consisting of large ice blocks, the backscattering has two contributions: flat ice blocks and super-imposed small-scale roughness. Based on *in situ* data, it is concluded that specular reflections from the flat block surfaces dominate, with the block slope distribution as the major parameter, while the small-scale roughness is of less importance. These results have also been used to construct an inverse model, which estimates the RMS surface height from a SAR image acquired during cold conditions.

The relation between ice deformation and SAR image characteristics is further analysed using helicopter photography in chapter E. The image brightness variations are characterised by the radar signature, which is defined by the mean and the coefficient of variation of the backscattering coefficient. The results show good correlation between different ice deformation classes and the radar signature, both during dry and wet conditions. However, the number of ice deformation classes which can be discriminated decreases during wet conditions. It is concluded that it is possible to discriminate up to seven and three classes during dry and wet conditions, respectively. However, the radar signature seems to change slightly for different years which limits the number to three or two broad classes during dry and wet conditions, respectively. The radar signature is not able to discriminate open water leads from ice, but this is not a major problem since a trained operator may visually discriminate the two rather easily. Information about the air temperature, precipitation, wind speed and direction improve interpretation accuracy.

The effects of temperature changes and precipitation during cold conditions is evaluated in chapter F. Time series of SAR image brightness for a number of test sites show no significant correlation with air temperature or precipitation except for reference sites located on land. The image brightness over sea ice is known to change significantly when the temperature rises above 0°C but this effect has not been quantified and is deferred for future work.

The correlation between icebreaker performance and SAR image brightness is investigated in chapter G. Ice resistance for different ice classes has been determined from measured ship performance data during BEERS-93 and BEERS-94. The results show that the ice resistance depends on the construction of the icebreaker. Preliminary analysis of the ERS-1 SAR images show a good correlation between image brightness and ice resistance, which opens up the possibility of more efficient use of the icebreakers for routing and assistance. More work is required to confirm these preliminary results.

A new and relatively unexplored technique is SAR interferometry which is studied in chapter H. It uses interference between two complex-valued images to obtain information on surface topography and small-scale motion. Movements in the fast ice have been measured with mm-accuracy and an attempt to determine ridge heights was also performed. In the latter case, however, the ambiguity between height and motion introduced large errors. The technique opens up the possibility of estimating displacement and stress fields on mechanical constructions.

### 5.2 Application Demonstration

Chapter C describes and evaluates the operational use of ERS-1 SAR images during the main experiment BEERS-94. The results demonstrate that SAR images were always used at the sea ice services when the sea ice was deforming, *i.e.* the ice field was converging or diverging, and when ice drift or ice growth took place. The problems encountered mainly concerned the technical restrictions of the ERS-1 SAR image data products with respect to spatial and temporal sampling.

For operational use in practise, it is essential to have a frequent coverage of the entire Baltic Sea area. The coverage of the ERS-1 SAR is too limited both in terms of swath width and processing capability. It is furthermore essential to minimise the delay after satellite acquisition before the user can access the data, *i.e.* a few hours. The latter imposes strict requirements on the different parts of the ground segment, including both processing chain and dissemination of images to the end user on the icebreaker.

A resolution of 200 m gave adequate information onboard the icebreakers, although 100-m resolution was preferred to preserve the small-scale features. At present, a finer resolution than 100 m severely limits the spatial coverage due to the limited bandwidth available in the communication link to the icebreakers. Reception of the SAR images onboard the icebreakers was quite successful and turned out to be very useful for both ship routing and assistance. Routing of cargo vessels with a high ice class is probably the most important operational application since it may save both energy and time for the icebreakers.

## Acknowledgements

The BEERS project has been funded and supported by the Swedish National Space Board ("The ERS-1 Project", headed by Prof. Jan Askne), the European Space Agency (ERS-1 SAR images and receiving facility at SMHI in Norrköping), the National Maritime Administration (icebreaker support), and COLDTECH (BEERS-92 land station). The Principal Investigator of the Swedish BEERS research project is Dr. Thomas Thompson, and co-investigators are Prof. Jan Askne, Dr. Hans Ottersten, and Mr. Olov Fäst. Special thanks to all the Swedish and Finnish scientists who participated in the field experiments, together with the captains, officers, and crew of the involved icebreakers including helicopter RX.

## References

ASKNE, J., LEPPÄRANTA, M. AND THOMPSON, T., 1992, The Bothnian Experiment in Preparation for ERS-1, 1988 (BEPERS-88) - an overview, *International Journal of Remote Sensing*, **13,** 2377-2398.

ASKNE, J., THOMPSON, T., OTTERSTEN, H. AND FÄST, O., 1994, From Research to Operational Ice Service using ERS-1, The Swedish Sea Ice Service for the Baltic, *Proceedings of the 13th EARSeL Symposium held in Dundee, 28 June - 1 July 1993*, (Budapest: Springer-Verlag), pp. 11-17.

BLOMQUIST, Å., PILO, C. AND THOMPSON, T., 1976, SEA ICE-75, Summary Report, Research Report 16:9, Winter Navigation Research Board, Swedish Administration of Shipping and Navigation, Norrköping, and Finnish Board of Navigation, Helsinki.

CARLSTRÖM, A., 1993, Baltic Experiment for ERS-1, BEERS-93: Swedish Calibration/Validation Data Report, Internal Report RSG 1993:3, Department of Radio and Space Science, Chalmers University of Technology, Göteborg.

CARLSTRÖM, A., 1994, Baltic Experiment for ERS-1, BEERS-94 Data Report, Internal Report RSG 1994:2, Department of Radio and Space Science, Chalmers University of Technology, Göteborg.

CARLSTRÖM, A., ULANDER, L., GUSTAVSSON, A., OTTERSTEN, H., HÅKANSSON, B. AND THOMPSON, T., 1993, Iskartläggning med radarsatellit - experimentet BEERS-92, *Proceedings of RVK-93 held in Lund, 5-8 April 1993*, (Lund: Lunds Tekniska Högskola), pp. 17-20.

CARLSTRÖM, A. AND ULANDER, L. M. H., 1994, Validation of Backscatter Models for Level and Deformed Sea Ice in ERS-1 SAR Images, *International Journal of Remote Sensing*, in press

CARLSTRÖM, A., ULANDER, L. M. H. AND DIERKING, W., 1994a, Influence of Ice and Snow Properties on Ice Ridge Mapping by SAR, *Proceedings of the 14th EARSeL Symposium held in Göteborg, Sweden, 6-8 June 1994*, in press

CARLSTRÖM, A., ULANDER, L. M. H. AND HÅKANSSON, B., 1994b, Model for Estimating Surface Roughness of Level and Ridged Sea Ice using ERS-1 SAR, *Proceedings of IGARSS'94 held in Pasadena, CA, 8-12 August 1994*, 94CH3378-7 (Piscataway: IEEE), pp. 168-170.

GUSTAVSSON, A., FRÖLIND, P. O., HELLSTEN, H., JONSSON, T., LARSSON, B. AND STENSTRÖM, G., 1993, The Airborne VHF SAR System CARABAS, *Proceedings of IGARSS'93 held in Tokyo, Japan, 18-21 August 1993*, (Piscataway: IEEE), pp. 558-562.

HAUTANIEMI, H., OKSAMA, M., MULTALA, J., LEPPÄRANTA, M., RISKA, K. AND SALMELA, O., 1994, Airborne Electromagnetic Mapping of Ice Thickness in the Baltic Sea, *Proceedings of IAHR Ice Symposium held in Trondheim, 23-26 August 1994*, (Trondheim: Norwegian Institute of Technology), pp. 530-539.

HERLAND, E.-A., 1994, Operational Ice Monitoring with the ERS-1 SAR, *Earth Observation Quarterly*, **45,** 6-8.

HERLAND, E.-A., SEINÄ, A. AND LEPPÄRANTA, M., 1994, ISY Real Time Ice Monitoring Demonstration in The Baltic Sea, Contract Report 125475, European Space Agency, Paris.

HÅKANSSON, B., MOBERG, M. AND THOMPSON, T., 1994, Real-Time Use of ERS-1 SAR Imagery for Ice Service and Icebreaking Operations in the Baltic Sea, *International Journal of Remote Sensing*, in press

LEPPÄRANTA, M. AND HAKALA, R., 1992, The Structure and Strength of First-Year Ice Ridges in the Baltic Sea, *Cold Regions Science and Technology*, **20,** 295-311.

LEPPÄRANTA, M., KUITTINEN, R. AND ASKNE, J., 1992, BEPERS Pilot Study: an Experiment with X-band Synthetic Aperture Radar over Baltic Sea ice, *Journal of Glaciology*, **38,** 23-35.

LEPPÄRANTA, M. AND THOMPSON, T., 1989, BEPERS-88, Sea Ice Remote Sensing with Synthetic Aperture Radar in the Baltic Sea, *EOS*, **70,** 698-699, 708-709.

PALOSUO, E., 1975, The Formation and Structure of Ice Ridges in the Baltic, Research Report 12, Winter Navigation Research Board, Helsinki and Stockholm.

PELTONIEMI, M., 1982, Characteristics and Results of an Airborne Electromagnetic Method of Geophysical Surveying, Bulletin 321, Geological Survey of Finland, Espoo.

PIPOR, 1985, A Programme for International Polar Oceans Research (PIPOR), SP-1074, European Space Agency, Paris.

SEINÄ, A. AND PALOSUO, E., 1993, The Classification of the Maximum Annual Extent of the Ice Cover in the Baltic Sea 1720-1992, *Meri*, **20**, 5-29.

SMHI AND FIMR, 1982, *Climatological Ice Atlas for the Baltic Sea, Kattegat, Skagerrak and Lake Vänern (1963-1979)* (Norrköping: Swedish Meteorological and Hydrological Institute, and Helsinki: Finnish Institute for Marine Research).

THOMPSON, T., 1986, Ice Surveillance by Satellite, *Proceedings of POLARTECH'86 held in Helsinki, 27-30 October 1986*, , pp. 179-186.

THOMPSON, T., HÅKANSSON, B., ULANDER, L. AND CARLSTRÖM, A., 1992a, Experiences from the Swedish Sea Ice Programme during BEERS-92, *Proceedings of the First ERS-1 Symposium held in Cannes, France, 4-6 November 1992*, SP-359 (Paris: European Space Agency), pp. 313-318.

THOMPSON, T., HÅKANSSON, B., ULANDER, L., CARLSTRÖM, A., GUSTAVSSON, A. AND LARSSON, B., 1994, The Use of ERS-1 SAR Data for Sea Ice Mapping and Icebreaker Operations in the Gulf of Bothnia, *Proceedings of the Second ERS-1 Symposium held in Hamburg, Germany, 11-14 October 1993*, SP-361 (Paris: European Space Agency), pp. 271-276.

THOMPSON, T., ULANDER, L., HÅKANSSON, B., BRUSMARK, B., CARLSTRÖM, A., GUSTAVSSON, A., CRONSTRÖM, E. AND FAEST, O., 1992b, BEERS-92, Baltic experiment for ERS-1, Experiment Plan, SMHI Oceanography 50, Swedish Meteorological and Hydrological Institute, Norrköping.

ULANDER, L. M. H., 1991, Radar Remote Sensing of Sea Ice: Measurements and Theory, Technical Report No. 212, Chalmers University of Technology, Göteborg.

ULANDER, L. M. H., 1992, Calibration of the ERS-1 SAR Fast-Delivery Images, *Proceedings of the First ERS-1 Symposium held in Cannes, France, 4-6 November 1992*, SP-359 (Paris: European Space Agency), pp. 173-178.

ULANDER, L. M. H. AND CARLSTRÖM, A., 1993, Baltic Experiment for ERS-1, BEERS-92: Swedish Calibration/Validation Data Report, Internal Report RSG 1993:1, Department of Radio and Space Science, Chalmers University of Technology, Göteborg.

VASS, P. AND BATTRICK, B., 1992, ERS-1 System, SP-1146, European Space Agency, Paris.

WMO, 1989, Sea-Ice Nomenclature, No. 259. TP. 145, World Meteorological Organization, Geneva.

# B. DESCRIPTION AND CALIBRATION OF ERS-1 SAR IMAGES

LARS M.H. ULANDER

Department of Radio and Space Science
Chalmers University of Technology
S-412 96 Göteborg, Sweden

**Abstract.** We describe basic properties of the ERS-1 SAR and different image data products used during the BEERS programme. A major problem with SAR images is the presence of speckle noise due to interfering scattering elements within a resolution cell. Speckle noise increases radiometric resolution, but can be reduced by spatial averaging at the expense of increased spatial resolution. We also study different methods for radiometric calibration of precision images (PRI) and fast-delivery images (FD or UI16), *i.e.* retrieval of the radar backscattering coefficient. Radiometric calibration of PRI images can be performed entirely based on the header information supplied with the data. The estimated accuracy is ±0.4 dB (max. error) within the image dynamic range, after special corrections for pulse replica power and saturation effects. Without these corrections, the accuracy is estimated to ±0.8 dB (max. error). FD calibration can also be performed based on the header information by additionally assuming that the image geometry is close to the nominal, *i.e.* the mid-swath incidence angle is 23°. Analysis shows that this is a good assumption and that the worst-case observed deviation is ±0.2°. The FD calibration constant has been determined with two different methods which result in slightly different values. The estimated accuracy of the FD calibration is ±1 dB (max. error) within the 10-90 km ground range interval.

## 1. Introduction

In the present chapter, we discuss characteristics of the ERS-1 synthetic-aperture radar (SAR) images used during the BEERS programme. The chapter starts with a brief description of the ERS-1 SAR images followed by a study of different methods to perform radiometric calibration, *i.e.* to retrieve the radar backscattering coefficient. The latter is a linear function of the mean-squared pixel value in an area of interest, and is defined to be a measure of surface characteristics and independent of SAR system parameters, *e.g.* antenna gain pattern, range spreading loss *etc*. The radar backscattering coefficient is also useful since it enables a direct comparison with electromagnetic scattering models (see chapter D) and with measurements made by other radar systems, *e.g.* scatterometers. Since the ERS-1 SAR is a very stable system, pixel value statistics can in fact also be used to study relative changes of the radar backscatter within and inbetween images (see chapters F and G). Note, however, that this simplified method is only valid for a constant ground range, *i.e.* systematic changes occur across the image as the ground range changes which must be taken into account.

## 2. Description of the ERS-1 SAR images

The ERS-1 SAR produces images along 100 km wide strips with a resolution of about 25 m as illustrated in figure 1. SAR images are essentially maps of the radar backscatter from the Earth's surface, which are used to retrieve information about surface characteristics independent of daylight, clouds and precipitation (Ulaby *et al.* 1986). The ERS-1 SAR operates with a centre frequency of 5.3 GHz, which corresponds to a wavelength of 5.7 cm, and vertical polarisation for both transmission and reception (VV). The incidence angle varies between 19° and 26° across the swath, with a nominal value of 23° at mid swath.

SAR images are corrupted by speckle noise which results from constructive or destructive interference between different scattering elements within a resolution element (Ulaby *et al.* 1986). Speckle is called multiplicative noise since the statistical fluctuation (standard deviation) is proportional to the average value. It is an inherent property of coherent imaging systems with a resolution much larger than the wavelength. Speckle results in large statistical fluctuations of the brightness and the image must be averaged to give confident results. Standard 25-m resolution ERS-1 SAR images are based on averaging three independent samples whereas 100-m images have approximately thirty independent samples. The coefficient of variation is 30% and 10%, respectively, for the image pixel values (Ulaby *et al.* 1986), *i.e.* there is much less speckle noise in the 100-m images. Additive noise is also present in SAR images and sets the lower limit for the dynamic range of the image, whereas saturation in the analogue-to-digital converters sets the upper limit.

ERS-1 SAR images are produced by the European Space Agency (ESA) in the form of different data products. Four products have been used during the BEERS programme: Precision images (PRI), fast-delivery images (UI16, also called FD), and low-resolution images (UILR and LRI) (Vass and Battrick 1992, Solaas and Laur 1993). All products have a nominal size of 100 x 100 km$^2$ but differ in other characteristics as indicated in table 1. Number of looks is the number of independent samples which have been averaged to reduce speckle noise. The averaging is called look summation and may be performed either as an arithmetic mean (amplitude) or a root-mean-square operation (power).

Table 1. Characteristics of a selection of the ERS-1 SAR data products. PRI is produced at the ESA Product and Archiving Facilities (PAFs), FD (UI16) at the Kiruna and Fucino receiving stations, UILR at ESA ESRIN in Frascati or ESTEC in Noordwijk, and LRI at Tromsö Satellite Station. Pixel size and resolution is given in ground range versus azimuth.

| Product | Pixel size (m) | Resolution (m) | Bits | Looks | Look summation |
|---|---|---|---|---|---|
| PRI | 12.5 x 12.5 | 25 x 22 | 16 | 3 | Power |
| FD (UI16) | 20.0 x 15.9 | ~ 25 x 22 | 16 | 3 | Amplitude |
| UILR | 100 x 100 | ~ 100 x 100 | 8 | ~ 30 | Amplitude |
| LRI | 100 x 80 | ~ 100 x 80 | 16 | ~ 30 | Power |

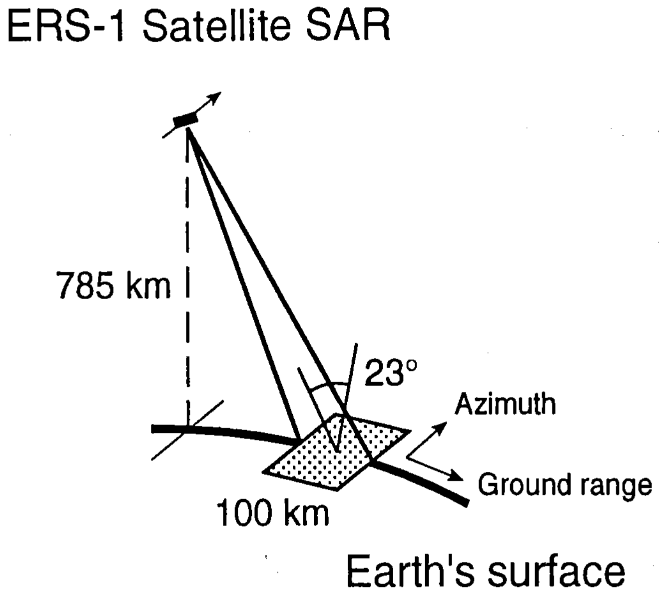

Figure 1. Illustration of the imaging geometry of the ERS-1 SAR.

## 3. SAR radiometric calibration

### 3.1. Introduction

Prior to image analysis, it is important to calibrate the images in order to remove sensor-induced artefacts. SAR calibration in general involves geometric, radiometric and phase calibration (Freeman 1992). In the present study, we will concentrate on radiometric calibration, *i.e.* relating an image pixel value to a radar backscatter value. The presence of speckle, however, means that a single pixel value has little statistical significance and that radar backscatter of extended objects is a random variable.

The PRI images are calibrated and corrected data products from which radar backscatter can easily be derived. Note, however, that geometric and radiometric corrections have been made with respect to an ellipsoidal Earth model which is adequate over sea ice and ocean but not over land. The FD product, on the other hand, is intended for rapid dissemination to users over satellite link. Corrections are only applied for geometric calibration but not for radiometric calibration.

Radiometric calibration of PRI images has been described by (Laur 1992, Laur *et al.* 1993). The calibration accuracy has continuously improved to the present ±0.4 dB (max. error) within the image dynamic range. This level of accuracy can only be achieved with special correction factors, *i.e.* corrections due to replica pulse power variations and analogue-to-digital converter saturation. Without these corrections, the accuracy is limited to ±0.8 dB (max. error).

The FD data product is not radiometrically calibrated but the high stability of the SAR system means good repeatability for backscatter measurements (Ulander 1992). In the next sections, we show that constant correction factors may be applied to the FD images to perform radiometric calibration.

### 3.2. Definitions

The basis for radiometric calibration is the concept of radar cross section (RCS) $\sigma$, which is defined for objects which behave as point targets (Ulaby *et al.* 1986). The RCS of an object can be measured relative a metallic sphere (radius >> wavelength), since the sphere RCS is equal to its geometrical cross section. The unknown RCS is thus equal to the cross-section area of the sphere which produces the same returned power to the radar as the object.

For extended objects (distributed targets) it is more convenient to use the average RCS per unit ground area, *i.e.* the backscattering coefficient $\sigma^o$. Averaging is necessary since a single sample has little significance due to the speckle as described earlier.

### 3.3. Radiometric calibration at constant range

The simplest case is to establish the radiometric calibration of the ERS-1 SAR images at constant range. This may be done by deploying a point target with accurately known $\sigma$ as a reference. An accurate and robust calibration can then be formulated based on the following equation (Gray *et al.* 1990, Ulander 1990, Ulander 1991)

$$\sigma^o = \kappa \xi \left( \frac{\sigma}{E} \right) P_{\sigma^o} \qquad (1)$$

where $E$ is the point target energy, $P_{\sigma^o}$ is the average image power (pixel value squared) of the distributed target with the noise power subtracted, $\kappa$ is a projection-factor from image to ground area and $\xi$ is dependent on the look summation technique used by the processor. The point target energy is determined by area integrating the image power over the point target response and subtracting the average background power.

A number of assumptions are implicit in (1). Most important is that the system is linear (with exception of the detection process) and that the system impulse response is spatially confined with low sidelobes and ambiguities.

The $\kappa$-factor depends on the geometry in which the image is represented. A special and important case is when the image has been transformed to ground coordinates, in which case $\kappa = 1$. This is true for the image products we consider over horizontal and flat surfaces such as sea ice.

The $\xi$-factor depends on the look summation in the processor, which may be performed either in amplitude or power as shown in table 1. The nominal case is power look summation for which $\xi = 1$. For amplitude look summation, an approximate expression is given by (Ulander 1990)

$$\xi = \frac{N}{1 + \frac{\pi}{4}(N-1)} \qquad (2)$$

where $N$ is the number of looks. In deriving (2), it is assumed that looks are independent and that the amplitude pixel values are squared prior to averaging. The interpretation of (2) is that the statistics of the distributed target are distorted by exchanging the order of look summation and squaring.

### 3.4. Radiometric calibration across the image

The calibration procedure according to (1) is used to determine the backscattering coefficient in the vicinity of a reference point target. Farther away we also have to account of system gain variations, *e.g.* antenna elevation gain pattern and range spreading loss. The starting point for deriving the image power of a distributed target is the radar equation, which gives the received power $P_r$ for a single transmitted pulse in terms of system parameters (Ulaby *et al.* 1986), *i.e.*

$$P_r = \frac{P_t \lambda^2 G_{tot}^2 \sigma}{(4\pi)^3 R^4 L} \tag{3}$$

where $P_t$ is the peak transmitted power, $\lambda$ is the radar wavelength, $G_{tot}$ is the one-way antenna gain (azimuth and elevation), $R$ is the slant range, $L$ is losses, and $\sigma$ is the RCS of the illuminated area. During SAR processing, a number of received pulses are processed through filters which affect the output image. A critical point is the normalisation of the filter coefficients which affects the dependency on slant range (Freeman and Curlander 1989). Independent of the normalisation, however, it can be shown that the ratio of the average image power over a horizontal distributed target $P_{\sigma^o}$ and the average noise power $P_n$ is given by (Ulander *et al.* 1991)

$$\frac{P_{\sigma^o}}{P_n} = \frac{P_{ave}}{v} \frac{\lambda^3 c}{4(4\pi)^3 k_B T_s B_r L} \frac{G^2}{R^3 \sin\theta_i} \sigma^o \propto \frac{G^2}{R^3 \sin\theta_i} \sigma^o \tag{4}$$

where $P_{ave}$ is the average transmitted power, $v$ is the in-orbit satellite velocity, $c$ is the velocity of light, $k_B$ is Boltzmann's constant, $T_s$ is the system noise temperature, $B_r$ is the receiver bandwidth, $G$ is the one-way antenna gain in elevation, $\theta_i$ is the local incidence angle, and the loss $L$ now also includes processing loss. The proportionality before the last expression in (4) assumes that the system is stable.

## 4. ERS-1 SAR radiometric calibration

### 4.1 Radiometric calibration equation

The SAR processors which are used to produce the ESA ERS-1 SAR images give a constant average noise power across the image, *i.e.* backscattering coefficient may be determined from (4) according to

$$\sigma^o = \frac{f}{K} P_{\sigma^o} = \frac{f}{K}(P - P_n) = \frac{f}{K}\left(\langle DN^2 \rangle - DN_n^2\right) = \frac{f}{K}\langle DN^2 \rangle - \sigma_{ne}^o \tag{5}$$

where $P = P_{\sigma^o} + P_n$ is the total average image power of the distributed target (including noise), $f$ is the range correction, $K$ is the calibration constant, $DN$ (digital number) is the pixel value, $DN_n$ is the rms noise pixel value, and $\sigma^o_{ne}$ is the noise-equivalent backscattering coefficient. Alternative forms are given in (5) which will be discussed in the following. If no radiometric corrections have been applied to the processor output, the range correction may be defined according to

$$f = \left(\frac{R}{R_{ref}}\right)^3 \frac{\sin\theta_i}{\sin\theta_{ref}} \frac{G^2(\vartheta_{ref})}{G^2(\vartheta)} \tag{6}$$

where we have introduced the antenna elevation angle $\vartheta$, and reference values $R_{ref}$, $\theta_{ref}$, and $\vartheta_{ref}$. The values adopted for ERS-1 SAR are: $R_{ref} = 847$ km, $\theta_{ref} = 23°$ and $\vartheta_{ref} = 20.35°$(Laur 1992).

Equation (6) is applicable to FD images, but not to PRI images since a range-dependent correction has been applied. Corrections for antenna gain and range spreading loss are applied to PRI images which results in the following calibration equation (Laur 1992)

$$\sigma^o = \frac{1}{K_{PRI}} \frac{\sin\theta_i}{\sin\theta_{ref}} \langle DN^2 \rangle - \sigma^o_{ne} \tag{7}$$

where $K_{PRI}$ is the PRI calibration constant given in the image header. Special range corrections apply for early PRI products, *i.e.* those processed before 1 September 1992 (Laur 1992) and for those processed at the UK PAF before 8 April 1993 (UK-PAF 1993).

### *4.2 Internal calibration*

The ERS-1 SAR was designed to use three internal calibration measurements, *i.e.* calibration pulse, replica pulse and noise measurements (Carter 1989). At the start and end of each SAR imaging sequence, a set of calibration pulse and noise measurements are performed. During an imaging sequence, one replica pulse appears in the data for each 24 transmitted pulses (Laur *et al.* 1993).

The original intention was to use the calibration pulse for normalisation of system gain drifts and the replica pulse for compression of the transmitted chirp pulse. However, all the ESA PRI processors use the replica pulse for both gain normalisation and pulse compression. This would be satisfactory if the replica pulse power was proportional to the system gain, but studies have shown that this is not the case (Laur *et al.* 1993). Both the calibration and replica pulse powers are normally stable to within ±0.1 dB (rms), but anomalous replica pulse power variations of up to 2 dB are observed during short periods. The consequence of this is that PRI image power values should be multiplied by the ratio of the image replica power given in the image header information and the reference value 205229 (Laur *et al.* 1993). A separate correction for calibration pulse power variations is not necessary due to the high stability of the system. It should be noticed that the pulse replica power correction should not be applied to FD images, since the gain normalisation has not been performed for these images.

### *4.3 Noise-equivalent backscattering coefficient*

In general, the noise-equivalent backscattering coefficient in (5) varies across the swath. It is therefore convenient to define a reference value corresponding to the reference geometry. The PRI header includes this value which varies in the range

$$\sigma^o_{ne,ref} = -25.5 \pm 0.5 \text{ dB} \tag{8}$$

The noise-equivalent backscattering coefficient across the image is determined by

$$\sigma^o_{ne} = f\,\sigma^o_{ne,ref} \tag{9}$$

It is useful to note that the rms noise pixel value is constant across the swath if no corrections have been applied, *i.e.* for FD, UILR and LRI images. The rms noise pixel value follows from (5)

$$DN_n^2 = \frac{K}{f}\sigma^o_{ne} = K\,\sigma^o_{ne,ref} \tag{10}$$

### *4.4 Range correction factor*

The range correction factor $f$ defined in (6) is important for two reasons: Firstly, it is the calibration correction across the image which is applied to retrieve the backscattering coefficient from FD images using (5). Secondly, it is used to determine the noise-equivalent backscattering coefficient from the reference value according to (9).

The satellite geometry is shown in figure 2 where the parameters $R$, $\theta_i$ and $\vartheta$ in (6) are indicated. Determination of the range correction requires that these parameters are known for each pixel in the image, although it in practise is sufficient to compute them with a spacing of a few hundred metres. There are two different methods to determine the range correction depending on whether a PRI image is available or not. Both methods assume that the antenna boresight is pointing at a fixed elevation angle of 20.35°. This means that $\vartheta$ - 20.35° is the elevation angle relative to antenna boresight. A single look-up table can then be used to determine the antenna gain. The error introduced by this assumption may be neglected since the antenna pointing error is less than ±0.03° due to the three-axis stabilisation of the satellite.

The first method to determine the range correction is based on the header information of a PRI image and is discussed in (Laur *et al.* 1993). The header includes information on $R$ and $\theta_i$ at the near edge of the image. The header also includes information on the image geodetic latitude $\lambda$ which together with the GEM-6 ellipsoid model gives the Earth radius $R_e$ according to

$$R_e = a\sqrt{\frac{\cos^2\lambda + (b/a)^4\sin^2\lambda}{\cos^2\lambda + (b/a)^2\sin^2\lambda}} \tag{11}$$

where $a$ is the equatorial Earth radius (= 6378.144 km) and $b$ is the polar Earth radius (= 6356.759 km). The satellite radius $R_s$ is then be given by

$$R_s = \sqrt{R_e^2 + R^2 + 2R_eR\cos\theta_i} \tag{12}$$

Values of $R$, $\theta_i$ and $\vartheta$ may now be determined using simple trigonometric formulas for each pixel.

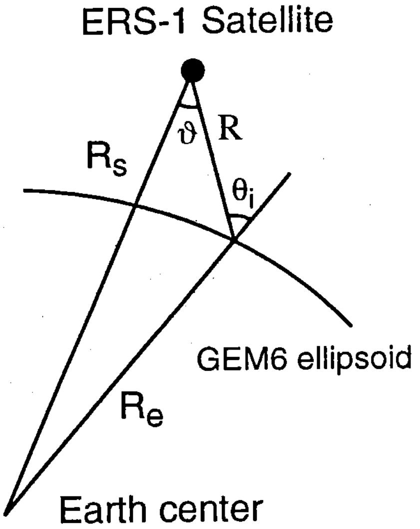

Figure 2. Image geometry for calculation of range correction factor.

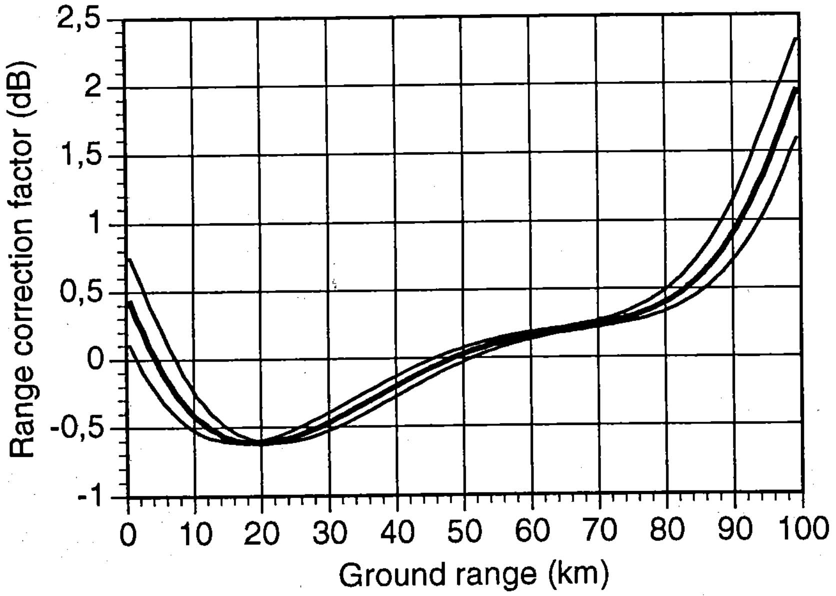

Figure 3. Range correction factor the FD images used for BEERS. The thicker line corresponds to the nominal image geometry, and the thinner lines to the worst-case observed deviation (±0.2° in incidence angle). Radiometric calibration is normally only performed for ground ranges 10 - 90 km.

The second method is used when the PRI header information is not available. The FD header also includes information on the near edge range but not the corresponding incidence angle, which means that the first method cannot be directly applied. Instead, we assume that the incidence angle in the middle of the image is equal to the nominal value of 23°. The corresponding nominal incidence angle at the near edge is 19.4°. Analysis of the PRI header information shows that the deviation from this value is mostly less than ±0.1° and never more than ±0.2°. With this assumption we could follow the first method and use (11) and (12) to determine a range correction for each image. However, due to the stable orbit it is often sufficient to use a single range correction for all images in the same region and for a single orbit phase. The range correction used for the BEERS images is shown in figure 3 and is based on $R_S = 7149$ km. The figure also shows the range correction for the worst case error of 0.2° from the nominal incidence angle. It should be noticed that the largest uncertainties occur at the edge of the swath due to the fall off of the antenna gain pattern. We therefore restrict the calibration to the 10 - 90 km swath, which gives a maximum error of ±0.25 dB.

## 5. Radiometric calibration of FD images

### 5.1 Calibration experiment during BEERS-92

A radiometric calibration experiment was conducted during BEERS-92 in order to establish the FD calibration constant. The experiment was planned and carried out in parallel with the ESA calibration experiments in Flevoland. This was motivated by the need to retrieve backscattering coefficients during BEERS-92, whether the ERS-1 SAR stability would allow extrapolation of the Flevoland results or not.

Two precision radar reflectors (trihedrals) were manufactured with a side length of 1.72 m. The theoretical maximum RCS is 40.6 $\mathrm{dBm}^2$ for 5.3 GHz (Robertson 1947), where the unit $\mathrm{dBm}^2$ is dB relative one square metre. In practise, small deformations of the trihedrals from their ideal shape together with diffraction from the edges introduce uncertainties. The actual RCS was not measured but other investigations have indicated that the accuracy of a precision trihedral is better than ±0.5 dB (Ulander *et al.* 1991, Bird *et al.* 1993). A thin plastic radome was used to cover the trihedrals but is not expected to introduce any significant additional errors. The azimuth and elevation angles were carefully adjusted so that the trihedrals would provide the maximum RCS. The error caused by mis-pointing can be neglected due to the wide response angle of trihedrals (~ 40°).

The trihedrals were deployed 750 m from each other on the frozen Lake Älgträsket about 50 km south east of the city of Skellefteå. A total of 15 overpasses occurred during the experiment period between 14 February and 30 March. The point target energy $E$ was determined by integrating over a cross-shaped area centred on the point target and subtracting the background clutter and noise power. The latter is estimated from the four remaining corners of the rectangle enclosing the cross. The size of the cross is determined by a trade off between bias due to loss of point target energy and rms error due to coherent interaction with the background (Ulander 1991). We choose a cross where each leg is 3 x 7 resolution cells by considering the impulse response sidelobes, the signal-to-clutter ratio (~ 26 dB), and the number of looks (3). The resulting bias and standard deviation are less than 0.1 dB and 0.2 dB (rms), respectively. In practise, the integration is carried out as a summation after reducing the pixel spacing a factor 8 using a truncated sinc interpolator.

The result from the data analysis is shown in figure 4. It shows that the repeatability of the FD radiometric calibration is ±0.8 dB (max. error). The standard deviation is 0.4 dB which is slightly larger than the expected 0.2 dB based on the background interaction. This result indicates that other random errors also contribute. The fluctuations for the two trihedrals show little correlation, which excludes errors due to system gain fluctuations. Instead, it is more likely that the random error is caused by RCS fluctuations due to wet snow or condensation of water on the radome.

The calibration constant $K_{FD}$ may now be estimated from (1) and (5) using the corrections given in (2) and (3). This results in

$$K_{FD} = \frac{f}{\xi}\frac{E}{\sigma} \doteq 0.31 - 0.67 + 114.2 - 40.6\,\mathrm{dB} = 73.2\,\mathrm{dB}$$

### *5.2 Inter-processor calibration using distributed targets*

An independent method of estimating the calibration constant of the FD images is to use calibrated PRI images as a reference. The basic idea is to analyse FD and PRI images of the same scene, *i.e.* processed from the same raw data. Identical homogeneous areas are selected in the images, a gain factor is determined taking the range-dependent corrections into account, and the calibration constant for FD is determined. Note that the replica pulse power correction is necessary for the PRI data using this approach.

Results from a comparison between FD and PRI from D-PAF is shown in figure 5. Although there is a systematic variation across the image, the range of the variation is only 0.3 dB which is satisfactory. The estimate of $K_{FD}$ is 72.3 dB.

The corresponding comparison for PRI from UK-PAF is shown in figure 6. Again, there is a systematic variation of 0.3 dB across the image although with a slightly different shape. The calibration constant is estimated to 71.9 dB in this case, which differs by 0.4 dB from the estimate based on the D-PAF PRI, and 1.3 dB from the trihedral calibration.

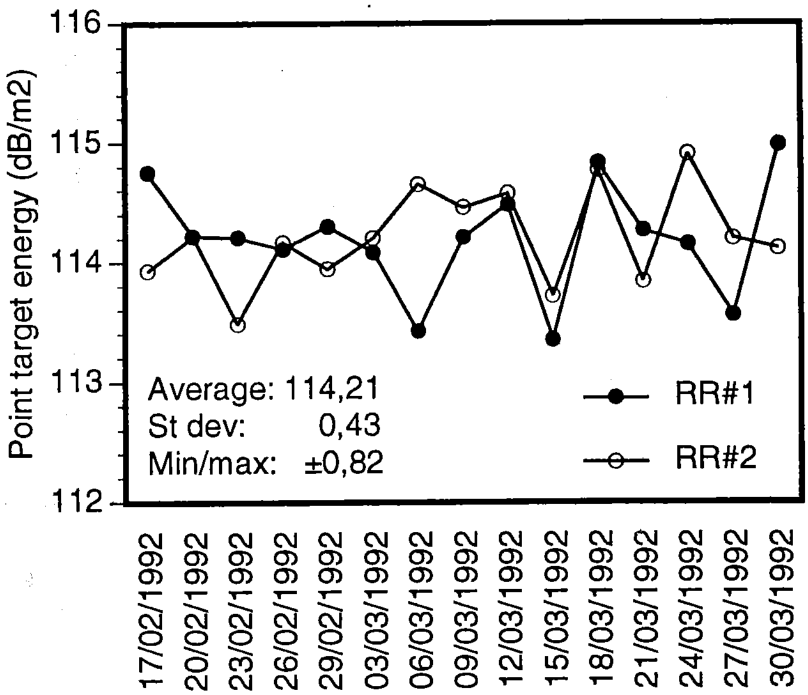

Figure 4. Time series of point target energy for the two trihedrals from FD images.

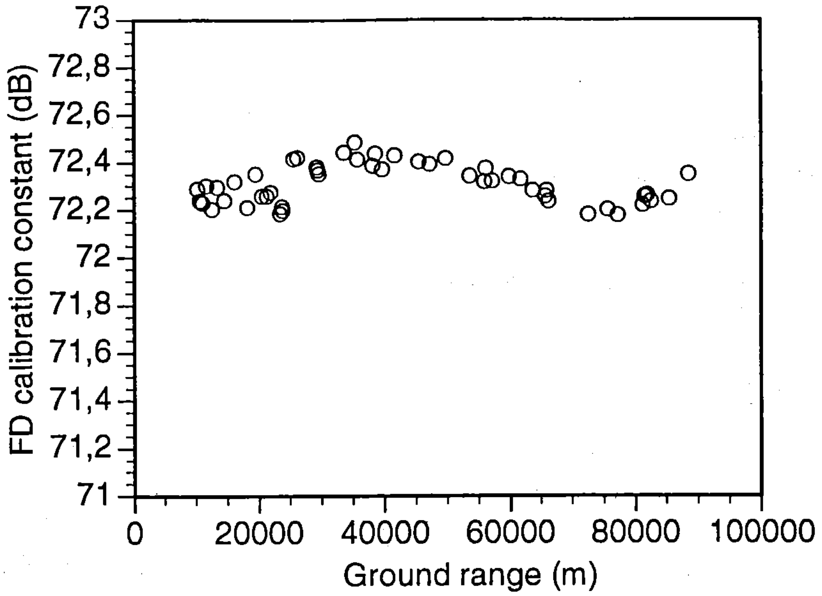

Figure 5. FD calibration constant from D-PAF PRI image (14 March 1993).

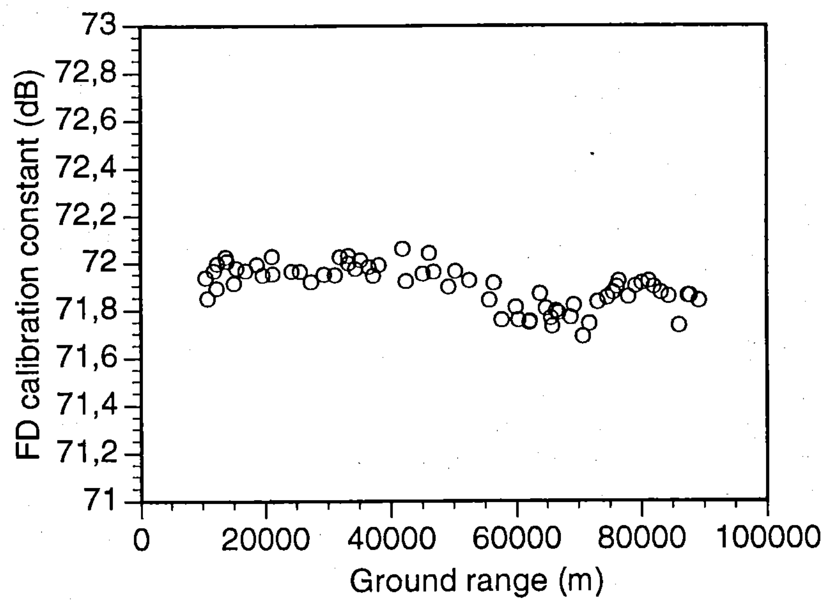

Figure 6. FD calibration constant from UK-PAF PRI image (17 March 1993).

### *5.3 Estimation of the $\xi$-factor*

The calibration equation at a constant range (1) assumes that the $\xi$-factor is accurately known. Independent of the theoretical expression (2), it may also be estimated from the data itself by analysing a distributed target and a point target close to each other in a FD image and a reference image. The latter should be an image from a precision processor and with a minimum of corrections applied. This implies that a single-look complex (SLC) image should be used. The $\xi$-factor for the FD image may thus be estimated by

$$\xi_{FD} = \frac{E_{FD}}{P_{FD}} \frac{P_{SLC}}{E_{SLC}} \sin\theta_i \tag{11}$$

where we have assumed that $\xi = 1$ for the SLC processor. The main difficulty with this estimate is to accurately determine $P$ in the two images. A large homogeneous area is required at approximately the same incidence angle as the point target.

Note that (11) does not require any gain correction and is only based on measured quantities except for the incidence angle which may be accurately determined. There is thus no need to compute a range correction or replica pulse correction.

Analysis of the two trihedrals and corresponding distributed targets in seven pairs of FD and SLC images was carried out which resulted in $\xi = 0.9$ dB. This is about 0.2 dB larger than expected from (2), which is probably due to some other processor-induced artefacts. The standard deviation of the measurements was 0.2 dB which gives a 95% confidence interval of ±0.1 dB for the estimated mean. We thus conclude that the estimate of the FD calibration constant using the trihedrals is

$$K_{FD} = \frac{f}{\xi}\frac{E}{\sigma} \triangleq 0.31 - 0.9 + 114.2 - 40.6\,\mathrm{dB} = 73.0\,\mathrm{dB}$$

## 6. Conclusions

We have described characteristics of the ERS-1 SAR images and different methods for radiometric calibration, *i.e.* retrieval of the radar backscattering coefficient $\sigma^o$.

The radiometric calibration of precision images (PRI) has been performed and verified by ESA with an estimated accuracy of ±0.4 dB (max. error) within the dynamic range of the image. This assumes that corrections for replica pulse power and saturation are applied. If these corrections are not applied, the accuracy is estimated to ±0.8 dB (max. error). PRI calibration is performed based on a few parameters given in the image header.

Fast-delivery images (FD, or UI16) are not calibrated data products and are mainly used for rapid dissemination to users. However, since they provide the most extensive source of ERS-1 SAR images to date, it is desirable that they also can be calibrated. We have shown that this is possible and that the estimated accuracy of ±1 dB (max. error) in the 10 - 90 km swath of the image. Other low-resolution data products which are based on the FD images, *i.e.* UILR (produced by ESA ESRIN or ESTEC) and LRI (produced by Tromsö receiving stations), may also be calibrated using the same methods.

Analysis of a calibration experiment during BEERS-92 using two precision trihedrals showed a rms variation of 0.4 dB with a maximum variation of ±0.8 dB from the average. This indicates the expected repeatability of the calibration. We note in passing that no correction for replica pulse power is needed as is the case for the PRI calibration.

Three corrections are required to perform radiometric calibration of FD images, *i.e.* an absolute calibration constant $K$, a range correction factor $f$, and a rms noise power $DN_n$, according to

$$\sigma^o = \frac{f}{K}\left(\left\langle DN^2\right\rangle - DN_n^2\right) \tag{12}$$

where *DN* is a sample of the FD pixel values in the distributed target area, and < > denotes spatial averaging. The size of the area average depends on the required measurement precision.

The FD range correction cannot be exactly determined from the information given in the image header. However, we may assume the nominal image geometry, *i.e.* that the incidence angle in the middle of the image is 23°. The largest observed deviation from the nominal incidence angle is ±0.2° which results in ±0.25 dB calibration error in the 10 - 90 km part of the imaged swath.

The FD calibration constant has been determined by two different methods. Firstly, it was determined from the BEERS-92 calibration experiment by analysing the response of precision trihedrals. A problem with this approach is that the FD processor sums multiple looks in amplitude which must be accounted for. Other artefacts of the FD processor may also introduce systematic errors. Secondly, the calibration constant was determined by analysing distributed targets in both FD and PRI images and determining the gain between the data products. This analysis was performed for PRI images from both UK-PAF and D-PAF. A problem with this approach is that it relies on the PRI calibration being perfect. This is known not to be true since the UK-PAF and D-PAF calibration differ by about 0.4 dB. The different methods give calibration constants in the range 71.9 -73.2 dB, and the FD calibration constant is chosen to 72.6 dB as a compromise in this interval. The calibration accuracy can only be estimated since all errors involved are currently not understood. The dominating errors are the absolute calibration constant and the range correction factor with worst-case estimates of 0.7 and 0.3 dB, respectively. The accuracy of the FD calibration is thus estimated to ±1 dB after linearly adding the errors. The rms noise pixel value is subsequently determined to 226 based on the FD calibration constant and the noise-equivalent backscattering coefficient.

## References

BIRD, P. J., KEYTE, G. E. and KENWARD, D. R. D., 1993, An Experiment for the Radiometric Calibration of the ERS-1 SAR, *Proceedings of the First ERS-1 Symposium held in Cannes, 4-6 November 1992*, SP-359 (Paris: European Space Agency), pp. 195-200.

CARTER, D. J. Q., 1989, ERS-1 Active Microwave Instrumentation Design and Performance Status, *Acta Astronautica*, **19,** 27-40.

FREEMAN, A., 1992, SAR Calibration: An Overview, *IEEE Transactions on Geoscience and Remote Sensing*, **30,** 1107-1121.

FREEMAN, A. and CURLANDER, J. C., 1989, Radiometric Correction and Calibration of SAR Images, *Photogrammetric Engineering and Remote Sensing*, **55,** 1295-1301.

GRAY, A. L., VACHON, P. W., LIVINGSTONE, C. E. and LUKOWSKI, T. I., 1990, Synthetic Aperture Radar Calibration using Reference Reflectors, *IEEE Transactions on Geoscience and Remote Sensing*, **28,** 374-383.

LAUR, H., 1992, ERS-1 SAR Calibration, Derivation of Backscatter Coefficient s° in ERS-1.SAR.PRI Products, ESA ESRIN Technical Note Issue 1, Rev 0, European Space Agency.

LAUR, H., MEADOWS, P., SANCHEZ, J. I. and DWYER, E., 1993, ERS-1 SAR Radiometric Calibration, *Proceedings of the SAR Calibration Workshop held in Noordwijk, 20-24 September 1993*, WPP-048 (Paris: European Space Agency), pp. 257-281.

ROBERTSON, S. D., 1947, Targets for Microwave Radar Navigation, *Bell System Tech. J.*, **26,** 852-869.

SOLAAS, G. and LAUR, H., 1993, An Assessment of ERS SAR Low Resolution Imagery, ESA ESRIN Report ES-TN-DPE-OM-GS01, European Space Agency.

UK-PAF, 1993, ERS1.SAR.PRI Health Report, National Remote Sensing Centre Limited, Farnborough.

ULABY, F. T., MOORE, R. K. and FUNG, A. K., 1986, *Microwave Remote Sensing, Active and Passive* (Artech House).

ULANDER, L. M. H., 1990, Theory of SAR Radiometric Calibration, Research Report 167, Department of Radio and Space Science, Chalmers University of Technology, Gothenburg, Sweden.

ULANDER, L. M. H., 1991, Accuracy of Using Point Targets for SAR Calibration, *IEEE Transactions on Aerospace and Electronic Systems*, **27,** 139-148.

ULANDER, L. M. H., 1992, Calibration of the ERS-1 SAR Fast-Delivery Images, *Proceedings of the First ERS-1 Symposium held in Cannes, France, 4-6 November 1992*, SP-359 (Paris: European Space Agency), pp. 173-178.

ULANDER, L. M. H., HAWKINS, R. K., LIVINGSTONE, C. E. and LUKOWSKI, T. I., 1991, Absolute Radiometric Calibration of the CCRS SAR, *IEEE Transactions on Geoscience and Remote Sensing*, **29,** 922-933.

VASS, P. and BATTRICK, B., 1992, ESA ERS-1 Product Specification, SP-1149, European Space Agency.

# C. REAL-TIME USE OF ERS-1 SAR IMAGERY FOR ICE SERVICE AND ICEBREAKING OPERATIONS

BERTIL HÅKANSSON, MATS MOBERG AND THOMAS THOMPSON
Swedish Meteorological and Hydrological Institute (SMHI), S-601 76, Norrköping, Sweden

ANDERS GUSTAVSSON, National Defence Research Establishment (FOA), P.O. Box 1165, S-581 11 Linköping, Sweden

**Abstract.** Two demonstration experiments has been carried out in the Baltic Sea, using ERS-1 SAR imagery. The benefits of these data for winter navigation purposes were evaluated during two winter seasons, using questionnaires and personal communication as the basic information sources for interpretations. Imagery was delivered in almost real-time to the SMHI ice center and to some icebreakers, operating in the Gulf of Bothnia. The satellite imagery proved to be uselful for ship routing of merchant vessels and for icebreaker assistance. Images presented onboard were mostly recognized as easily interpretated by the crew and it was concluded that an image resolution of about 100 meters was preferred, since both ridged areas could be distinguished and a reasonable geographical coverage was obtained.

## 1. Introduction

In this study we present results from the pre-operational use of ERS-1 SAR imagery for winter navigation purposes. The aim of this project is to evaluate the use of SAR information for ice mapping in a real-time operational situation at the SMHI ice service center and at some Swedish icebreakers. Demonstration projects were realized both in 1992 and 1994. The first winter period was extremely mild and only a few demonstration tests were made (Thompson *et al.,* 1993 and Grafström and Håkansson, 1993), whereas the winter season of 1994 was normal and hence a dedicated demonstration programme could be realized (Håkansson *et al.* 1994).

Due to varying ice extent and ice dynamics, SAR imagery should ideally be available once a day with a possibility to cover all areas of the Baltic Sea. The delay between registration and evaluation of the data should not exceed 3 hours for operational reasons. However, these prerequisites for operational use were only partly achieved, taking into consideration the research nature of the ERS-1 orbit configuration, swath width and the processed data transmission system.

## 2. Winter navigation and sea ice conditions

The icebreaking season in 1991/92 started in late November and was ended in the middle of May. Three icebreakers were involved during this very mild winter and only 121 assists including 19 tugging operations were made. This can be compared with the severe winter season 1986/87 when 6415 assists including 1748 tugging operations were carried out.

The icebreaking season, during the second demonstration campaign, lasted from late November 1993 to the middle of April 1994. In total six icebreakers were simultaneously involved, including operations in lake Vänern. The total workdays for all the icebreakers sums up to 534. This time was divided mainly in transportation 7800 h, asisst missions 4700 h and tugging 660 h. As a whole 1620 assists were carried out and the total cost for the icebreaker service during this winter was 140 MSEK (*cf.* Lundqvist and Årnell 1994).

At the Swedish coastal station Ratan in the western Bothnian Bay the largest ice thickness of 0.40 m was observed in the beginning of March during 1991/92, whereas the corresponding date in 1993/94 occurred one month later with a maximum ice thickness of 0.70 m. This variability in ice thickness as well as in other ice variables is typical for the winter conditions in the Baltic (*i.e.* SMHI and FIMR 1982, Seinä and Palusuo 1993). As an illustration of this variability we present in figure 1 the time series from Seinä and Palusuo, including the annual Swedish icebreaking assists. The correlation between maximum ice cover and assists is obvious and self explaining to some extent, since the maximum annual ice coverage reflects the severity of the ice winter season.

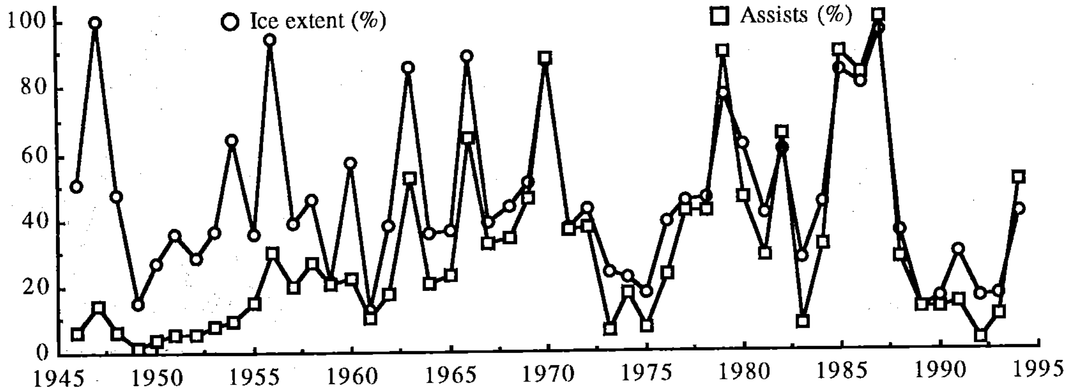

Figure 1. Time series of the maximum annual sea ice extent in the Baltic area (*cf.* Seinä and Palusuo 1993) and the annual number of icebreaking assists.

## 3. Demonstrations of ERS-1 SAR

During January to April in 1992 and in 1994 the ERS-1 satellite was orbiting the Earth in the so called ice orbit, covering the same areas on ground every third day. One particular imaging swath (*cf.* figure 2) was dedicated to cover the northern Baltic, a prerequisite for a demonstration of the capability of the SAR for sea ice operations. During the former period the techniques and methods were developed and tested, whereas the users had limited benefit of the SAR information due to the extra mild winter. However, the latter time period was coincident with a normal winter situation, making the evaluation results more representative compared to the 1992 results. An example of the type of SAR information that was presented to icebreakers is shown in figure 3.

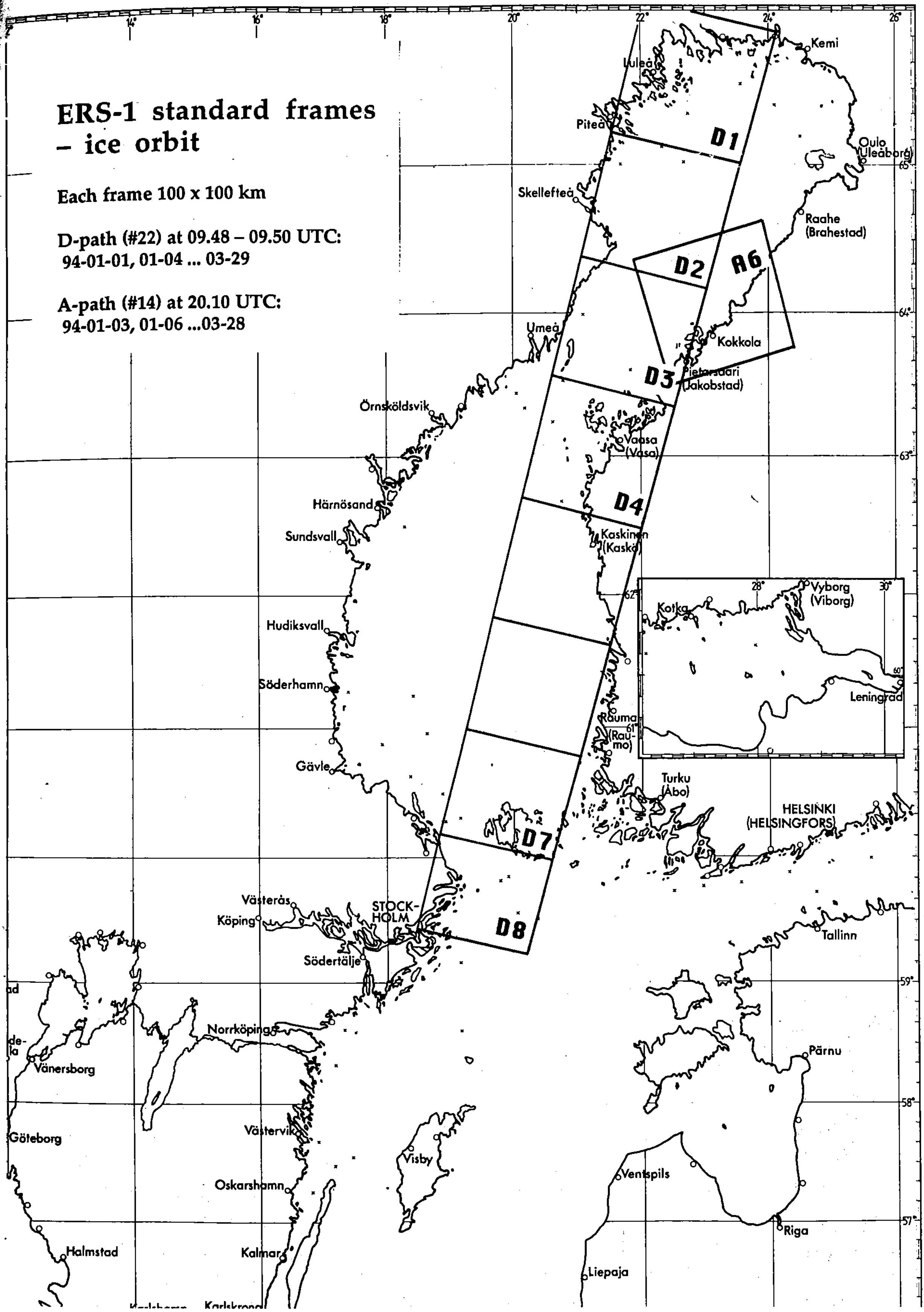

Figure 2. A schematic view of the SAR track and image frames used in the application/demonstration project.

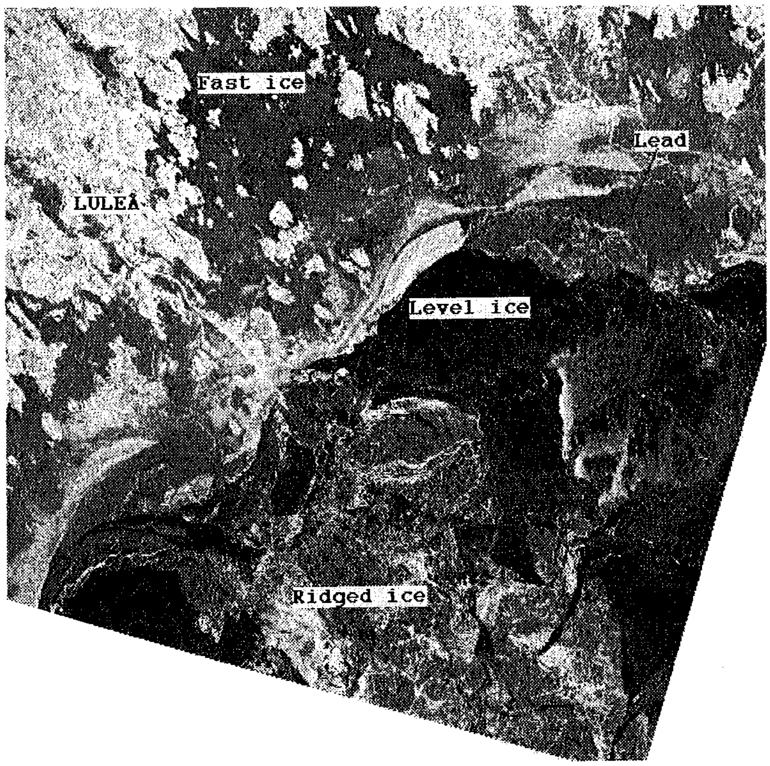

Figure 3. SAR imagery from frame D1 with ice types manually classified but based on observations. It was this type of information that icebreaker officers were given.

Within the 3-day orbit, the descending track 22 is the optimal in order to cover the Baltic Sea. Due to technical restraints, a maximum of 4 of the frames D1 to D8 could be accessible for the user. Thus the data request to ESA implied that the large-scale ice situation would govern which, within 14 days time of notice, of these frames should be transmitted for a certain period. Satellite overflight time for the frames D1-D8 was about 0950 UTC. As a compliment, data were also received from the ascending track 14, covering the frames A6 and A7 with an overflight time at 2010 UTC.

For graphical presentation of maritime information onboard icebreakers, such as satellite images, weather and ice forecasts, the Iceplott software is used. This is an application developed jointly for the National Maritime Administration in Sweden and the Finnish Board of Navigation. The software resides on Macintosh and PC compatible computers connected by a Novell network and using the Nordic Mobile Telephone System operating at 450 MHz (NMT-450) as the transmission method. The information is presented on Macintosh computers with large screens, situated at the icebreaker bridges. Positions of icebreakers, merchant ships and harbours are plotted on a graphic coordinate system showing the contour map of the Baltic Sea. When available, satellite images as AVHRR or SAR, overlay the contour map, giving information of the ice conditions. In order to reduce transmission time, the system has the capacity of compressing the images before they are sent, using the Adaptive Laplacian Pyramid method (Mäkisara 1991). Satellite images of arbitrary pixelsizes are correctly placed in the coordinate system based upon information found in the original satellite image file headers. The Iceplott operator has access to some tools *e.g.* dynamic tracking of the cursor in latitude/longitude, indication of distance and bearing between two points, a route-tool by which the operator can draw on the screen and, based on the overlayed ice information, plot a suggested direction way through the ice field, suitable for the merchant traffic. The way-point coordinates of this route are easily extracted for transmission to merchant ships requiring the information.

At most during the 1993/94 winter season, 6 icebreakers were simultaneously engaged in operations in the Baltic Sea, of which 5 carried the Iceplott system. Depending on the area of operation and whether this area was included in the available SAR frames, 200 meters low resolution images were distributed to the relevant icebreakers. On certain occasions 100 meters resolution images, covering areas of specific interest, were also distributed. Specific SAR log forms were used to evaluate the benefits of the radar images, and were supposed to be filled in by icebreaker officers on each occasion when reception of SAR data were at hand.

## 4. Evaluation of results

During the experiment period January 18 to March 31 1994 there were 24 occasions of SAR data access. Here an occasion is defined as 1 - 2 frames from ascending orbit in the evening and 3 - 4 frames from descending orbit the following morning. Various technical obstacles (SAR failure, reception failure, Internet problem) caused total loss of data on 6 of these occasions and delay in 3 cases. In total about 62 frames were received, processed and evaluated at the ice service center of which approximately 50 were distributed to 5 different icebreakers.

Low resolution images (see table 1) obtained on Internet from Tromsö Telemetri Station were, on average, available at the SMHI computer 2 hours after satellite acquisition time. The various processing steps took in general another 1.5 hours before the images were available. Fast delivery data (see table 1) received by BDDN communication satellite link were available at the SMHI computer typically 19 hours after satellite acquisition time and the following processing took another 2 hours. The average

Table 4.1. UI16 and LRI characteristics obtained from Battrick (1993) and TSS Product Specification SAR LRI, respectively.

| CHARACTERSITICS | UI16/BDDN | LRI/TROMSÖ | OVERVIEW/SMHI |
|---|---|---|---|
| Pixel size across track | 20.0 m | 100 m | 200 m |
| Pixel size along track | ≈ 15.9 m | 80 m | 200 m |
| Scene area across track | 100 km | 100 km | 100 km |
| Scene area along track | ≈ 96 km | 100 km | 100 km |
| Scene size across track | 5000 pixels/line | 1000 pixels/line | 512 pixels/line |
| Scene size along track | 6300 pixels/line | 1260 pixels/line | 512 pixels/line |
| Pixel depth | 16 bits | 16 bits | 8 bits |
| Product location accuracy | 200 m | ≈ 1 km | ≈ 1.85 km |
| Total product volume | 63 Mbytes | 2.5 Mbytes | ≈ 75 Kbytes |
| Projection | ground range | ground range | Mercator |
| Number of looks | 3 | 3 | 3 |

transmission time between the ice service and the icebreakers, using the Iceplott system and the mobile telephone network, was 40 minutes for each frame. This transmission system has a fault check which means that a data file is received as a whole or not at all. Depending on the stability of the mobile telephone link during such a rather long transmission time, any dropouts would cause a new transmission from the beginning. At SMHI only one telephone line is used for the Iceplott communication. Thus the icebreakers could be called only once at a time. Another concern was to inhibit saturation of the link in a way that ordinary text messages on icebreaker operations always would come through. The transmission link was originally designed primarily for text information and does not really have the capacity for an extensive image distribution.

## *4.1 Evaluation of SAR onboard the icebreakers*

As mentioned, five different icebreakers received SAR images. However, the limitations of the transmission system and the principle that only icebreakers with an activity in the current SAR frames should be furnished with SAR data had the consequence that in general two icebreakers had regular SAR information. These icebreakers were answering questionnaires for each occasion SAR images were obtained, covering in total 36 frames. In addition to this information, personal communication with several icebreaker officers took place during the evaluation period. In summary, we found that the following conclusions can be made:

- Interpretation of the imagery was not a problem.
- Information about ridges, an important ice feature in winter navigation, was quite well furnished by the SAR images.
- There were many occasions with operational use of the SAR information.

The interpretation of the images was evaluated, using a scale going from 1 (interpretation easy) to 5 (difficult). Icebreaker officers are used to sophisticated ship radars and seem to have no problem adopting to the SAR. The weather conditions also favoured the interpretation as air temperatures were mostly below 0°C, which kept the wetness in the snow low enough to give high contrasts in the SAR images. Hence, the overall ranking turned out to be good and was on average 1.9.

According to the questionnaires known ridges were almost always recognized in the images (86%) and in less than one fifth of the cases (19%) new, previously unknown ridges were detected. In a few cases (8%) ice features with relevance to ice navigation, could not be recognized in the corresponding image. Quite often SAR information was reported to have had a direct influence on which way to go when assisting merchant ships in a convoy and for routing merchant ships going by their own. During the period January 19 to March 11 53% of the images were used for vessel assistance and 33% for ship routing. Note however, that these figures are to some extent approximate in that the data material is not extensive enough for a statistical analysis, since only 19 questionnaires are available. Nevertheless, the results broadly indicate the usefulness of this information and how the imagery were used onboard the icebreakers. Comments added to the questionnaires indeed strenghten this conclusion, as well as addressing some of the well-known interpretation problems of single frequency sea ice SAR imagery:

- Very sharp image.
- Difficult to distinguish between open water and level ice.
- The image shows that we took the right way.
- Ice type somewhat difficult to estimate.
- Leads and cracks are easily recognized.

- Ridged areas stand out well.

An interesting case was reported on January 19 from the icebreaker Ymer, heading north in the central part of the Bothnian Bay at the time for the SAR data acquisition (*cf.* figure 4 a, small circle, enlarged in figure 4 b). Several hours earlier she assisted a merchant vessel, which was got caught in an area of thick ice ridges (indicated by a large circle in figure 4 a, enlarged in figure 4 c) outside the port she just left assisted by the local icebreaking tug. However, they did not have any information on the prevailing ice situation, so the merchant vessel was left in the drift ice, awaiting icebreaker assistance. As noted by the master onboard Ymer, he could have informed the local harbour authorities about the ice situation and told the tug to assist the merchant vessel some nautical miles further ahead, where there was only a thin ice cover which the vessel could manage by herself, if there had been a SAR image registration a day before.

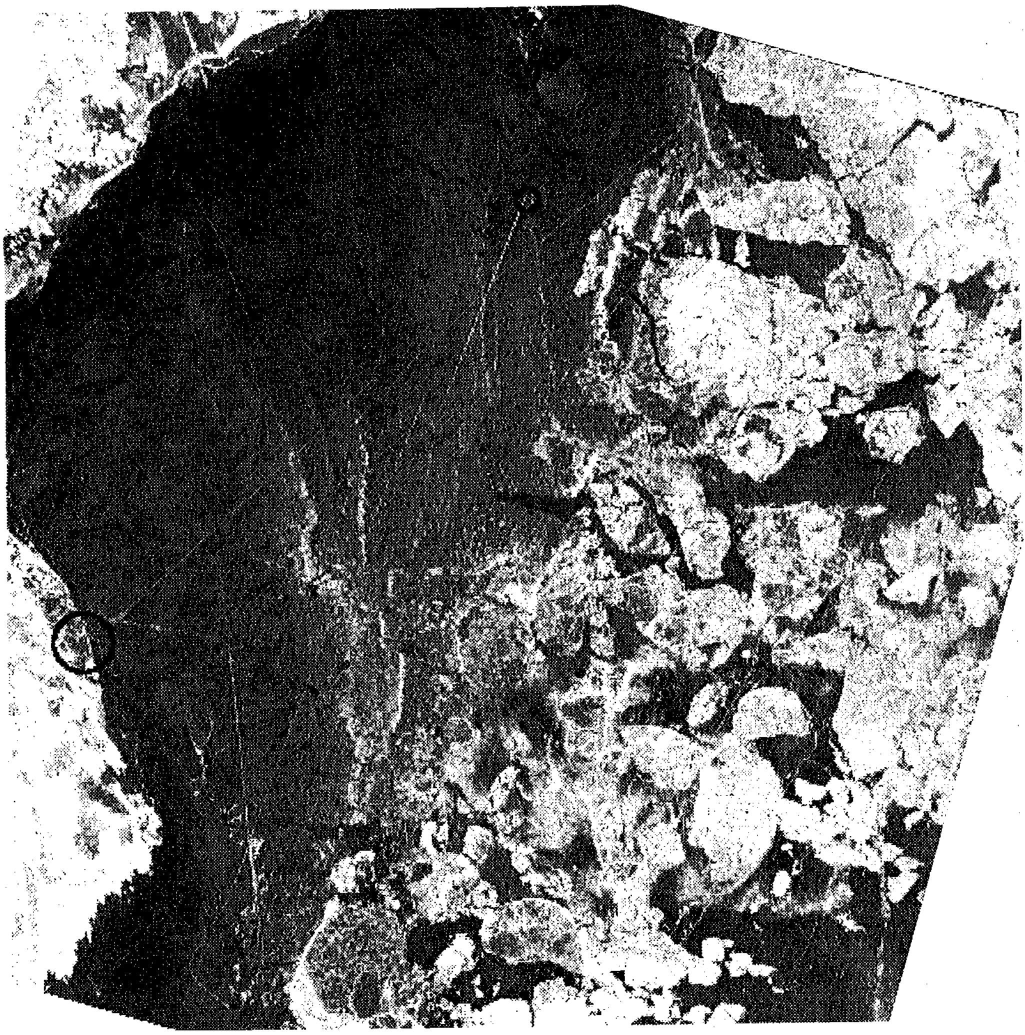

Figure 4 a. An example of a 200 meter resolution SAR imagery from January 19 1994, covering the frame area D2 in the Bothnian Bay. Ship tracks are clearly visible in the image. The small and large circles indicate the position of icebreaker Ymer and the former approximate position of the cargo vessel, respectively.

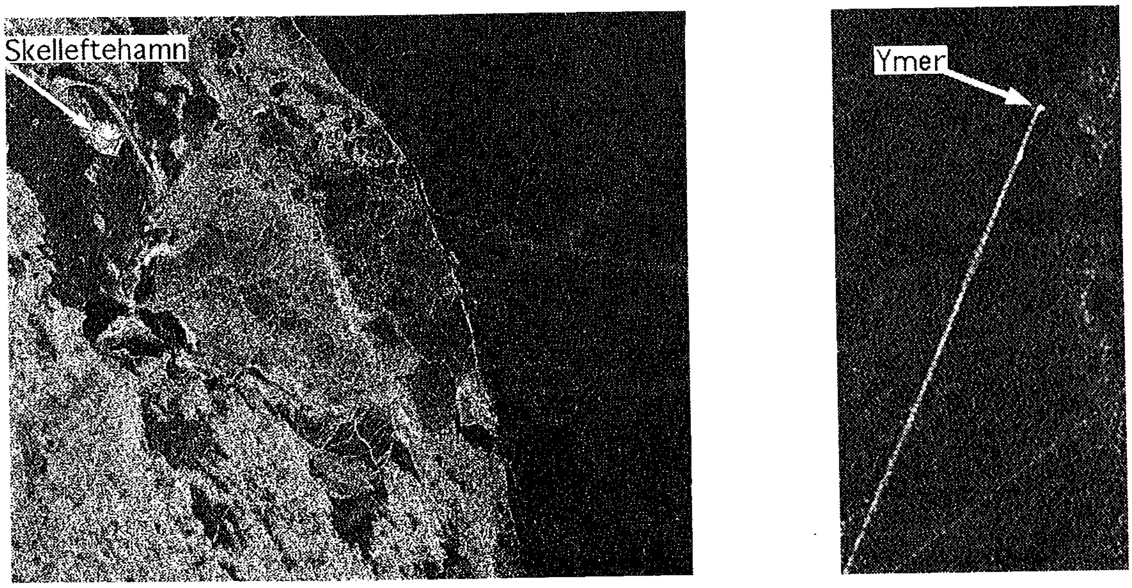

Figure 4 b and c. The cargo vessel was locked in a ridged area outside the port of Skelleftehamn (4 b), awaiting icebreaker assistance which was already realized when the image was sampled by ERS-1 (UI16 imagery).

## *4.2 The usefulness of SAR for sea ice mapping*

The ice map of the Baltic Sea is drawn every day but distributed twice a week to various users. It is based on observations from vessels and landshore bases, airborne observations and satellite imagery. All information is put together by the ice service meteorologists, who also need to have experience of the sea ice in the Baltic. The scale of the ice map is of low resolution and presents only the large-scale ice characteristics. There are several reasons for this choice of resolution and coverage. One is to present an overview for users and another is to be a documentation of available knowledge of the near-real time ice situation, since the history of the sea ice evolution is also important information for the sea ice mapping. The ice map presents the ice extent, ridged areas, larger leads, ice thickness and to some extent the quality of the ice. The AVHRR imagery fits the geometric scale of the ice map and gives information on larger leads, drift ice and fast ice extent, which of course is also the case with SAR, which in addition can give input on ridged areas and the quality of ice such as thin or thick ice.

During the full 73-day period in 1994 72 questionnaires were filled in almost daily *i.e.* one for each chart made. The results upon the question on which information sources that were used for the ice chart were as follows: previous ice chart (86%), icebreaker information (76%), AVHRR imagery (71%), ERS-1 SAR imagery (11%) and air reconnaissance (4%). There are several reasons for the rather low SAR data figure, which are discussed in detail in the next section. Here, however, it is worth mentioning that the ice map was drawn before noon each day in order to deliver it to the users as early as possible. Despite the fast delivery of SAR from Tromsö, using the Internet facility, we were not able to present the descending SAR images to the ice service before the ice map had to be mailed to users. These images were acquired by ERS-1 about 0950 UTC and after 2 hours of processing at Tromsö and 1.5 hours of processing at SMHI on average, they were presented on the screen for the ice service between 1300 and 1500 (LT) the same day. Hence, the imagery to a great extent was used for controlling the previously drawn ice map and used as input the day after acquisition for ice mapping.

## 5. Discussion

The SAR imagery was frequently used in producing and controlling the daily ice map of the northernmost part of the Baltic Sea. However, there were several reasons which limited the practical use of the imagery, depending on circumstances connected with the ERS-1 SAR coverage and the winter weather situation. The ice season of 1994 was normal in ice extent, but ice growth was fast during a short period in the end of January, when weak wind speeds (< 8 m/s in general ) in combination with low temperatures (around - 10°C) built up a thick sea ice layer (.3 - 1.0 m), covering the whole Bothnian Bay. Ten days later in mid February the Bothnian Sea was also totally ice covered. The prevailing weather situation produced a stable and almost stationary sea ice field with minor amount of ice drift and deformation, which in the Bothnian Bay lasted until the end of March.

The SAR coverage of the Bothnian Bay turned out to be most interesting, since the imagery covered the areas where shipping and icebreaking operations are frequent. In the Bothnian Sea the SAR coverage was outside the most intensive areas of shipping operations, except the Åland Sea area, where ice was formed during a short period in February 17 to March 7. The SAR information, like any imagery, is of great practical use when the sea ice is dynamic. The stable situation that was formed in the Bothnian Bay made the SAR time series information, from an operative point of view, to some extent redundant since only a few smaller sea ice changes took place. Another weather dependent reason was the prolonged high air pressure situation over the northern Baltic Sea this winter, favouring a large number of cloudfree AVHRR imagery available for the ice map production. These also cover the whole area of interest, and were therefore frequently used.

The SMHI ice service also faced the difficulty with the limited SAR imagery coverage, as already mentioned above. It was good in the Bothnian Bay but less good in the Bothnian Sea. For example, the area west and southwest of the frame D3 in the northern Bothnian Sea was not covered by SAR, where icebreaking operations were lively and the ice situation dynamic but not so difficult as in the central part. Hence, the operative use of SAR was limited in time to periods when most traffic problems took place in the northernmost sub-basin in connection with sea ice changes. During calm weather periods the cargo vessels were guided through already existing icebreaker tracks where the local ice situation was quite well-known.

Nevertheless, there is no doubt about the operational usefulness of SAR imagery for sea ice mapping in the Baltic Sea, and our experiences demonstrate that it was always used at the ice service center when the sea ice was deforming *i.e.* convergence/divergence of the ice field and ice drift or ice growth took place. The problems we faced and mention here have to do with the technical restrictions put on ERS-1 SAR image products, taking into account the high geometrical resolution but narrow swath width.

The image pixel size of 200 meters gave enough information onboard the icebreakers, although 100 meters would be preferred since small-scale structures can be distinguished better. However, imagery with a pixel size less than 100 meters will limit the coverage too much, taking into account the present status of the technical equipment and especially the communication link to the icebreakers. From an operational point of view it is necessary to obtain SAR imagery on a daily basis with a larger spatial coverage of the Baltic Sea than is presently possible. On the other hand, the investigation presented here has shown that the SAR imagery onboard the icebreakers was greatly appreciated and turned out to be very useful for ship routing and assistance. Routing cargo vessels with high ice class and icegoing capabilities is perhaps the most important operative application, since it may save energy and time for the icebreakers.

## Acknowledgements

Sincere thanks for the financial support from the Swedish National Space Board and the National Maritime Administration and for the willingness of officers in charge of the icebreakers to take part in the evaluation of the SAR imagery. We also indeed acknowledge the ice service staff at SMHI for the extra work of SAR imagery handling, interpretion and evaluation. SAR imagery from ERS-1 was kindly supported by the European Space Agency as part of two Announcements of Opportunity projects.

## References

BATTRICK, B., 1993, ERS user handbook, SP-1148, (Paris: European Space Agency).

GRAFSTRÖM, T., and HÅKANSSON, B., 1993, The usefulness of SAR images in operational sea ice mapping, forecasting and ship routing. *Proceedings of Technical Conference on space-based ocean observation in Bergen, Norway, September 5-10, 1993.*

HÅKANSSON, B., MOBERG, M., and THOMPSON, T., 1994, Real-time use of ERS-1 SAR imagery for ice service and icebreaking operations in the Baltic Sea. To appear in *International Journal of Remote Sensing*.

LUNDQVIST, J.-E., and ÅRNELL, T., 1994, A summary of the ice season and icebreaking activities 1993/94. SMHI and Sjöfartsverket report.

MÄKISARA, K., 1991, Adaptive laplacian pyramid compression of remote sensing images. *Proceedings of IGARSS'91, Espoo, Finland, June 3-6, 1991*, pp. 1439-1442.

SEINÄ, A., and PALOSUO, E., 1993, The classification of the maximum annual extent of ice cover in the Baltic Sea 1720 - 1992. *Meri*, **20**, pp. 5-20.

SMHI, and FIMR, 1982, *Climatological ice atlas for the Baltic Sea, Kattegat, Skagerrak and lake Vänern (1961 -1979)* (Swedish Meteorological and Hydrological Institute, Norrköping, Sweden and Finnish Institute of Marine Research, Helsinki, Finland).

THOMPSON, T., HÅKANSSON, B., ULANDER, L., and CARLSTRÖM, A., 1993, Experiences from the Swedish sea ice programme during BEERS-92, *Proceedings of the first ERS-1 Symposium - Space at the Service of our Environment, Cannes, 4-6 November 1992*, SP-359 (Paris: European Space Agency), pp. 313 -318.

# D. RADAR SCATTERING MODELS AND ERS-1 SAR DATA INVERSION FOR BALTIC SEA ICE

ANDERS CARLSTRÖM, LARS M. H. ULANDER, and
WOLFGANG DIERKING

Department of Radio and Space Science, Chalmers University of Technology,
S-412 96 Göteborg, Sweden

**Abstract.** Backscatter models for level and deformed ice are investigated using *in situ* measurements and comparisons with coincident ERS-1 SAR data over Baltic sea ice. A two-layer scattering model is used for snow-covered level ice. For dry snow conditions, the results show that ice surface scattering dominates except for smooth ice with very low salinity, as found in the archipelago fast ice, where volume scattering from air bubbles is also important. An increasing snow wetness to about 10% was found to increase the level ice backscatter, due to scattering from the snow surface. The model for level ice with a dry snow cover is most sensitive to the standard deviation of surface heights. However, when the ice surface is deformed with roughness elements of sizes comparable to the radar wavelength, the surface slope distribution becomes increasingly important. This was confirmed by comparisons between a physical-optics scattering model and scatterometer measurements of a brash ice surface. For surfaces consisting of large ice blocks, a two-component model is formulated and shown to be independent of the block size distribution. The model consists of a specular component and a diffuse rough surface scattering component. By evaluating the model based on *in situ* data it is concluded that specular reflections dominate, with the block slope distribution as the major parameter, while the small-scale roughness is of less importance. An approach for data inversion is also described, which estimates the ice surface roughness from ERS-1 SAR images during dry snow conditions. The inversion is based on the level ice scattering model together with an experimentally obtained relation for deformed ice.

## 1. Introduction

### 1.1. Background

One of the main anticipated results of the Baltic Experiment for ERS-1 (BEERS) was to increase the knowledge of the backscatter mechanisms and their relation to the stage of development of the ice cover during various conditions (see Chapter A). Earlier studies of radar backscatter from level sea ice in the Baltic Sea have concluded that surface scattering from the ice surface is the dominating mechanism for the frequency, polarization and incidence angle used by the ERS-1 SAR (Ulander *et al.* 1992). The study was, however, limited to a single test area where the air temperature was about -2°C and the ice salinity was about 1 ppt. Studies of ice ridge backscattering indicated that diffuse (incoherent) scattering from the small-scale roughness on ice blocks modulated by the block slope distribution was the dominating mechanism (Johansson and Askne 1987, Manninen 1992) However, it is not clear what role specular-point scattering from the ice blocks have, i.e. specular (coherent) scattering from individual ice blocks which add incoherently between blocks.

When liquid water is present in the snow cover on the ice , it is well known that the snow wetness will affect the backscattering (Kim *et al.* 1984, Onstott and Gogineni 1985, Livingstone *et al.* 1987, Onstott *et al.* 1987). For small wetness values (a few percent), the snow cover will reduce the backscattering due to attenuation, whereas surface scattering from the snow surface will dominate for high wetness values. Volume scattering from the snow pack may also be important when the snow cover is thick. Experimental studies have shown a reduced contrast between level and deformed ice during very wet conditions (Hallikainen *et al.* 1991, Toikka and Hallikainen 1992).

In light of past experiments and results, several important questions remain to be answered:

- Is ice surface scattering the dominant mechanism for all level ice types found in the Baltic Sea? What is the role of volume scattering for the ice found in the northern part of the Bay of Bothnia, which has a very low salinity?
- Is ice surface scattering also the dominating mechanism for deformed ice in the Baltic Sea? If so, is it caused by diffuse scattering from the small-scale roughness of ice blocks, by specular-point scattering from ice blocks, or some other mechanism?
- What is the effect of azimuth look direction for ice ridge scattering?
- What is the effect of snow wetness when the air temperature rises above 0°C?
- Can we construct an inversion model for retrieving ice deformation parameters from the ERS-1 SAR images? If so, what is the accuracy we can expect?

These are the main questions to be approached in this chapter. The principle idea is to compare *in situ* measurements of various ice types through scattering models with calibrated backscattering coefficients as measured by SAR or scatterometer. We will then attempt a model inversion for surface roughness based on the modelling and the experimental results.

In the first section we describe the background, the objectives and how the field experiments were outlined. We will also define the nomenclature used for the different ice types. In Section 2, the experimental techniques are described and the acquired data are summarized. In Section 3, we describe different theoretical backscatter models, apply them to the *in situ* data, and compare the results with the measured backscatter. In Section 4, we then suggest a method for SAR data inversion, which generates a map of the RMS surface height on the millimetre to decimetre scale when applied to a SAR image. The inversion method is partly based on experimental results from Section 2 and partly on a theoretical scattering model described in Section 3.

### *1.2. Field experiments*

The BEERS field experiment plans included the following basic principles: Firstly, we recognized the need to cover a broad range of ice and meteorological conditions since they show a large variability in both time and space. This implied that the objectives could only be fulfilled with a number of field experiments during several years. Secondly, we needed to include a range of surface roughness scales to make our results statistically significant. This implied that we had to cover many measurement sites at the expense of the number of samples per site. Thirdly, we had to focus on a minimum set of *in situ* measurements, i.e. surface roughness on horizontal scales from 2 mm to 10 m, snow volume parameters during wet conditions, and temperatures of air, snow, and ice. Ice volume measurements were also measured but with lower priority.

The selection of measurement sites and the sampling strategy are important to consider. Besides the geophysical variability we also have to consider the spatial resolution of the SAR. Although the resolution is about 25 m for the fast-delivery SAR images, much larger areas have to be averaged to reduce speckle and achieve statistically confident results. It is therefore advantageous to choose measurement sites which have similar properties over a larger area. For example, homogeneous areas larger than about 250 x 250 $m^2$ in size were chosen for the level ice sites resulting in a 95% confidence interval of ±0.5 dB for the backscattering coefficient. Homogeneous areas of this size could also be found for deformed ice in the form of jammed brash barriers, but most often not for other types of deformed ice. Ice ridges pose a particular problem since they inherently have variable characteristics of the same order of magnitude as the SAR resolution, i.e. 10 - 100 m. Aerial photography is therefore essential to determine the extent of the roughness features and their variability.

The sampling strategy for the surface roughness measurement is a further complication since it requires many height profiles to achieve statistical confidence of the auto-correlation function or roughness spectrum. Numerical simulations and past experience (Carlström and Ulander 1993, Carlström and Ulander 1994) have shown that approximately 10 height profiles per site is a reasonable compromise. The time required for each measurement site is thus from about 1 hour and upwards, depending on the local ice and snow conditions. A deep snow cover, for example, may take one hour to remove for a 10 m long height profile measurement with a laser profiler.

Four field experiments were conducted during the three ice winters 1992 (Ulander and Carlström 1993), 1993 (Carlström 1993), and 1994 (Carlström 1994). The first two experiments were conducted in February and March 1992. The general weather conditions were quite similar, i.e. cold conditions preceded by warmer periods with melting conditions. The measurement sites included both fast and drift ice, of which the latter were situated in sea ice of about 2-4 weeks age. The third experiment was conducted in March 1993 with warm weather conditions, i.e. air temperatures above but dropping slightly below 0°C during the last days. Rain also occurred during the experiment on two days. The fourth experiment was conducted in March 1994 with cold conditions, i.e. air temperatures well below 0°C except during a blizzard storm which occurred during several days when the air temperature rose to 0°C. In summary, the four field experiments covered a broad range of ice and weather conditions which implies that our results are valid for a wide range of conditions.

### *1.4. Definition of ice types*

The different ice types which are discussed in this study are divided in level ice and deformed ice. The latter include jammed brash barriers, hummocked ice, and ice ridges. The ice type terminology is often ambiguous and confusing, and we will therefore follow the definitions of the World Meteorological Organization (WMO 1989) as close as possible:

- Level ice: Sea ice which has not been affected by deformation.
- Deformed ice: A general term for ice which has been squeezed together.
- Jammed brash barrier: A strip of new, young or brash ice at the edge of drift or fast ice. It is typically a few kilometres wide. It is heavily compacted mostly due to wind action but does not normally have appreciable topography. The ice blocks have a thickness in the 0-30 cm range.
- Hummocked ice: Broken ice piled haphazardly one piece over the other to form an uneven surface with a certain topography due to pressure forces.
- Ice ridges: Ice piled haphazardly up one piece over the other. Formed as a line or wall of broken ice forced upwards by pressure.

## 2. Experimental techniques and data summary

### *2.1. Surface roughness of ice and snow*

#### 2.1.1. Small-scale surface roughness

The small-scale roughness of level ice, snow, and large ice blocks in ridges was measured by a laser profiler (Carlström and Ulander 1993). The instrument acquires surface profiles along a one-metre track with a horizontal sampling distance of 0.5 mm. A triangulating laser sensor illuminates the surface with infra-red light over a circular spot (0.15 mm diameter) which is projected on a detector. The system takes advantage of the detector's ability to discriminate between reflections from the surface and from beneath, which otherwise is an error source for semi-transparent surfaces such as sea ice. The data are transferred to a portable computer which also controls the instrument. Post-processing of the data consists of a filtering process to detect the centre of the laser spot in each point and to translate it into a height value using a calibrated look-up table. A height profile is thus obtained from which the surface height autocorrelation function, or (shorter) correlation function, may be evaluated. The autocorrelation of several height profiles within the same area are then averaged before normalization to reduce statistical fluctuations.

The vertical measurement precision for an ideal diffuse surface is better than 0.1 mm. However, the varying reflectivity and transmissivity of an ice surface introduce a random noise error, which limits the measurement precision in single points to almost 1 mm (RMS). This error has the characteristics of additive white noise. By low-pass filtering the profiles to a horizontal resolution of 2 mm, the random error is reduced to 0.5 mm (RMS). For very clear ice, the accuracy may be improved further by spray-painting the surface before the measurement. The total measurement range is 62 mm which is adequate for level ice measurements. When profiling the snow/ice interface, the snow cover was removed by brushing the surface. Care was taken not to deform the ice surface and any errors introduced by this process are believed to be negligible.

Between four and twelve profiles were acquired at each site. The analysis of the measured correlation functions showed that an exponential could be used as a model (see figure 1) for both ice and snow surfaces. We also found that the surface height distribution was well represented by a Gaussian when its mean value and any linear trend is subtracted. Another fundamental assumption is that the surface height profile is a wide-sense stationary process, i.e. that the RMS height and correlation function are

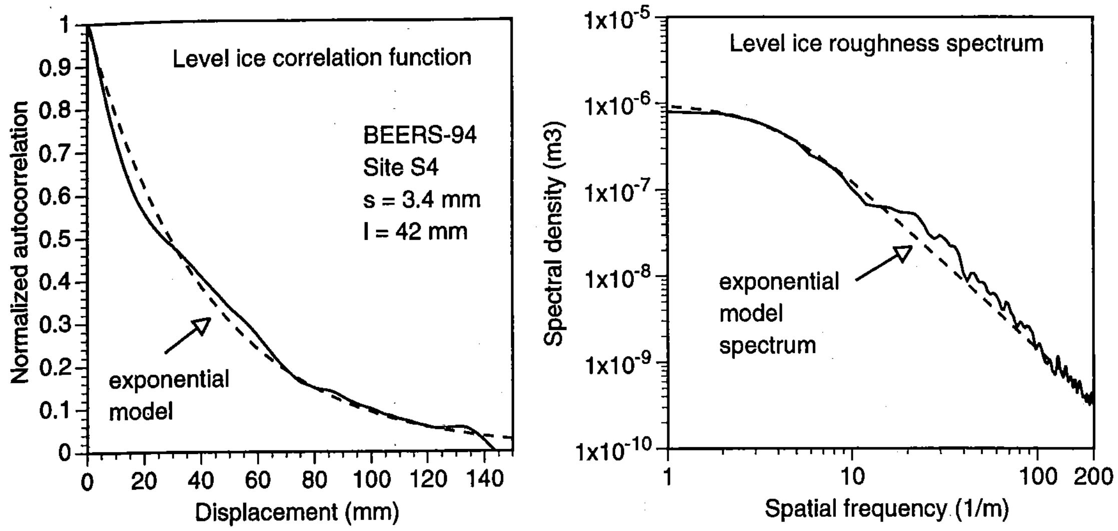

Figure 1. An example of a measured correlation function for level ice and its Fourier transform (the roughness spectrum). An exponential model is fit to the correlation function and gives a good fit also in the spatial frequency domain.

independent of the measurement location. According to these assumptions, the RMS height and the $e^{-1}$ correlation length fully characterize the ice surface roughness. The correlation lengths were determined by a least-squares fit of an exponential to the part of the correlation function with normalized autocorrelation higher than $e^{-2}$. The statistical fluctuations of the estimated RMS height and correlation length for an exponential correlation function are (see e.g. Kendall and Stuart 1963, pp. 231-236)

$$\begin{aligned} Var\{\tilde{s}\} &= \frac{s^2}{2n} \\ Var\{\tilde{l}\} &= \frac{l^2 e^2}{n}\left(1 - e^{-2}\right)^2 \end{aligned} \tag{1}$$

where $s$ is the RMS height, $l$ is the correlation length, and $n$ is the number of independent samples. The number of independent samples is approximated by $n = NL/l$, where $N$ is the number of acquired profiles and $L$ is the length of each profile. The relative error of the correlation length is thus approximately a factor 2.4 larger than the relative error of the measured RMS height. The latter typically varied between 1.5-6 % (RMS) as estimated from (1).

Figure 2 summarizes the surface roughness measurements of ice and snow surfaces. Each measurement point corresponds to one measurement site. Since the snow cover was often found to be dry, and thus did not significantly affect the backscatter, more data were acquired from the ice surface than from the snow surface. From the figure we can not observe any correlation between the two parameters. The correlation length of the snow surface was always less than 40 mm, which we may attribute to wind induced cm-scale undulations. The small-scale roughness of ice blocks in ridges showed a variation in correlation length similar to the one for level ice, whereas the RMS height was fairly constant.

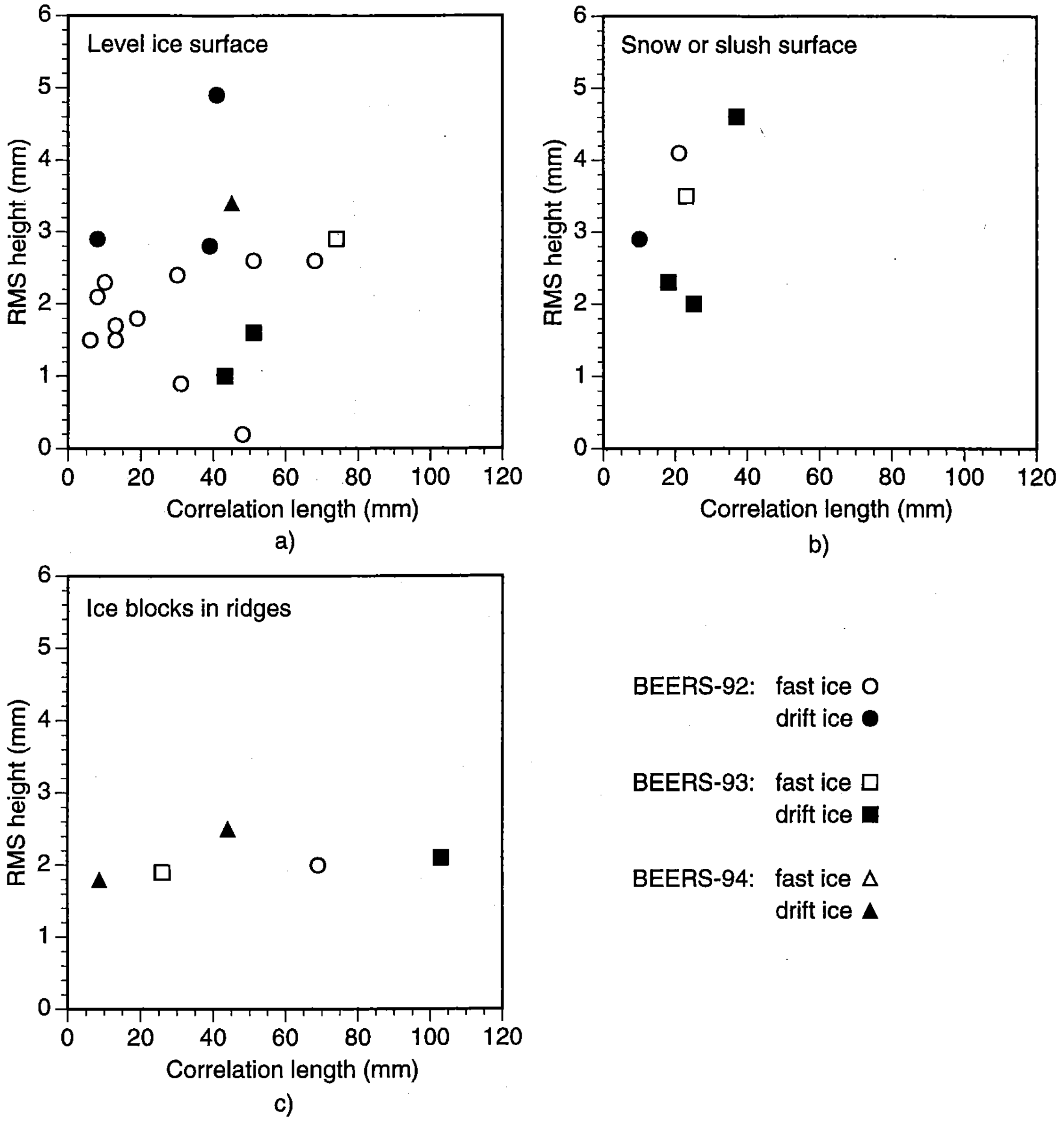

Figure 2. Small-scale surface roughness measurements of ice and snow. The correlation lengths are obtained from a least-squares fit of an exponential to the measured correlation functions.

### 2.1.2. Large-scale surface roughness

Due to the limitation in vertical measurement range of the small-scale laser profiler, a manual profiling technique was used to sample the height profiles of deformed ice during BEERS-92. A 10-m string was used as a reference when regularly sampling the surface height every 5 or 10 cm. The sampling distance was chosen so that the smallest ice blocks were sampled with at least two points. The deflection of the string was accounted for by subtracting a least-squares fit parabola from the obtained height profile. The precision of the height measurements was estimated to 3 mm (RMS) by measuring a flat surface.

A profiling instrument was later developed and measured the roughness of deformed ice during BEERS-93 and -94. The profiler consists of a pulsed laser distance meter which is mounted on a 10-metre traverse. The laser is moved along the traverse by an electrical motor at a constant speed while the distance measurements are stored on a computer. The measurement time for one profile is about six minutes. The laser output consists of averaged distance measurements with a spacing of about 5 mm. The length of the acquired profile is 9.3 m, the vertical precision is approximately 3 mm, and the measurement range is limited by the height of the construction which is about 2 metres. The effective horizontal resolution has been measured to 20 mm and is mainly determined by the width of the laser beam.

For the deformed ice we chose to estimate the surface height and slope statistics. The reason for choosing the slope distribution as a measure of second order statistics instead of the conventional correlation function is that the slope distribution enters directly into the scattering models when the RMS height is larger than about half a wavelength (Barrick 1968). To investigate the statistical properties of the data we estimated the power spectrum of the height profiles, which also is known as the roughness spectrum. The shape of the roughness spectrum or, equivalently, the correlation function becomes important for scattering from brash ice where the RMS height is sometimes slightly less than half a wavelength at C-band.

The roughness spectrum of a deformed ice area is shown in figure 3. The figure illustrates the general observation that the one-dimensional roughness spectrum showed a spectral decay according to an inverse power law

$$W(2\pi f_x) = K_n / f_x^n \tag{2}$$

where $f_x$ is the spatial frequency, and $n$ and $K_n$ are constants. Based on 29 measurements using the 10-m profiler $n$ was found to vary between 1.3 and 2.6. In some cases, $n$ may also vary between different frequency bands within the same spectrum. For a surface with exponential correlation, $n = 2$ in the high frequency part of the spectrum (see figure 1) and for Brownian motion, $n = 2$ for all frequencies. For a power-law spectrum, it can be shown that the measured RMS height and correlation length will be determined not only by $K_n$ and $n$, but also by the length of the profile (Church 1988). An interpretation of this is that the height statistics is non-stationary over the measured distance. It implies that the statistical fluctuations of the roughness parameters are not decreasing with increasing profile length, but only with an increasing number of profiles of a given length. Typically, 2-5 profiles were acquired at each site, which does not give sufficient accuracy for estimating the RMS height of the 10-m profiles. However, the roughness statistics of shorter wavelength components may be more accurately determined from the high frequency end of the spectrum, where we have a larger number of independent samples. The high-pass filtering is equivalent to dividing the measurements into shorter sub-profiles with lengths corresponding to the filter cut-off wavelength. However, the cut-off wavelength must be chosen so that the important spectral components of the surface height variations are preserved. For our measurements, it was found possible to high-pass filter with a cut-off at 1 m without changing the slope distribution significantly. The physical explanation for this is that the large majority of ice blocks are less than one metre across. Hence, the spectral components of the surface that are important for radar scattering are estimated more accurately by computing the RMS of the high-pass filtered than of the original height profiles.

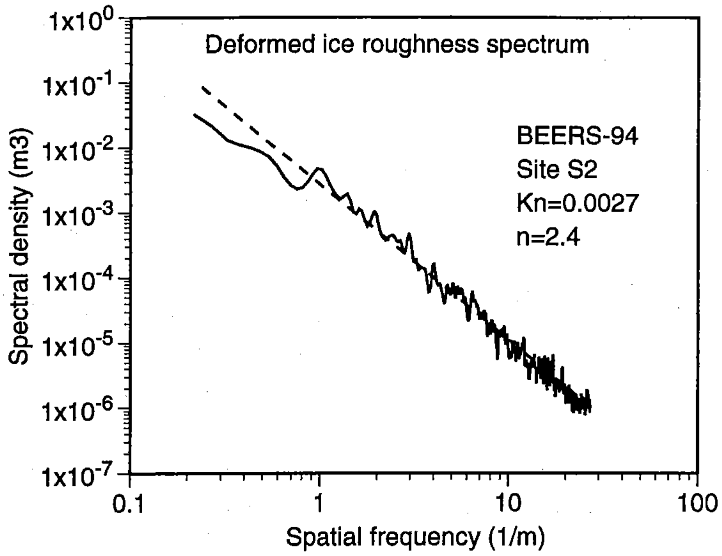

Figure 3. Roughness spectrum of a hummocked ice surface measured by 10-m laser profiler. The spectrum is an average over eight profiles and is plotted together with a power-law model for comparison.

The surface slope distribution was estimated by differentiating the original (unfiltered) profiles in intervals of $\Delta x$. As a model function, we choose the Cauchy probability density function, since it showed a good agreement with the data.

$$p(z') = \frac{m}{\pi} \frac{1}{m^2 + z'^2} \tag{3}$$

where $z'$ is the approximate surface height derivative. An extreme case of the slope distribution is $m = 1$, which is the slope distribution of a uniform angular distribution of the surface normal. The parameter $m$ is the half-value point of the distribution, which was estimated by a least-squares fit of the Cauchy function to the distribution of height increments for each profile. The choice of $\Delta x$ was determined from the condition $s/m \ll \Delta x \ll d$, where $s$ is the RMS height of the small-scale roughness and $d$ is the diameter of the blocks. This condition must be fulfilled to estimate the slope of the ice blocks with a minimal influence of small-scale roughness and discontinuities between blocks. Hence, we used $\Delta x$ = 50 mm, except in those cases where the sample spacing was 100 mm.

Figure 4 shows the resulting parameters derived from the deformed ice profiles. We have distinguished between distributed areas and line-shaped areas of deformed ice, i.e. between jammed brash or hummocked ice and ice ridges, respectively. Profiles were usually acquired both across and along the ridge sails. When deriving the statistics for ice ridges which did not extend over the entire profiled distance, the undeformed parts of the profile were first removed. The measurements along and across the ridges are presented separately but are connected in the figure. The profiles taken along the ridges have similar characteristics, while the across-ridge values are similar to the corresponding along-ridge ones in some cases and considerably higher in other. In two cases, only across-ridge profiles are available. Most of the jammed brash sites have a higher ratio between the slope and height parameters than the other sites. This is related to that the size of the ice fragments or blocks are generally smaller in jammed brash than in hummocked ice and ridges.

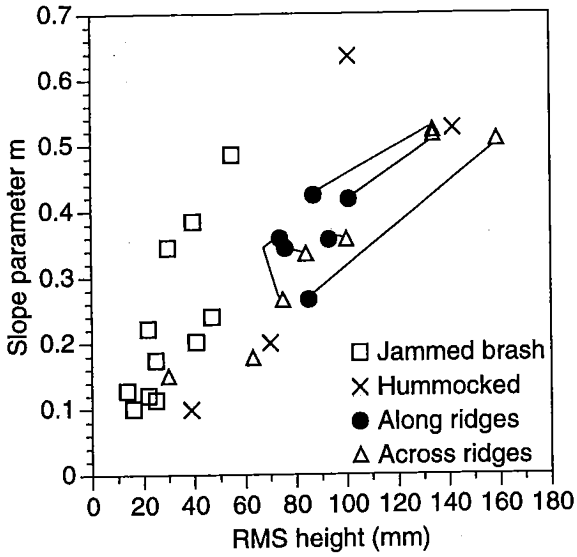

Figure 4. Large scale surface roughness parameters of deformed sea ice. The RMS height was determined using a maximum wavelength of one metre and the slope parameter is the half-value point of a Cauchy distribution function. Data obtained from profiles acquired along and across the same ridge are connected with lines in the graph.

### 2.1.3. Ice block parameters

During BEERS-93, the thickness and area distributions of ice blocks in ridges were sampled. During BEERS-94, also the distributions of tilt and azimuthal orientation angles were determined. A folding rule was used to estimate the sides of a best-fit rectangular model for the surface area and the average thickness of the block with an expected accuracy of about ±10%. The maximum tilt angle of the block was measured by an inclinometer with an accuracy of ±3°, and the direction of the maximum tilt was read from a compass with about 10° accuracy. Between 15 and 73 blocks were sampled in each ridge.

Surface slope distributions along certain azimuthal directions may be derived from the tilt angle distributions. A comparison between the slope distributions derived from laser profiles and from tilt angle measurements of 73 blocks in one ridge are shown in figure 5. The agreement between the data sets shows that the surface slopes measured by the laser are dominated by the slope of the blocks rather than by discontinuities between the blocks.

The average block thickness ranged between 0.14 m and 0.40 m, while the average block area was between 0.5 $m^2$ and 2.4 $m^2$. The distributions of block thickness and area agreed well with earlier observations in the Baltic (Kankaanpää 1991), considering that the number of blocks in our data set is fewer. In an extensive study of ridge block dimensions Kankaanpää found that the block thickness followed a gamma distribution, while the block area was close to a log normal distribution.

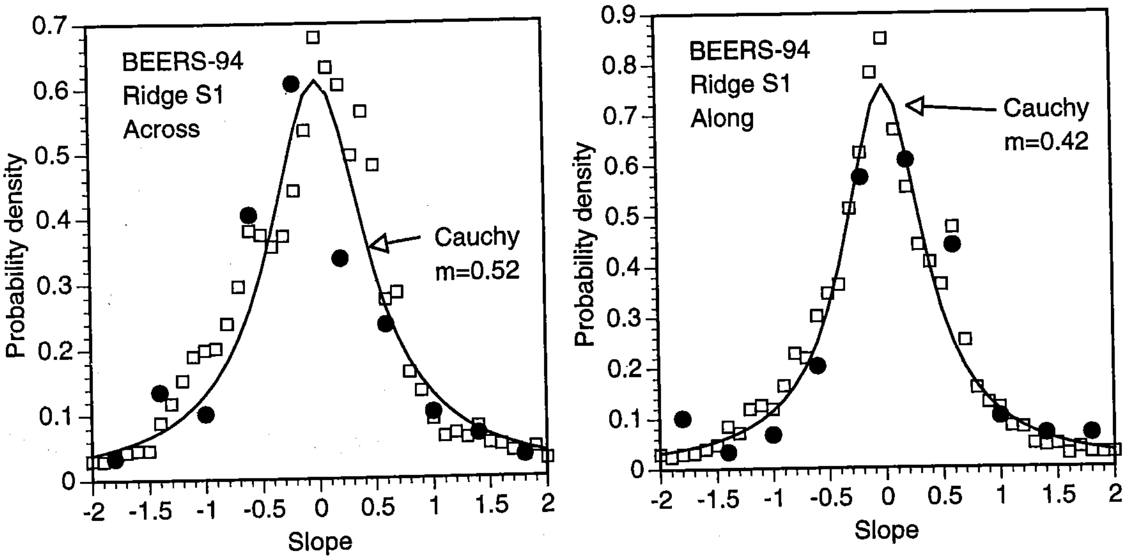

Figure 5. Surface slope distributions derived from laser profile data (squares) and block inclination measurements (points). The line denotes a least-squares fit of a Cauchy distribution to the laser data.

## *2.2. Volumetric Properties*

### 2.2.1. Ice

Volumetric ice properties (density, salinity, temperature, volume fraction and dimensions of air inclusions) are important to measure because they enter into calculations of both the dielectric constant of the ice (which is difficult to measure in the field) and the volume scattering contribution. During the BEERS campaigns, the ice density was determined with an accuracy of ± 0.03 g/cm$^3$ from measurements of volume and weight of ice samples. The salinity of melted ice samples was measured using a Beckman Solubridge calibrated to an accuracy of 0.1 ppt. Ice and snow temperature measurements were carried out with a battery driven thermometer and a PT 100 probe with an accuracy of ± 0.1°C. The ice densities, salinities and temperatures obtained during the BEERS campaigns at different measurement sites are shown in figures 6 and 7.

During BEERS-92 the ice density of the uppermost ice layer (0-10 cm) as observed at 21 different measurement sites varied between 0.81 g/cm$^3$ and 0.89 g/cm$^3$. The measured salinities ranged from 0 to 2.0 ppt, and the temperature from -4.0°C to -0.1°C (measured at air temperatures between -7°C and -0.2°C). In some cases density, salinity and temperature were determined as a function of ice depth. The shapes of the profiles were highly variable. An increase of density and salinity with increasing depth was observed as well as a decrease or no dependence on depth at all. The density and salinity values measured in lower ice layers were within the ranges observed near the ice surface. The temperature always increased near the ice-water interface but showed both positive and negative gradients near the ice surface.

Size distributions of air bubbles were measured during BEERS-92 from samples of the surface layer of the ice. Vertical sections of 3 mm in thickness were illuminated from the side and photographed on a dark background. Number and sizes of bubbles were then determined from the photographs. The largest bubble diameters observed in the samples usually lay between 0.4 mm and 0.7 mm; the air volume fraction varied between 0.2% and 18.5%. At one site on fast level ice the largest bubbles were 2.4 mm in diameter, whereas the total air volume was only 0.3%.

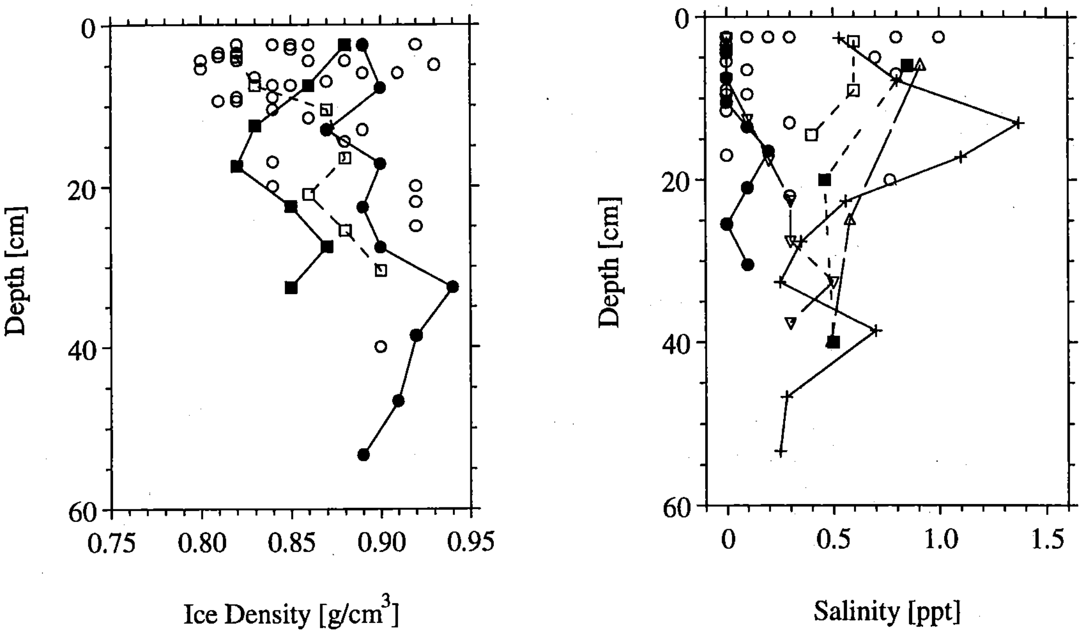

Figure 6. Ice densities (left) and salinities (right) as a function of depth measured at different sites during the BEERS campaigns 1992-94. Profile measurements are connected by lines. The open circles indicate point measurements or short profile segments (≤3 data points).

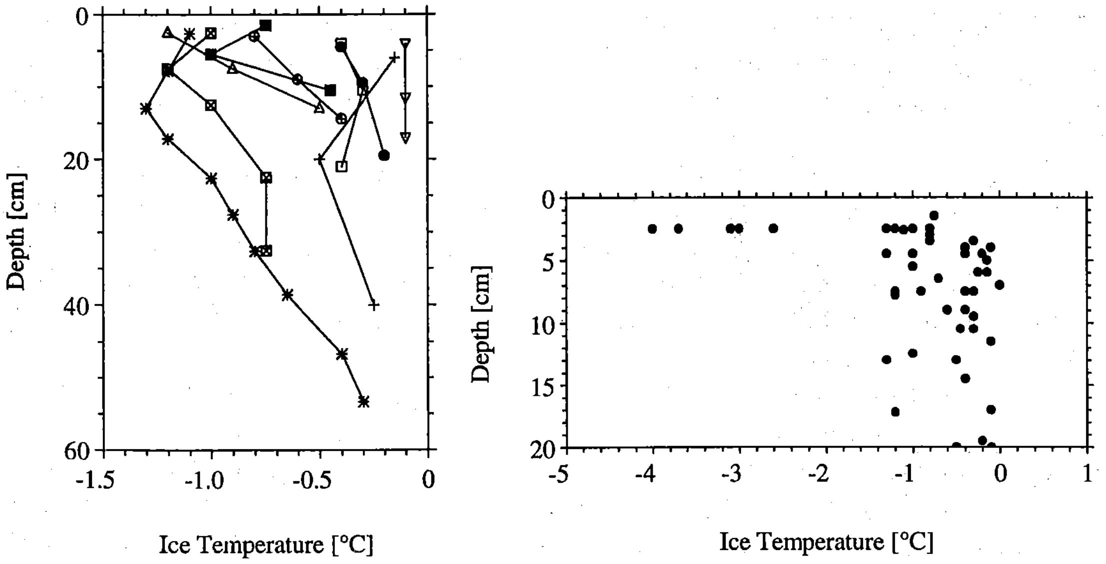

Figure 7. Ice temperature profiles (left) and temperature data measured in depths between 0 and 20 cm (right). The data were acquired at different measurement sites during the BEERS campaigns 1992-94.

The densities and salinities as measured during BEERS-93 ranged from 0.84 g/cm$^3$ to 0.93 g/cm$^3$ and from 0.3 ppt to 0.9 ppt, respectively. They were determined at 5 different sites from the uppermost ice layer (depth 5-7 cm) and in depths of about 20 cm and 40 cm (the latter only at 2 sites). Ice temperatures varied between -0.5°C and 0°C, while the air temperatures during the measurements were between 1.1°C and 2.2°C.

During BEERS-94, density, salinity, and temperature profiles were measured at one site. The density (as a function of depth) varied between 0.87 g/cm$^3$ and 0.94 g/cm$^3$, the salinity between 0.2 ppt (near the ice water interface) and 1.4 ppt (at a depth of 13 cm) with variable gradients (both negative and positive) over the whole profile. The salinities determined from ice samples of another 2 sites were 0.2 ppt and 0.5 ppt. The temperature varied between -1.4°C (at a depth of 15 cm) and -0.3°C near the ice-water interface.

The reported measurement results do not necessarily cover the whole range of possible variations of the ice properties. Local and temporal variations in the ice temperature near the ice surface, e.g., reflect the changes in air temperature (and under certain conditions in wind speed and air humidity). In the presence of a snow layer they depend also on the snow layer properties.

### 2.2.2. Snow

Density and wetness of the snow cover were measured using a radio wave sensor, the so called snow fork (Shivola and Tiuri 1986). A standard procedure was used at most measurement sites whereby three vertical profiles with an equidistant spacing between 2 cm and 5 cm were recorded in each of 3 representative pits. The measured data were stored together with the corresponding snow depths and later transferred to a personal computer. It has been evaluated (Carlström 1993) that the relative error of wetness and density $\rho$ is small in a density range from 0.3 g/cm$^3$ to 0.5 g/cm$^3$ at a snow wetness of less than 6% ($\rho$=0.5 g/cm$^3$) and 8% ($\rho$=0.3 g/cm$^3$) (by volume), respectively. An additional error is induced if the material around the fork is compressed as is possible in the case of fine grained, dense snow. Dependent on the snow density, the relative error may increase up to 3% and more (Shivola and Tiuri 1986). In layers of large, loosely packed snow crystals the snow structure may be destroyed when pushing the fork into the snow, leaving larger air filled voids. In this case the measured value of the dielectric constant is too low.

During BEERS-92 the snow cover on the level ice was in general thin during the two field experiment periods. Usually 9 profiles were acquired and averaged for each of altogether 26 measurement sites. The snow depths varied from 0.5 cm to 9 cm, the densities from 0.09 g/cm$^3$ to 0.3 g/cm$^3$, and the wetnesses from 0.2% to 2.9% (volume). If measured in a distance less than 5 cm from the ice surface, the snow data are biased by the underlying sea ice.The given wetness values may thus be too large. A snow layer thickness of more than 30 cm was only observed at one site on rough ice; the snow density there was 0.34 g/cm$^3$ . Occasionally the snow was slightly saline on single, isolated spots, the measured salinities ranged from 0.2 ppt to 4.4 ppt.

The snow cover as observed during the BEERS-93 field campaign was rather sparse, but some snow had accumulated along the ridges and on rough ice. The snow depths at the 4 selected measurement sites varied between 10 cm and 30 cm. The first measurements were carried out after rainfall. Near the snow surface, the wetness measured with the snow fork was larger than 8%, so that the measurement error became too large. Snow density was estimated by using the weight/volume method. The values obtained ranged from 0.48 g/cm$^3$ to 0.55 g/cm$^3$ in the upper snowlayer, and were about 0.3 g/cm$^3$ in the lower snow bulk. Later during the experiment, the mean wetness was largest near the ice surface (>4%) and decreased down to <1% near the snow surface. However, occasionally the measured wetness was again >8%. Since these values were not included in the estimation of the average values, the given mean values of wetness may be too low. The densities as estimated from the snow fork data and from the weight/volume method agreed well and lay between 0.33 g/cm$^3$ and 0.36 g/cm$^3$.

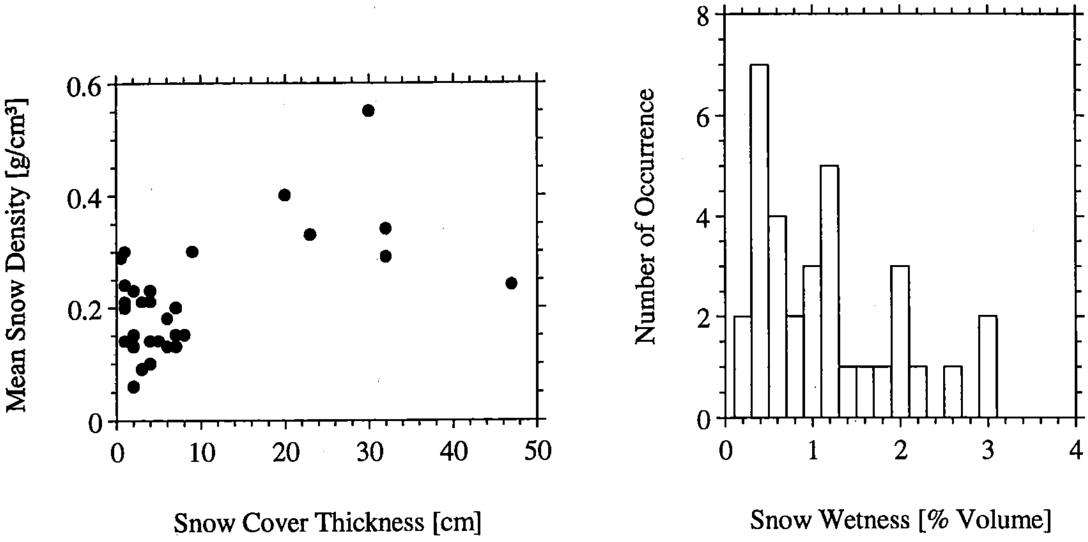

Figure 8. Snow densities as a function of snow layer thickness (left) and snow wetness histogram (right). The data were gathered during the BEERS campaigns 1992-94 and were averaged for each measurement site.

During BEERS-94, 6 snow profiles were acquired over rough ice and at a ridge. The measured snow depths ranged from 20 cm to 50 cm. The snow layer consisted mainly of small snow grains (< 1 mm), but larger crystalls (1-3 mm) were occasionally observed near the ice surface. After a storm had passed the measurement sites, accompanied by an increase in temperature up to the melting point, the average snow density increased from about 0.25 g/cm$^3$ to more than 0.3 g/cm$^3$. This can be explained by additional snow deposition during the storm. In addition, the increase in temperature to the melting point probably caused clustering of the snow crystals typical for wet snow at low liquid contents (Colbeck 1987). The observed mean wetness was slightly larger after the storm, but always less than 1%. The salinity was not measured but is believed to be negligible. The ranges of snow thickness, density and wetness observed at different sites during the BEERS campaigns 1992-94 are depicted in figure 8.

### *2.3. Scatterometer Measurements*

During BEERS-94 backscatter measurements were carried out for different incidence angles at a site of jammed brash ice. In addition, surface roughness data were acquired using the 10m-laser profiler. The scatterometer consisted of an HP8720B vector network analyser, a dipole-fed parabolic dish antenna and a control computer. The system characteristics of the scatterometer are given in Table 1. The center frequency of the stepped CW-signal was 5.4 GHz, and the bandwidth was 960 MHz. Examples of the received power signal in time domain (hereinafter referred to as waveform) averaged over different azimuth directions are shown in figure 9.

Table 1. Scatterometer Characteristics

| | |
|---|---|
| Frequency | 5.4 GHz |
| Polarization | VV, VH, HH, HV |
| 3-dB 1-way antenna beamwidth | 4.7° |
| Equivalent rectangle width of the 2-way antenna azimuth pattern | 0.061 rad |
| Equivalent rectangle range resolution | 0.3 m |
| Maximum unambiguous range | 125 m |
| Altitude of antenna phase center | 23.6 m |
| Incidence angle range | 20 - 65° |
| Cross-polarization isolation | 28.5 dB |
| Peak sidelobe ratio | 18 dB |
| Equivalent noise level $\sigma^0_{ne}(20°)$ | -35 dB (like-pol.),<br>-38 dB (cross-pol.) |
| Equivalent noise level $\sigma^0_{ne}(60°)$ | -25 dB (like-pol.),<br>-31 dB (cross-pol.) |

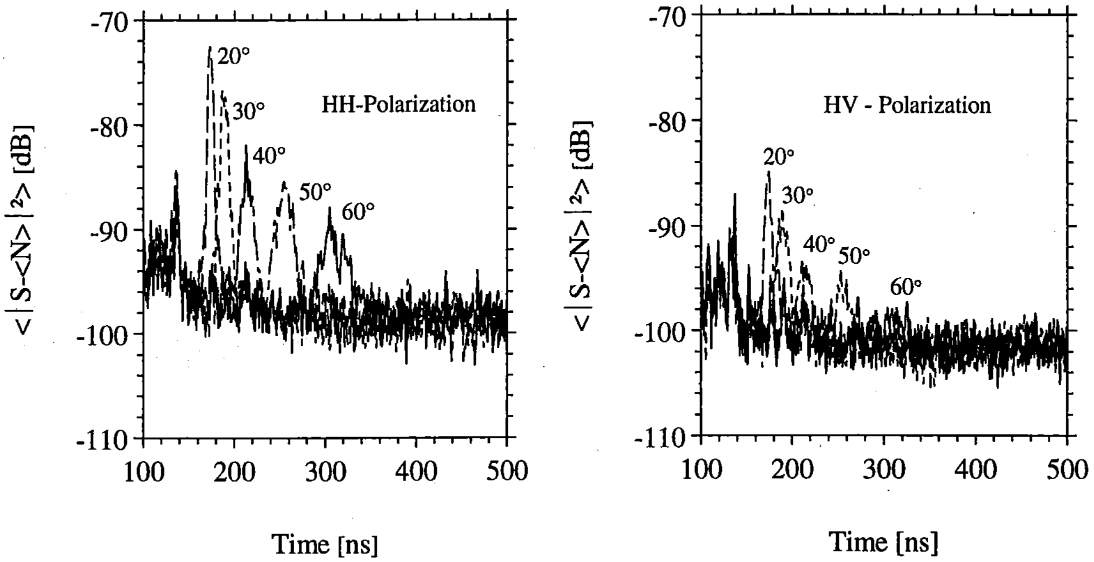

Figure 9. Average waveforms at like- and cross-polarization for different nominal incidence angles. The sampling interval is 1 ns (corresponding to 0.15 m), *S* is complex amplitude, *N* is complex noise.

Comparisons of ground based scattering measurements with SAR image signatures require a careful absolute calibration of the scatterometer data. The network analyser was calibrated prior to the measurements by using a short and a matched load on the like-polarization channels, and a through and matched load on the cross-polarized channels (response and isolation technique). External calibration of the scatterometer was performed by recording the radar response of a 47-cm trihedral. The trihedral was mounted on a tripod and carefully positioned in order to give the maximum returned power. The system noise level was determined by carrying out backscattering measurements while the antenna was pointing to the sky. In order to suppress a constant noise phasor, the average complex noise was subtracted prior to averaging and noise subtraction in power. The backscattering coefficient was measured for different incidence angles ranging from 20° to 65° in steps of 5°. For each incidence angle, data for 14 different azimuth angles were obtained by rotating the antenna around the vertical axis in steps of 5°.

The calibration procedure which is described in (Carlström and Ulander 1993; Carlström 1994) is based on the area-extensive form of the radar equation, which gives the expected received power $P_r(t)$ as a function of time delay (Ulaby *et al.* 1982, Vol. 2, p.752). It is assumed that the range extent of the power impulse response function is small compared to the antenna footprint, the antenna gain function is separable into components in the range and the azimuth direction, and target range and antenna gain function are slowly varying compared to the power impulse response. All system gain factors at boresight are determined by using the trihedral as an external calibration reference. The trihedral response is integrated over a number of range gates to include all significant parts of the impulse response. In this manner, the calibration does not have to consider the exact shape of the impulse response. The backscattering coefficient $\sigma^o$ is then determined by

$$\sigma^o(\theta_o) = \frac{\sigma_\Delta}{\varepsilon_\Delta R_\Delta^4 \Delta\varphi_e} \frac{\int\left[P_r(2R/c) - P_n\right] dR}{\int \frac{g_\theta^2(\theta_0 - \theta)}{R^3 \sin\theta} dR} \tag{4}$$

where $R=ct/2$ is target range; c is speed of light; $\theta$ is incidence angle (which is dependent on $R$); $\theta_o$ is incidence angle at boresight; $P_r$ is received power; $P_n$ is incoherent noise power; $R_\Delta$, $\sigma_\Delta$ are range and radar cross section of the trihedral, respectively; $\varepsilon$ is the range-integrated return power of the trihedral; and $\Delta\varphi_e$ is the equivalent rectangle width of the 2-way antenna azimuth pattern. The integrals are evaluated within the 3dB beamwidth of the antenna pattern in range. The effect of fading can be further reduced by averaging over different azimuth angles.

The standard deviation $\Delta\sigma_P$ of the average signal power $\overline{P}$ depends on the number of independent samples $n$ and the signal-to-noise ratio $S_N$ (Ulaby *et al.* 1982, Vol. 2, pp. 492-495):

$$\Delta\sigma_P = \overline{P}\sqrt{\frac{1}{n}\left(1+\frac{1}{S_N}\right)^2 + \frac{1}{n_N}\left(\frac{1}{S_N}\right)^2} \tag{5}$$

where $n_N$ is number of noise samples; and $n$ is the product of independent samples in range and azimuth, $n=n_r \times n_\Phi$. If it is assumed that the effective rectangle range resolution $\Delta r_e$ and the equivalent rectangle width of the antenna azimuth pattern $\Delta\varphi_e$ are equal to the minimum range distance and the minimum azimuth angle between independent samples, respectively, the number of independent samples in range is

$$n_r = \Delta R_A / \Delta r_e \tag{6}$$

where $\Delta R_A$ is range extent of the antenna footprint (one-way 3-dB beamwidth). The number of independent samples in azimuth $n_\Phi$ is

$$n_\Phi = 1 + \Delta\Phi / 2 \arctan\left( \tan \frac{\Delta\varphi_e}{2 \sin\theta_0} \right) \tag{7}$$

where $\Delta\Phi = 65°$ is the total rotation angle of the antenna during the measurements.

The backscattering coefficients $\sigma^o$ observed over brash ice during BEERS'94 are shown in figure 10 for different incidence angles and different polarizations. The strong decrease of $\sigma^o$ with increasing incidence angles indicates the dominance of surface scattering contributions. The cross-polarized return may be caused by multiple scattering processes both on the ice surface and within the ice volume.

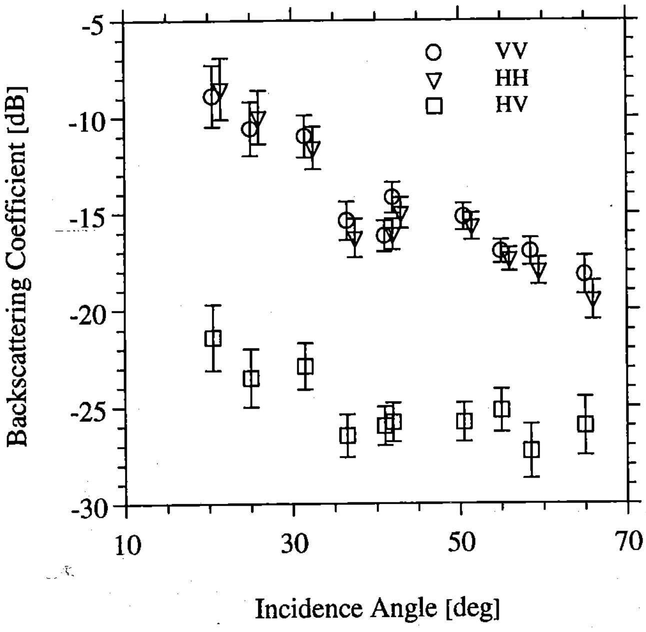

Figure 10. Backscattering coefficients with error bars indicating the 95% confidence interval. In order to reduce overlapping, the data points for HH-polarization are shifted by +1° on the x-axis. The backscattering coefficients at VH and HV polarization were almost identical, therefore only the latter are shown here. In the computations of $\sigma^o$ the nominal incidence angles measured by the inclinometer were replaced by the incidence angles determined from the reception times of the radar returns.

## *2.4. SAR data analysis*

### 2.4.1. Spatially homogeneous ice types

Each measurement area was located in the SAR image using information from GPS (Global Positioning System) positions acquired at the sites and at a reference point visible in the image, e.g. a ship stationed in the ice close to the site. A polygon was then outlined in the image to enclose the area of interest. For the ice types with homogeneous properties over larger areas, i.e. level ice, jammed brash, or hummocked ice, it may be assumed that the target has uniform properties that extends over the entire polygon. Depending on the homogeneity of the area, between 50 and 500 pixels were extracted from the image, resulting in 95% confidence intervals for the backscattered power of ± 1 dB and ± 0.1 dB, respectively. The backscattering coefficient $\sigma^0$ is then determined as described in Chapter B of this report. The SAR data used was processed by ESA to the UI16 (BEERS-92) or PRI (93-94) formats and calibrated accordingly. The absolute calibration accuracy is estimated to better than ±1.0 dB.

In figure 11, the backscattering coefficients of all sites are plotted versus the measured RMS heights with the general ice types indicated. The plot indicates that the principal backscatter mechanism is related to the RMS surface height of both level and deformed ice in the form of jammed brash and hummocked ice. All data were collected during dry snow conditions.

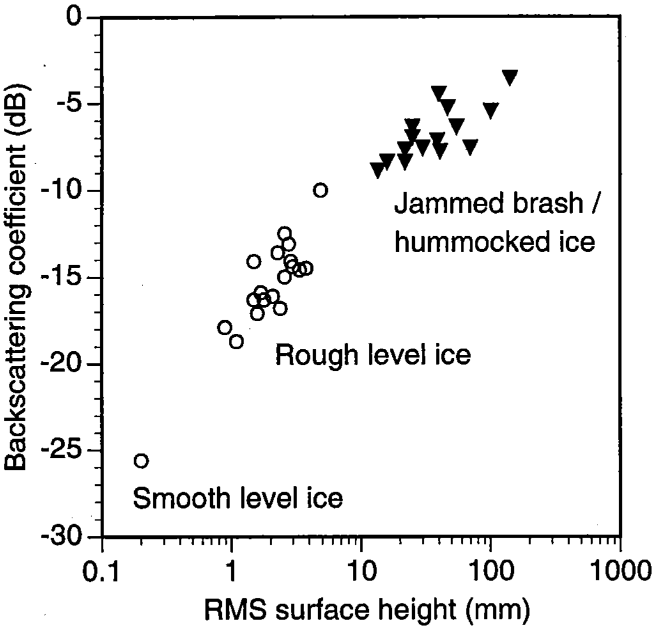

Figure 11. Measured backscattering coefficients versus measured RMS heights of spatially homogeneous ice types.

### 2.4.2. Ice ridges

The estimation of scattering coefficients of ice ridges from SAR images requires special considerations. The basic problem is that the width of the ridge may be smaller than the resolution of the SAR and therefore must be treated as a collection of point targets. Since the resolution cell is larger than the pixel spacing, it is also necessary to integrate over a few pixels on both sides of the actual ridge to estimate the total scattered power. In this estimate, however, scattering from the surrounding ice is also included, which must be subtracted. The ridge area must therefore be known. We have estimated the ridge area using aerial photographs, defined as the total area that was identified as deformed ice in the photograph.

The radar cross section of the ridge is then obtained by

$$\sigma_r = A\frac{1}{N}\sum_{i=1}^{N}\sigma_i^0 - (A - A_r)\sigma_{bg}^0 \tag{8}$$

where $\sigma^0{}_i$ is the apparent backscattering coefficient of each image pixel, $N$ is the number of pixels averaged, $A$ is the total area covered by $N$ image pixels, $\sigma^0{}_{bg}$ is the backscattering coefficient of the surrounding ice, and $A_r$ is the area covered by the ridge. The background scattering $\sigma^0{}_{bg}$ is estimated from an area of undeformed ice close to the ridge.

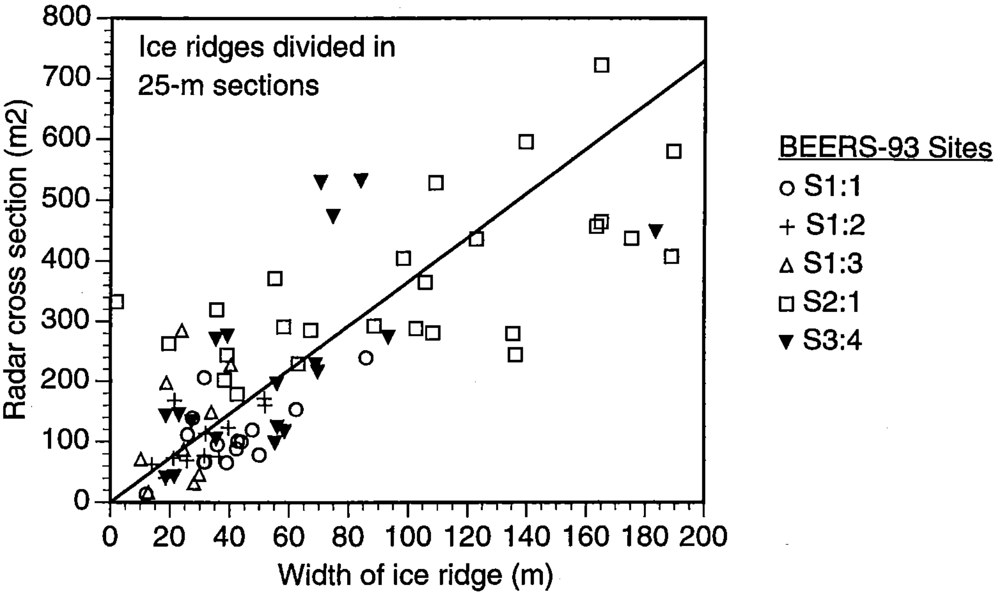

Figure 12. Radar cross section of 25-metre ridge sections versus the average widths. The line represents the radar cross section of an ideal homogeneous target with a backscattering coefficient of -8.4 dB and the spread of the data points corresponds to a standard deviation of ±2 dB in backscattering coefficient.

Figure 12 shows the radar cross section of sub-sections of the five ridges from BEERS-93 plotted versus the average width of the ridge section. The clustering of points along a straight line indicates that the scattering from the ridges is due to a number of scatterers distributed over the entire ridge area. Over a larger area we may thus define a backscattering coefficient for the ridge as

$$\sigma_r^0 = \frac{\sigma_r}{A_r} \tag{9}$$

The backscattering coefficient may thus be interpreted as the slope of the straight line in figure 12. Two of the ridges from BEERS-93 (S3:1 and S3:3) were located within a jammed brash barrier and the background scattering was there so strong that the ridges were not visible in the SAR image and their backscatter could thus also not be estimated. From the BEERS-94 experiment one ridge was analysed. It was less than 10 metres wide and is therefore not included in figure 12. The SAR images from ascending and descending orbits had a difference in incidence angle of 4.5° and 5° at the two experiments. It was found that the scattering was 1-2 dB lower in the image where the incidence angle was higher, except in one case (BEERS-93, S1:3) where the difference was 3.9 dB. The latter may be due to an anisotropy in the scattering properties of the ridge. Any systematic look direction dependence was thus not found but the differences observed were more related to the changes in incidence angle.

## 3. Scattering models and comparisons with data

### *3.1. Dielectric models for ice and snow*

The dielectric properties of sea ice mainly depend on the volumetric fraction of liquid brine which is computed from temperature, salinity, and density measurements. The method devised by Cox and Weeks (1983) has been extended to low salinities and temperatures above -2°C by Leppäranta and Manninen (1988).

Since the salinity of the ice in the Bay of Bothnia is very low, the dielectric constant is similar to that of fresh-water ice. Measurements of fresh-water ice have shown that the imaginary part of the dielectric constant $\varepsilon'' \approx 0.001$ at C-band (Ulaby *et al.* 1986). Further, the complex dielectric constant has been shown to be approximately linearly dependent of the brine volume (Vant *et al.* 1978). Since the linear equations determined by Vant were for higher salinities (between 1.3 and 10.5 ppt), we modify the constant term of the imaginary part to make it approach the measurements of fresh-water ice. Hence, the resulting equations for the dielectric constant are

$$\begin{aligned} \varepsilon' &= 3.05 + 7.2 v_{br} \\ \varepsilon'' &= 0.001 + 3.3 v_{br} \end{aligned} \tag{10}$$

where $v_{br}$ is the brine volume. The modification of $\varepsilon''$ from Vant's equations is less than 0.02, so it is negligible in the salinity ranges where the equations were determined. However, it affects the calculation of the extinction coefficient for low-salinity ice significantly.

The dielectric properties of snow have been reviewed by Hallikainen *et al.* (1986). They propose a semi-empirical Debye-like model and show it to be accurate over the frequency range 3-37 GHz. We used this model to compute the dielectric constant of the snow layer.

### *3.2. Scattering from level ice*

The backscattering coefficient of snow-covered sea ice may be considered as composed of the backscattering from the snow surface and volume, the snow-ice interface, and the ice volume. Neglecting the interactions between surface and volume scattering, the backscattering coefficient of snow-covered sea ice may be expressed as (Kim *et al.* 1984)

$$\sigma^0(\theta) = \sigma^0_{ss}(\theta) + \Upsilon^2_{as}(\theta)\left\{\sigma^0_{sv}(\theta') + \frac{1}{L^2_s(\theta')}\left[\sigma^0_{is}(\theta') + \Upsilon^2_{si}\,\sigma^0_{iv}(\theta'')\right]\right\} \tag{11}$$

where the contributing backscattering coefficients are denoted with $\sigma^0{}_{ss}$ for the snow surface, $\sigma^0{}_{sv}$ for the snow volume, $\sigma^0{}_{is}$ for the ice surface, and $\sigma^0{}_{iv}$ for the ice volume. The Fresnel power transmission coefficients for the air/snow and snow/ice interfaces are denoted $\Upsilon_{as}$ and $\Upsilon_{si}$ respectively, and $L_s$ is the loss factor of the snow layer. The incidence angle is denoted by $\theta$, and the refracted angles in the snow and ice volumes by $\theta'$, and $\theta''$, respectively. Interactions between surface and volume scattering are not included in (11), but may be neglected for like-polarization (Fung and Eom 1982). The backscattering contributions and the model parameters are illustrated in figure 13. Scattering from the ice-water interface is neglected since the attenuation is usually high in the lower part of the ice sheet where the ice temperature is close to the melting point. We also have very few measurements of salinity and temperature in the lower part of the ice sheet and no information about the roughness of the ice-water interface. However, when the salinity is close to zero it is not unlikely that contributions from bottom surface reflections are significant.

The scattering from the snow and ice surfaces are modelled by the single scattering term of the integral equation model (IEM) (Fung *et al.* 1992).

$$\sigma^0_{is}(\theta) = \frac{k^2}{2}\exp\left(-2s^2k_z^2\right)\sum_{n=1}^{\infty} s^{2n}\left|I^n_{pp}\right|^2 \frac{W^n(-2k_x,0)}{n!} \tag{12}$$

where $s$ is the RMS height, $k_z = k\cos\theta$ and $k_x = k\sin\theta$. The coefficients $I^n{}_{pp}$ are functions of polarization state, dielectric constant, incidence angle, and radar wave number $k$. $W^n$ is the two-dimensional Fourier transform of the $n$th power of the surface autocorrelation function. We assume that the surface is isotropic and use an exponential model with correlation length $l$ for the autocorrelation function. The validity of this model has been

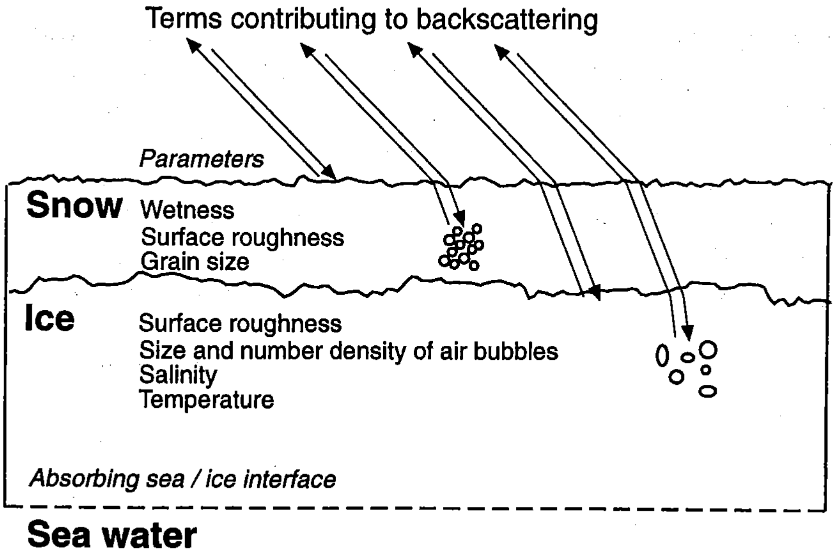

Figure 13. Scattering mechanisms for snow-covered level ice.

verified for surfaces with exponential correlation functions with $s/l < 0.4$ and $ks < 3$ (Fung *et al.* 1992), which means that IEM covers the validity ranges of the conventional small perturbation and physical optics models (Ulaby *et al.* 1986) as well as the roughness region between the two.

Volume scattering from air bubbles in the ice volume are modelled as independent Rayleigh scatterers according to (Kim *et al.* 1985)

$$\sigma^0_{iv}(\theta) = \frac{N\sigma_v \cos\theta}{2\kappa_e}\left(1 - \frac{1}{L_i^2}\right) \tag{13}$$

where $N$ is the number density, $\sigma_v$ is the radar cross section of a single air bubble, $\kappa_e$ is the extinction coefficient, and $L_i = \exp(\kappa_e\, d_i / \cos\theta)$ is the loss factor of an ice layer with thickness $d_i$. To account for a linear vertical temperature profile, the volume scattering contributions for a number of thin layers are summed. The volume scattering is very sensitive to the air void diameter, which makes it difficult to validate with *in situ* measurements. In fact, a factor-two change in the air void diameter gives a 9 dB change in the volume scattering component. The maximum air bubble diameter was measured in a few ice samples and was found to vary between 0.5 mm and 2.4 mm. The snow volume scattering was estimated using this model as well and was found to be insignificant compared to the other scattering terms.

The measured ice properties and backscattering coefficients of level ice are listed in Table 2. The model computations based on these parameters are also given in the table.

Table 2. Measured level ice parameters and backscattering coefficients

| Year, Site | RMS height, $s$ (mm) | Corr. length, $l$ (mm) | Salinity (ppt) | Temp. (°C) | Density (g/cm$^3$) | Thickness (m) | Incidence angle, $\theta$ (deg) | Measured $\sigma^0$ (dB) | Modelled $\sigma^0$ (dB) |
|---|---|---|---|---|---|---|---|---|---|
| '92 S3:1 | 2.8 | 39 | 0.8 | -1.3 | 0.86 | 0.35 | 20.5 | -13.1 | -14.2 |
| '92 S3:4 | 2.9 | 8 | 0.2 | -1.3 | 0.89 | 0.20 | 20.4 | -14.1 | -15.7 |
| '92 S4:1 | 1.8 | 19 | 0.8 | -1.3 | 0.86 | 0.14 | 20.5 | -16.3 | -16.8 |
| '92 S5:1 | 2.6 | 51 | 0.2 | -1.3 | 0.86 | 0.35 | 21.2 | -12.5 | -16.7 |
| '92 S5:2 | 2.6 | 68 | 0.3 | -1.3 | 0.85 | 0.45 | 21.3 | -15.0 | -17.6 |
| '92 S5:4 | 2.3 | 10 | 0.0 | -1.3 | 0.86 | 0.27 | 21.0 | -13.6 | -16.5 |
| '92 S6:1 | 4.9 | 41 | 0.2 | -0.8 | 0.90 | 0.12 | 22.2 | -10.0 | -11.0 |
| '92 S7:1 | 2.4 | 30 | 0.1 | -0.8 | 0.86 | 0.33 | 25.5 | -16.8 | -17.8 |
| '92 S7:2 | 0.2 | 48 | 0.6 | -0.8 | 0.85 | 0.16 | 25.4 | -25.6 | -31.9 |
| '92 S8:1 | 2.1 | 8 | 0.0 | -1.0 | 0.80 | 0.27 | 22.0 | -16.1 | -18.8 |
| '92 S8:2 | 0.9 | 31 | 0.0 | -1.0 | 0.88 | 0.48 | 23.1 | -17.9 | -23.8 |
| '92 S8:3 | 1.5 | 6 | 0.0 | -1.0 | 0.86 | 0.48 | 23.1 | -16.3 | -21.3 |
| '92 S8:4 | 1.5 | 13 | 0.0 | -1.0 | 0.81 | 0.45 | 23.0 | -14.1 | -20.0 |
| '92 S8:8 | 1.7 | 13 | 0.0 | -1.0 | 0.82 | 0.40 | 21.1 | -15.9 | -17.8 |
| '93 S1 14/3 | 1.6 | 51 | 0.8 | -0.15 | 0.92 | 0.32 | 20.8 | -14.0 | -14.4 |
| '93 S1 17/3 | 2.0 | 23 | 0.8 | -0.9 | 0.92 | 0.32 | 25.5 | -17.1 | -17.7 |
| '93 S2 14/3 | 2.9 | 74 | 0.85 | -0.15 | 0.9 | 0.53 | 20.8 | -10.1 | -11.8 |
| '93 S2 17/3 | 2.9 | 74 | 0.85 | -0.9 | 0.9 | 0.53 | 26.0 | -14.4 | -16.3 |
| '93 S3 | 1.0 | 43 | 0.8 | -0.9 | 0.86 | 0.34 | 25.5 | -18.7 | -23.6 |
| '94 S4 | 3.4 | 42 | 0.5 | -2 | 0.9 | 0.5 | 21.4 | -14.6 | -14.3 |

During the '92 and '94 experiments, the snow cover was dry and the model did not give any significant scattering contribution from the snow layer. During BEERS-93, a wet snow layer was present at the SAR overpass on the 14/3. At site S1, the snow layer was thin and most of it had melted and refrozen until the 17/3. The snow parameters used in the model predictions for the 14/3 are shown in Table 3, whereas a bare ice surface was used to model the conditions of the 17/3. At the second site (S2), the snow cover was still present on the 17/3 and was thus included in the model but with lower wetness according to measurements from that date. The measured backscattering coefficients decreased 3-4 dB from the 14/3 to the 17/3. The change was in good agreement with the model results when a snow wetness of 10% was assumed on the 14/3. Since the snow wetness was too high to be measured by the snow fork, this value was estimated from qualitative observations and density measurements. About 1.5-2 dB of the decrease in backscatter may be attributed to the difference in incidence angle between the two dates but the decreasing snow wetness is responsible for the additional change.

Table 3. Snow parameters used for BEERS-93 model computations

| Year, Site | RMS height (mm) | Corr. length (mm) | Density ($g/cm^3$) | Wetness (%) | Snow depth (m) | Temperature (°C) |
|---|---|---|---|---|---|---|
| '93 S1 14/3 | 2.3 | 17 | 0.55 | 10 | 0.01 | 0 |
| '93 S2 14/3 | 3.5 | 22 | 0.55 | 10 | 0.02 | 0 |
| '93 S2 17/3 | 3.5 | 22 | 0.55 | 1.6 | 0.02 | -1 |

Figure 14 compares the model computations of surface, volume, and total backscattering coefficients with the measured backscattering coefficients of each measurement site. In the model predictions we have used an air bubble diameter of 1 mm. The error bars indicate the sensitivity of the model prediction to a factor-two uncertainty in the air bubble diameter in both directions. The model clearly underestimates the measurements when the RMS height $s < 1$ mm or the salinity $S < 0.1$ ppt. In those cases, the agreement is improved when the air bubble diameter is increased. Another reason for the differences may be scattering from the ice/water interface, which is dependent on a very low salinity in the bottom of the ice layer. The salinity and the roughness at the interface were not characterized and that scattering contribution is therefore difficult to estimate. When the ice surface is very smooth, the scattering may also be dominated by the snow surface, which is neglected in these computations. However, when $s > 1.5$ mm and $S > 0.5$ ppt, the ice surface scattering is totally dominating and the deviations between model and measurements are always less than 2 dB. The errors caused by the standard error of the roughness parameters (see Section 2.1.1) are less than 1 dB, but errors are also introduced in the assumption of stationarity for the surface height profile and in deviations from the exponential model for the correlation function. Small deformation features in the ice, as e.g. cracks or rafts, are also likely to contribute to the backscattered power registered by the SAR.

### *3.2 Scattering from deformed ice with a rough surface or small blocks*

During BEERS-94, backscatter measurements were carried out on an area of frozen jammed brash using the C-band scatterometer operated from the icebreaker *Oden*. The

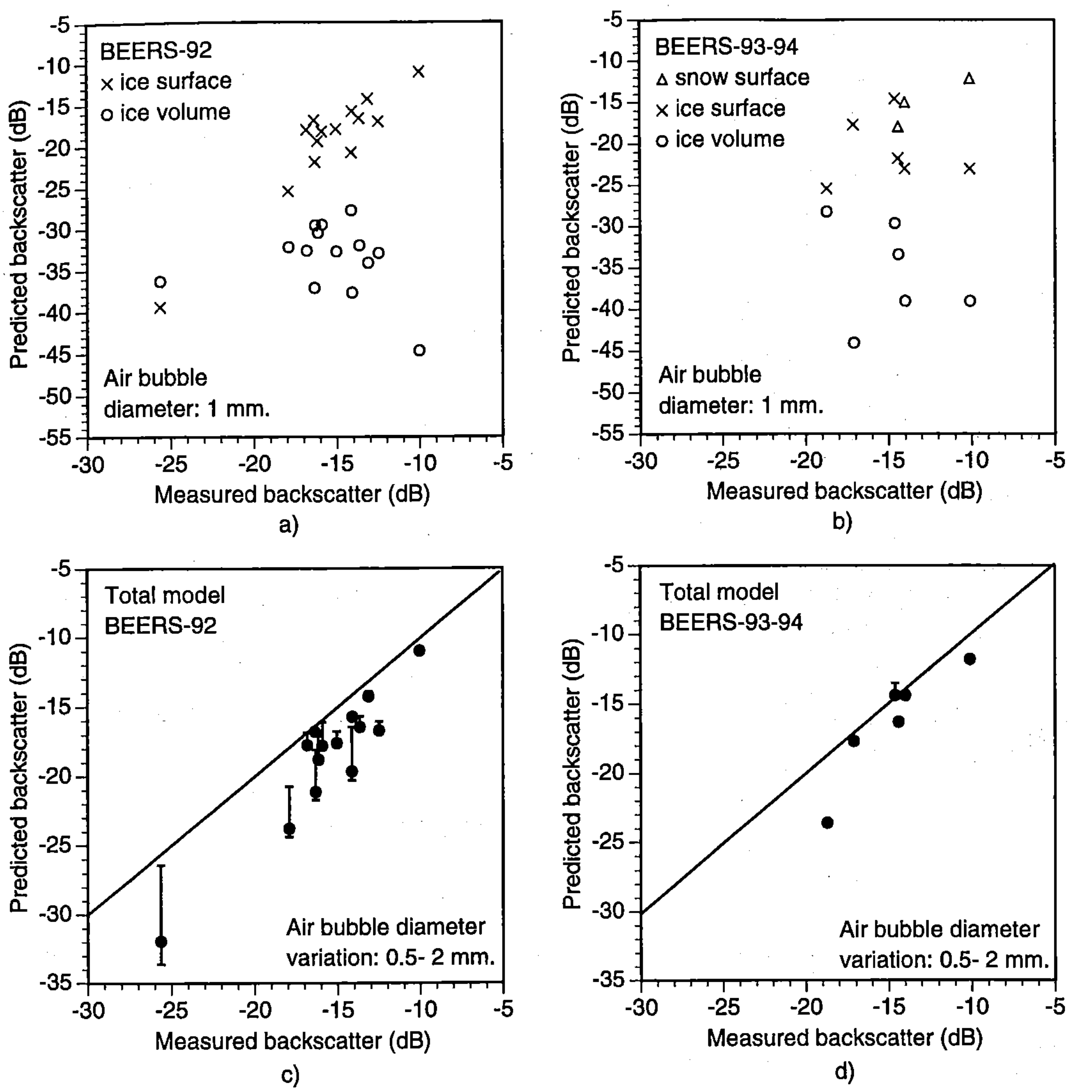

a) b) c) d)

Figure 14. Model results versus measured backscatter of level ice. a) and b) compares the contributions of surface and volume scattering, which are summed in c) and d) to give the total model prediction. The error bars show the sensitivity to a factor two variation in air bubble diameter around 1 mm.

ice surface was rough but without any distinct blocks and was covered by a 2-5 cm layer of dry snow. This was the site with the lowest RMS height of the deformed ice investigated during BEERS.

Altogether eight surface elevation profiles were measured with the 10-m laser profiler. Autocorrelation functions were evaluated for all profiles and then averaged before normalizing. In this case there was not any dominant surface topography on scales comparable to the profile length. Therefore we assumed stationarity and analysed the 10-m profiles in full length. The resulting RMS height is 24 mm and the correlation length determined from the mean correlation function is 0.31 m. For a surface that is smooth on the wavelength scale, the physical-optics model as described in (Fung and Eom 1981) can be applied in order to calculate the surface scattering contribution. The backscattering coefficient is

$$\sigma^0(\theta) = \frac{2k^2|R(0)|^2}{\cos^2\theta} e^{-4k^2 s^2 \cos^2\theta} \int_0^\infty \left( e^{4k^2 \cos^2\theta \, s^2 \rho(r)} - 1 \right) J_0(2kr\sin\theta) r dr \qquad (14)$$

where $\rho$ is the normalized correlation function and $J_0$ is the zeroth order Bessel function. The physical model consists of a layer of dry snow above a rough ice surface. The effect of the dry snow cover is to reduce the dielectric contrast, the wavelength, and the incidence angle on the ice surface. Compared to the case of a bare ice surface, the backscattering coefficients at lower incidence angles are reduced, whereas they are increased at larger incidence angles (Carlström *et al.* 1994).

Since the computed backscattering is very sensitive to the shape of the correlation function $\rho$ within a small region close to the origin, different correlation models were fitted to the measured $\rho$ within a range of displacement from 0 to 0.1 m. A good fit was obtained using the function $\exp(-x^2/(l^2x^2+l'^4)^{1/2})$ with a large-scale correlation length $l$ of 0.28 m and a small-scale correlation length $l'$ of 81 mm (see figure 15). The resolution of the laser profiler, which is shown in figure 15 as the autocorrelation of its impulse response, does not permit a detailed analysis of the small-scale surface structure. Due to the 20 mm footprint of the laser, we do not have any information about surface wavelength components shorter than about 40 mm. However, since the Gaussian correlation length $l'$ is considerably larger than the laser footprint the Gaussian shape is considered geophysically significant, although the accuracy of $l'$ is difficult to estimate. Due to the Gaussian-like origin of the measured correlation function it can be assumed that the surface undulations are smooth enough so that the tangent plane approximation can be used which is the basis of the physical optics model.

Results of the model computations are shown together with the scatterometer measurements in figure 16. The figure also shows the SAR backscatter observed from the ascending and descending orbits of ERS-1 at incidence angles of 25° and 21°, respectively. The model results are mainly sensitive to changes in the ratio $s/l'$, whereas corresponding relative changes in $l$ are less recognizable. This may be interpreted as a sensitivity to the surface slope distribution, since the RMS slope is proportional to the ratio $s/l'$.

Since the ice cover consisted of small pieces of frozen brash, the presence of volume inhomogeneities is likely. Thus a volume scattering contribution can not be totally excluded. The sudden drop of the $\sigma^o$ measurements at incidence angles around 35-40 degrees may indicate a change in the surface and/or volume characteristic.

We applied the same model to other sites with similar properties as shown in Table 4. Since the profiles at these sites were obtained by manual sampling, we had to apply linear interpolation before computing the correlation functions. The deviations from the measurements were 0.3-2.5 dB (see Table 4). This model is restricted to surfaces with low RMS heights relative to the small-scale correlation length. Hence, we could only apply it for the jammed brash ice surfaces with the lowest RMS heights.

Table 4. Results of backscatter model for deformed ice with a rough surface

| Site | $s$ (mm) | $l'$ (mm) | $l$ (m) | $\theta$ | SAR $\sigma^o$ (dB) | Model $\sigma^o$ (dB) |
|---|---|---|---|---|---|---|
| '94 S3 | 24 | 81 | 0.28 | 21.3° | -8.1 | -10.3 |
| '92 S8:6 | 33 | 180 | 0.50 | 21.5° | -8.4 | -8.7 |
| '92 S9:1 | 45 | 190 | 320 | 21.4° | -7.0 | -9.5 |
| '92 S9:2 | 34 | 170 | 250 | 21.3° | -8.5 | -8.8 |

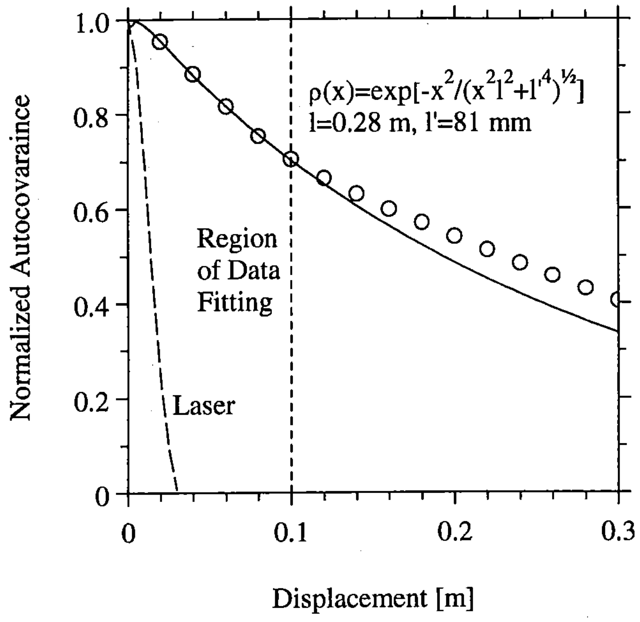

Figure 15. Normalized mean autocorrelation function (circels) and theoretical correlation model (solid line) for the scatterometer measurement site. The theoretical function was fitted within the range 0 - 0.1 m. The correlation function of random noise which was convolved with the laser impulse response function is also shown (dashed line).

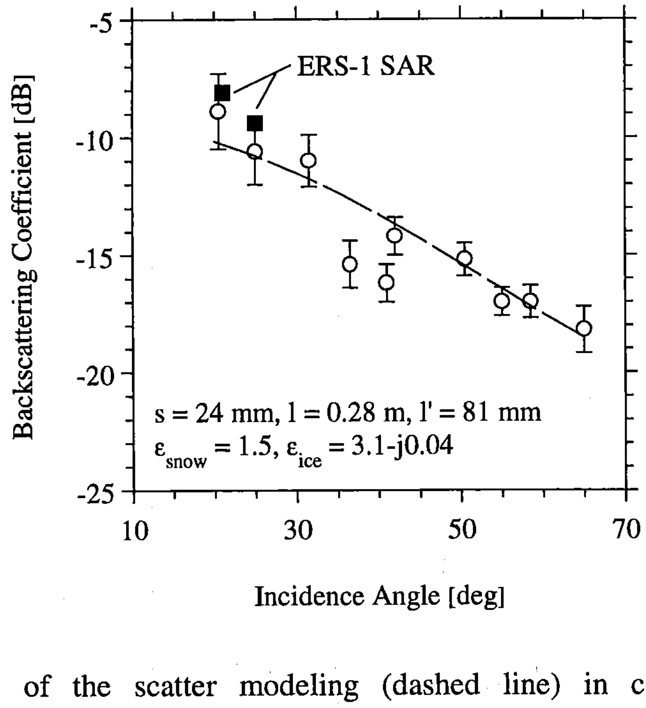

Figure 16. Results of the scatter modeling (dashed line) in comparison to the backscattering coefficients at VV-polarization measured with the scatterometer (circles) and the ERS-1 SAR (dark squares). For modeling, the theoretical correlation function shown in figure 15 was used.

### 3.3 Scattering from deformed ice with large blocks

Characteristic for the studied deformed ice types is that the surface consists entirely of broken pieces of ice. These pieces are usually in the shape of blocks with dimensions of the order of decimetres to several metres. From a scattering point of view, the surface of a jammed brash barrier is similar to that of an ice ridge. The main difference is that the ice ridge blocks are distributed within a narrow sail, while a jammed brash barrier may cover kilometre sized areas. We will thus use the same scattering model for jammed brash and hummocked ice as for ridges. Scattering models for ice ridges which average the scattering from randomly oriented ice blocks was suggested in (Johansson and Askne 1987, Manninen 1992). We will here make a comparison of the results from a similar block scattering model under some simplifying conditions with the measured backscattering coefficients of the deformed ice features.

The mean backscattering coefficient of an ensemble of equally sized, randomly oriented ice blocks is

$$\sigma^0(\theta) = \frac{1}{\langle A_h \rangle} \iint p\left(z_x', z_y'\right) \sigma\left(\theta_i\right) dz_x' dz_y' \tag{15}$$

where $\sigma$ is the radar cross section of a single ice block at the local incidence angle $\theta_i$, $z'_x$ and $z'_y$ are the slopes of the major facet along the $x$ and $y$ directions, respectively, and $p(z'_x, z'_y)$ is the joint probability density of the facet slopes. The projection of the block area on the horizontal plane is denoted $A_h$ and <...> denotes the ensemble average. We may evaluate (15) approximately for flat facets using the fact that the probability density function is slowly varying compared to the scattering pattern of the facet, which is evaluated under the physical-optics approximation. The validity conditions are that $r >> \lambda$ and $m >> \lambda / 4r$, where $m$ is the RMS slope, $\lambda$ is the radar wavelength, and $r$ is the radius of an assumed circular facet. The result is (Carlström and Ulander 1994)

$$\sigma^0(\theta) = \frac{A}{\langle A_h \rangle} \left\{ \Gamma \frac{\pi}{\cos^3 \theta} p(\tan\theta, 0) + \iint p\left(z_x', z_y'\right) \sigma_s^0\left(\theta_i\right) dz_x' dz_y' \right\} \tag{16}$$

where $A = \pi r^2$ and $\Gamma$ is the effective reflectivity of the ice block surface given by

$$\Gamma = \left\langle |R(0)|^2 \right\rangle e^{-4k^2 s^2} \tag{17}$$

In (17), $R(0)$ is the Fresnel reflection coefficient at normal incidence and $k = 2\pi/\lambda$ is the radar wave number. The first term in (16) represents specular (or coherent) reflections from the block facets and is similar to the specular point scattering (or geometrical optics) model (Barrick 1968). A small-scale roughness on the facet is accounted for by a mean rough surface backscattering coefficient $\sigma^0_s$ in (16) and the exponential factor which reduces the magnitude of specular reflections in (17). For simplicity we may neglect the polarization dependence since we are only interested in like-polarized scattering. We see that the backscatter is independent of the size of the facets as long as $r >> \lambda$, and is mainly determined by the facet slope distribution. Hence, (16) is a good approximation also for an ensemble of blocks with different sizes.

To take into account the effect of interactions between the upper and lower interfaces of the ice blocks, we use the effective reflection coefficient for a plane-parallel layer.

We thus assume that the space on the shadow side of the block is air filled. If the blocks are of randomly varying thickness, phase interactions will average out and the mean effective reflectivity Γ is given by the incoherent model for a dielectric slab (Ulaby et al. 1986)

$$\Gamma = \Gamma_1 \left\{ 1 + \frac{\Upsilon_1^2 / L^2}{1 - \Gamma_1^2 / L^2} \right\} \tag{18}$$

where $\Gamma_1$ and $\Upsilon_1$ are respectively the reflectivity and transmissivity of the air-ice interface, and L is the one-way power loss through the ice block. For blocks with low losses the interaction gives an increase in the backscattering coefficient of 2.7 dB, as compared to the case of lossy blocks. For rough blocks, the reflection and transmission coefficients are modified by the small-scale roughness and the specular term is reduced.

The Cauchy distribution observed for the one-dimensional surface slope distribution corresponds to the isotropic two-dimensional probability density function

$$p(z'_x, z'_y) = \frac{m}{2\pi \left(m^2 + z_x'^2 + z_y'^2\right)^{3/2}} \tag{19}$$

in which $m = 1$ corresponds to a uniform distribution of the facet normal in solid angle. For this distribution we get $\langle A_h \rangle = A/(1+m)$. We may now apply our in situ data to the model in the form of estimates of the surface slope distribution. For this we have to make some general assumptions about the surfaces. For the model to be valid we must assume that the surface consists of blocks that are much larger than the wavelength. The measured average block cross sections were in the region between 0.7 m and 1.6 m and thus fulfil this condition, although smaller blocks were observed at other sites. Because we retrieve the slope distributions from profile data we must also assume that the slope distribution is uncorrelated to the size distribution. The block parameter measurements did not indicate any such correlation. We must also assume that the surface slope distribution is isotropic, which is considered reasonable for the studied cases, although there were some differences observed for the profiles acquired along and across ice ridges. If we use the effective reflectivity together with (16) and the Cauchy-type distribution we get the result shown in figure 17, which also includes the surface slope and SAR measurements according to Table 5.

The model shows a small difference between flat facets and facets with a small-scale roughness of $s = 3$ mm and $l = 70$ mm. These values represents relatively rough blocks compared to the roughness measurements (see Section 2.1.1). Diffuse scattering from both the upper and lower surfaces of the ice blocks are included. The reason for the small difference is that an increase in the rough surface scattering is partly compensated by a decrease in the specular component. We found that the specular component dominates for blocks with small-scale roughness within the observed range and that a simple geometrical optics model for flat facets approximates also rough facets well.

The incidence angles for the given data points are here only varying between 20.5° and 22.3°. The model predicts a backscatter decrease with incidence angle of 0.3 dB/° within the incidence angle range of ERS-1, which agrees with differences observed between ascending and descending orbits of ERS-1 (see Section 2.4). The model fails to explain the backscattering coefficients between -3 and -5 dB measured for high surface slopes. The model actually predicts a decrease with increasing slope. Possible reasons for the deviations are effects like multiple scattering and scattering from the end facets of blocks, which become important for large slopes. Diffraction effects are also important for small block sizes where physical-optics theory is not valid. Interactions within the ice blocks other than those considered may also be important. Shadowing is neglected in the model but is expected to be of minor importance for single scattering at the low incidence angles used by the ERS-1 SAR.

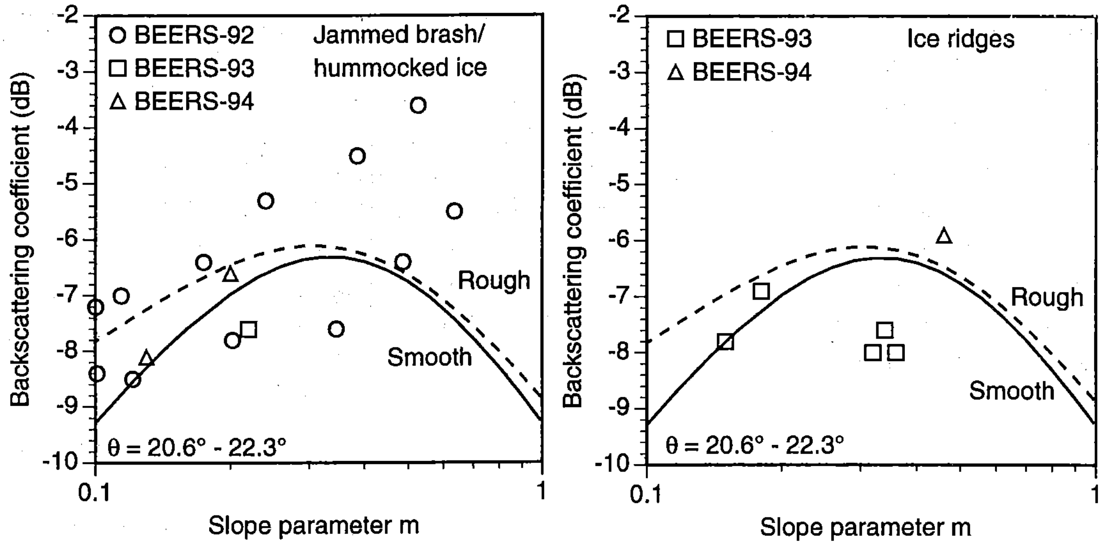

a) b)

Figure 17. Comparison between scattering model and SAR measurements of a) jammed brash and hummocked ice and b) ice ridges. The model computations are for blocks with different surface roughness and includes scattering from both upper and lower interfaces with an assumed propagation loss $L = 1.8$ dB through the blocks. The incidence angles varies between 20.6° and 22.3° in the measurements and the model uses the average value.

## 4. Model inversion

A major objective and an application of backscatter modelling is to enable data inversion. For a single channel sensor like the ERS-1 SAR, we are restricted to estimate the dominant scattering source. In this case we have found that the rough ice surface dominates the scattering. Hence, we assume that the backscattering coefficient is only dependent of the ice surface roughness and the radar incidence angle. This is a realistic assumption when the snow cover is dry, except for the smoothest ice where volume scattering is dominant. Apart from a dry and thin snow cover, we also adopt the average values of the measured ice volume parameters and the correlation lengths.

For the deformed ice, backscatter models suggest that the scattering is determined by the slope distribution rather than the RMS height. However, the measurements show a strong correlation between the slope parameter and the RMS height of high-pass filtered profiles (see figure 4). Also the backscattering coefficient is increasing with increasing RMS height as can be seen in figure 11. Based on these data we propose an empirical relation between roughness and backscatter of deformed ice according to

$$\sigma^0 = a\left(s/s_0\right)^b e^{-4(\theta-\theta_0)} \tag{20}$$

Table 5. Measured deformed ice parameters and backscattering coefficients.

| Year, Site | Ice type | RMS height 1m high-pass (mm) | Width of slope distribution, $m$ | Incidence angle, $\theta$ (deg) | Backscattering coefficient, $\sigma^0$ (dB) |
|---|---|---|---|---|---|
| '92 S4:2 | Jammed brash | 55 | 0.49 | 20.5 | -6.4 |
| '92 S4:3 | " | 30 | 0.35 | 20.5 | -7.6 |
| '92 S5:3 | " | 101 | 0.64 | 20.9 | -5.5 |
| '92 S6:2 | " | 25 | 0.17 | 22.2 | -6.4 |
| '92 S6:3 | " | 47 | 0.24 | 22.2 | -5.3 |
| '92 S6:4 | " | 40 | 0.38 | 22.2 | -4.5 |
| '92 S6:5 | " | 41 | 0.20 | 22.2 | -7.8 |
| '92 S8:5 | Hummocked | 142 | 0.53 | 22.3 | -3.6 |
| '92 S8:6 | Jammed brash | 16 | 0.10 | 21.5 | -8.4 |
| '92 S8:7 | Hummocked | 39 | 0.10 | 21.6 | -7.2 |
| '92 S9:1 | Jammed brash | 25 | 0.11 | 21.4 | -7 |
| '92 S9:2 | " | 22 | 0.12 | 21.3 | -8.5 |
| '93 S3:2 | " | 22 | 0.22 | 21.3 | -7.7 |
| '94 S2 | Hummocked | 70 | 0.20 | 21.3 | -6.6 |
| '94 S3 | Jammed brash | 14 | 0.13 | 21.3 | -8.1 |
| '93 S1:1 | Ridge | 96 | 0.36 | 21.0 | -8.0 |
| '93 S1:2 | " | 75 | 0.31 | 21.0 | -8.0 |
| '93 S1:3 | " | 80 | 0.34 | 21.0 | -7.6 |
| '93 S2:1 | " | 30 | 0.15 | 21.0 | -7.8 |
| '93 S3:4 | " | 63 | 0.18 | 21.4 | -6.9 |
| '94 S1 | " | 118 | 0.47 | 21.3 | -5.9 |

where $s$ is the RMS height of surface Fourier components with wavelengths shorter than one metre, $s_0 = 0.040$ m, and $\theta_0 = 21.6°$. A least-squares fit to the BEERS-92 data in log-log space gives $a = -6.5 \pm 0.4$ dB and $b = 0.44 \pm 0.16$ with a correlation coefficient of 0.77. Also the '93 and '94 data were in agreement with this model. An incidence angle dependence of 0.3 dB/° is assumed in (20) in order to obtain agreement with the theoretical model (16) and with the observed differences between ascending and descending orbits. The relatively good fit of the empirical relation to the data makes it possible to apply for data inversion.

The total inversion model may be compared with the measured data in figure 18. There is a gap between the level ice model and the deformed ice model between RMS heights 5-15 mm, which is bridged by linear interpolations in log-log space. The effect of volume scattering causes the plateau value for smooth ice at a level which is determined by the size of air bubbles, ice salinity, and ice density. The deviation between the measured RMS height and the model estimate is approximately ±50%. The measurements which deviates the most from the inversion model are the fast ice measurements with the lowest salinity ($S < 0.2$ ppt). In those cases we expect that interactions with the ice/water interface, which are not included in the model, may be important. Hence, the inversion model over estimates the surface roughness in the fast ice, close to river outlets or in other regions with a salinity close to zero. Other errors are induced by deviations of parameters as e.g. the correlation length and the air void diameter from the assumed values. When the ice surface is very smooth ($s < 1$ mm), the scattering is dominated by other scattering mechanisms than ice surface scattering and the inversion result is obviously not meaningful.

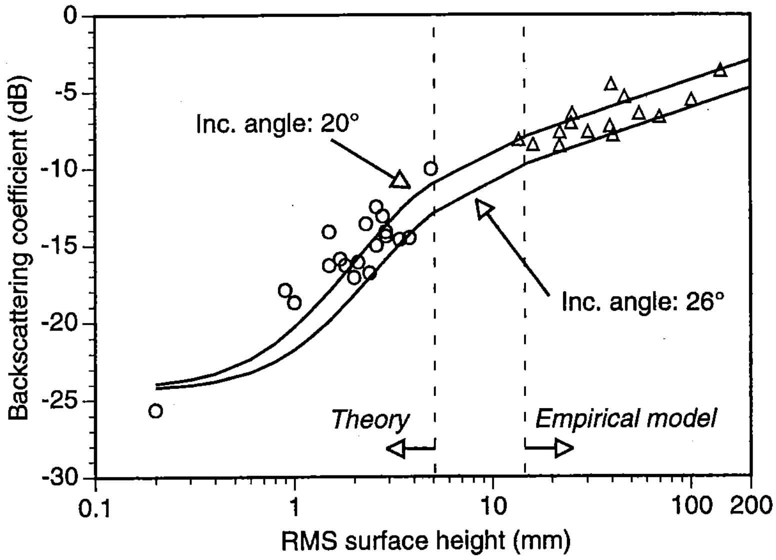

Figure 18. Model for estimation of surface roughness compared with measured data of level (circles) and deformed (triangles) ice. The model uncertainty is largest for very smooth ice ($s \leq 1$ mm) and for ice with very low salinity ($S \leq 0.2$ ppt).

Figure 19 shows an example of a SAR image from the BEERS-92 experiment. The image was averaged to 80 by 80 m resolution and radiometrically calibrated before the inversion model was applied. The incidence angle variation is accounted for by the model and the roughness estimates shown in the pseudo-coloured image were computed. The image is from the northernmost part of the Bay of Bothnia and the land areas are not masked out from the image. The ice floes in the lower right part consists to a large extent of jammed brash barriers with very rough surfaces. Around and between the floes new ice is formed with a smooth surface. The compressed fast ice boundary in the upper part of the image is also very rough. An open water lead extends from left to right across the image below the fast ice boundary. Open water is not treated correctly by the model since the strong radar return is ambiguous with the backscatter from very rough ice like jammed brash or ice ridges.

Figure 20 shows a roughness map computed from a SAR image from BEERS-94. The 1994 winter was colder and the ice situation was therefore different compared to 1992, with e.g. thicker and older drift ice present. The deformation features were more in the shape of ridges and hummocked ice. Jammed brash barriers were not as common and mainly located at the fast ice boundary. It is also apparent that the roughness of the fast ice in the archipelago is over estimated, due to the very low salinity in those areas.

It is important to note that the model is developed for distributed areas with homogeneous roughness statistics, while the width of ice ridges is often only a couple of metres. Hence, there radar response will be averaged with the surrounding ice signature and the result is often more related to the width than to the roughness of the ridge. The inversion model in its present form is expected to work during cold conditions, while the presence of wet snow would require the model parameters to be adjusted accordingly and is a matter for further investigation.

## 5. Discussion and conclusions

We have investigated backscattering mechanisms for level and deformed sea ice in ERS-1 SAR images during winter conditions. Different backscatter models have been evaluated based on an extensive data set with *in situ* measurements of different sea ice types in the Baltic Sea. The *in situ* data include surface height measurements which cover horizontal scales between 2 mm and 10 m together with ice and snow physics measurements.

The backscattering model for level ice consists of two contributions: rough surface scattering from the ice surface and volume scattering from air voids in the ice sheet. Surface scattering is calculated using the single-scattering integral-equation model (IEM) and volume scattering using independent Rayleigh scatterers. The results of the model were in correspondence with the ERS-1 SAR backscatter measurements. Our results also agree with earlier studies and show that rough surface scattering dominates despite the low salinity of Baltic sea ice. The only exception from this is for smooth ice with very low salinity mainly found in the fast ice close to river outlets.

A two-component backscattering model is proposed for deformed ice where the ice surface height variations are divided into two parts: flat ice blocks and super-imposed small-scale roughness. The solution is simplified by assuming large blocks and moderate to large slopes, in which case no consideration of the block size distribution is necessary. The backscattering consists of specular reflections from ice blocks calculated using physical optics and diffuse surface scattering from the super-imposed roughness using IEM. By evaluating the model based on the *in situ* data, we conclude that the backscattering in ERS-1 SAR images is dominated by specular reflections from ice blocks and not by surface scattering from the small-scale surface roughness. In contrast to earlier results, we note that the small-scale roughness has in fact very little effect on the backscatter unless the block slopes are very small or the incidence angle is very large. The reason is that an increased small-scale roughness is partly compensated by a decrease of specular reflection. The deformed ice model includes reflections from both sides of the ice blocks, and uses a Cauchy-type slope distribution. A comparison with the ERS-1 backscatter measurements shows good agreement except in a few cases where the measured backscatter is 2-3 dB higher than the model prediction. The latter suggests that multiple and/or edge scattering should be included in future model developments.

When the deformed ice consists of ice fragments of the order of the wavelength in size it may not be described by a block model. Instead, we used the RMS height and the surface height autocorrelation function as input to the physical-optics model. Good agreement was obtained to both scatterometer measurements at incidence angles between 20°-60° and with the ERS-1 SAR for several cases. For RMS heights of the order of half a wavelength, the model is mainly sensitive to the shape of the correlation function close to the origin, which is related to the RMS slope and average radius of curvature of the surface. The small-scale structure showed to be more important than what was expected and the analysis would have been improved if also the small-scale laser profiler had been used together with the scatterometer.

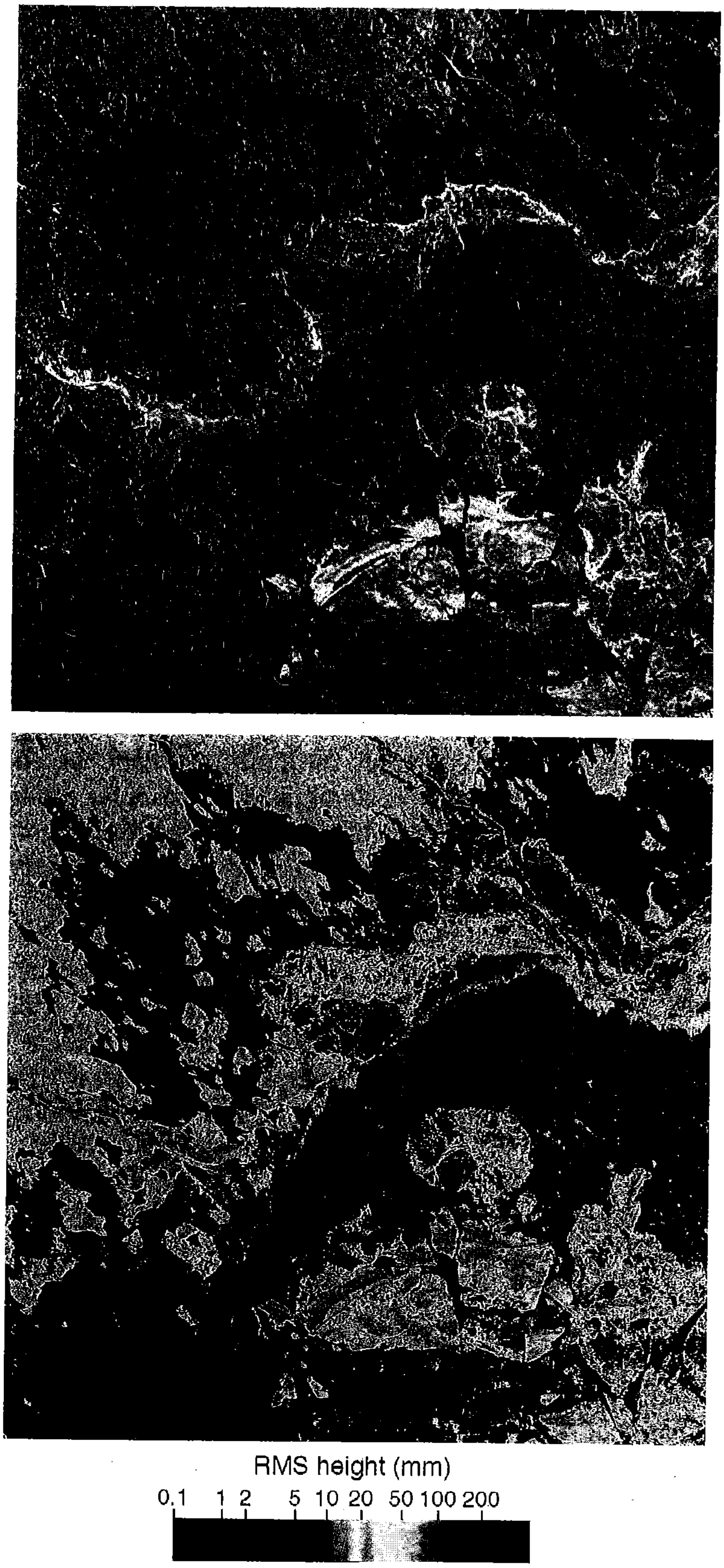

Figure 19. (a) ERS-1 SAR image (© ESA-ERS 1992) from 30 March 1992 covering 80 km x 80 km of northern Bay of Bothnia. The city of Luleå is visible in the left part of the image. (b) Pseudo-coloured result of model inversion showing estimated ice surface RMS height. The land contours have not been masked out.

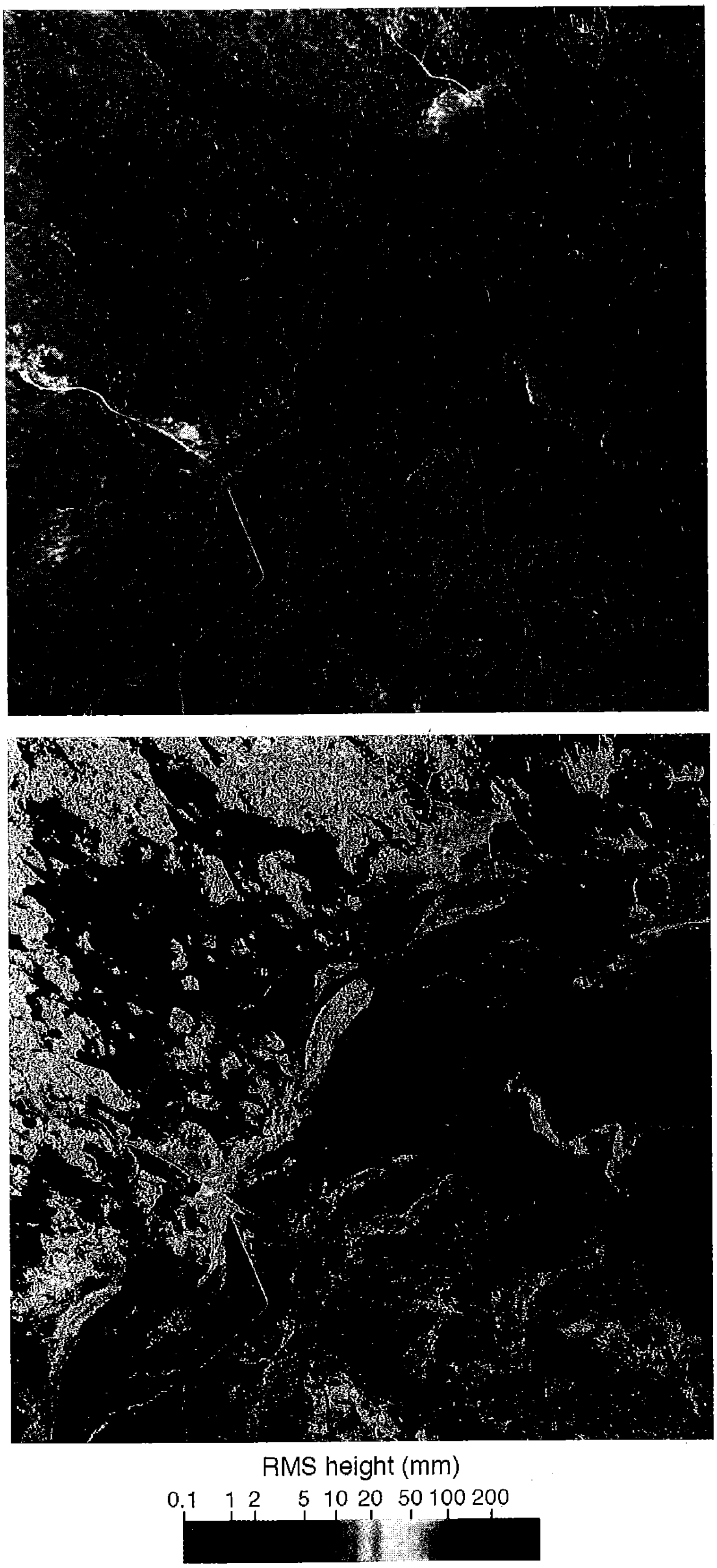

Figure 20. ERS-1 SAR image (© ESA-ERS 1994) and estimated ice surface RMS height in the Gulf of Bothnia on 5 March 1994. The image covers the same area as figure 19.

Dry snow slightly modifies the backscattering coefficient of rough ice, since it changes the dielectric contrast, wavelength, and incidence angle on the ice surface. Modelling results indicate that a dry snow cover lowers the scattering at lower incidence angles. If the penetration depth of the radar wave is substantially reduced due to snow wetness, the dominant scattering source is the snow surface. Since the snow surface roughness is not necessarily correlated to the roughness of the ice, rough ice areas may be masked and identification of deformed areas becomes difficult.

An empirical model is proposed for deformed ice which relates the backscattering coefficient to the RMS surface height. A backscattering model valid for both level and deformed ice is then constructed which is only a function of the RMS surface height and the radar incidence angle. A model inversion is used to estimate the RMS surface heights in ERS-1 SAR images, and the results show a standard deviation of ±50% compared with the *in situ* data. The main limitations of the roughness inversion are that the snow cover must be dry, the RMS height must be more than 1 mm, and the salinity should be above 0.2 ppt for ice surface scattering to be dominant.

## Acknowledgement

Participants in the BEERS experiment from the Swedish Meteorological and Hydrological Institute, the National Defence Research Establishment, and Luleå University of Technology are acknowledged for contributions during the field data collection. Financial support was provided by the Swedish National Space Board.

## References

BARRICK, D. E., 1968, Rough surface scattering based on the specular point theory. *IEEE Transactions on Antennas and Propagation,* **AP-16,** 449-454.

CARLSTRÖM, A. (editor), 1993, Baltic Experiment for ERS-1, BEERS-93: Swedish calibration validation data report, Internal report, RSG 1993:3, Dept. Radio and Space Science, Chalmers University of Technology, Göteborg, Sweden.

CARLSTRÖM, A. (editor), 1994, Baltic Experiment for ERS-1, BEERS-94 data report, Internal report, RSG 1994:2, Dept. Radio and Space Science, Chalmers University of Technology, Göteborg, Sweden.

CARLSTRÖM, A. and ULANDER, L. M. H., 1993, C-band radar backscatter signatures of old sea ice in the central Arctic during freeze-up. *IEEE Transactions on Geoscience and Remote Sensing*, **31,** 819-829.

CARLSTRÖM, A. and ULANDER, L. M. H., 1995, Validation of backscatter models for level and deformed sea ice in ERS-1 SAR images. *Int. J. Remote Sensing*, in press.

CARLSTRÖM, A., ULANDER, L. M. H. and DIERKING, W., 1994, Influence of ice and snow properties on ice ridge mapping by SAR. *14th EARSeL Symposium, Göteborg, Sweden, 6-8 June 1994*, in press.

CHURCH, E. L., 1988, Fractal surface finish. *Applied Optics*, **27,** 1518-1526.

COLBECK, S. C., 1987, Snow metamorphism and classification. In *Seasonal Snowcovers: Physics, Chemistry, Hydrology,* edited by H. G. Lones and W. J. Orville-Thomas, (D. Reidel Publishing Comp.), pp. 1-35.

COX, G. F. N. and WEEKS, W. F., 1983, Equations for determining the gas and brine volumes in sea-ice samples. *Journal of Glaciology,* **29,** 306-316.

FUNG, A. K. and EOM, H. J., 1981, Note on the Kirchhoff rough surface solution in backscattering. *Radio Science*, **16,** 299-302.

FUNG, A. K. and EOM, H. J., 1982, Application of a combined rough surface and volume scattering theory to sea ice and snow backscattering. *IEEE Transactions on Geoscience and Remote Sensing*, **20,** 528-535.

FUNG, A. K., LI, Z. and CHEN, K. S., 1992, Backscattering from a randomly rough dielectric surface. *IEEE Transactions on Geoscience and Remote Sensing*, **30,** 356-69.

HALLIKAINEN, M., TARES, T., TOIKKA, M. and HEISKA, K., 1991, Classification of low-salinity sea ice types by dual-frequency multipolarization scatterometer. *Proceedings of IGARSS '91, held in Espoo, Finland, on June 3-6 1991*, 91CH2971-0 (New York: IEEE ), pp. 1211-1214.

HALLIKAINEN, M. T., ULABY, F. T. and ABDELRAZIK, M., 1986, Dielectric properties of snow in the 3 to 37 GHz range. *IEEE Transactions on Antennas and Propagation*, **34,** 1329-1340.

JOHANSSON, R. and ASKNE, J., 1987, Modelling of radar backscattering from low-salinity ice with ice ridges. *International Journal of Remote Sensing*, **8,** 1667-1677.

KANKAANPÄÄ, P., 1991, Morphology of sea ice pressure ridges in the Baltic sea, Licentiate thesis, Department of Geography, Univ. of Helsinki.

KENDALL, M. G. and STUART, A. S., 1963, *The advanced theory of statistics, Volume I,* (New York: Hafner Publishers).

KIM, Y.-S., ONSTOTT, R. G. and MOORE, R. K., 1984, The effect of a snow cover on microwave backscatter from sea ice. *IEEE Journal of Oceanic Engineering*, **OE-9,** 383-388.

KIM, Y. S., MOORE, R. K., ONSTOTT, R. G. and GOGINENI, S., 1985, Towards identification of optimum radar parameters for sea-ice monitoring. *Journal of Glaciology*, **31,** 214-219.

LEPPÄRANTA, M. and MANNINEN, T., 1988, The brine and gas content of sea ice with attention to low salinities and high temperatures, Internal Report, 2, Finnish Institute of Marine Research, Helsinki, Finland.

LIVINGSTONE, C. E., ONSTOTT, R. G., ARSENAULT, L. D., GRAY, A. L. and SINGH, K. P., 1987, Microwave sea-ice signatures near the onset of melt. *IEEE Transactions on Geoscience and Remote Sensing*, **GE-25,** 174-187.

MANNINEN, A. T., 1992, Effects of ice ridge properties on calculated surface backscattering in BEPERS-88. *International Journal of Remote Sensing*, **13,** 2469-2487.

ONSTOTT, R. G. and GOGINENI, S. P., 1985, Active microwave measurements of Arctic sea ice under summer conditions. *Journal of Geophysical Research*, **90,** 5035-5044.

ONSTOTT, R. G., GRENFELL, T. C., MÄTZLER, C., LUTHER, C. A. and SVENDSEN, E. A., 1987, Evolution of microwave sea ice signatures during early summer and midsummer in the marginal ice zone. *Journal of Geophysical Research*, **92,** 6825-6835.

SIHVOLA, A. and TIURI, M., 1986, Snow fork for field determination of the density and wetness of a snow pack. *IEEE Transactions on Geoscience and Remote Sensing,* **24,** 717-721.

TIURI, M., SHIVOLA, A. H., NYFORS, E. G. and HALLIKAINEN, M. T., 1984, The complex dielectric constant of snow at microwave frequencies. *IEEE Journal of Oceanic Engineering*, **OE-9,** 377-382.

TOIKKA, M. and HALLIKAINEN, M., 1992, Radar backscatter signatures of Baltic sea ice. *Proceedings of IGARSS '92, held in Houston, Texas, on 26-29 May 1992*, 92CH3041-1 (New York: IEEE), pp. 1527-1529.

ULABY, F. T., MOORE, R. K. and FUNG, A. K., 1986, *Microwave remote sensing: Active and passive, 3 volumes,* (Dedham, MA: Artech House).

ULANDER, L. M. H. and CARLSTRÖM, A. (editors), 1993, Baltic Experiment for ERS-1, BEERS-92: Swedish calibration validation data report, Internal report, RSG 1993:1, Dept. Radio and Space Science, Chalmers University of Technology, Göteborg, Sweden.

ULANDER, L. M. H., JOHANSSON, R. and ASKNE, J., 1992, C-band radar backscatter of Baltic sea ice: theoretical predictions compared with calibrated SAR measurements. *International Journal of Remote Sensing*, **13,** 2447-2468.

VANT, M. R., RAMSEIER, R. O. and MAKIOS, V., 1978, The complex-dielectric constant of sea ice at frequencies in the range 0.1-40 GHz. *Journal of Applied Physics*, **49,** 1264-1280.

WMO, 1989, Sea ice nomenclature, WMO/OMM/BMO - No. 259. TP. 145, World Meteorological Organization, Geneva, Switzerland.

# E. ERS-1 SAR SIGNATURES OF SEA ICE AND LEADS

PATRIK B.G. DAMMERT and LARS M.H. ULANDER

Department of Radio and Space Science
Chalmers University of Technology
S-412 96 Göteborg, Sweden

BJÖRN LARSSON

National Defence Research Establishment (FOA)
P.O. Box 1165
S-581 11 Linköping, Sweden

**Abstract.** This study analyses field experiment data collected during the BEERS programme and ERS-1 satellite SAR images from the same periods. The satellite images have been used to determine the radar signatures for the major ice types. The radar signature consists of the mean and the coefficient of variation of the backscattering. Test areas have been classified using helicopter photographs and a specially developed ice classification table. The relation between ice deformation features and radar signature has been analysed and the results show good correlation during both dry and wet conditions. However, the number of ice classes which may be discriminated decreases during wet conditions compared to dry conditions. It is concluded that about seven and three ice classes can be reliably discriminated during dry and wet conditions, respectively. Discrimination of ice and open water leads is not possible using the radar signature but is rather easy for a trained operator. We conclude that the radar signature in ERS-1 SAR images provides a useful classification technique for the major ice types, which could form the basis for an automatic ice classification algorithm.

## 1. Introduction

A number of field experiments were carried out as part of the BEERS program (see Chapter A) which included aerial photography to map the large scale features close in time with the ERS-1 SAR overpasses. We used a helicopter which could take off with short notice to make maximum use of the short periods of suitable weather conditions. This study gives results from analysing radar backscatter signatures of the major ice types in ERS-1 SAR images which have been classified using the helicopter photography.

Several investigations of the backscatter signatures of Baltic sea ice have been reported in the literature. Both C- and X-band measurements have been carried out for different incidence angles and polarisation states. We mainly consider results for C-band and VV-polarisation since the ERS-1 SAR operates in this frequency band and with this polarisation state. Results for different incidence angles will be discussed with emphasis on 23° which is the incidence angle in the middle of the ERS-1 SAR images.

Helicopter scatterometer measurements during cold and dry conditions in 1991 show good discrimination between level and very deformed ice using the backscatter in like- and cross-polarisation together (Toikka and Hallikainen, 1992). This conclusion was based on incidence angles of 23° and 45°, whereas no discrimination was possible at 0°. It was also concluded that a single channel is not sufficient for ice type classification. Examination of their results, however, indicate that a distinct threshold between the two ice types occurs at a backscattering coefficient of about -17 dB for C-band and VV-polarisation. Results from warm and very wet conditions in 1990, on the other hand, show very little promise for ice type classification (Hallikainen *et al.* 1991). The discrimination of level and deformed ice is approximately at the same backscatter level, but is much less distinct. Scatterometer measurements were also performed in 1988 when air temperatures were slightly below 0°C and the snow conditions were mainly dry (Hyyppä and Hallikainen, 1992). Results show that the discrimination threshold between level and deformed ice is approximately -11 dB, *i.e.* considerably higher than during the 1991 experiment.

Studies of radar backscattering signatures using airborne SAR images have also been reported. Results at 60° of incidence angle show that three surface types can be discriminated with 90% accuracy: (1) level ice, (2) brash and rubble, and (3) open water and young ice (Sun *et al.* 1992). The discrimination threshold between level and deformed ice was found to be about -17 dB at 60° of incidence angle (Sun *et al.* 1992), and about -13 dB at 40° of incidence angle (Ulander *et al.* 1992). The latter result was based on HH-polarisation measurements but is also expected to be accurate for VV-polarisation, since the backscatter of deformed ice shows little difference between the two like-polarisation states. The 4 dB difference between the two measurements is explained by the 20° difference in incidence angle. Extrapolation of these results to 23° of incidence angles gives a discrimination threshold of about -10 dB, which is in good agreement with the -11 dB based on the helicopter scatterometer measurements during 1988.

It is clear that most previous investigations have been based on a fairly limited data set. A number of research questions therefore need to be addressed using a large data set of ERS-1 SAR images, *e.g.*

- How many ice type classes can reliably be discriminated using the single channel ERS-1 SAR?
- Are the radar signatures of the ice types stable in space and time?
- What is the backscattering coefficient which separates level and deformed ice?
- What is the effect of wet snow and flooding on the radar signatures?

## 2. Experiment data set

### *2.1. General conditions*

Three field experiments were carried out in the Bay of Bothnia during the winters of 1992, 1993 and 1994. The ice and weather conditions were considerably different for the three experiments, including both cold and warm temperatures as well as mild and severe ice deformation (Ulander and Carlström 1993, Carlström 1993, Carlström 1994).

The 1992 experiment (BEERS-92) was divided into two parts. The first part took place between 15 and 21 February and the other part between 26 and 30 March. The weather during these periods was cold (below 0° C) and with shifting winds. During the experiment period there was no precipitation and any snow on top of the ice was rather dry. The ice conditions during this winter was generally mild and there were few ridges, although the wind created a number of jammed brash barriers in March. Two charts illustrating the ice situations during both parts are found in figure 1.

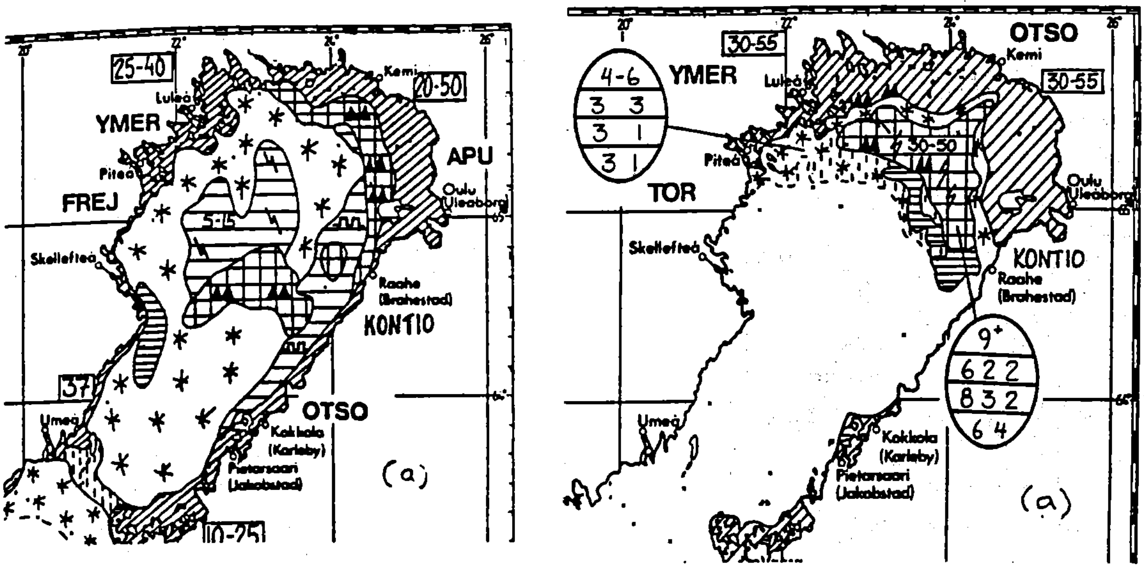

(a) (b)

Figure 1. Ice chart from (a) 20 February and (b) 29 March 1992

The 1993 experiment (BEERS-93) was carried out between 14 and 18 March. The weather during these days was warm with temperatures fluctuating around 0° C. During the period, some rain occurred which made the snow very wet. In some places the snow even had a wetness above the range of the instruments. Although the weather in February was cold, the ice conditions were mild but with more ridges than the year before. Figure 2 illustrates the ice conditions at the beginning and at the end of the experiment.

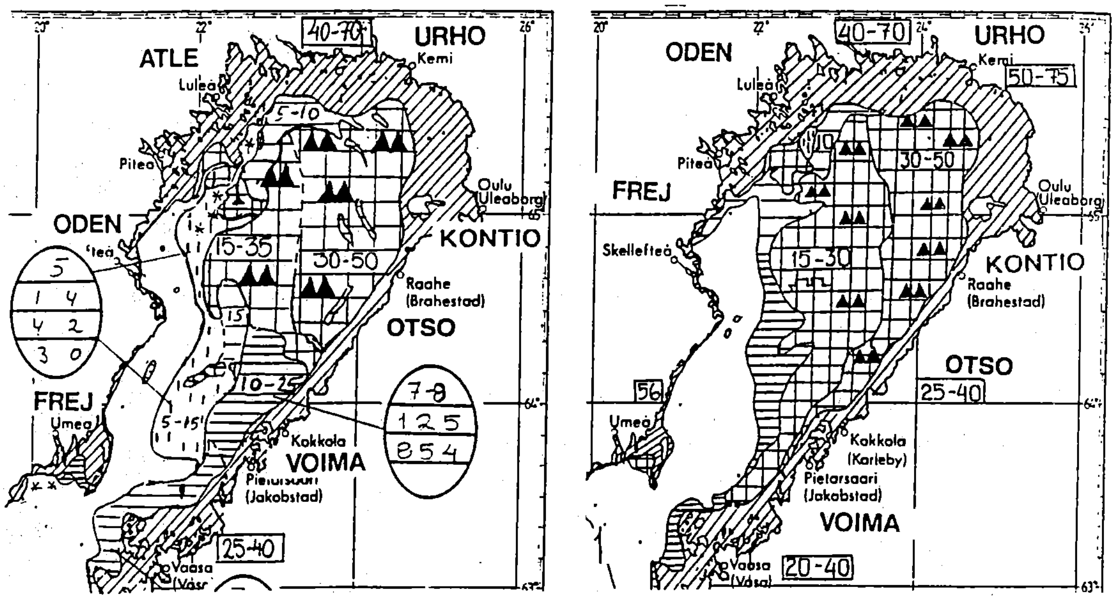

(a) (b)

Figure 2. Ice chart from (a) 14 March and (b) 18 March 1993

The 1994 experiment (BEERS-94) was carried out between 1 and 10 March. This winter was a normal ice winter with fast ice as far south as Stockholm and with a level thickness of 0.8 m. Throughout the experiment period as well as the winter season, the whole Bay of Bothnia was covered with 0.5 m thick consolidated ice. There were a lot of ridges but not so many jammed brash barriers, probably due to the consolidated ice which did not break up until the end of April. The weather was cold and dry during the field experiments except during a storm which hit the ice camp in the middle of the experiment period. The BEERS-94 period experienced normal to severe ice conditions which was a good complement to the earlier experiments. The ice conditions are illustrated in figure 3.

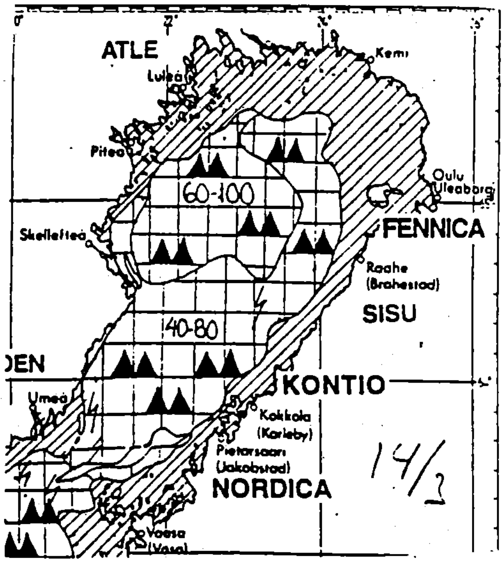

Figure 3. Ice chart from 14 March 1994

## 2.2. *SAR images*

SAR data were acquired by the ERS-1 satellite and processed by the European Space Agency. Most images were obtained during descending (north to south) satellite passes and a few from ascending (south to north) passes. During BEERS-92 and BEERS-94, the ERS-1 satellite was in a 3-day repeat orbit, *i.e.* it repeats the coverage after three days. During BEERS-93, ERS-1 was in its normal 35-day repeat orbit which provides a better spatial coverage of the Earth at the expense of temporal sampling.

A total number of ten images have been analysed in this study. A more detailed description of the images is found in appendix A.

### *2.3. Helicopter photographs*

Helicopter photography was acquired (see appendix B) using a Hasselblad camera with a wide-angle lens mounted under the fuselage. In addition some films were taken by hand-held cameras from the cockpit. The objectives of the flight programme was to map the large scale ice conditions and to take point photographs at different heights over interesting ice features.

### *2.4. Additional data*

Other information which has been used in this analysis are weather statistics from SMHI, field site descriptions in the data reports, field notes taken by the participants and personal comments by the participants.

Weather statistics were retrieved from Storöhamn, Farstugrunden and from icebreakers operating in the area. Weather statistics at the times of the SAR image acquisitions are found in appendix A.

## 3. Ice deformation classes

### *3.1. Ice table*

Since the radar signature mainly depends on ice roughness, a special ice classification table has been developed by Dammert (1993) and is as far as possible based on the World Meteorological Organization nomenclature (WMO 1989). The classification table is shown in table 1.

Table 1. Ice classification table

| Main group | Sub group |
|---|---|
| Level ice | Smooth level ice |
| | Rough level ice |
| Deformed ice | Slightly deformed ice |
| | Ridged ice |
| | Hummocked ice |
| | Rubble field |
| | Jammed brash barrier |
| Open water leads | |

The class smooth level ice has no evident deformation features in the helicopter photographs. Rough level ice includes rafted nilas and level ice which has less than one deformation feature per km.

The class slightly deformed ice has at least a few deformation features and/or small ridge lines per km. When ridges and hummocks cover up to about 20% of an area, the area is called ridged ice.

As the ridges get larger and broader and there is little level ice in between, the area is called hummocked ice. At the fast-ice boundary large and broad fields with heavily deformed ice may form which are called rubble fields.

A jammed brash barrier is made up of brash and small rubble jammed together by wind and wave action. These barriers can be very long and broad (up to several kilometres). A jammed brash barrier is easily recognised in photographs.

Open water leads are easily recognised in helicopter photographs, although it is difficult to determine if they are covered by new ice.

### *3.2. Examples of ice classes*

On the following pages, there are four satellite images with corresponding helicopter photographs. The photographs show the most important ice classes for every experiment period. The arrows at the sides point out the specific areas within the photographs to which the classes are referred. Note the difficulties in classifying areas in the photographs. Deformed areas can often be delineated but other surface characteristics are also visible which may obscure interpretation, *e.g.* snow cover and level ice thickness variations. However, the analysis is carried out with enlarged photographs which make more details appear in them. Note also that deformation features tend to dominate the SAR image although they only cover a fraction of the surface area.

## 4. Radar backscattering from sea ice

Sea ice consists of pure ice mixed with liquid brine pockets, air bubbles and salt crystals and is often covered by a snow layer as illustrated in figure 4. The radar backscatter from sea ice is very complex and may have both surface and volume components, depending on surface roughness and dielectric properties of the ice and snow. There is also a dependency on the radar frequency, although that is not further investigated or discussed here.

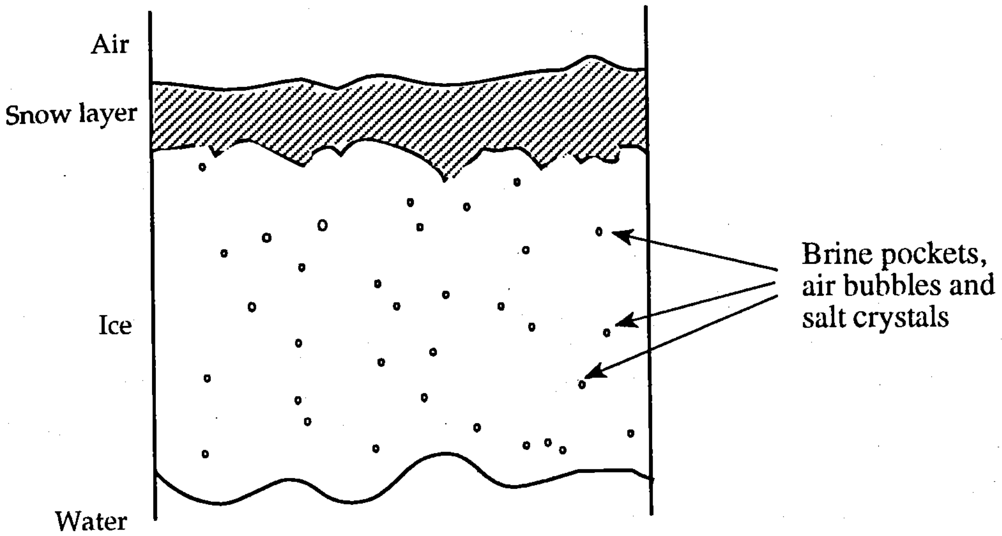

Figure 4. Cross section of sea ice

Surface backscatter will occur when the dielectric constant changes at an interface. Significant backscatter, however, will only occur when the interface has roughness components on the same scale length as the radar wavelength (diffuse scattering), or when the surface normal is nearly perpendicular to the incident wave (specular reflection). The former mechanism dominates for level ice, whereas the latter dominates for deformed ice (see Chapter D).

Volume scattering may also become important, particularly when the level ice is very smooth and produces very little surface backscatter. Voids within the ice, *e.g.* air bubbles, may then produce significant volume scattering if the penetration depth is sufficient. The combination of a very smooth surface, low ice salinity, low temperature and many large voids gives the largest volume scattering contribution. In practise, however, volume scattering is negligible for ERS-1 SAR images except for very smooth ice found in the archipelago. An analogous situation occurs in the Arctic Ocean when the low salinity and large air volume fraction in multi-year ice gives a significant volume scattering contribution (Carlström and Ulander, 1993).

The snow cover is essentially transparent to the radar wave during cold and dry conditions and the backscatter from the ice surface dominates. During warm conditions, however, liquid water appears in the snow pack which affects the backscattering. For low wetness values (a few percent), the snow will mainly attenuate and scattering from the ice surface is still dominating. As the snow wetness increases, the snow will subsequently mask the ice surface and snow surface scattering will eventually dominate. This normally results in a higher backscattering coefficient compared to dry snow since the dielectric constant of water is significantly higher than that of ice. Volume scattering from liquid water particles in the snow is normally negligible due to the limited snow depth.

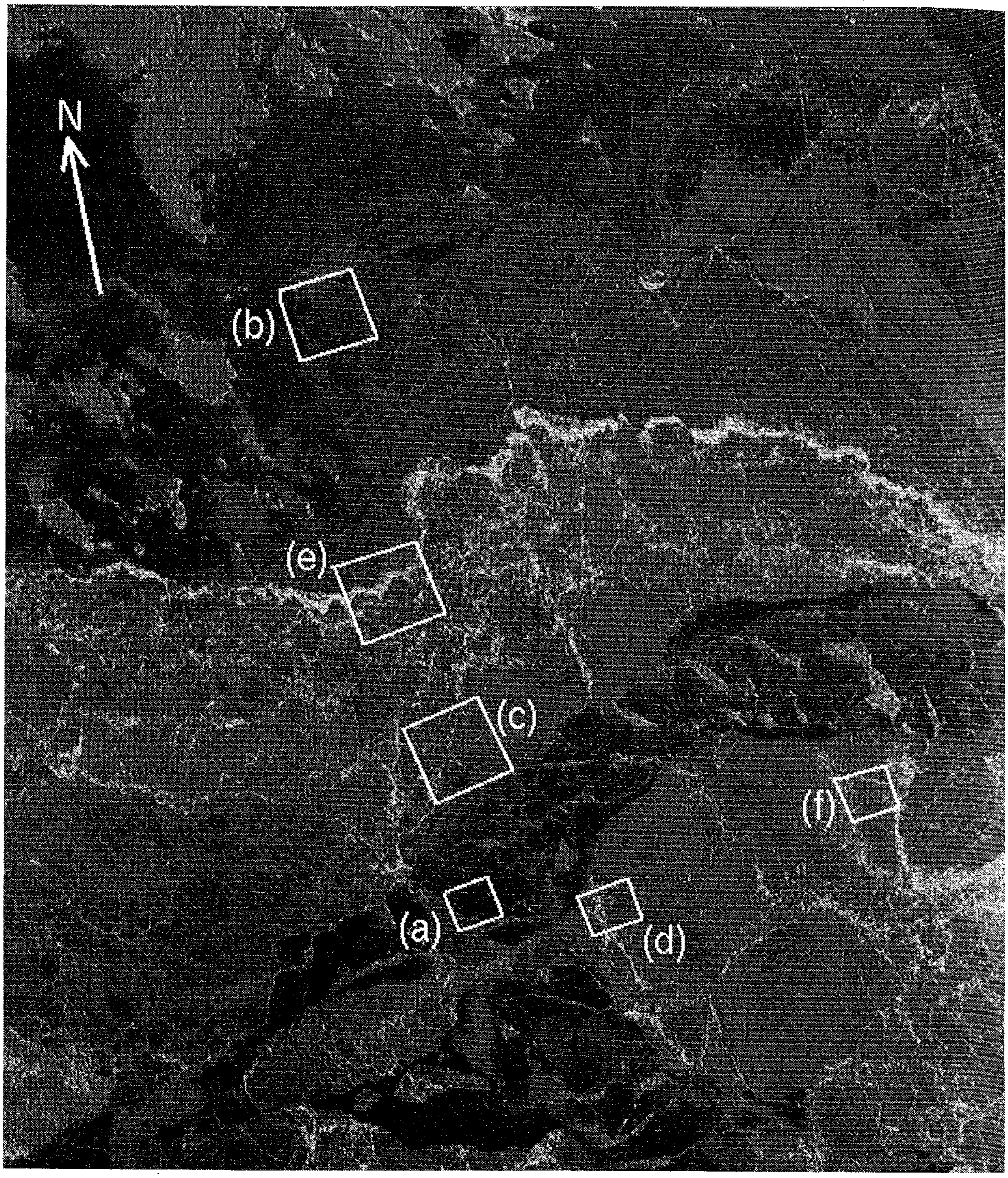

Figure 5. BEERS-92 ERS-1 SAR image obtained 27 March 1992, © ESA 1992 (size 30×22 km)

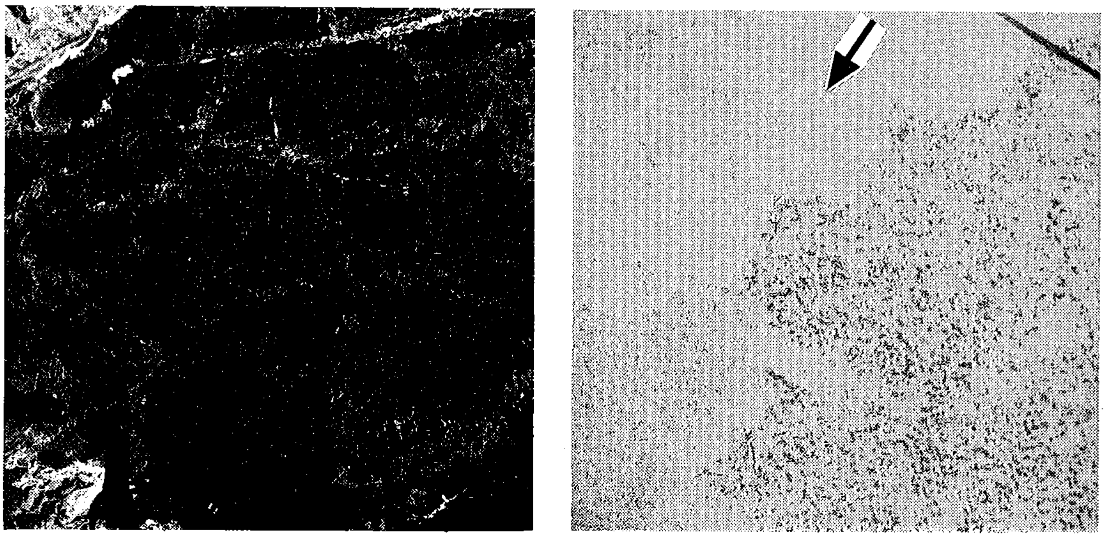

(a) Smooth level ice (1100×1100 m) (b) Rough level ice (2200×2200 m)

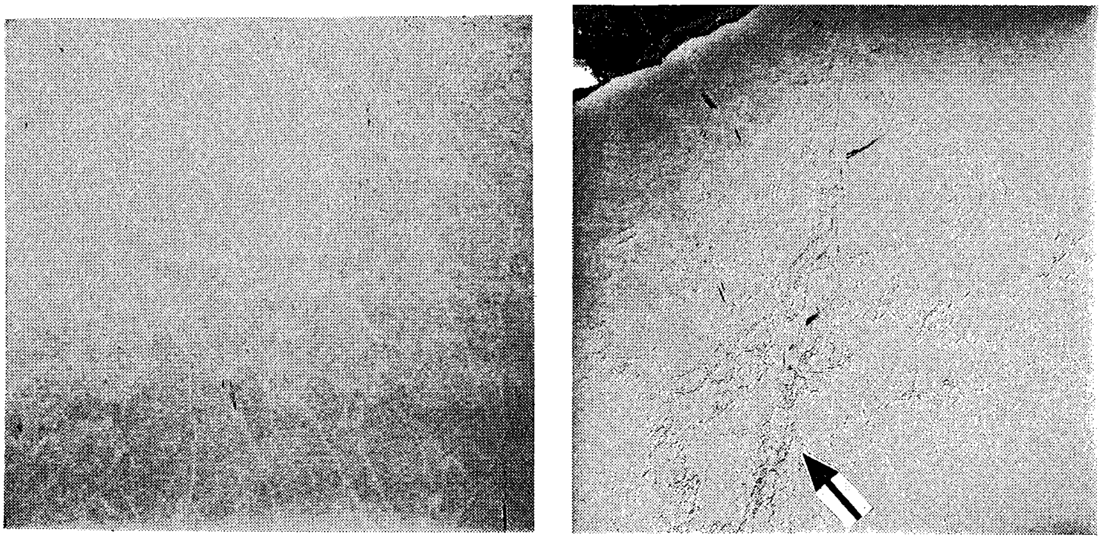

(c) Ridged ice (2200×2200 m) (d) Hummocked ice (1100×1100 m)

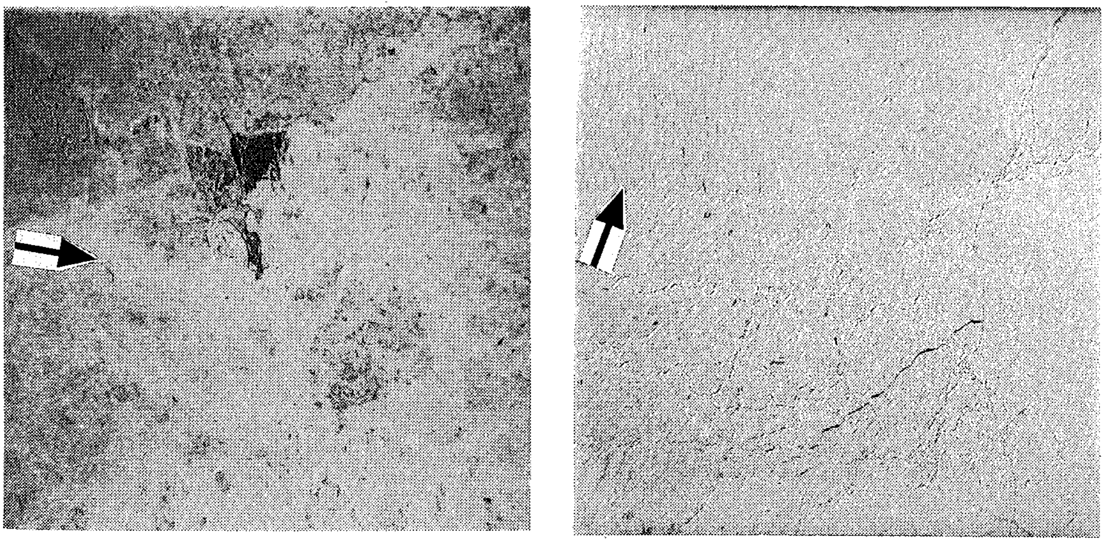

(e) Rubble fields (2200×2200 m) (on some breakers) (f) Jammed brash barrier (1100×1100 m)

Figure 6. BEERS-92 helicopter photos obtained 26 and 27 March 1992

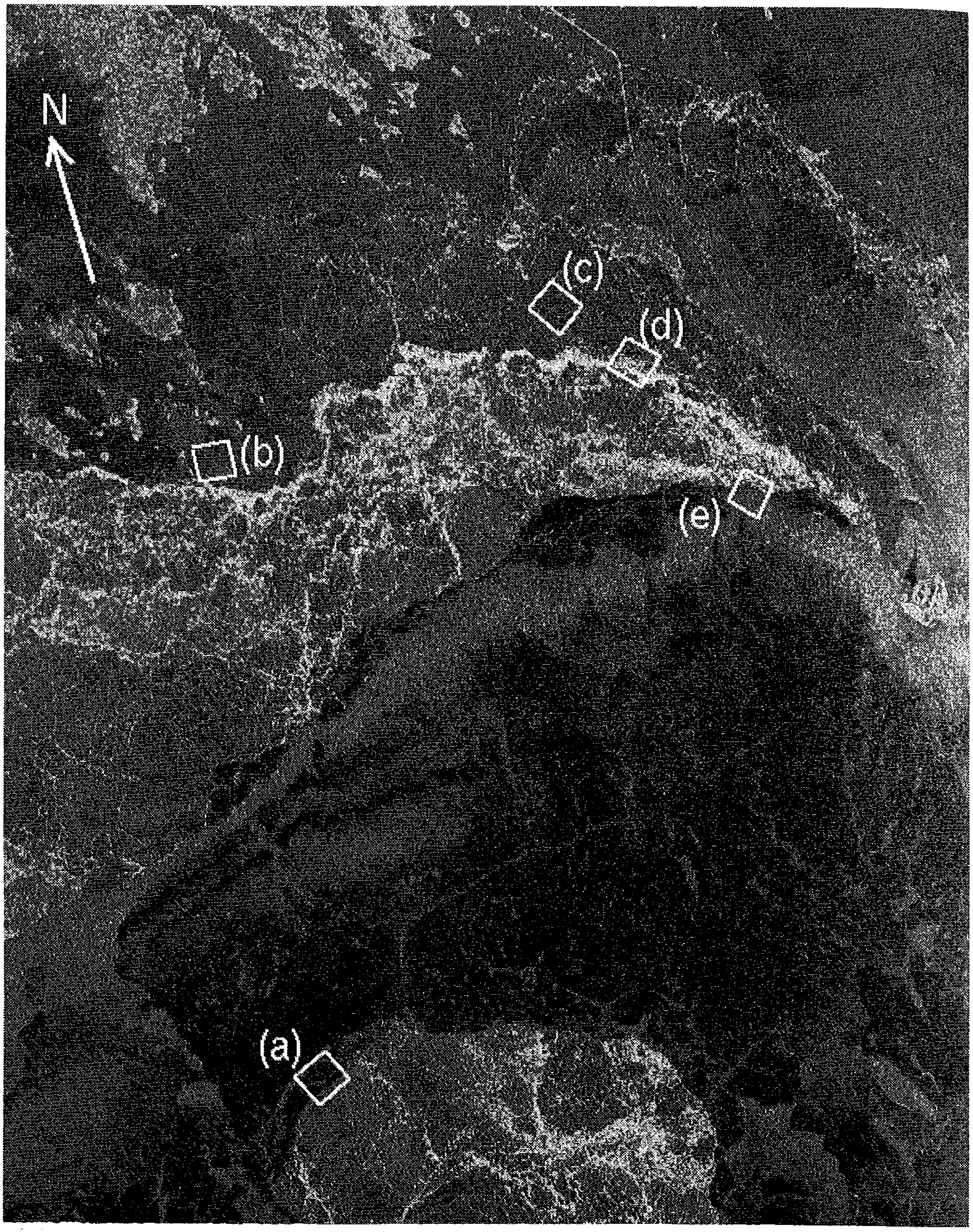

Figure 7. BEERS-92 ERS-1 SAR image obtained 30 March 1992, © ESA 1992
(size 32×40 km)

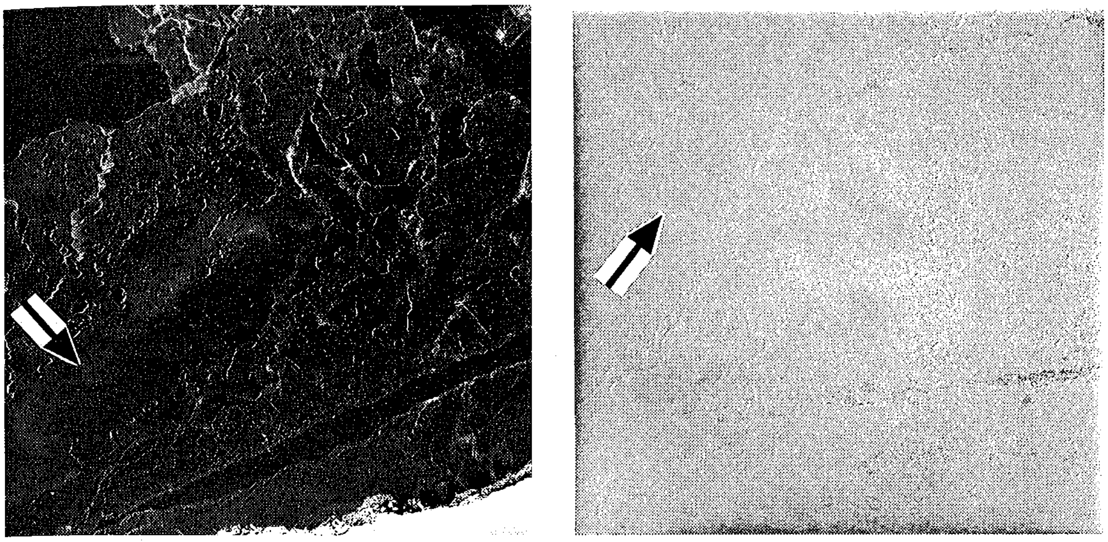

(a) Smooth level ice (900×900m)

(b) Slightly deformed ice (750×750m)

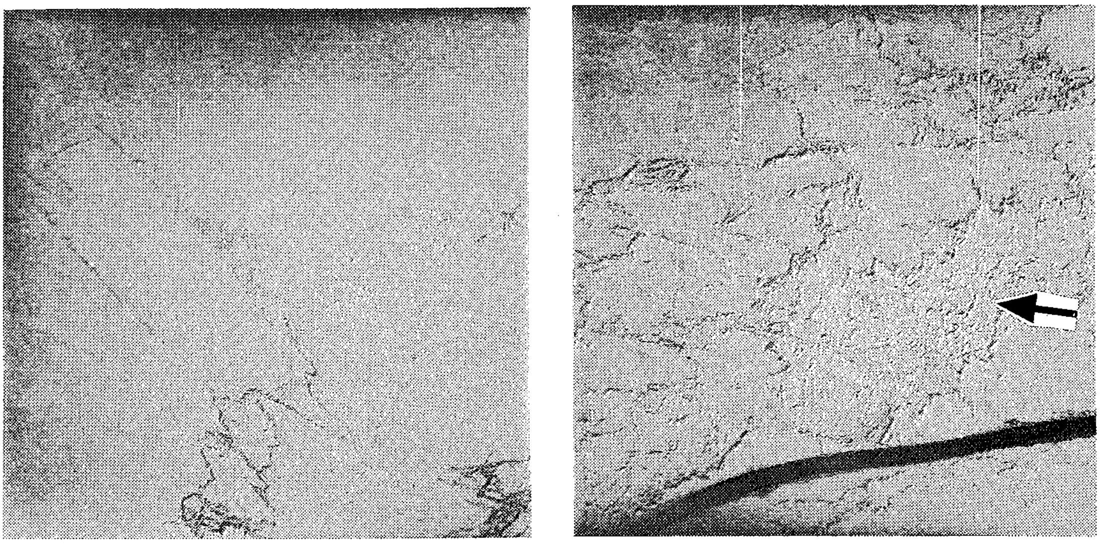

(c) Slightly deformed ice (750×750m)

(d) Rubble fields (750×750m) (sitting on some breakers)

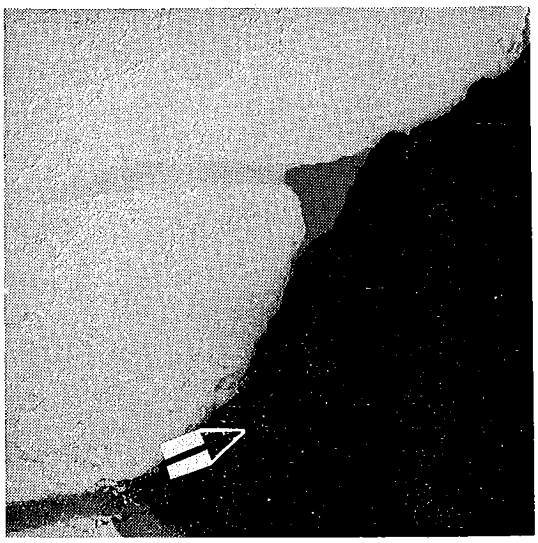

(e) Lead (750×750m)

Figure 8. BEERS-92 helicopter photos obtained 30 March 1992

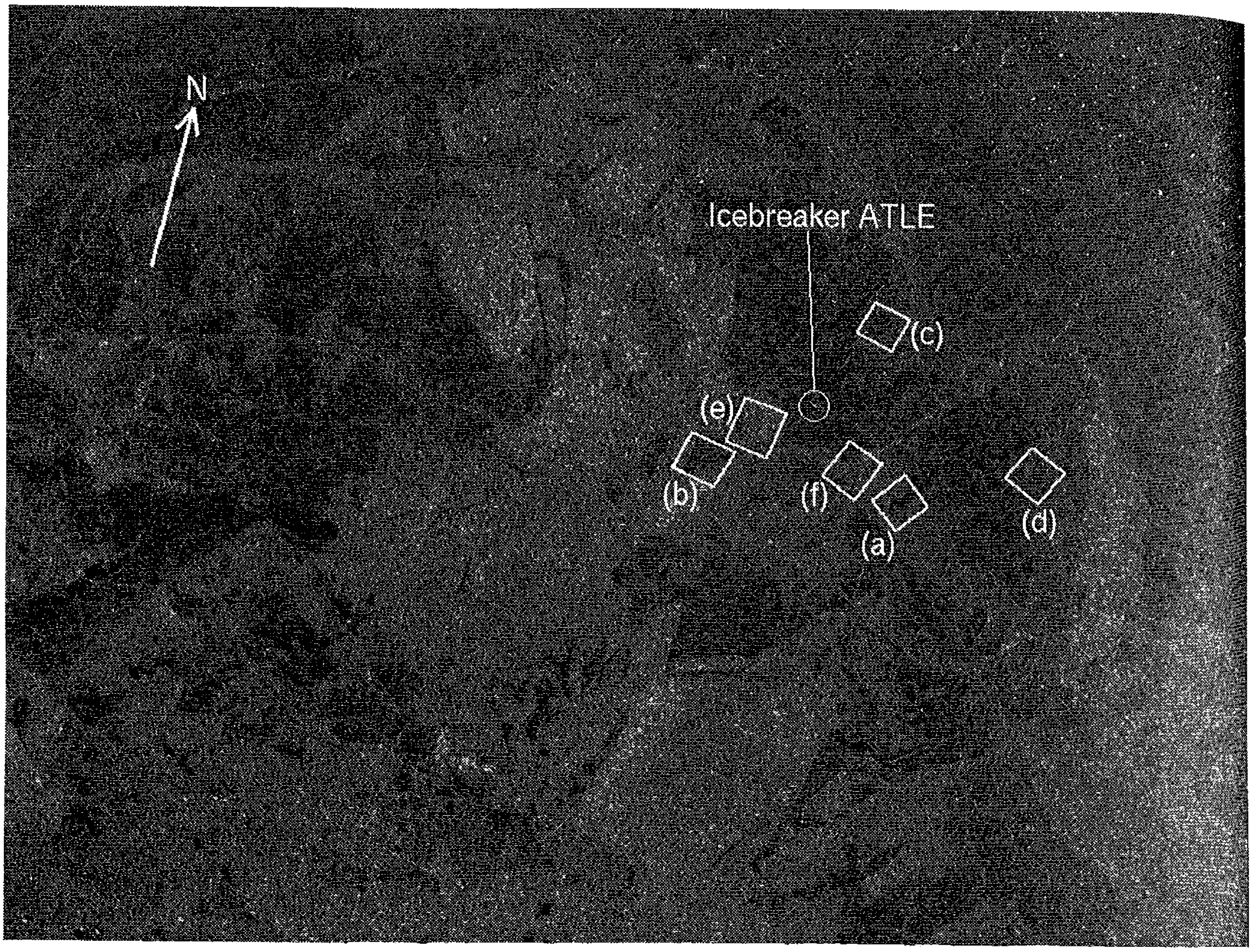

Figure 9. BEERS-93 ERS-1 SAR image obtained 14 March 1993, © ESA 1993
(size 30×22 km)

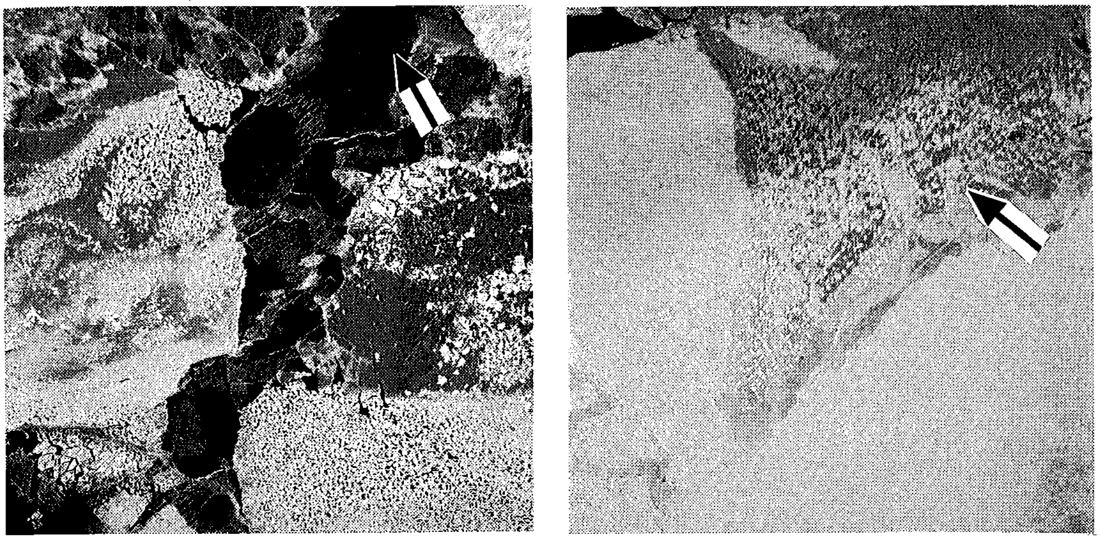

(a) Smooth level ice (1600×1600 m)

(b) Rough level ice (1600×1600 m)

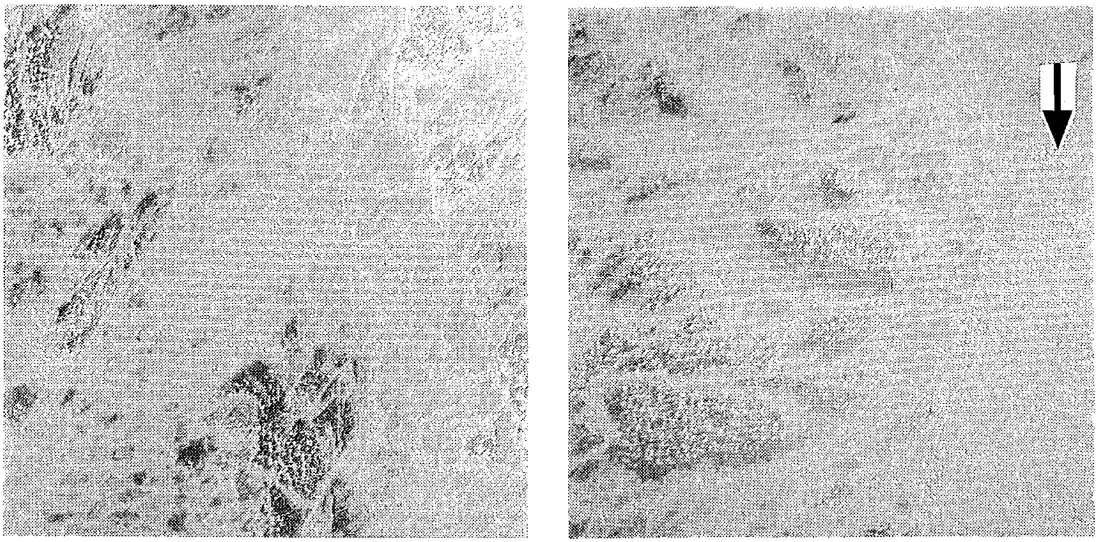

(c) Ridged ice (1600×1600 m)

(d) Hummocked ice (1600×1600 m)

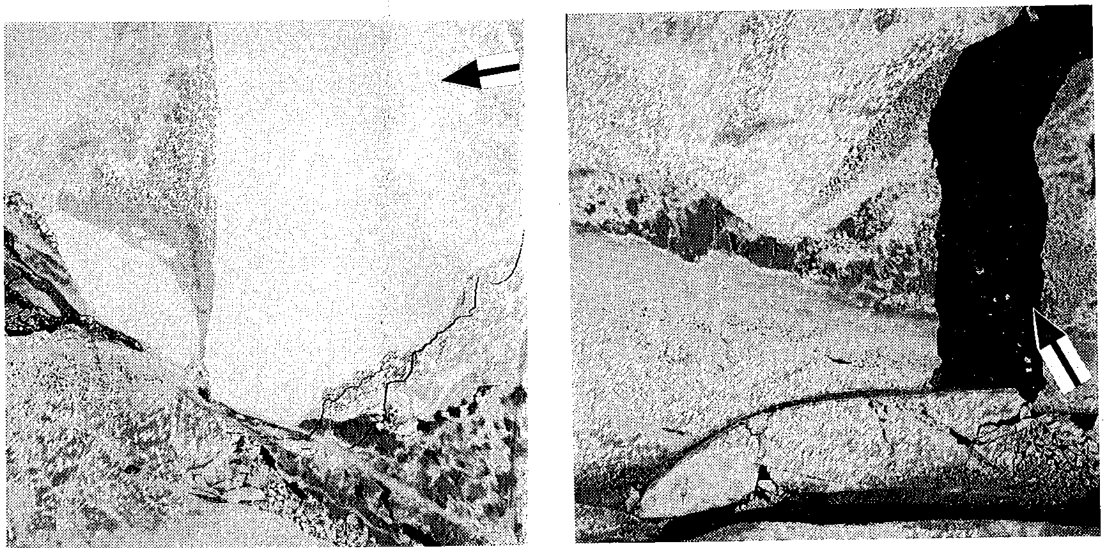

(e) Jammed brash barrier (1600×1600 m)

(f) Lead (1600×1600 m)

Figure 10. BEERS-93 helicopter photos obtained 14 March 1993

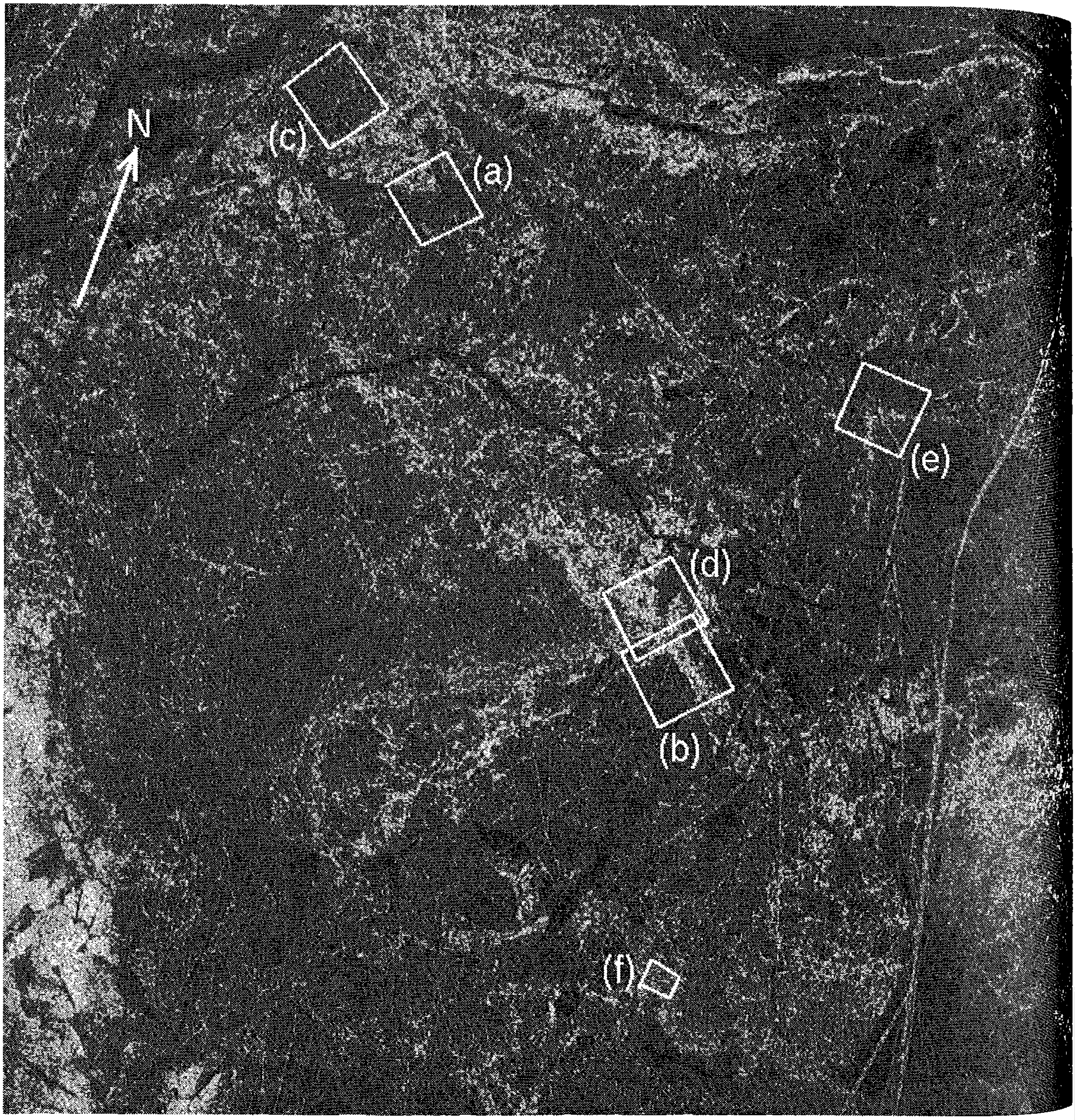

Figure 11. BEERS-94 ERS-1 SAR image obtained 4 March 1994, © ESA 1994
(size 25×25 km)

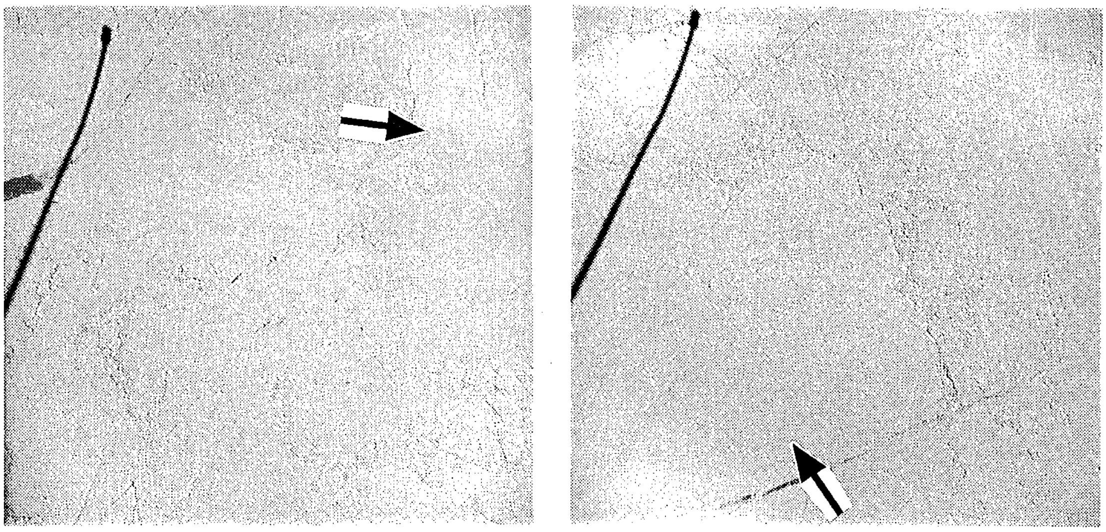

(a) Smooth level ice (2200×2200 m)

(b) Rough level ice (2200×2200 m)

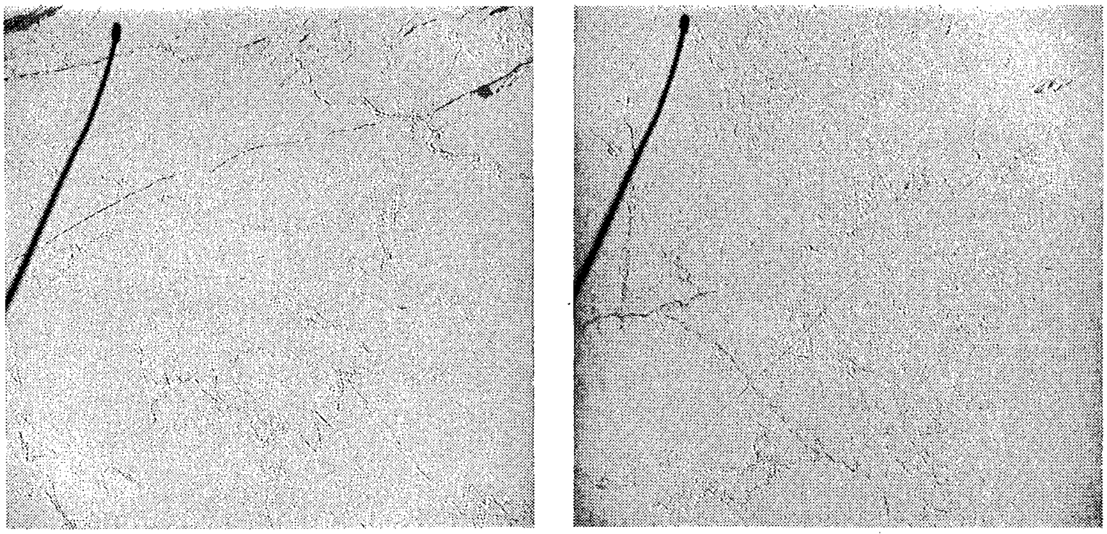

(c) Slightly deformed ice (2200×2200 m)

(d) Ridged ice (2200×2200 m)

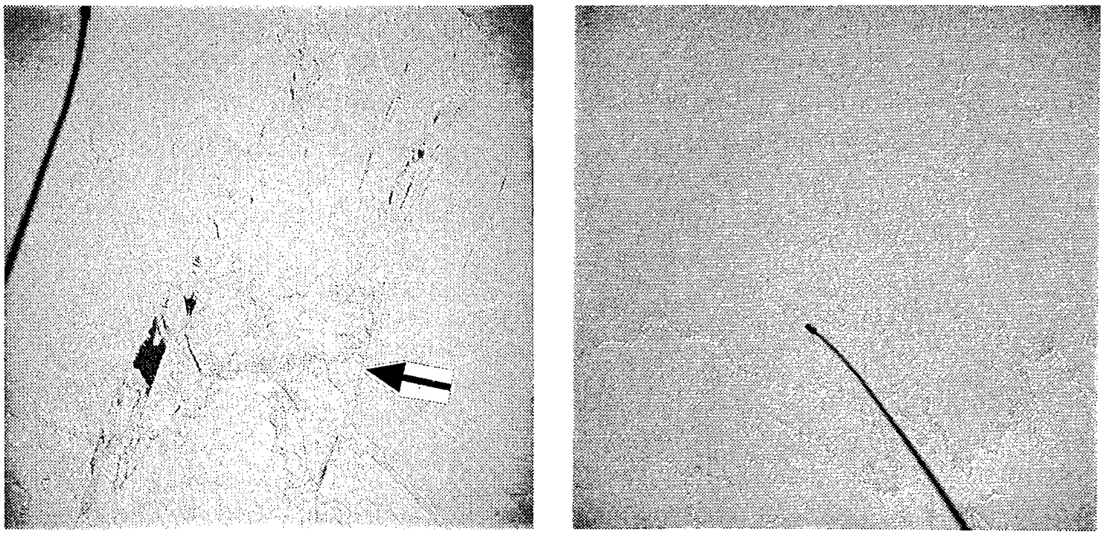

(e) Hummocked ice (2200×2200 m)

(f) Jammed brash barrier (400×400 m)

Figure 12. BEERS-94 helicopter photos obtained 3 March 1994

Ice floes may also be flooded by water due to snow loading or internal stresses which depress the ice surface below the water level. The mechanism which controls the backscatter in this case has not been extensively investigated. One experiment in an indoor facility has been reported where snow-covered ice was flooded by water. The results at 20° of incidence angle and Ku-band (13.9 GHz) showed a 5 dB increase of the backscattering coefficient which was attributed to the increase in dielectric constant (Lytle *et al.* 1993). After the snow cover is flooded by water, it subsequently freezes as snow-ice. This results in more air bubbles, lower density, and normally also a rougher surface. All these effects tend to increase the backscattering coefficient, and is likely to increase the backscatter as the level ice ages. An investigation of these phenomena, however, has not been reported in the literature.

## 5. Multiplicative SAR image model

A SAR image is distorted by multiplicative noise called speckle. Speckle is present since the SAR is a coherent system and normally has many elementary scattering centres within its resolution cell. The interaction between the returned signals from individual scatterers cause constructive and destructive interference which results in the statistical fluctuations observed in a geophysically homogeneous area. In areas which are not homogeneous, the statistical fluctuations are caused by a combination of speckle noise and geophysical texture. A simple and useful model which incorporates both speckle and texture is the multiplicative SAR image model (Rignot and Kwok 1992, Ulaby *et al.* 1986). In this model, the image pixel value *DN* (digital number) is related to the random variables of texture *T* and speckle *S* according to

$$DN(i,j)^2 = \left[P_{\sigma^\circ}\, T(i,j) + P_n\right] S(i,j) \tag{1}$$

where $P_{\sigma^\circ}$ and $P_n$ are the mean image powers of the distributed target and image noise, respectively, and $(i,j)$ is the pixel position. The model assumes that $T$ and $S$ are independent stationary processes with unity mean, and that $P_{\sigma^\circ}$ varies slowly. It is a useful model for distributed targets with a correlation length of $T$ which is much greater than that of $S$.

The distributed target is characterised by $P_{\sigma^\circ}$ and the statistical properties of the texture variable $T$. In this study, we will use the simplest parameterisation, *i.e.* based on $P_{\sigma^\circ}$ and the texture standard deviation $\sigma_T$. Although second-order statistics of $T$ would give a more complete characterisation, other studies have shown them to be second order effects (Skriver 1989). We define the radar signature by two parameters, *i.e.* the backscattering coefficient $\sigma^\circ$ which is proportional to $P_{\sigma^\circ}$ and the ice texture coefficient $\sigma_T$.

### 5.1. Backscattering coefficient

The image brightness in SAR images is proportional to the returned power from a ground resolution element, *i.e.* the radar backscattering coefficient $\sigma^\circ$ of the ground. The backscattering coefficient is defined as the ensemble average of the ratio of the radar cross section $\sigma$ and the ground area element $\Delta A$ according to (Ulaby *et al.* 1982)

$$\sigma^{\circ} = E\left\{\frac{\sigma}{\Delta A}\right\} \tag{2}$$

where E{ } denotes the expectation value. In practise, the ensemble average is estimated by spatial averaging over an area in the SAR image. The backscattering coefficient has the units $m^2/m^2$ but is normally expressed in decibel (dB).

The backscattering coefficient is estimated from the average image power by the following equation (see also Chapter B)

$$\sigma^{\circ} = \frac{f}{K} P_{\sigma^{\circ}} = \frac{f}{K}\left(P - P_n\right) \tag{3}$$

where $P$ is the mean-squared pixel value in the area of interest, $K$ is a calibration constant, and $f$ is a calibration factor which varies across the image. The relative rms error of the backscattering coefficient is given by

$$\frac{1}{\sqrt{N_e n}} \tag{4}$$

where $N_e$ is the effective number of looks and $n$ is the number of independent samples in the measured area.

### 5.2. *Ice texture coefficient*

The standard deviation, $\sigma_T$, of the texture variable $T$ may be derived from (1) which results in the following equation (Rignot and Kwok, 1992)

$$\sigma_T^2 = \frac{N_e\left(\frac{\sigma_P}{P}\right)^2 - 1}{N_e + 1} \frac{CNR + 1}{CNR} \tag{5}$$

where $\sigma_P$ is the standard deviation of the squared pixel values and $CNR = P_{\sigma^{\circ}} / P_n$ is the clutter to noise ratio. The rms error of an estimate of the ice texture coefficient is given by

$$\sqrt{\frac{2}{(N_e + 1)N_e n}} \tag{6}$$

where we have assumed that $N_e$ and $CNR$ are exactly known. These assumptions are normally valid, although the latter breaks down when the clutter-to-noise ratio approaches unity.

## 6. Parameter retrieval

The test areas were chosen exclusively based on their appearance in the SAR images. The helicopter photography was not considered in this selection, since the objective was to evaluate the SAR images without ground truth available.

The areas were selected with a uniform texture. Both gradual and distinct transitions in image features have been considered. For example, large dark areas have not been measured together with large areas with lighter tones. In areas with many small ridge lines, the whole area has been measured. It was not possible to separate the individual small bright lines and darker regions in between the lines. With larger and broader ridges it was possible to measure the ridge line itself.

The jammed brash barrier has a rather unique appearance in SAR images. It is easy to visually identify and it has therefore been measured as a whole.

The analysis of the test areas was performed according to the following scheme:

1. Helicopter flights have been noted in the SAR images. Both photographs and SAR images have GPS logging.
2. Areas have been selected in the SAR images and their radar signatures have been determined.
3. The ice in the selected areas has been classified according to the ice table using the helicopter photographs.

## 7. Analysis of sea ice signatures

### *7.1. BEERS-92*

A total number of 109 areas have been selected and measured in the SAR images from BEERS-92. Of the 109 areas, 15 are over leads (see section 8). The remaining 94 areas are over ice and the measurement results are shown in figure 13. The signatures are believed to have an accuracy better than ±1 dB for the backscattering coefficient (see appendix A), since the speckle induced error is negligible, and better than 0.02 for the ice texture coefficient.

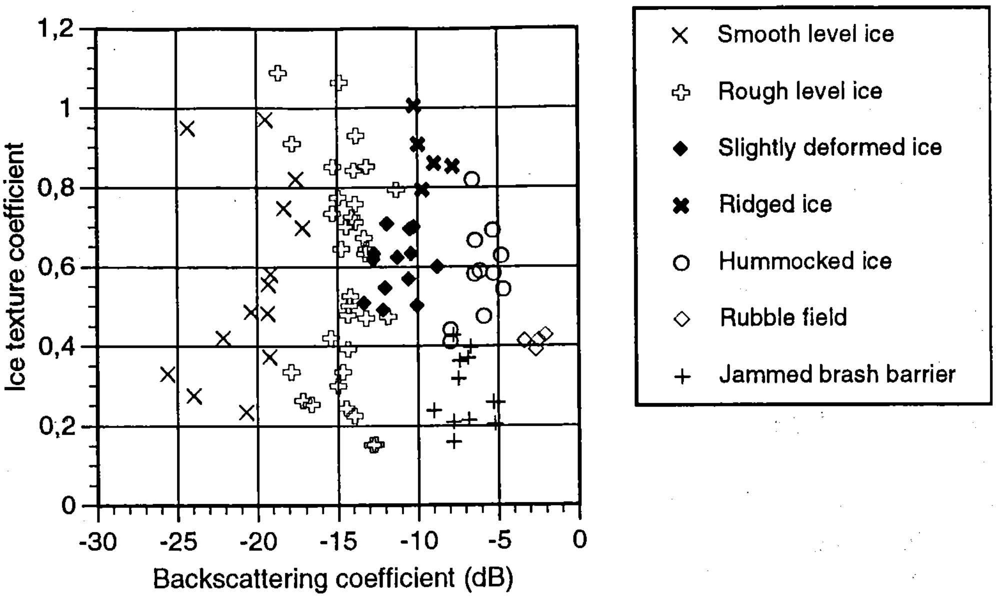

Figure 13. BEERS-92 radar signatures of sea ice

As seen in figure 13, all the ice classes have more or less clearly separated radar signatures. The SAR images are rich in contrast and all major ice ridges could easily be identified. As the weather was cold and dry, any snow layer on top of the ice did not interfere with the radar signature.

The two classes smooth and rough level ice have similar radar signatures in several cases. An explanation for this might be that it is hard to define a distinct border between the two ice classes using helicopter photography. An area may appear smooth in helicopter photographs but may be rough on scale close to the radar wavelength and therefore has a higher backscattering coefficient. These two classes are also spread out in their ice texture coefficients. This is caused by small bright spots in the selected image areas which dominate the ice texture coefficient since the background backscattering coefficient is low.

The five remaining ice classes have much more narrow ranges in their radar signatures. Slightly deformed ice has a radar signature within a narrow range, but it may be mixed up with small-scale rough level ice in a few cases. The high ice texture coefficient in the class ridged ice is due to presence of ridges and level ice in between. The ridges appear bright and the level ice between them appears dark which thus results in a high texture coefficient.

The two classes hummocked ice and rubble fields also have unique radar signatures. Note, however, that the class rubble field only consists of five measurements.

The class jammed brash barrier can easily be separated from the others using merely the radar signature. It is one of the classes which has the most unique and narrow range in its radar signature.

## *7.2. BEERS-93*

A total number of 81 areas have been selected and measured in the SAR images from BEERS-93. Of the 81 areas, 3 are over leads (see section 8). The remaining 78 areas are over ice and the measurement results are shown in figure 14. The signatures are believed to have an accuracy better than ±0.8 dB for the backscattering coefficient (see appendix

A), since the speckle induced error is negligible, and better than 0.03 for the ice texture coefficient.

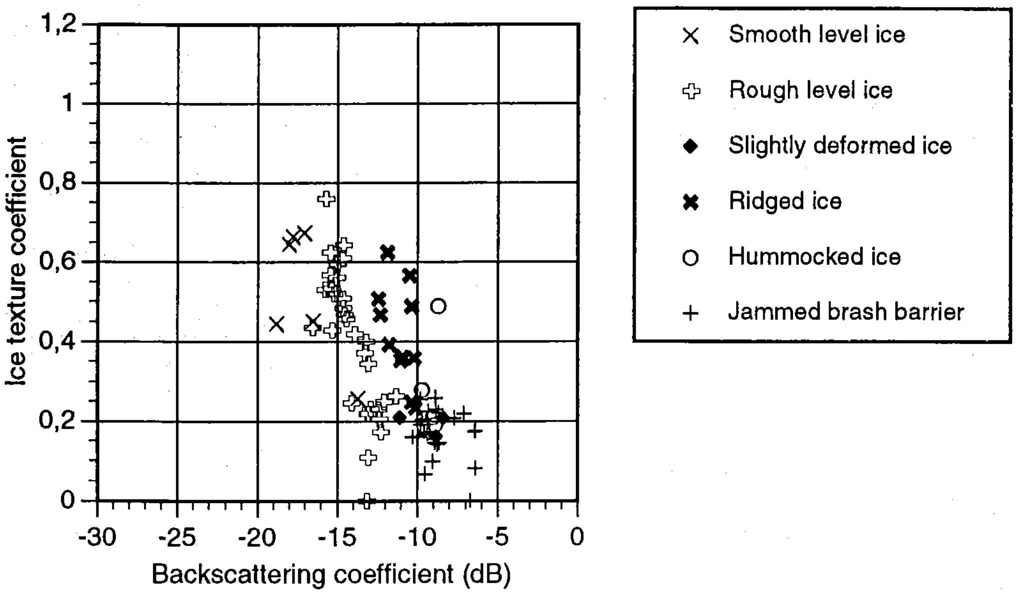

Figure 14. BEERS-93 radar signatures of sea ice

It is noted that the ice texture coefficients have decreased compared to BEERS-92. This fact could be due to several different factors, but is probably caused by the mild and rainy weather during BEERS-93. This caused the snow layer on top of the ice to be wet and partly melt which changes the snow dielectric properties. As the snow layer gets more and more wet, it blocks out the radar wave. Eventually, the radar signature shows the signature of the wet snow layer and not the signature of the ice.

As seen in figure 14, the backscattering coefficients of the classes smooth and rough level ice approximately have the same values as during BEERS-92. The ice texture coefficient, on the other hand, is considerably lower .

The remaining classes have slightly lower backscattering coefficients compared to BEERS-92, but they have considerably lower ice texture coefficients. During these mild weather conditions, it is almost impossible to discriminate between slightly deformed ice, hummocked ice and jammed brash barrier by merely using the radar signature. The decrease in ice texture coefficient might be due to the fact that the wet snow layer dominates the backscattering from the ridges and since a snow layer is smoother than the deformed ice surface, there will be less spatial variability in backscattering coefficient and thereby less texture coefficient. The fact that a wet surface masks lower scattering interfaces in ridges and hummocks might also be an explanation for the slight decrease in backscattering coefficients.

An important feature of the SAR images from BEERS-93 compared to those of BEERS-92, is that there are considerably fewer ice ridges observed in the BEERS-93 images. There are, however, many ridges observed in the helicopter photographs. The wet snow layer has masked the ridges in the SAR images causing the images to show less contrasts.

## 7.3. BEERS-94

A total number of 50 areas have been selected and measured in the SAR images from BEERS-94. All these areas are over ice and the measurement results are shown in figure 15. The signatures are believed to have an accuracy better than ±1 dB for the backscattering coefficient (see appendix A), since the speckle induced error is negligible, and better than 0.03 for the ice texture coefficient.

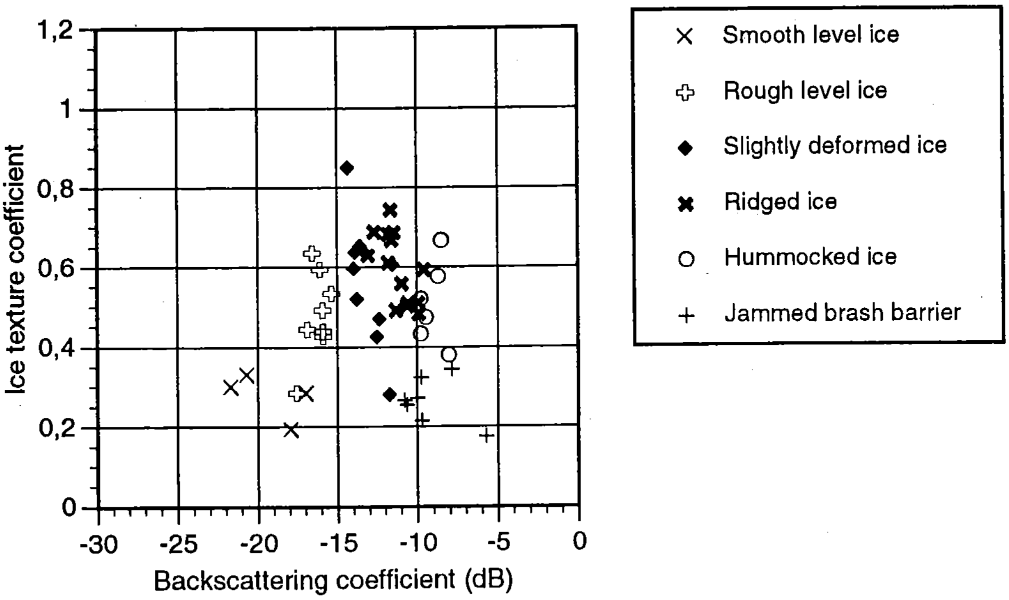

Figure 15. BEERS-94 radar signatures of sea ice

Since the weather was cold and dry during BEERS-94 , these measurements should be similar to the BEERS-92 measurements. The different classes seem to have the same constellation as in BEERS-92, but they have slightly different backscattering and ice texture coefficients.

The class smooth level ice appears at the same place as in BEERS-92, but it only includes four areas. The class rough level ice shows a similar pattern as in both BEERS-92 and 93. These two classes show reasonable agreement with measurements from BEERS-92 and 93.

The other four classes from BEERS-94 have slightly lower backscattering coefficients than in BEERS-92. The decrease might be due to differences in deformation processes and weather conditions between the two ice seasons. It is also noted that their ice texture coefficients have decreased significantly. That might also be due to different weather conditions between the two ice seasons. Both hummocked ice and jammed brash barriers have lower backscattering coefficients compared to BEERS-92. This may be caused by that these areas had formed early in the ice season leaving the areas older and more weathered (*i.e.* a smoother surface) in March than similar classes during BEERS-92. *In-situ* observation of one of the jammed brash barriers describes it as older and made up of smaller brash than usual.

An important feature of the BEERS-94 SAR images is that they are rich in contrast as in the BEERS-92 images. That was, however, expected since the weather was cold and dry during BEERS-94.

## 8. Analysis of lead signatures

To illuminate the problem of discriminating open water leads and sea ice in SAR images, several radar signatures have been measured over leads. Since there was almost only consolidated ice in the Bay of Bothnia in the winter of 1994, no lead signatures were obtained from those images. Most of the lead signatures originate from the winter of 1992 and some from the winter of 1993. The lead signatures are presented in figure 16.

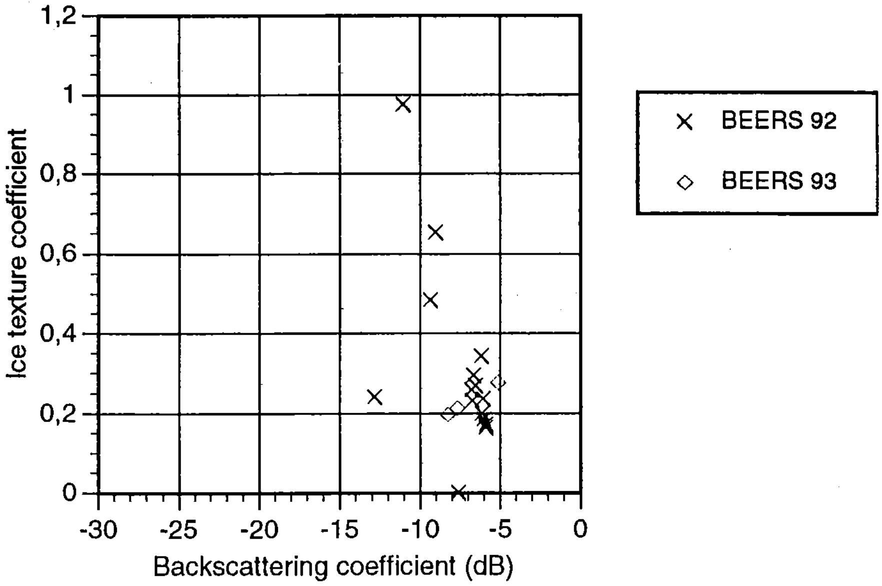

Figure 16. Lead signatures

It is important to recognise that the radar signatures of leads are mainly controlled by the wind speed and wind direction. Leads could actually cover the full range of backscattering coefficients. In figure 16 most of the signatures coincide with the signature of the jammed brash barrier (*cf.* figures 13, 14 and 15.). It can therefore be impossible to discriminate between leads and jammed brash barrier using merely the radar signature. Nevertheless, a trained observer may rather easily detect leads due to their characteristic form in SAR images. Although the radar signatures are the same for leads and jammed brash barriers, there are still some visible texture in jammed brash barriers and apparently no visible texture in leads. General weather information and a time sequence of SAR images would also improve the lead detection process.

Knowledge of the wind speed and direction when the SAR images were obtained will simplify the discrimination between certain ice classes and leads. This information may help to see what ice class(-es) will be mixed up with leads using merely the radar signature. For example, during BEERS-92 and 93 the wind speed was roughly 5-8 m/s which made the lead signatures similar to those of jammed brash barriers.

## 9. Discussion

A major problem is caused by wet snow layers on top of the ice. If the snow is dry and cold, the snow does not affect the radar wave significantly and the radar signature mainly describes the features of the ice surface. As the snow wetness increases, its dielectric properties start to change and the snow backscattering increases. With a very wet snow layer, the radar signature will mainly describe the features of the snow layer. Information about the snow layer is of little importance for icebreakers and merchant ships.

Nevertheless, there are features of the ice which are still visible under reasonably wet conditions (*cf.* figure 14). Deformed ice seems to decrease in ice texture coefficients (in the order of 0.1 to 0.3) but less in backscattering coefficients. The radar signature seems to be rather stable concerning level ice and small ridges. SAR images are thus helpful even under reasonably wet conditions, since it is still possible to discriminate between level ice and deformed ice. A comparison between dry (BEERS-92 and -94) and wet (BEERS-93) conditions is shown in figure 17 to illustrate ice classification during these conditions.

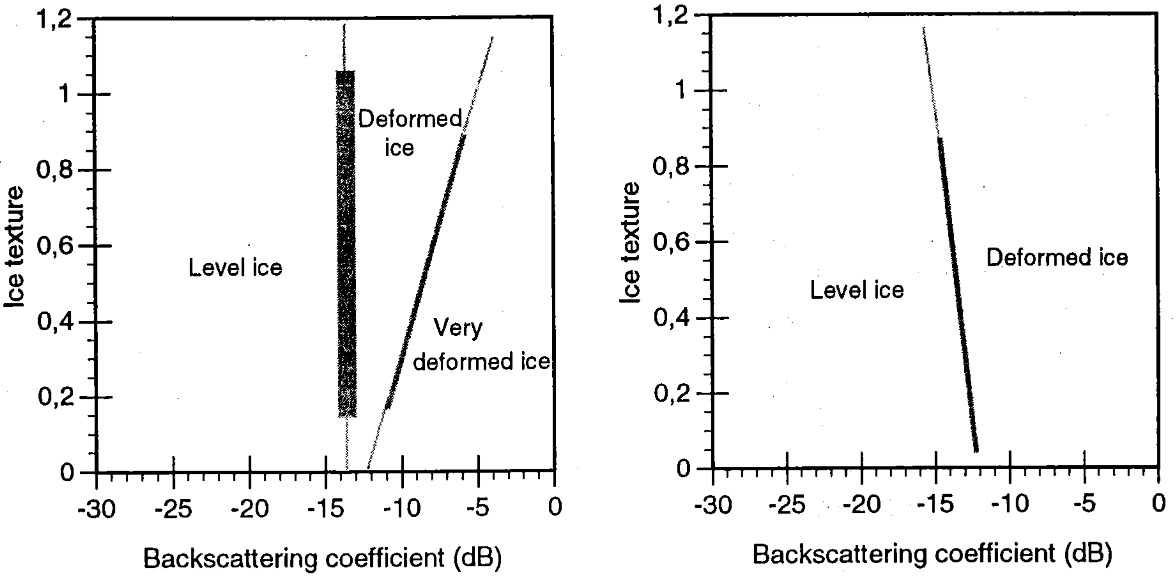

(a) Cold and dry (b) Warm and wet

Figure 17. Comparison between different conditions

As seen in figure 17 (and figures 13, 14 and 15), a wet snow layer mainly affects the radar signature for deformed ice. A probable cause is that a snow layer is more homogeneous than the deformed ice which gives less texture coefficients during wet circumstances.

The backscattering coefficient border between level and deformed ice is reasonably stable during the three experiments. During cold and dry circumstances it is about -14 dB and during wet and warm circumstances it is about -12 dB. A wet snow layer normally scatters the radar wave more than level ice and that may explain the slight increase in backscattering coefficient. It is also noted that there are three and two broad ice classes which may be discriminated during dry and wet conditions, respectively. Nevertheless, we suggest that during one season, it is possible to discriminate more than these ice classes. A special classification manual for every season should make it possible to discriminate about seven ice classes.

The significance of having five sub-classes for deformed ice may be discussed. To set a specific border between for example hummocked ice and rubble fields is difficult. Perhaps it would be better to have a broad class of deformed ice combined with an index, which for example could describe the areal coverage of ridges or the ice resistance (see chapter G). This should be investigated in further work.

Another problem with ERS-1 SAR images is open water leads. It is impossible to discriminate leads from ice using merely the radar signature. To improve discrimination, information about the prevailing wind conditions would make it possible to estimate which ice classes that will be mixed up with leads. However, more work is necessary to understand the backscattering from leads. This problem is, however, a minor issue for winter navigation support since a trained operator may easily detect leads in SAR images.

A future automatic ice-chart system will face other problems too. The selection of areas has to be automated. This may be done with a ridge detector (edge detector) for the images, but this detector also has to detect when the ridges get larger and broader. On the other hand, the selection could perhaps even be a simple one, *i.e.* dividing the image into smaller rectangular areas without considering the boundaries of homogeneous areas. The system also has to handle the large SAR images better than today. To decrease transmission times, pixels in a SAR image are averaged (*e.g.* from a pixel size 16x20 meters to 100x100 meters). However, this causes the ice texture coefficient to change and information is undoubtedly lost (Dammert 1993). More work is required to understand this process.

## 10. Conclusions

The results in this study show that it is possible to discriminate a number of ice classes in ERS-1 SAR images. The maximum number of ice classes which may be discriminated is around seven during cold and dry conditions. During warm and wet conditions the number decreases to around three. A general classification manual stretching over several ice seasons would only be able to discriminate three and two, respectively, due to small changes in radar signatures from season to season. It is noted that ERS-1 SAR images have most information during cold and dry conditions and that the number of ice classes that may be discriminated is closely related to prevailing weather conditions.

The radar signature is probably stable during one ice season but it tends to vary slightly between seasons. BEERS-92 and BEERS-94 show slightly different backscattering coefficients. We believe this is due to differences in the ice formation developments; BEERS-92 measurements are mostly obtained from younger ice than the measurements from BEERS-94. In the winter of 1994 the Bay of Bothnia was covered with fast ice for two months. The shift is about ±2 dB in $\sigma^\circ$ and ±0.2 in $\sigma_T$ between seasons. With the given dataset, the radar signature reveals no spatial dependency, but all measurements were obtained in the Bay of Bothnia. In the Bothnian Sea and the Baltic Proper with a higher salinity, one may find differences in radar signatures.

The backscattering coefficient which separates level and deformed ice differs during the three experiments. For BEERS-92 and -94 the backscattering coefficient is -14 dB and BEERS-93 -12 dB. Since the estimated error for the backscattering coefficient is roughly 1 dB, this difference is statistically confident. A probable explanation is the warm and wet conditions during 1993.

A wet snow layer affects different ice classes differently. The backscattering coefficient seems to decrease slightly for all classes, but within the range of error estimates. Level ice decreases slightly in texture coefficient and deformed ice decreases roughly 0.1 to 0.3 in texture coefficient. The effect of a wet snow layer is therefore mainly a decrease in texture coefficients for ice. No measurements have been obtained which allow us to study the effect of flooding on the radar signature.

Open water leads and sea ice cannot be discriminated based on the radar signature alone. This is a minor issue, however, since leads are easily detected by a trained operator taking other image characteristics into account..

We suggest that a future ice classification algorithm should be based on the radar signature since it has been shown to discriminate the major ice types in ERS-1 SAR images. We also believe that an automatic ice classification system based on ERS-1 SAR images are highly valuable both as help for producing ice-charts as well as near real-time operational use, *e.g.* icebreaker support.

## Acknowledgements

This study would never have been completed without the help of Jan Hagberg with the computers. We would also like to acknowledge comments from other BEERS scientists.

## References

CARLSTRÖM A., and ULANDER L.M.H., 1993, C-band backscatter signatures of old sea ice in the central Arctic during freeze-up, *IEEE Transactions on Geoscience and Remote Sensing*, 31, 4, pp. 819-829

CARLSTRÖM A. (Editor), 1993, Baltic experiment for ERS-1, BEERS-93: Swedish calibration/validation data report, Internal report RSG 1993:3, Department of Radio and Space Science, Chalmers University of Technology, Gothenburg, Sweden

CARLSTRÖM A. (Editor), 1994, Baltic experiment for ERS-1, BEERS-94 data report, Internal report RSG 1994:2, Department of Radio and Space Science, Chalmers University of Technology, Gothenburg, Sweden

DAMMERT P.B.G., 1993, Radarsignaturer av havsis i Bottenviken [Radar Signatures of Sea Ice in the Bay of Bothnia], M Sc Thesis, Department of Radio and Space Science, Chalmers University of Technology, Gothenburg, Sweden

HALLIKAINEN M., TARES T., TOIKKA M., and HEISKA K., 1991, Classification of low-salinity sea ice types by dual-frequency multi-polarisation scatterometer, *Proceedings of IGARSS'91 held in Espoo, 3-6 June 1991*, pp. 1211-1214

HYYPPÄ J., and HALLIKAINEN M., 1992, Classification of low-salinity sea ice types by ranging scatterometer, *International Journal of Remote Sensing*, vol. 13, no. 13, pp. 2399-2413

LYTLE V.I., JEZEK K.C., HOSSEINMOSTAFA A.R., and GOGINENI S.P., 1993, Laboratory backscatter measurements over urea ice with a snow cover at Ku band, *IEEE Transactions on Geoscience and Remote Sensing*, 31, 5, pp. 1009-1016

RIGNOT E., and KWOK R., 1992, Characterization of Spatial Statistics of Distributed Targets in SAR Data, *International Journal of Remote Sensing*, vol. 14, no. 2, pp 345-363

SKRIVER H., 1989, Extraction of sea ice parameters from Synthetic Aperture Radar images, Ph.D. Thesis, Electromagnetics Institue, Technical University of Denmark, LD 74, Lyngby, Denmark

SUN Y., CARLSTRÖM A., and ASKNE J., 1992, SAR Image Classification of Ice in the Gulf of Bothnia, *International Journal of Remote Sensing*, vol. 13, no. 13, pp 2489-2514

TOIKKA M., and HALLIKAINEN M., 1992, Radar Backscatter Signatures of Baltic Sea Ice, *Proceedings of IGARSS'92 held in Houston, 26-29 May 1992*, pp. 1527-1529

ULABY F.T., MOORE R.K., and FUNG A.K., 1982, *Microwave Remote Sensing*, Vol. 1-3, (Reading, Massachusetts: Addison-Wesley)

ULABY F.T., KOUYATE F., BRISCO B., and WILLIAMS T.H., 1986, Textural Information in SAR Images, *IEEE Transactions on Geoscience and Remote Sensing*, vol. GE-24, no. 2, pp 235-245

ULANDER L.M.H., JOHANSSON R., and ASKNE J., 1992, C-band Radar Backscatter of Baltic Sea Ice: Theoretical Predictions Compared with Calibrated SAR Measurements, *International Journal of Remote Sensing*, vol. 13, no. 13, pp 2447-2468

ULANDER L.M.H., and CARLSTRÖM A. (Editors), 1993, Baltic experiment for ERS-1, BEERS-92: Swedish calibration/validation data report, Internal report RSG 1993:1, Department of Radio and Space Science, Chalmers University of Technology, Gothenburg, Sweden

WMO Sea Ice Nomenclature, supplement no. 5, 1989, World Meteorological Organization, Geneva

## Appendix A: SAR image data

The analysed SAR images and the weather conditions at the time of acquisitions are presented in the table below. The images are of two types, FD and PRI images. The major differences between the two types are that the PRI images have slightly better radiometric calibration and are less affected by speckle noise (*i.e.* a higher effective number of looks).

**ERS-1 SAR FD (Fast Delivery, UI16) images:**

| | |
|---|---|
| Calibration accuracy: | ±1 dB |
| Effective number of looks (Dammert, 1993): | $N_e$=2.8 |

**Period BEERS-92** : Five images

| Acquisition date | Time | Centre position | Pass | Ground temperature | Wind speed and direction |
|---|---|---|---|---|---|
| 1992-02-17 | 09:48:12 | N 65.59° E 22.84° | Descending | -0.6° C | 7 m/s, N |
| 1992-02-17 | 09:48:27 | N 64.72° E 22.23° | Descending | -0.6° C | 7 m/s, N |
| 1992-02-20 | 09:48:26 | N 64.73° E 22.24° | Descending | -5.8° C | 5 m/s, ENE |
| 1992-03-27 | 09:48:10 | N 65.59° E 22.81° | Descending | -1.5° C | 5 m/s, ESE |
| 1992-03-30 | 09:48:08 | N 65.59° E 22.82° | Descending | -3.5° C | 5 m/s, N |

**Period BEERS-94** : Two images

| Acquisition date | Time | Centre position | Pass | Ground temperature | Wind speed and direction |
|---|---|---|---|---|---|
| 1994-03-01 | 20:10:57 | N 64.96° E 22.64° | Ascending | -11.3° | 1 m/s, NW |
| 1994-03-04 | 20:10:57 | N 64.96° E 22.64° | Ascending | -7.3° C<br>(snow fall) | 10 m/s, S |

## ERS-1 SAR PRI (Precision) images:

| | |
|---|---|
| Calibration accuracy: | ±0.8 dB |
| Effective number of looks: | $N_e$=3.0 |

**Period BEERS-93** : Three images

| Acquisition date | Time | Centre position | Pass | Ground temperature | Wind speed and direction |
|---|---|---|---|---|---|
| 1993-03-14 | 20:04:09 | N 65.83° E 23.87° | Ascending | +3.3° C | 8 m/s, WSW |
| 1993-03-17 | 20:04:42 | N 64.97° E 23.05° | Ascending | -0.6°C | 6 m/s, SSW |
| 1993-03-18 | 09:41:19 | N 65.59° E 22.97° | Descending | 0° C | 5 m/s, W |

# Appendix B:
# Helicopter data

Several photographic films were acquired, during the three experiments BEERS-92, 93 and 94. Some films could, however, not be used in this study due to, for example, bad focus, bad exposure, bad developing or no visible ground features in the photographs. Of the total 25 films only 13 films were actually used in this study. An additional film from the Swedish Airforce (BEERS-94) was also used. A list of the films follows in the table below.

| Period | Film no. | Date | Used in this study |
|---|---|---|---|
| BEERS-92 | 1:1 | 920215 | No |
| | 1:2 | 920215 | No |
| | 1:3 | 920216 | No |
| | 1:4 | 920217 | Yes |
| | 1:5 | 920218 | No |
| | 1:6 | 920220 | Yes |

| | | | |
|---|---|---|---|
| | 1:7 | 920220 | Yes |
| | 1:8 | 920221 | Yes |
| | 2:1 | 920326 | Yes |
| | 2:2 | 920327 | Yes |
| | 2:3 | 920328 | No |
| | 2:4 | 920329-30 | No |
| | 2:5 | 920330 | Yes |
| | 2:6 | 920330 | Yes |
| BEERS-93 | 1 | 930314 | Yes |
| | 2 | 930315 | No |
| | 3 | 930316 | No |
| | 4 | 930317 | Yes |
| | 5 | 930318 | Yes |
| | 6 | 930319 | Yes |
| BEERS-94 | Airforce film | 940302 | Yes |
| | 1 | 940303 | Yes |
| | 2 | 940303 | No |
| | 3 | 940309-10 | No |
| | 4 | 940310 | No |
| | 5 | 940310 | No |

# F. INFLUENCE OF TEMPERATURE AND PRECIPITATION DURING COLD CONDITIONS ON ERS-1 SAR SEA ICE IMAGERY.

MATS MOBERG and BERTIL HÅKANSSON

Swedish Meteorological and Hydrological Institute,
S-601 76 Norrköping, Sweden.

**Abstract.** A time series of 15 SAR images, covering a part of the northern Baltic Sea, was collected during the period January 13 to March 11 1994. Seven test sites were identified in the images, representing level smooth ice, level rough ice and land. All test sites had snow-covers of varying thicknesses. Weather parameters, primarily air temperature and precipitation, from nearby synoptic weather stations were collected. First order statistics were calculated from SAR digital counts for each test site and date, showing a slight variation over time. Comparisons made with daily means of air temperature showed weak or no correlation with air temperature or precipitation apart from the land areas which showed a good correlation with air temperature. The variation of means of SAR digital counts did not present any problems as far as interpretation of images was concerned. Known degradation of SAR images due to above zero air temperatures could not be evaluated as the daily mean of air temperature ranged between ≈-2°C to ≈-28°C during the test period.

## 1. Introduction

SAR is sometimes described as an weather-independent remote sensing tool when a more appropriate term would be cloud-independent. When used in sea ice studies, it is quite obvious even for a novice interpreter, that the appearance of SAR images is very much depending on various weather factors, especially air and snow/ice temperatures and humidity. Large scale (whole SAR scene) and lasting (couple of days) variations of these weather parameters can be illustrated in Figure 1. SAR scenes from March 26 and April 7 1994 covering the northernmost part of the Bothnian Bay give quite a different possibility to distinguish between various ice features even if the general ice situation is practically the same. The degradation of the latter scene is due to a longer period with moist and mild weather (±0°C) while the earlier scene was acquisitied when the air temperature was about -10°C.

During the BEERS-94 campaign, with the access of fast-delivery (FD) SAR data, a study was made with the aim of investigating the effects of weather influence, primarily air temperature and precipitation, on SAR data when used operational for winter navigation. Among the questions raised are:

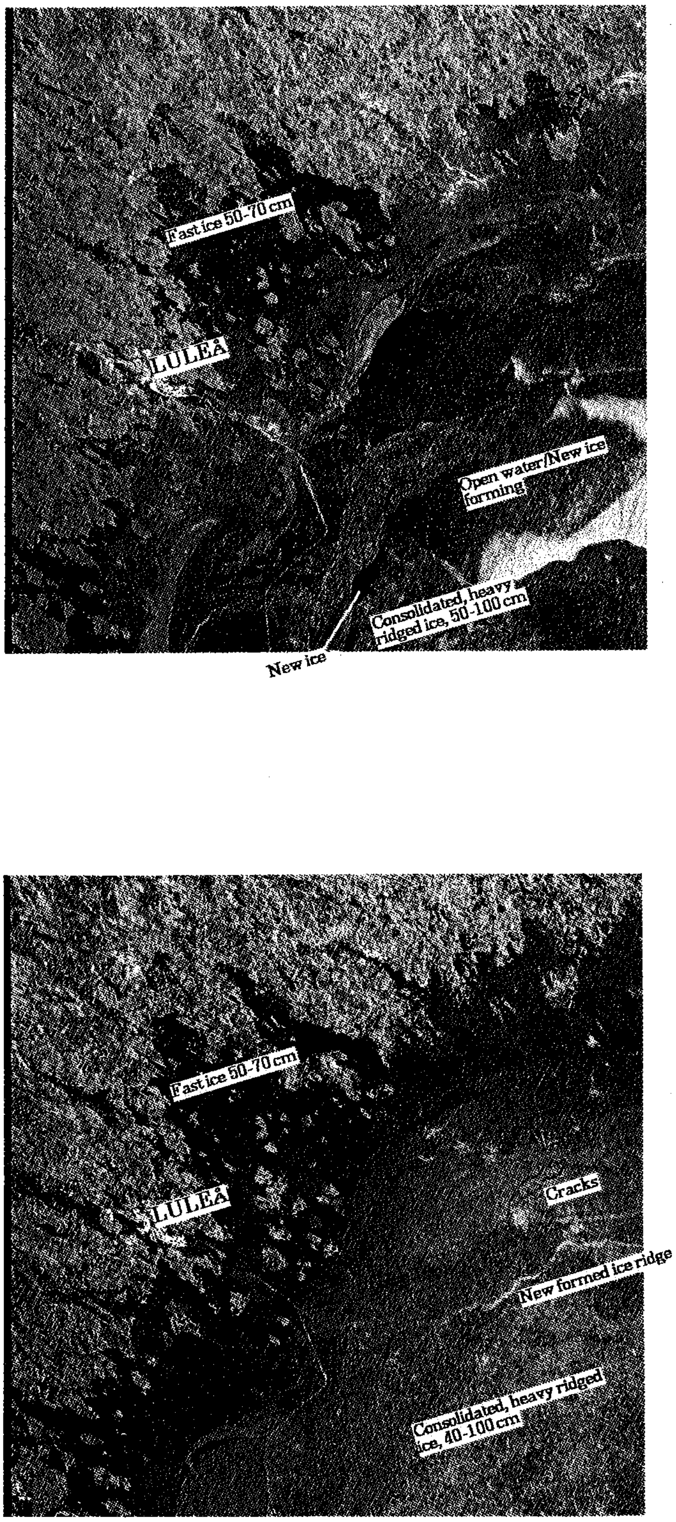

Figure 1. SAR scenes from March 26 (upper) and April 7, 1994 (lower) covering the northern part of Bothnian Bay, showing image degradation due to mild weather (lower).

Given information of relevant weather parameters would it be possible to faciliate interpretation of SAR images of the sea ice?

Which of these parameters are the most important and if identified how to apply them?

The study is restricted by the facts that no ice ground truth measurements were available and that the ERS-1 ice orbit was commenced at January 1 when the ice season was already well established.

## 2. Data description

During the second ice orbit phase of ERS-1 from January 1 to April 7 1994 SAR data from the tracks covering the Baltic Sea were aquired at SMHI under BEERS-94. This orbit is configured such that a given area is covered every third day. Tromsö Satellite Station (TSS) was one of the receiving stations with a reception zone covering the Baltic Sea. From there low-resolution SAR data were accessed via the Internet short after satellite overflight.

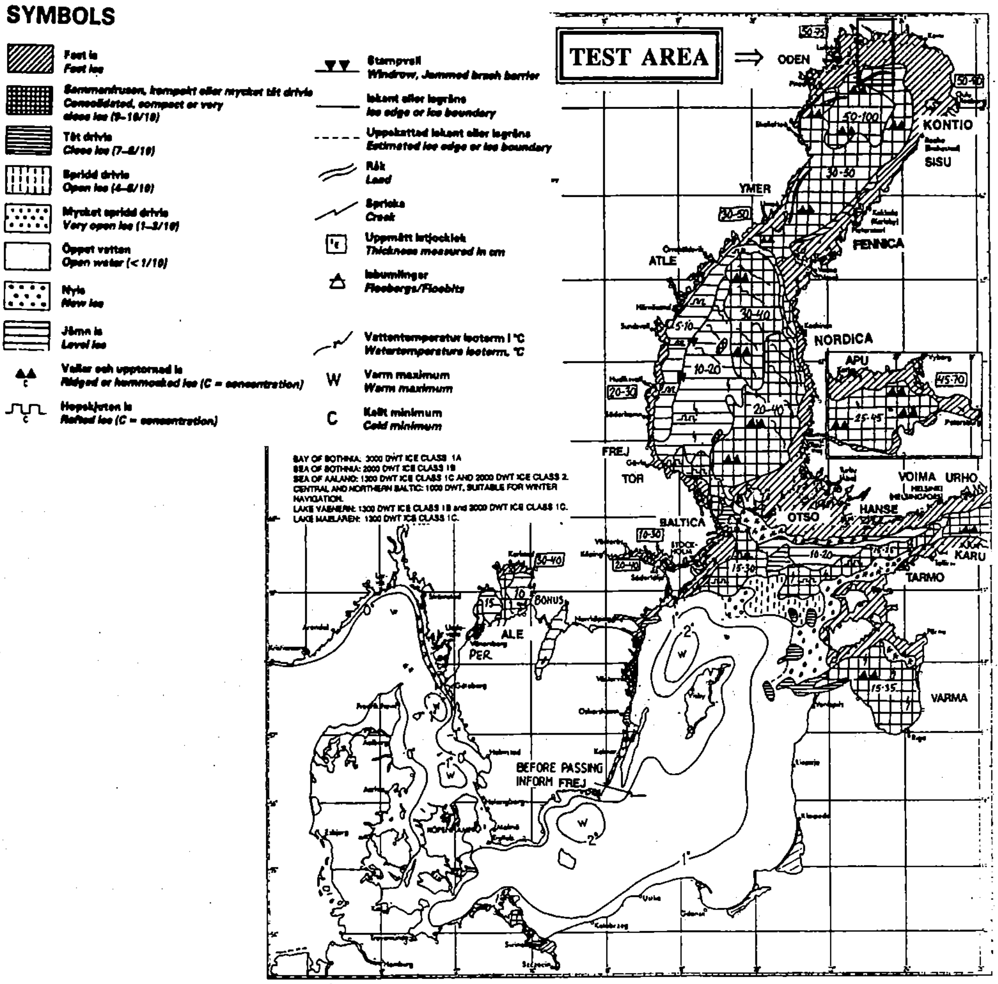

Figure 2. Ice chart from March 3, 1994, showing the maximum ice extent during the winter and position of the test area.

The TSS low-resolution data are made by 5 by 5 averaging of the original high-resolution data and have a pixel spacing of 100 * 80 m. For the test area Mercator transformations were made for each qualified received scene. The test area represents a ground area of the size 65 by 38 km which is situated between 65° 52' and 65°17' N and 22°54' and 23°44' E (Figure 2). The transformation polynom was calculated based on the data file header information of the geodetic latitudes and longitudes for five image points: the four corners and the image center. This process also takes care of the linearization of pixels x- and y-scale. The actual pixelsize in the resulting image varies between 85,5 m in the northern image border and 87,5 m i the south. No calibration was made. In total 15 Mercator images of the test area were accepted for statistical interpretation covering the time span from January 13 to March 11. They were all registered during descending passes with acquisition times at ≈1050 (LT).

Based on the time series of the test area images and ice charts seven test sites were identified for the study (Table 1). As the aim of the study was weather influence on SAR data rather than ice dynamics these test sites were chosen in different areas of fast ice where ice motion or ridging were less probable to occur. The studied ice types present no obstacles as ice breaking is concerned with the possible exception of site 3 with consolidated shuga. Two land areas close to the coast were also included.

Table 1. Test sites for SAR time series evaluation.

| **Site** | **Size pixels/km$^2$** | **Description** | **Formed** | **Distance to weather station,km** |
|---|---|---|---|---|
| 1 | 889/ 6,7 | Level smooth ice 500-800 mm. Snow-covered. Archipelago with no river runoff. | Late Nov. | Haparanda 20 |
| 2 | 1468/ 11,0 | Level smooth ice 500-800 mm. Snow-covered. River estuary with fresh water discharge. | Early Dec. | Storöhamn 4 |
| 3 | 1965/ 14,7 | Rough ice 500-800 mm (consolidated shuga). Snow-covered. | Early Dec. | Storöhamn 8 |
| 4 | 1397/ 10,5 | Level ice 500-800 mm, some roughness. Snow-covered. | Middle Dec. | Storöhamn 25 |
| 5 | 1735/ 13,0 | Level ice 500-800 mm, belts of ridges. Snow-covered. | Middle Dec. | Storöhamn 25 |
| 6 | 690/ 5,2 | Land, island. Coniferous forest with cuttings. Snow-cover 800-900 mm. | | Haparanda 22 |
| 7 | 2498/ 18,7 | Land. Coniferous forest with cuttings.Swamps. Snow-cover 800-900 mm. | | Storöhamn 7 |

## 3. Weather and ice conditions

### 3.1 General conditions

The winter 1994 can be defined as normal, since the whole Gulf of Bothnia and the northern part of the Baltic proper were ice covered in the beginning of March.

The ice season started in late November 1993 with ice formation in the archipelagos in the Gulf of Bothnia during a cold weather period. However, this period was overtaken by warm winds from the south, packing the ice along the northernmost part of the Bothnian Bay. In January the ice formation took place in the open sea in the Bothnian Bay with some ridge formations. The cold weather covering the whole Scandinavia prolonged even in February, characterized by a high pressure system with weak northeasterly winds and cloudless conditions over the Baltic Sea. During this period the ice conditions in the Bothnian Bay were stabilized and only minor changes in the ice formation took place in late February and March, whereas the Bothnian Sea was ice covered during this period but with varying conditions in the western part due to an easterly ice drift. Maximum ice extent was obtained in March 3 to 4 1994 (Figure 2). Strong winds from the south broke up the ice in the southern Bothnian Sea and created strong ice pressure with ridge formations in the northern part, a few days later. In the end of April the ice concentration started to decrease in the Bothnian Bay and in mid May the western part was ice free with open water, whereas some ice were left along the Finnish coast. This ice-breakup occured about one week earlier than normal (Carlström,1994).

Winter weather in the northern part of Bothnian Bay where the test area was situated can be illustrated by some weather station data from Haparanda and Holmögadd, representing more continental and more maritime climates, respectively (Table 2).

Table 2. Monthly mean air temperature and precipitation for the winter 1993/94.

| **Period** | **Haparanda** | | | | **Holmögadd** | | | |
|---|---|---|---|---|---|---|---|---|
| | **Air temp °C** | | **Precip. mm** | | **Air temp °C** | | **Precip. mm** | |
| | **93/94** | **Norm** | **93/94** | **Norm** | **93/94** | **Norm** | **93/94** | **Norm** |
| Nov | -1,8 | -4,2 | 34 | 59 | 0,0 | 0,6 | 13 | 64 |
| Dec | -8,2 | -9,5 | 145 | 42 | -2,5 | -3,1 | 100 | 51 |
| Jan | -13,9 | -12,1 | 50 | 44 | -6,0 | -6,0 | 65 | 48 |
| Feb | -16,2 | -11,4 | 4 | 32 | -11,2 | -6,9 | 2 | 38 |
| Mar | -6,8 | -6,8 | 41 | 35 | -4,7 | -4,1 | 52 | 37 |
| Apr | 2,0 | -0,5 | 29 | 29 | 1,3 | 0,1 | 26 | 29 |

*Note: Norm. refers to the reference period 1961-90*

### 3.2 Weather at the test area

Two weather stations are situated fairly close to the test area - Storöhamn on the peninsula between test site 2 and 3 and Haparanda which is situated about 20 km east of site 1. These are synoptic stations where observations are made every 3rd hour between 0100 and 1900 (LT) every day. The observations include, among other parameters, air temperature, precipitation, wind speed and direction and snow depth. In order to catch the more maritime weather conditions, wind and air temperature data from the lighthouse Farstugrunden (position 65°20' N, 22°45' E) were used too. No observations of precipitation are made here. A time series of weather data from the test period are presented in Figure 3.

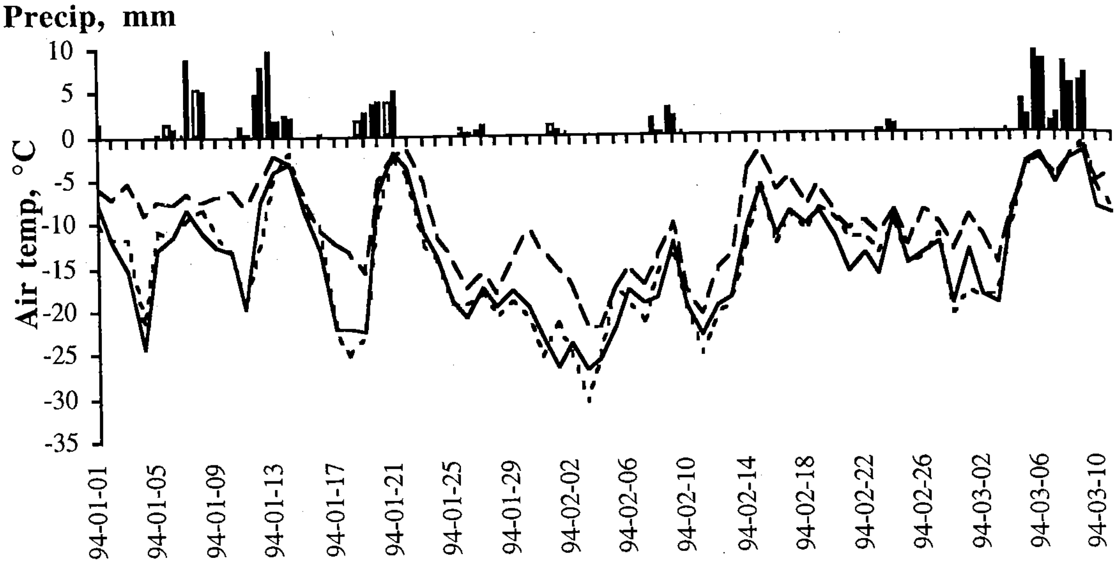

Figure 3. Daily precipitation (unfilled bars Storöhamn, filled bars Haparanda) and daily mean of air temperature from some synoptic weather stations.
(Solid line Storöhamn, dotted line Haparanda, dashed line Farstugrunden).

A comparison between the stations Storöhamn and Haparanda shows no significant differences as far as air temperature, precipitation and snowdepth are concerned. There is a difference though in wind conditions where the more easterly situated station Storöhamn is more exposed. One can assume that there is no significant difference in air temperature and preciptation in the east-west direction of the test area during this period and that meteorological data from any one of the stations could be valid for the test area. Snowdepths measured on land can not a priori be regarded as valid for the surrounding sea ice due to different wind exposure and heat balance.

Table 3. Comparison of some weather characterizing parameters for the period Jan 1 to Mar 11 1994.

| **Item** | **Param.** | **Storöhamn** | **Haparanda** | **Farstugrunden** |
|---|---|---|---|---|
| 1 | Degree days, Θ | -983,5 | -984,4 | -694,6 |
| 2 | Accum. precip.,mm | 71,1 | 69,2 | – |
| 3 | Rel. humidity,% | 85 | 81 | – |
| 4 | Cloud cover, % | 58 | 53 | – |
| 5 | Mean snowdepth, mm | 842 | 807 | – |
| 6 | Days with wind speed >=8 m/s | 21 | 2 | 36 |
| 7 | Days with wind speed >=14 m/s | 4 | 0 | 3 |

*1: Defined as* $\Theta=\int(T_0 - T_a)dt$ *where* $T_0$ *and* $T_a$ *are the freezing (0°C) and air temperature (daily mean) respectively.*

*3-5: Based on daily means.*

As for north-south weather variations air temperatures from the lighthouse Farstugrunden indicate, as expected, generally higher values than ashore with a mean difference of 4,5°C compared to Haparanda. A reasonable assumption is that this temperature gradient is linear from the coast and offshore. As precipitation is not observed at Farstugrunden it is very difficult to estimate this parameter over the sea and especially the snowdepths for the ice covered parts.

## 5. Evaluation in time of SAR signatures

### *5.1 Geographic location quality of the SAR data.*

The transformations to Mercator projection of the SAR scenes showed in some cases unacceptable differences when the output images were compared. That is supposed to be caused by inaccurate data file header information of the geodetic coordinates of the five image points. The differences were corrected by resampling those images by means of ground control points. As a visual test of the final spatial correspondence between the 15 images, an averaged image was made by calculating the mean value for each pixel in the time series. (Figure 4). This image shows, apart from the location of the test sites, that the northern part bears a rather distinct pattern, indicating firstly land and stationary ice features and secondly an acceptable co-registration of the separate scenes. South of the fast ice in the archipelago, the pattern is more blurred due to ice dynamics over the time. Notable is also that one SAR scene did not cover the eastern part of the test area resulting in the loss of information from test sites 1, 4 and 6 for that date (Feb 9). An estimation of the spatial error was made by extracting image coordinates from some outstanding, common features in the different images. The overall displacement is estimated to be whitin ±5 pixels in x and y direction.

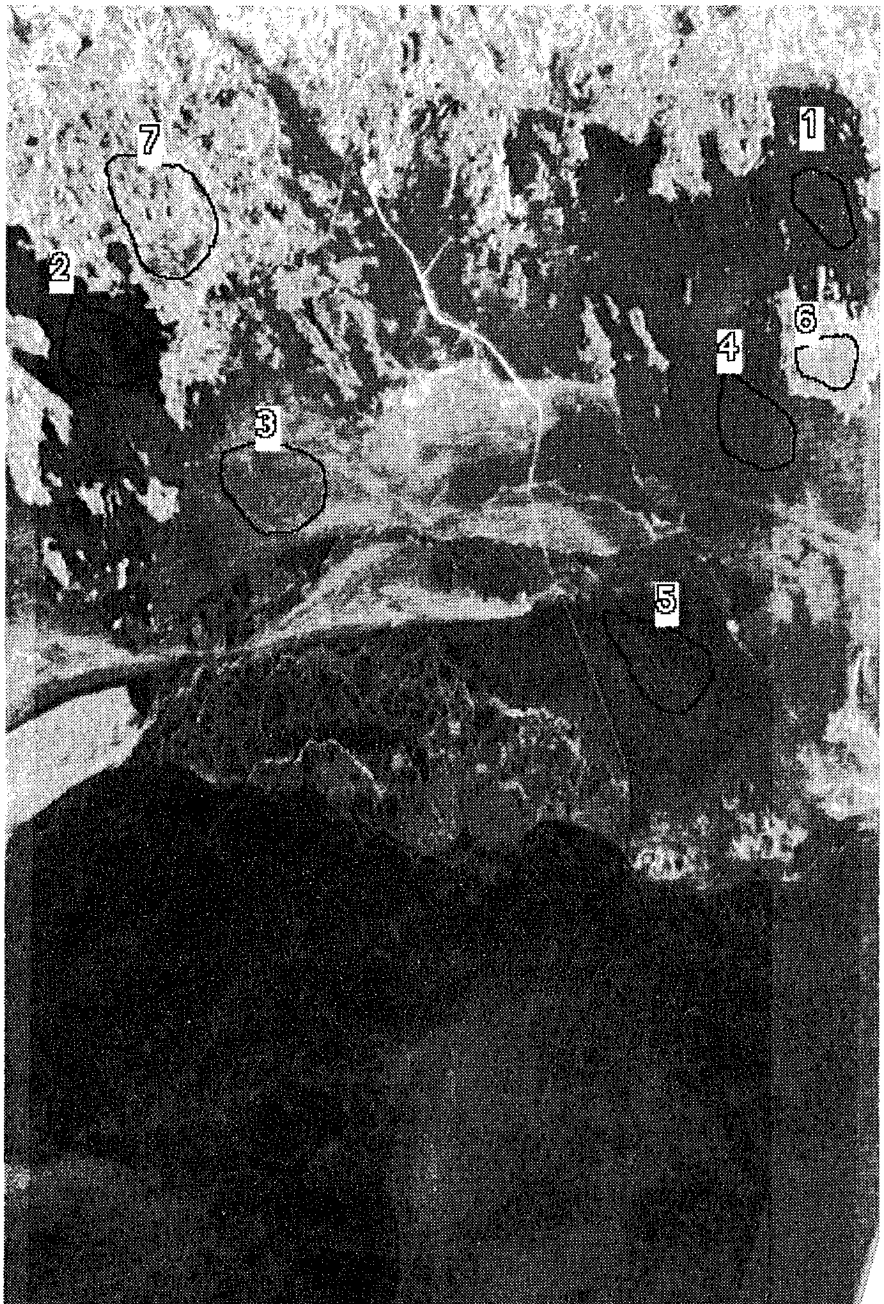

Figure 4. Average SAR image made of the 15 SAR images from the test period. The test sites are indicated.

### *5.2 Methodology*

For each of the 15 SAR images, mean values and standard deviations of digital counts were calculated for the test sites (Table 4).

Table 4. Summarized SAR data statistics from the test period Jan 13 to Mar 11 1994.

| Site | Numb.of images | Mean of site mean | Site mean range | Mean of site stddev |
|---|---|---|---|---|
| 1 | 14 | 53,3 | 43,3 – 59,6 | 5,9 |
| 2 | 15 | 45,7 | 41,6 – 48,7 | 6,4 |
| 3 | 15 | 80,9 | 72,7 – 88,0 | 9,8 |
| 4 | 14 | 62,2 | 53,9 – 67,6 | 6,4 |
| 5 | 15 | 50,2 | 43,7 – 60,4 | 6,3 |
| 6 | 14 | 102,9 | 94,3 – 113,1 | 14,5 |
| 7 | 15 | 105,0 | 93,8 – 113,3 | 18,5 |

The mean values versus weather parameters are shown in Figure 5. Some variations of the mean values over time are present, but in principle there is no problem regarding discrimination of the various ice types. Correlations are also calculated between site means and weather (Table 5).

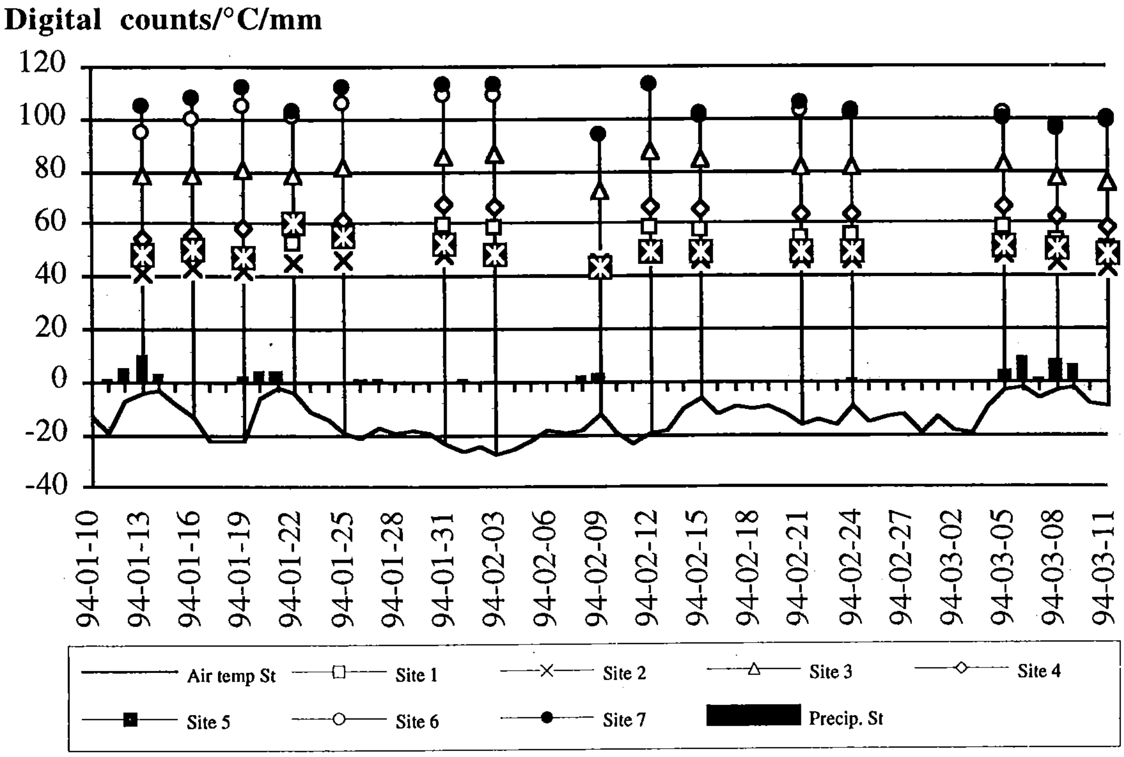

Figure 5. Test site variation of mean of SAR digital counts and some weather parameters from Storöhamn (St).

Table 5. Correlation matrix for mean of SAR digital counts and daily mean of air temperature and precipitation from Storöhamn.

| | *St air* | *St prec* | *mean-1* | *mean-2* | *mean-3* | *mean-4* | *mean-5* | *mean-6* | *mean-7* |
|---|---|---|---|---|---|---|---|---|---|
| *St air* | 1,000 | ,533 | -,237 | -,336 | -,590 | -,316 | ,216 | -,804 | -,896 |
| *St prec* | ,533 | 1,000 | -,406 | -,394 | -,375 | -,364 | -,241 | -,635 | -,414 |
| *mean-1* | -,237 | -,406 | 1,000 | ,957 | ,692 | ,984 | ,149 | ,628 | ,103 |
| *mean-2* | -,336 | -,394 | ,957 | 1,000 | ,786 | ,967 | ,255 | ,693 | ,282 |
| *mean-3* | -,590 | -,375 | ,692 | ,786 | 1,000 | ,778 | -,066 | ,821 | ,664 |
| *mean-4* | -,316 | -,364 | ,984 | ,967 | ,778 | 1,000 | ,093 | ,677 | ,207 |
| *mean-5* | ,216 | -,241 | ,149 | ,255 | -,066 | ,093 | 1,000 | ,019 | -,043 |
| *mean-6* | -,804 | -,635 | ,628 | ,693 | ,821 | ,677 | ,019 | 1,000 | ,759 |
| *mean-7* | -,896 | -,414 | ,103 | ,282 | ,664 | ,207 | -,043 | ,759 | 1,000 |

### *5.3 Contrast*

One aspect of degradation of SAR images by weather factors are visualized by a decrease in the contrast. Here contrast is defined as the possibility to distinguish ice types in terms of differences between the mean digital numbers of the various test sites and the possibility to extract small scale ice features within each test site in terms of varying coefficient of variation ($100s/\bar{x}$). Figure 6 shows scattergrams of the between-sites contrast, (6-1), (6-2), (6-4) and (3-1), (3-2), (3-4) versus air temperature. Within-site contrasts are shown by the normalized coefficients of variation for some test sites versus air temperature (Figure 7). Normalization is done by, for each test site series, subtraction of the temporal mean.

Between-sites contrast seems to correlate fairly well with air tempearture as far as Site 6 - Site 2 differences (land-level smooth ice) are concerned but the correlation are more uncertain with the other two land-ice comparisons. Contrast between different ice types shows weak or no correlation with air tempearture. Within-site contrast scattergrams, also, show a more random distribution with the exception of Site 6, where a weak correlation can be at hand.

The correlation is of course not a priori of a continous nature but, perhaps more likely, with contrast changes depending on certain discrete air temperatures. One such step is of course ≈ 0°C and temperatures above – conditions unfortunately not present during this study. Another factor to consider is how snow/ice temperatures correspond to registered air temperatures. The heat storage present in the water body makes the temperature distribution in the snow-covered sea ice behave differently compared to a land surface.

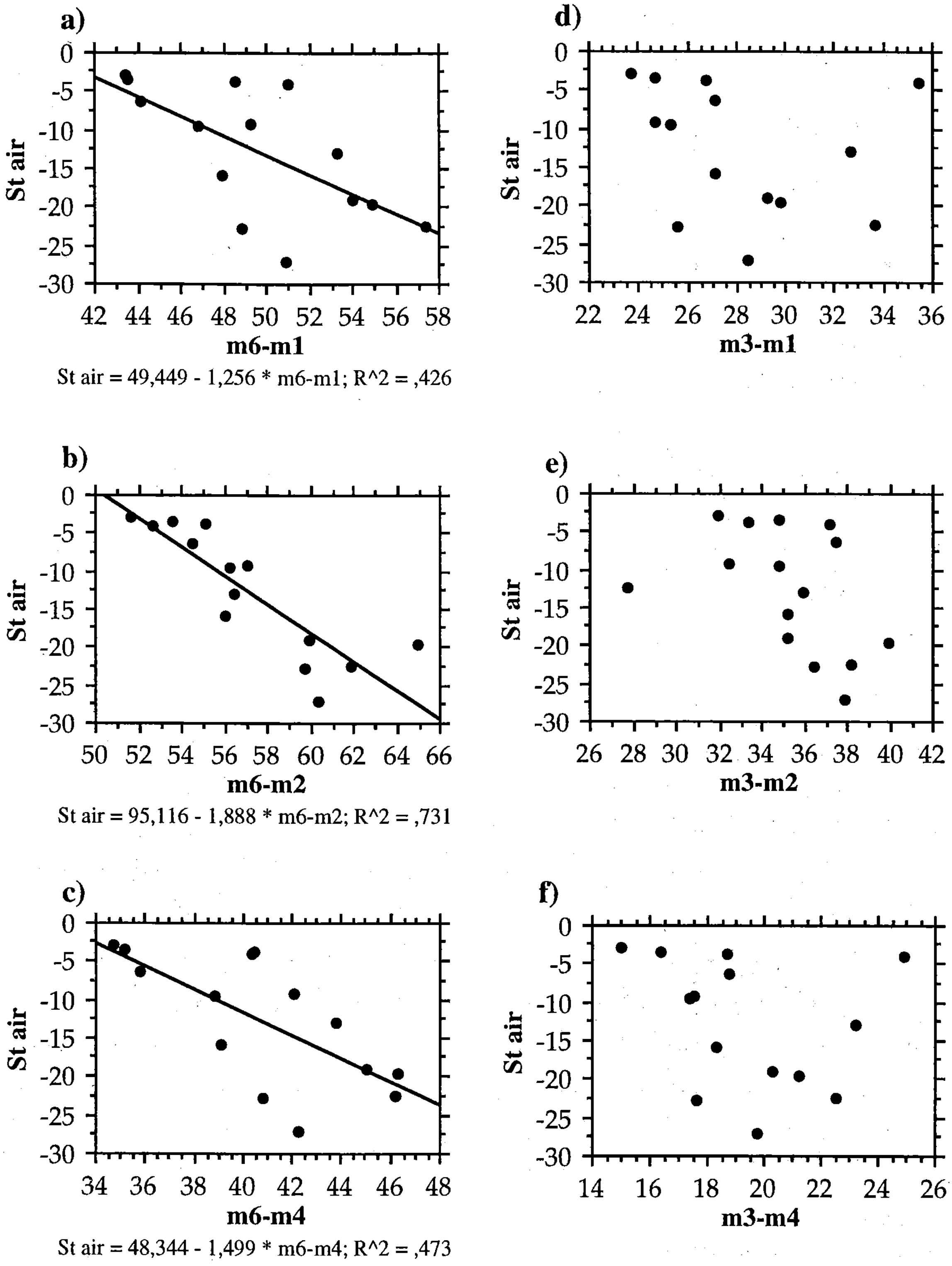

St air = 49,449 - 1,256 * m6-m1; R^2 = ,426

St air = 95,116 - 1,888 * m6-m2; R^2 = ,731

St air = 48,344 - 1,499 * m6-m4; R^2 = ,473

Figure 6. Scatterplot of differences of mean of SAR digital counts between some test sites versus air temperature.

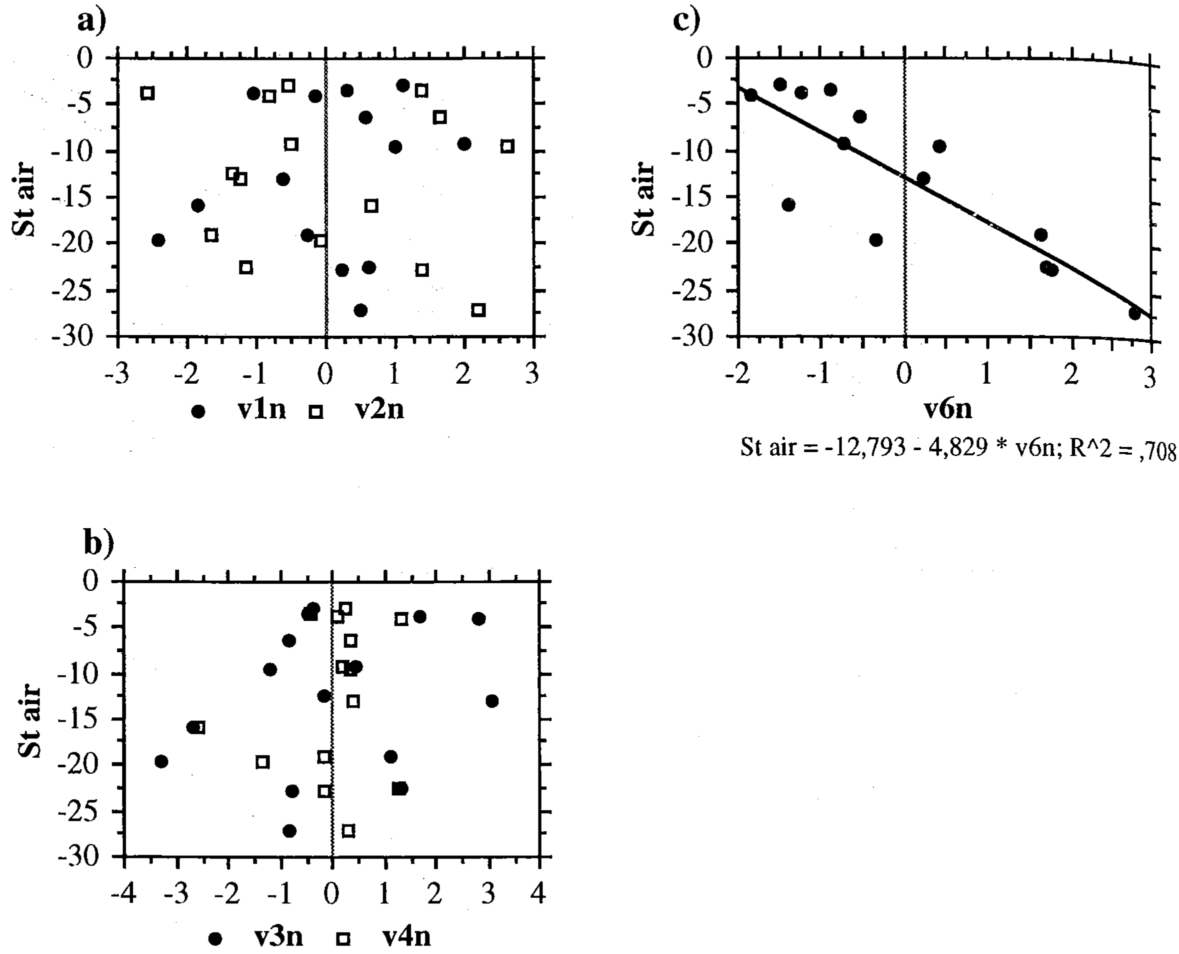

Figure 7. Scatterplot of normalized coefficients of variation from some test sites versus air temperature.

### *5.4 Precipitation*

The coastal areas surrounding the Bothnian Bay are every winter snow-covered with a typical snow depth of 400 - 500 mm. The distribution of snow-cover over the sea ice is more uncertain to estimate but is known to show a great spatial and temporal variability and the depths are commonly less than those recorded at land areas. Important differences of a snow pack on sea ice compared to that on land are that the former is exposed to flooding and wind, causing e.g. redistribution of the snow and wind crust and by the fact that the snow pack rests on an elastic medium, beneath which a heat supply is present. When sea ice is covered with snow the effects on the ice are mainly due to the snow load and by the change of temperature gradient between the water and the ice surface.

As for the first effect, consider an ice cover with a thickness of 200 mm. It has an ice height over the water level of 20 mm caused by the buoyancy force (ice and water density of 900 and1000 kg/m$^3$ resp.). A snow-cover whith a depth exceeding about 90 mm (snow density 200 kg/m$^3$) will depress the ice surface beneath the water level – and if cracks are present – cause flooding of the sea ice.

The temperature profile running from the down side of the ice (i.e. freezing temperature of water) to the air is heavily dependant on the snow-cover. The insulation capability of snow very much exceeds that of ice. Depending on snow density, thermal conductivity of snow is only 1/8 to 1/10 of that of sea ice. One consequense is that ice growth is inhibited or reduced and that snow characteristics, dependent of temperature, not can be resolved properly by knowledge of air temperature alone.

During these processes and varying air tempeartures over time, the wet snow will freeze, becoming snow or granular ice, whereas clear or columnar ice is formed from freezeing water. Both phenomena affect the SAR backscattering such that the initial roughness characteristics of the ice could be changed and, from time to time, water or wet snow can be at hand at the snow-ice interface, thus influencing the SAR backscatter.

## 6. Conclusion

During the test period, characterized by cold to very cold weather, the time series of mean of digital counts of SAR images for various ice types show a small variability over time and only weakly correlate with daily mean air temperature. The study is restricted by the fact that no above zero air temperatures are present as the daily mean air temperatures ranges between -2° and -27°C. On the other hand, SAR data from the reference test sites on land correlate well with air temperature which is believed to be an effect of backscattering sensitive to some snow properties influenced by the heat storage in the snow.

The various ice types identified in Table 1 can be distinguished throughout the whole test period, an important fact for operational use of SAR imagery.

## 7. Discussion

The Baltic Sea area, which is covered with a dense synoptic weather observation network, implies good possibilties of real-time access to relevant weather information obtained by direct use of these data or via meteorological analysis schemes.

As mentioned in the Introduction, radical weather changes caused by e.g. a frontal passage can severely degrade SAR images. Thus knowledge of air temperature, precipitation and snow-cover can be used as a first-order quality estimation of the images. Our study indicate, however, that at temperatures below 0°C, SAR sea ice imagery contrast variability is small and hence one can restrict air temperature information to a step function (>,< 0°C) in practical applications. This information could be used directly as a quality estimation of a certain image or a part of an image.

It is believed, though, that the variability over time of SAR digital counts are caused by weather influence and that SAR interpretation could benefit further by a more sophisticated use of this weather information. In order to describe snow and ice status, an ice-snow interaction model could be used which, based on current relevant weather parameters, should keep track of, mainly, ice growth, snowdepth, snow-humidity, temperature profile, existing slush and any crust layers (Kim *et al*, 1984). Further investigations on SAR backscattering response to these snow characteristics in a low-salinity environment is probably needed.

## References

CARLSTRÖM, A. Ed., 1994, Baltic Experiment for ERS-1, BEERS-94 data report, 5.

KIM, Y.S., ONSTOTT, R.G and MOORE, R.K., 1984, The effect of a snow cover on microwave backscatter from sea ice, *I.E.E.E. J. Oceanic Engineering.*, **OE-9**, 383.

# G. SHIP PERFORMANCE AND ICE RESISTANCE INDEX

THOMAS THOMPSON

SIOC,*Satellite, Ice and Ocean Consultant*
Kungsholms Strand 159, 112 48 Stockholm, Sweden

and

GÖRAN LILJESTRÖM

Bureau ODEN Icebreaker Design AB
Vipgatan 2, 426 69 Västra Frölunda, Sweden

**Abstract.** A simple method for calculating ice resistance indexes for various ice types from ship performance data is described. The index is derived from a simple relation between ship propulsion power and speed when forcing an ice field. If a correlation can be found between this index and the backscatter level of a SAR image it should be possible to calculate a ships speed through ice from the backscatter level of a SAR image.

During the ice seasons 1993 and 1994 performance tests were carried out in the Gulf of Bothnia with two Swedish icebreakers. From the very successful data obtained, ice resistance indexes have been calculated. The indexes show a good correlation with the corresponding ice types. A substantial set of ERS-1 SAR images covering the periods of the performance tests have been collected. The first results show a good correlation between the SAR backscatter level and the ice resistance index. The results are preliminary and further work is required.

## 1. Introduction

### 1.1. Background

The ship traffic in the Baltic Sea area is of great importance for the economy of the surrounding countries, and all major ports are kept open on a year round basis by the help of powerful icebreakers. The merchant ships used during the ice season are ice classed and a few are even built with breaking capabilities. Most of the traffic is however assisted by icebreakers but also to a certain extent routed when the ice situation so permits. (THOMPSON *et al.* 1994)

When an icebreaker assists a ship or convoys a group of ships through the ice, it is important to find the easiest possible way through the ice since this will save time and fuel for the icebreaker as well as the ships. With the conventional ice mapping methods used up to now one can only make a qualitative mapping with respect to ice types and ice resistance to icebreaking. With the introduction of radar remote sensing, and in particular satellite SAR, we now see a possibility for more quantitative mapping which would allow a more efficient routing when knowing the performance characteristics of icebreakers and merchant vessels.

### 1.2. Ship performance in ice and ice resistance

When a ship or an icebreaker makes its way through an ice field its speed will be reduced. The speed reduction will depend on the resistance of ice to be forced and the performance characteristics of the particular ship such as the shape of the hull, the length, the beam and its engine power. The resistance of the ice will vary from one ice type to another. It will increase with increasing thickness, but the most important resistance factor will be the roughness and deformation of the ice.

It is reasonable to assume a relation between ice resistance, speed of a ship and the power used to proceed through the ice. The speed is greatly influenced by the shape of the hull along with the beam, length, draft and the friction between the hull steel and the ice. This beam has the major influence on the ice resistance. For the sake of simplisity this influence is however neglected in this study where we by using a simple relation are trying to get a first indication of the validity of the above assumption. The following equation expresses a simple relation between an ice resistance index, ship propulsion power and speed:

$$Ri = a(P/S) \tag{1}$$

where

$Ri =$ ice resistance index ,

$P =$ propulsion power in kW,

$S =$ ship speed in knots,

$a =$ constant which may vary from ship to ship as a function of length, beam ,draft and propeller arrangements. In this study ship characteristics are not taken into account and the constant is set to 0.01.

By logging speed and propulsion power an ice resistance index may be obtained from (1).

### 1. 3 . Radar backscatter from SAR images

SAR images show the backscatter of radar signals from the ice, and studies of ERS-1 SAR images combined with field experiments such as BEERS, clearly demonstrate that the backscatter increases with increasing roughness of the ice (See Chapter D and E, this report). It is possible to discriminate a number of ice types based on roughness characteristics and the backscatter coefficient. It is however difficult to get a reliable indication of the ice thickness. For navigation in ice, the thickness of the level ice is however of less importance compared to the deformed ice, and since deformed ice has a high backscatter level, SAR images could be a very valuable tool for ice routing. By carrying out ship performance tests close in time to SAR images it is possible to correlate the various backscatter levels of the SAR image to the ice resistance indexes calculated from the performance of the ship.

### 1.4. Ship performance from SAR backscatter

As the ice resistance index is a function of propulsion power and speed of a ship it should be possible, from the SAR backscatter level, to calculate the ship speed versus propulsion power.

Assuming a linear relation between the ice resistance index $R_i$ and the corresponding backscatter level of a SAR image the following equation could be set up:

$$Bs = b+cRi = b+ac(P/S) \tag{2}$$

where

$Bs$ = SAR backscatter level
$a,b$ and $c$ = constants

This equation can be solved to express the speed as a function of power and SAR backscatter:

$$S = acP/(Bs-b) \tag{3}$$

From a SAR image the speed of a ship could then be calculated for various SAR backscatter levels as a function of the engine power used. It would then not only be possible to find the easiest route through the ice but also to *eg* calculate the estimated time of arrival (ETA) or the most economic route for given time limits.

## 2. Field Experiments

### 2.1. Background

The Gulf of Bothnia is an area where ice occurs every winter and where icebreakers are operating to assist the ship traffic. Access to ERS-1 SAR images were also secured through the field experiments of the BEERS programme in 1993 and 1994 as well as an operational SAR pilot project in 1994 (See chapter A, this report and CARLSTRÖM 1993 and 1994)). The Gulf of Bothnia was therefore selected for the performance studies. Icebreakers were used due to their high performance capacity in all types of ice, thus securing the most complete set of data.

### 2. 2. Performance tests, winter 1993

The 1993 programme was carried out on the icebreaker ATLE which has the following main characteristics:

| | |
|---|---|
| Length: | 104.6 m |
| Beam: | 22.5 m |
| Draft: | 7.3 m |
| Machinery: | dieselelectric |
| Max. propulsion power: | 16200 kW |

ATLE has a typical Baltic icebreaker design with a pointed bow, two aft and two bow propellers, a 14$^0$ heeling capability, but no air bubbling or water lubrication system.

To keep the measurements as simple as possible it was decided to connect only a few machinery signals to a plotter on the bridge. The equipment was capable of scanning each channel at eight second intervals. Channels recorded were:

- Total power
- Power of each electric propulsion motor

It was unfortunately not possible to record the rpms of the propellers since the signal output exceeded the 10V limit of the recorder. Time and position were recorded from the DGPS of the ships ordinary navigational system and the speed calculated from the Differential GPS positions.

Ice conditions were observed from the bridge every 1-5 minutes and noted in a special log during all test runs.

### 2. 2.1. Test runs

Since ATLE was used as a base for the scientific field programme and had to spend long periods at test stations, it was not possible to run long performance tests or to cover larger test areas. Altogether 5 test runs were made resulting in about 11 hours of data covering some 80-90 nautical miles.

Three of the test runs were reasonably close in time with ERS-1 SAR passes over the area and the track of the icebreaker is visible in most of the images. As the ice movements are well known from the logged movements of the field stations it is possible to accurately plot the route of the icebreaker even in the cases where the tests runs were made after the the satellite passage and therefore no visible track on the SAR image.

### 2. 2. 2. The ice conditions

The winter 1993 was very mild with many ice types lacking, in particular ice thicker than 40 cm and isolated heavy ridges. On the other hand there were unusually many, and large areas with consolidated jammed brash barriers. Jammed brash barriers are formed when brash ice is compressed against a coast or an ice edge and they typically have thicknesses of several meters. In cold weather they will freeze and consolidate and due to the movements of the ice they may drift out to sea and occur at locations far from where they were formed. Jammed brash barriers are very difficult to force, even for powerful icebreakers. The following ice types were observed and recorded during the test runs:

| | |
|---|---|
| - Thin level ice 20 - 40 cm | (TL2) |
| - Thin level ice 40 - 50 cm | (TL4) |
| - Few small ridges | (FSR) |
| - Consecutive ridges | (CR) |
| - Jammed brash barrier | (JBB) |
| - Heavy ridges | (HR) |

### 2. 2. 3. Ice resistance indexes

Ice resistance indexes have been calculated for some 300 individual cases where ship performance data were available together with corresponding ice type observations. They have then been grouped according to ice type and averaged. The result can be seen from the graph in figure 1 showing ice resistance index for the different ice types. The correlation between the index values and the severity of the different ice types can clearly seen.

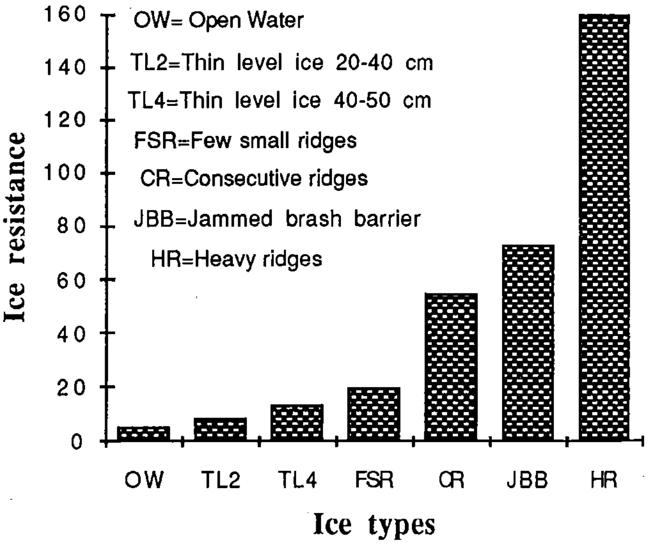

*Figure 1. Ice resistance from icebreaker ATLE performance tests in different types of ice.*

## *2.3. Performance tests, winter 1994*

The performance tests carried out in 1993 clearly demonstrated that realistic ice resistance indexes can be derived from the performance data of an icebreaker. As the winter of 1993 was very mild, with only a limited number of ice types compared to a normal winter, it was decided to continue the performance tests during the ice season in 1994 which turned out to be close to normal.

This time the icebreaker ODEN was selected for the performance tests due to the availability of an onboard measuring system owned and operated by "Bureau ODEN Icebreaker Design AB". The system is able of logging performance data and ship position at a high recording rate. During the 1994 field tests the following sampling rates were used:

- Performance data: every 2nd second
- GPR position data: every 6th second

The measuring system also provided an online printout of the performance data.

The icebreaker ODEN has a totally different design compared with ATLE. It has a blunt bow with a water jet system for lubrication of the ice surface and a very efficient heeling system. ODEN has only two aft propellers mounterd in nozzles. It has the following characteristics:

Length: 107.8 m
Beam: 29.4 m
Draft: 8.0 m
Machinery: Geared diesels with controllable picth propellers
Maximum output power: 18.000 kW

### 2. 3. 1. Test runs

Since the traffic situation did not allow the icebreaker to be specially dedicated for the performance tests, these were carried out during normal operational conditions while ODEN was assisting or convoying ships, or on route to assist ships. This restricted the number of cases with performance tests close in time to ERS-1 satellite passes. A dedicated test run could however be made on 5 March shortly before and after the pass of the satellite and it provided exellent data with the first section of the track of the ship visible in the SAR image. (LILJESTRÖM, 1994)

The measuring system on ODEN provided an online printout of performance data. The system could also provide averages over shorter or longer time periods. Typical averages used for this project are 10 and 2 minutes. figure 2 shows a time plot of the ships speed and figure 3 a typical performance data printout.

Altogether 220 hours of performance data were logged during the experiment which was carried out during two periods, 1-15 February and 1-9 March. Most of the data were stored on 5 1/4" disks for further analysis.

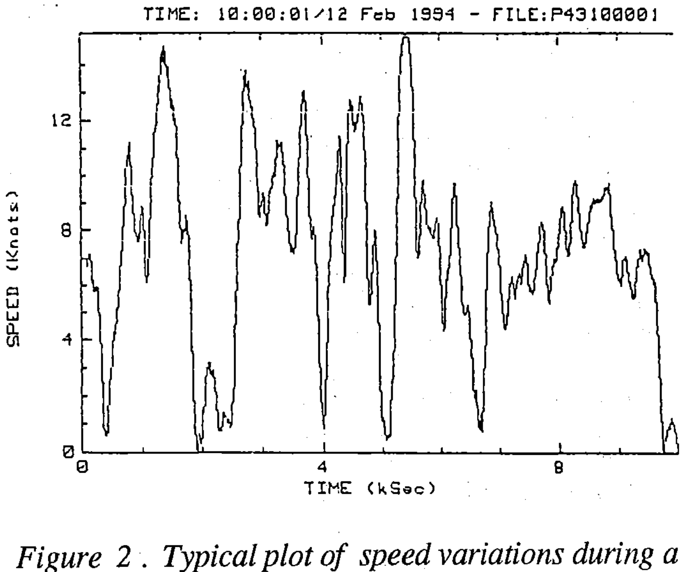

*Figure 2 . Typical plot of speed variations during a performance test with icebreaker ODEN*

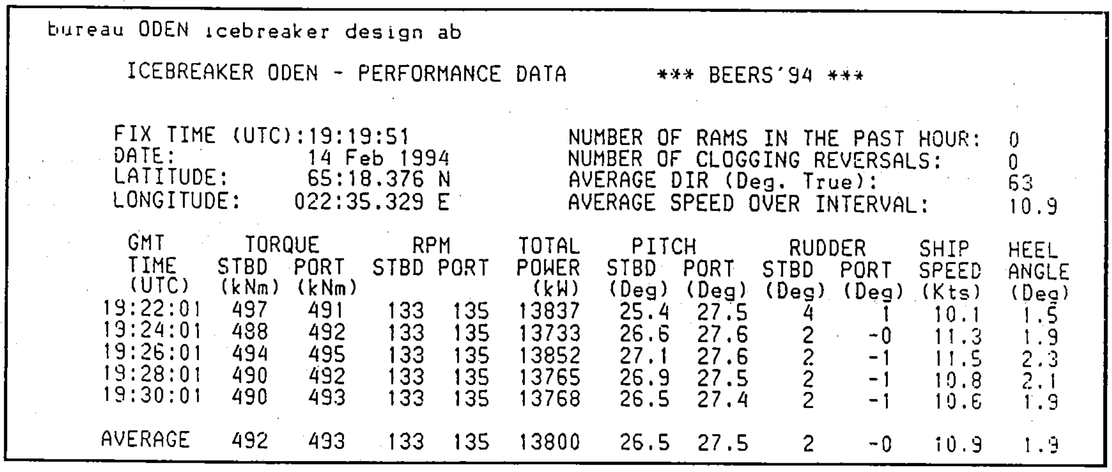

```
bureau ODEN icebreaker design ab

      ICEBREAKER ODEN - PERFORMANCE DATA       *** BEERS'94 ***

     FIX TIME (UTC):19:19:51           NUMBER OF RAMS IN THE PAST HOUR:  0
     DATE:          14 Feb 1994        NUMBER OF CLOGGING REVERSALS:     0
     LATITUDE:      65:18.376 N        AVERAGE DIR (Deg. True):          63
     LONGITUDE:    022:35.329 E        AVERAGE SPEED OVER INTERVAL:      10.9

      GMT      TORQUE       RPM      TOTAL    PITCH       RUDDER     SHIP   HEEL
      TIME   STBD  PORT  STBD PORT  POWER  STBD  PORT  STBD  PORT  SPEED  ANGLE
      (UTC)  (kNm) (kNm)             (kW)  (Deg) (Deg) (Deg) (Deg) (Kts)  (Deg)
    19:22:01  497   491   133  135  13837  25.4  27.5    4     1   10.1   1.5
    19:24:01  488   492   133  135  13733  26.6  27.6    2    -0   11.3   1.9
    19:26:01  494   495   133  135  13852  27.1  27.6    2    -1   11.5   2.3
    19:28:01  490   492   133  135  13765  26.9  27.5    2    -1   10.8   2.1
    19:30:01  490   493   133  135  13768  26.5  27.4    2    -1   10.6   1.9

    AVERAGE   492   493   133  135  13800  26.5  27.5    2    -0   10.9   1.9
```

*Figure 3. Example of a typical printout of performance data on icebreaker ODEN*

Parallell to the logging of performance data, trafficability logs with ice and meteorological data were kept on the bridge. The most important parameter to be logged was the ice condition. The code and the exact time of the entry into each ice type was logged, often with only a few minutes intervalls. The meteorological conditions, to be regarded as supplementary data were logged at longer intervalls. Table 1. shows the codes used for logging the ice and weather conditions.

Table 1. Codes used for logging ice and weather conditions

**ICE**

| Code | Ice type |
|---|---|
| 1 | New ice |
| 2 | Thin level ice 10-30 cm |
| 3 | Level ice, 30-50 cm |
| 4 | Level ice, >50 cm |
| 5 | Small ridges |
| 6 | Few larger ridges |
| 7 | Several larger ridges |
| 8 | Jammed brash barrier, unconsolidated |
| 9 | Jammed brash barrier, consolidated |
| 10 | Open water |
| 11 | Icebreaker lead |

**WEATHER**

| Code | Type |
|---|---|
| R | Rain |
| W | Showers |
| L | Drizzle |
| SD | Dry Snow |
| SW | Wet Snow |
| Z | Freezing precipitation |

Altogether some 65 hours of ice and weather data were logged during the experiment. The data were entered in the performance logs, and the ice resistance index has been calculated for each individual ice type observation.

## 3. Results

### 3.1. Ice resistance indexes

The ice resistance indexes calculated from the performance data of ODEN are shown in figure 4. Also from these data the correlation between the index values and the severity of the ice can be clearly seen. The indexes increase in value as the ice gets thicker and more deformed. The small difference between the ice types 3, 4 and 5 (level ice, 30-50 cm,

>50 cm and small ridges) is probably due to the small thickness difference between the 30-50 and >50 cm thick ice and that small ridges mainly occurred in thinner ice types.

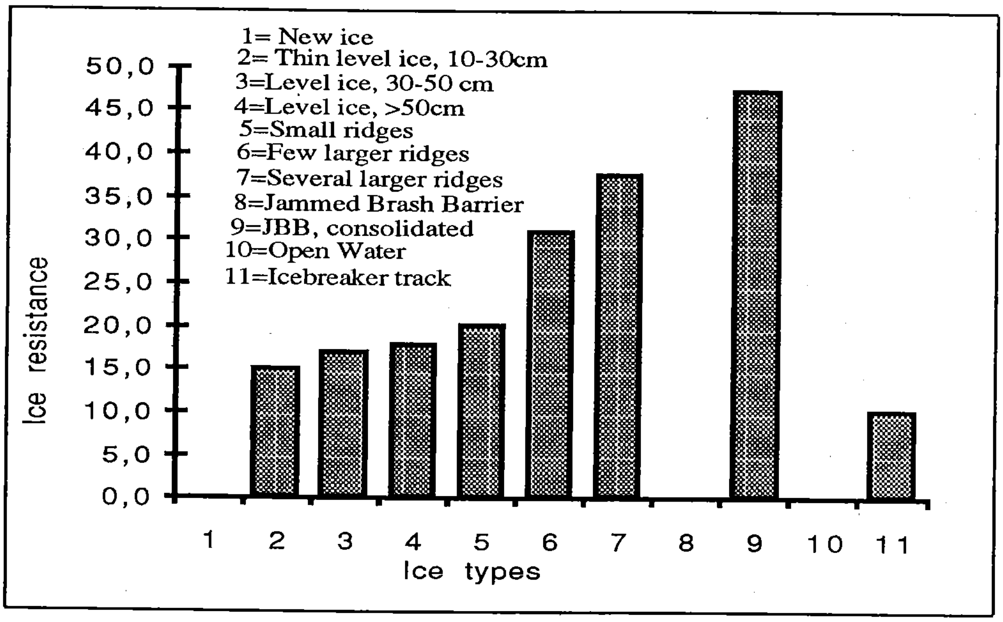

*Figure 4. Ice resistance indexes from performance tests with icebreaker ODEN*

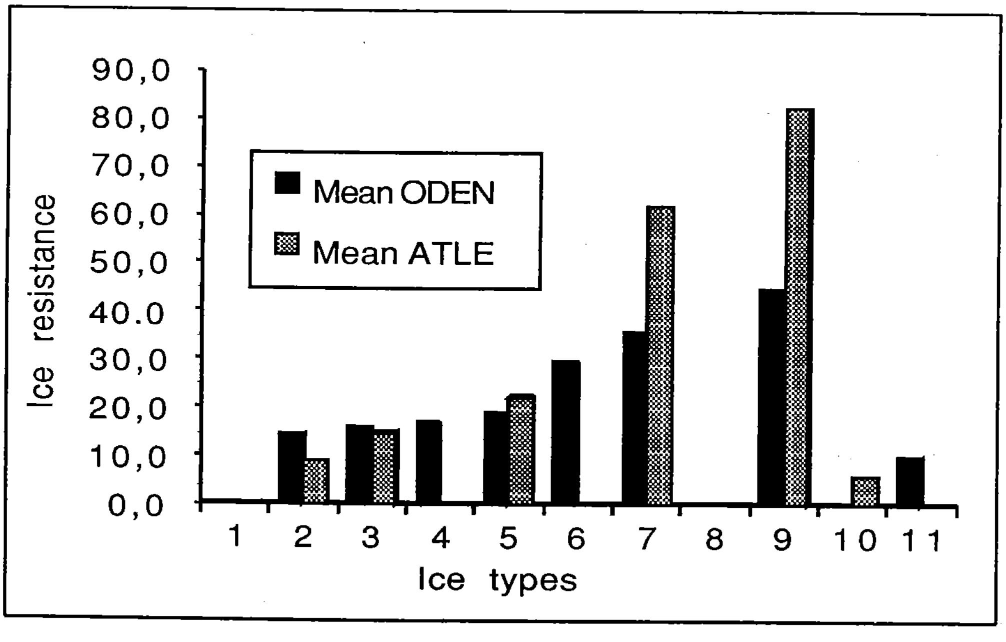

*Figure 5. Ice resistance indexes from icebreakers ATLE(-93) and ODEN(-94)*

In order to compare the results from 1993 and 1994, the corresponding ice types have been plotted together and the result is shown in figure 5. It can be seen that the resistance index for the same type of ice is different for the two icebreakers. While the resistance values for the lighter types of ice are of the same magnitude for the two, ATLE gives consideraby higher values for the more severe types of ice compared to ODEN. The explanation to this is the different design of the two icebreakers. ODEN with its greater beam (29.4 meters) and blunt bow compared to ATLE (22.5 meters) has a higher initial resistance in open water and thin level ice but breaks heavier ice more efficiently due to its special hull form and considerably higher propeller thrust.

In order to obtaine a more ship independant ice resistance index it would be neccessary to include the ships characteristics in the constant (a) in equation (1). This has for simplisity reasons not been done in this first preliminary study.

### 3.2. Radar backscatter and ship performance

The final performance logs from the tests in 1993 and 1994 give the exact time and position of the starting point of each individual ice type along the track of the icebreaker. The logs also give the propulsion power and speed of the icebreaker for each of the ice type sections. This has allowed the calculation of ice resistance indexes for all occurring ice type sections. By locating these sections in the corresponding SAR image, the mean backscatter level of each ice type section can be obtained and the correlation between the ice resistance index and the backscatter level calculated.

The SAR images from BEERS -93 and -94 have been geometrically corrected and transformed into a Mercator projection for presentation on the "Iceplot" image presentation system. In this system a given lat./long. position can be exactly located in the SAR image and sections corresponding to each ice type can be localised in the image.

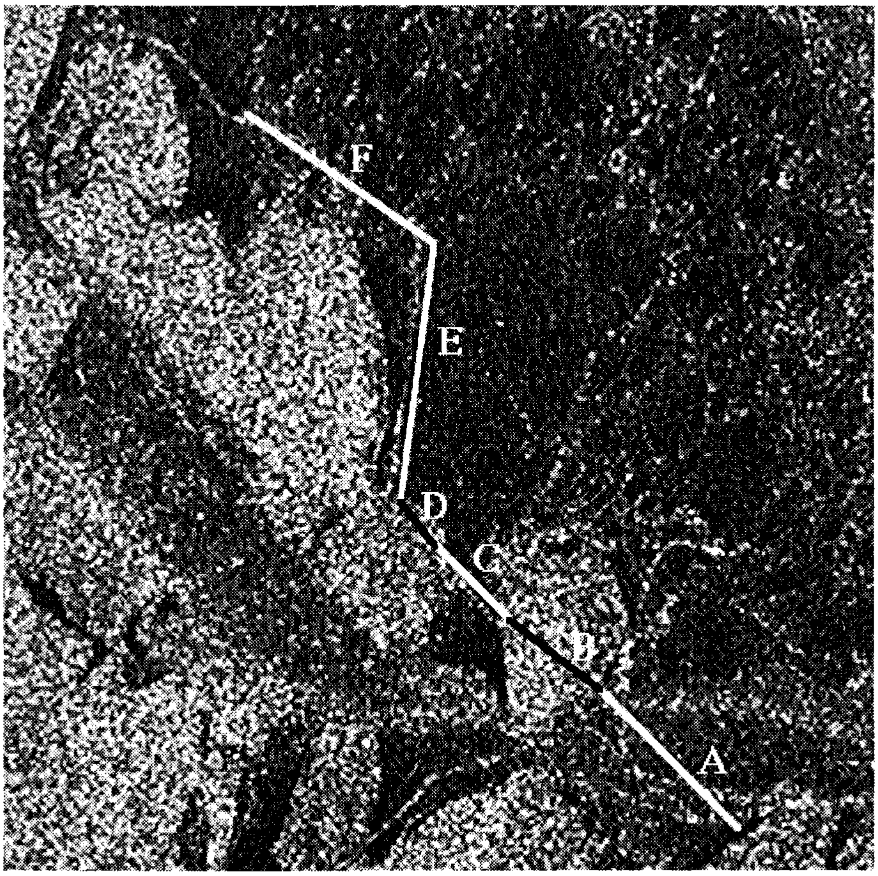

*Figure 6. SAR image from 15 March 1993 showing the track of icebreaker ATLE and the sections for which the mean backscatter levels have been calculated © ESA 1993*

From the SAR image from 15 March 1993 ( se figure 6 ), where several tracks of the icebreaker ATLE can be seen, 6 separate track sections (A -F) have been selected and the mean backscatter levels for these have been calculated.They represent three different ice types: thin level ice (sections A, C and E), jammed brash barrier (B and D) and consecutive ridges (F). The difference in the backscatter level of the different ice types can be clearly seen in the image. figure 7 shows a plot of the ice resistance index (squares) and the backscatter level (triangles) for the 6 sections (A-F) and it reveals a good correlation between the two.

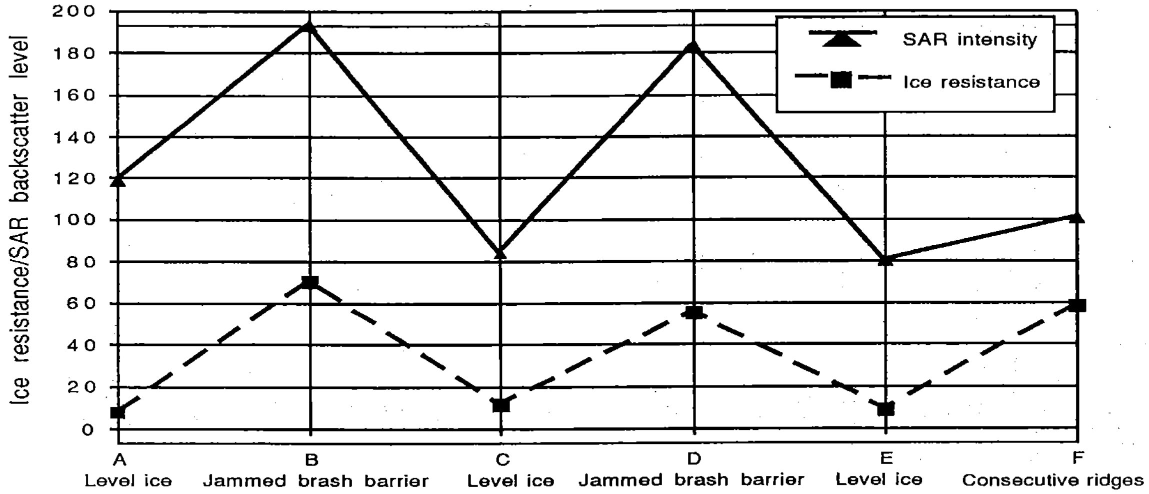

*Figure 7. Ice resistance indexes (squares) and SAR backscatter levels (triangles) for the icebreaker tracks A to F (shown in figure 6).*

This is only the first attempt to demonstrate the correlation between the backscatter level of SAR images and the resistance index of various ice types. The material from BEERS-93 and BEERS-94 includes many SAR images corresponding well in time with icebreaker performance measurements. It is the intention to continue the processing of this material and to ultimately arrive at an operational model for quantitative routing of ships through ice covered areas.

## 4. Conclusions

The icebreaker performance tests carried out in 1993 and 1994 in conjunction with BEERS-93 and -94 and an Operational Pilot Project in 1994 provided an excellent data set together with ERS-1 SAR images over the Gulf of Bothnia. The ice resistance indexes derived from the performance data seem to correlate well to the corresponding ice types and their expected resistance distribution. A good correlation between the ice resistance index and the backscatter level of SAR images has been demonstrated from the one SAR image that has been processed.

There is a need to continue the work with SAR images in order to have a more complete material before any final conclusions can be drawn. The results up to now are however very promising and open the prospects for the development of an operational model for quantitative routing of ships in ice covered areas.

## Acknowledgements

This project could never have been carried out without the kind support provided by the officers on the icebreakers ATLE and ODEN and the Icebreaker Department of the Swedish National Maritime Administration. Thanks are also conveyed to the Swedish Meteorological and Hydrological Institute (SMHI) for financial support and SAR image processing assistance.

## References

CARLSTRÖM, A. (editor), 1993, Baltic Experiment for ERS-1, BEERS-93: Swedish calibration/validation report, *Internal Report RSG* **1993:3**, Dep. Radio and Space Science, Chalmers University of Technology, Göteborg, Sweden,

CARLSTRÖM, A., (editor) 1994, Baltic Experiment for ERS-1, BEERS-94: BEERS-94 Data Report, *Internal Report RSG* **1994:2**, Dep. Radio and Space Science, Chalmers University of Technology, Göteborg, Sweden,

LILJESTRÖM, G., 1994, BEERS-94 Trafficability Data, Data Report, *Internal Report*, Bureau ODEN Icebreaker Design AB, Göteborg, Sweden,

THOMPSON T., HÅKANSSON, B., ULANDER, L., CARLSTRÖM, A., GUSTAVSSON, A., LARSSON, B., 1994, The Use of ERS-1 SAR Data for Sea Ice Mapping and Icebreaker Operations in the Gulf of Bothnia, Procedings of the Second ERS-1 Symposium - Space at the Service of our Environment, Hamburg, Germany, 11-14 October 1993, *ESA SP* **-36**, pp 172 -276.

# H. SAR INTERFEROMETRY FOR MEASURING FAST ICE DISPLACEMENT AND ICE RIDGE HEIGHT

PATRIK B.G. DAMMERT and JAN O. HAGBERG

Department of Radio and Space Science
Chalmers University of Technology
S-412 96 Göteborg, Sweden

**Abstract.** Interferometric SAR, InSAR, is a relatively new technology based on combinations of multiple SAR images obtained from slightly different sensor positions. InSAR may be used to measure various geophysical parameters, such as heights, displacements *etc.* and it is expected to produce precise topographic maps in the future. Unfortunately, there are yet some restraints in the InSAR technology; geometric distortions, ambiguities between heights and movements *etc.* In this study we have tried to point out significant similarities and differences between conventional intensity images and InSAR images over ice. We have measured relative cm-movements over very large areas in the fast ice with mm-accuracy and tried to conclude to what the movements are correlated. We have also obtained measurements over an ice ridge. In our measurements, we have shown the ambiguity between height of the ice ridge and relative movements of the surrounding ice. With our dataset, though, very small displacements (sub-mm movements) may be interpreted as very high ridges (~ 2-4 meters). The conclusion is that our measurements mainly originate from relative movements along the ice ridge rather than from its height and that the main application for this technology is mapping of such movements over large areas. However, with larger distance between sensor positions (*i.e.* baseline) or with no time lag (for example from an airborne system) between image acquisitions, topographic maps over ice and ice ridges should be possible. One has to keep in mind, however, that icebreaker support requires maps of the present ice situation, not of the situation several days ago. Real-time mapping of ice topography is therefore necessary.

## 1. Introduction

The backscattered intensity in a conventional synthetic aperture radar (SAR) image is mainly sensitive to surface roughness and dielectric properties of the ground. Constructive or destructive interference between elementary scatterers within a resolution cell (*i.e.* 'speckle noise') effectively destroys phase information. However, by acquiring another SAR image over the same area, but from a slightly different sensor position, and combining them into an interferogram, it is possible to retrieve geophysical information from the phase. It was shown by Graham (1974), Zebker and Goldstein (1986), Li and Goldstein (1990) and Prati and Rocca (1990), that the phase of such an interferogram is related to the large scale topography. This makes it possible to produce topographic maps in adverse weather independent of sun illumination and cloud coverage.

Multiple SAR images may also be used to detect very small (~ 1 mm) surface changes over very large areas (50x50 km$^2$). The method, based on SAR interferometry (InSAR), uses the phase information in two or more single-look complex SAR images which are separated in time. The extreme sensitivity of this technology combined with high resolution and broad coverage makes it useful for extensive and accurate measurements of various geophysical parameters, including heaving and buckling in fault zones, displacements caused by seismic events (Gabriel *et al.* 1989, Massonnet *et al.* 1993 and Rignot and Zyl 1993) and glacier movements (Goldstein *et al.* 1993), but also displacements of fast ice due to internal or external forces as we propose in this paper.

A crucial parameter for icebreaker support is ice ridge height. Larger ice ridges usually mean larger ice keels as well and thereby greater ice volume, which of course is more difficult for ice breakers to ram. InSAR gives us a possibility to produce height maps of ice ridges over large areas. In this work we have studied interferograms and intensity images from the northern part of the Bay of Bothnia acquired during the BEERS-92 experiments. We have identified different features in the images and tried to measure the height of an ice ridge south of Kalix.

## 2. Experiment data set

This study uses three complex SAR images obtained 24, 27 and 30 March during the winter of 1992. All three images are from descending morning passes. These images originate from the BEERS-92 experiment and normal intensity images from that period have been examined in detail (see for example Chapter E). Since the weather during this period was cold (below zero degrees Celsius), there probably was no wet snow layer on top of the ice, which could interfere with the radar pulse return. The winds were shifting and drift ice has moved around south of the fast ice in the archipelago.

The three complex images have been used to produce two interferograms. Interferogram no. 1 originates from the complex images of 27 and 30 March, thus three days between passes. Interferogram no. 2 originates from the complex images of 24 and 30 March, thus six days between passes. Both interferograms cover the same 50x50 $km^2$ large area; the archipelago south of the city Kalix.

## 3. Images

On the following pages, interferogram no. 1, an intensity image from 27 March and interferogram no. 2 are found. Note that the fringes show topography over land and mainly temporal movements over the ice.

The area marked with open water/drift ice in the interferograms appears as a noisy region. When an area moves or changes a lot between image acquisitions, it will loose coherence. Such areas appear noisy. The coherence will of course be lost over open water since the surface changes completely on the cm-scale over several days. One may see noisy regions in the estuary of the Kalix river and in the river-channel itself (especially in interferogram no.2), probably due to changes in wetness on top of the ice. Over the mainland, one may discern the Kalix river valley, another valley north of the river, a small crest south of the river and several other hills and such.

Two icebreaker tracks are marked with '1'. They have fractured the ice sheet and made it possible for the narrow area in between to move differently compared to the surrounding ice. The most southern part of this narrow ice floe between the leads has moved approximately 19 cm (in slant-range) relative to the north part of it. Since the ice floe is around 16 km long, such measurements with cm accuracy over such large distances are rather unique.

The area marked '2' is a part of the long ridge at the fast-ice boundary. A ridge feature may be seen in both interferograms, although it is more clear in interferogram no. 2.

One also sees movements in the estuary of the Kalix river. This could be due to the traffic to Kalix harbour or the water from Kalix river. In interferogram no. 2, one detects several areas which have moved a few centimetres between acquisitions. For example look at the area marked '3' in interferogram no. 2. It seems that the sea water level has sunk but the ice near those islands have stranded and could therefore not sink. In general, there are more noise in interferogram no. 2, but that is expected due the longer time period between acquisitions.

## 4. InSAR technology

### 4.1. Basic idea

The basic idea of SAR interferometry is that the backscattered signal is correlated, both in amplitude and phase, within a small angle interval (called a 'celestial footprint', approximately 1200 meters for ERS-1). An interferogram is produced by multiplication of two complex SAR images (either one is conjugated), pixel by pixel, and the phase is extracted. The geometry of a spaceborne repeat-pass SAR system with a stable imaged scene is shown in figure 1.

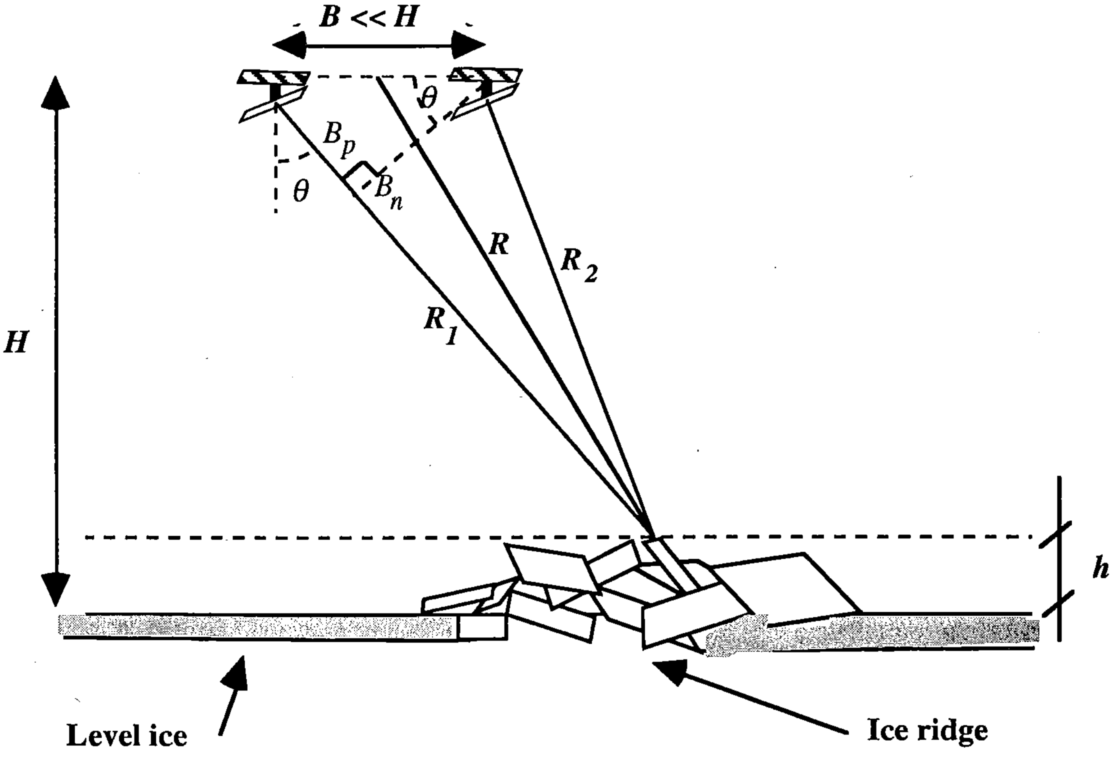

Figure 1. The geometry of a spaceborne repeat-pass SAR system.

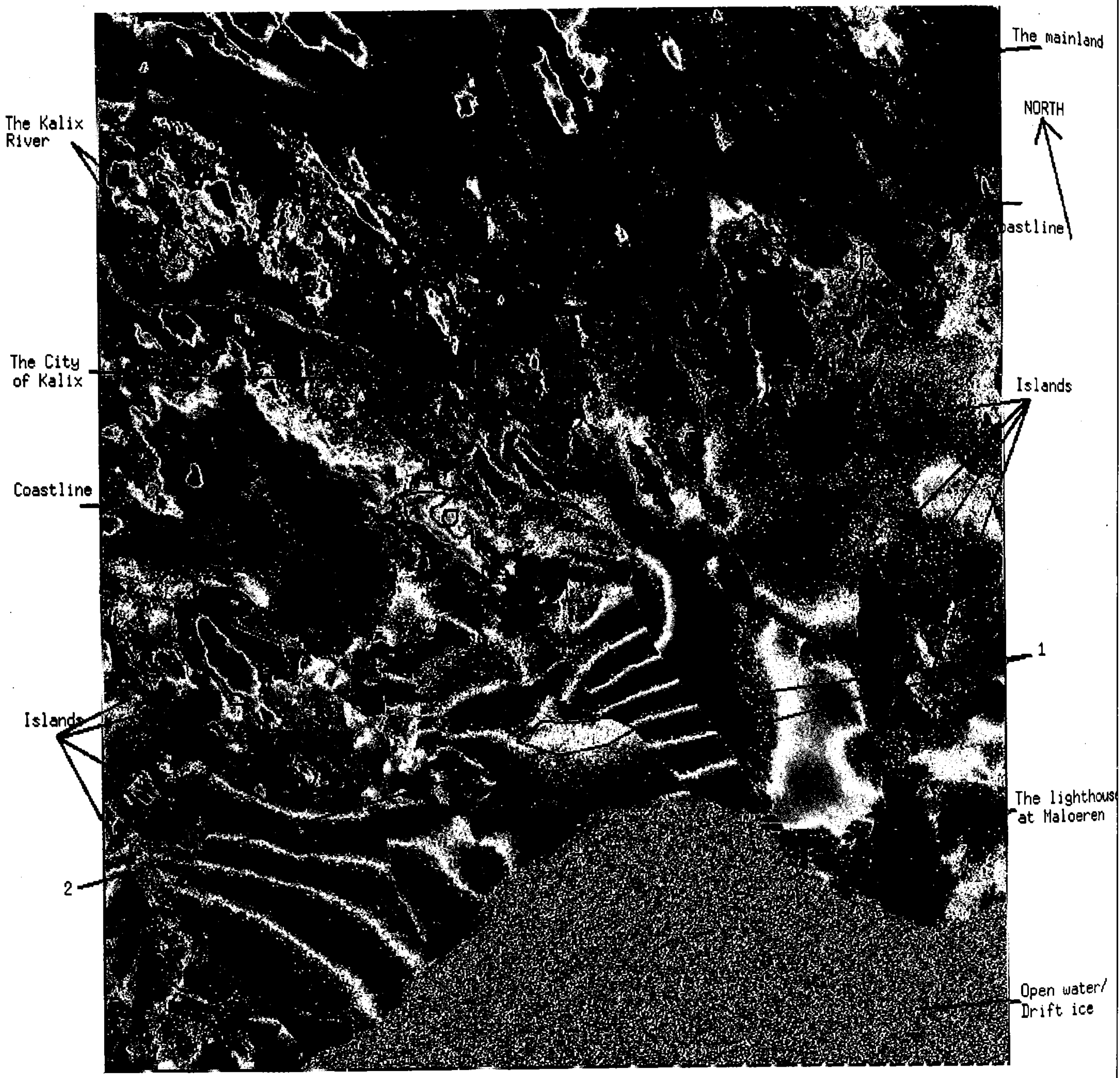

Figure 2. Interferogram no. 1, 27 and 30 March 1992. Red to red means 65 meters in height or 28 mm in movements.

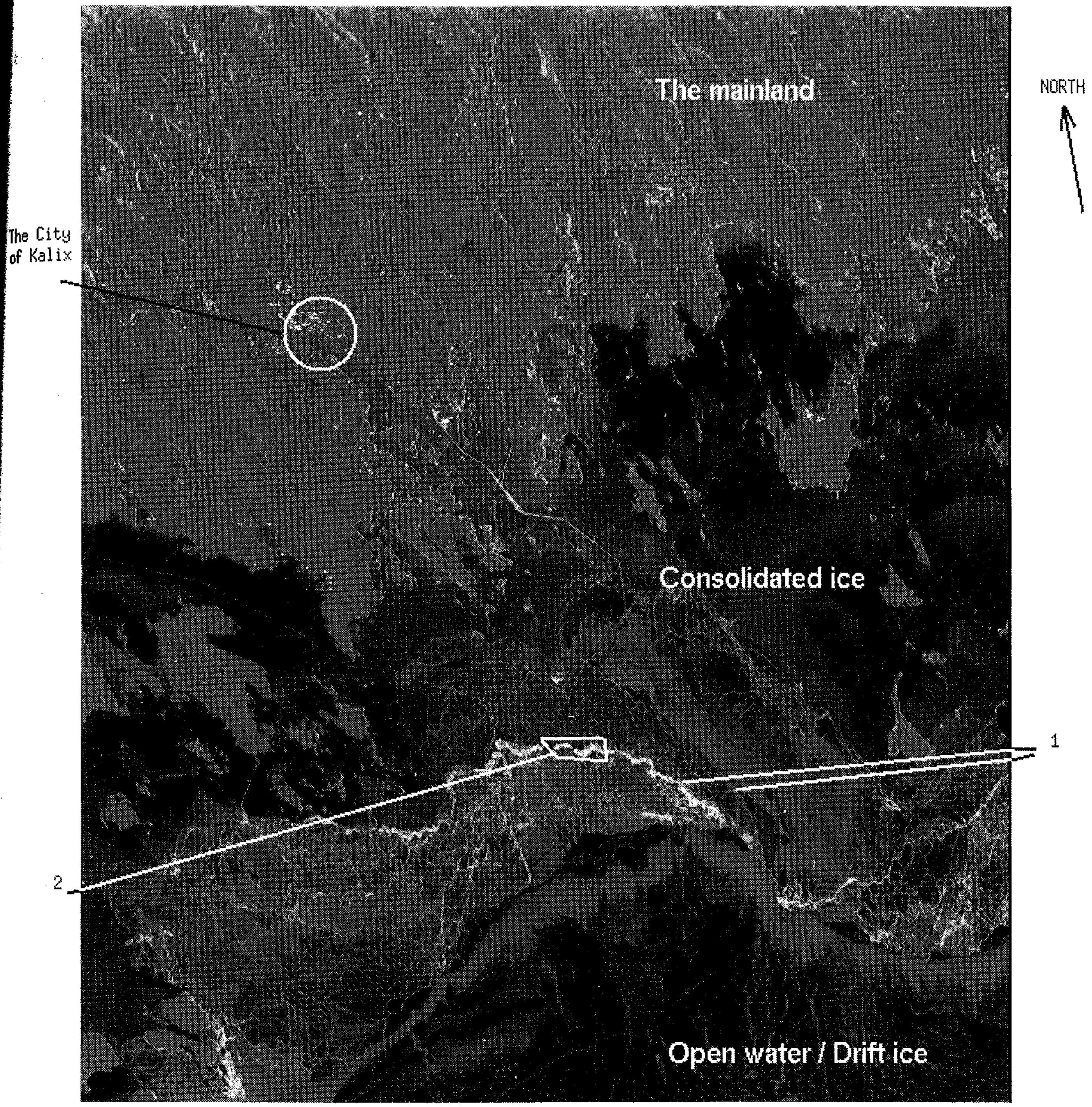

Figure 3. Intensity image, obtained 27 March 1992. © ESA 1992.

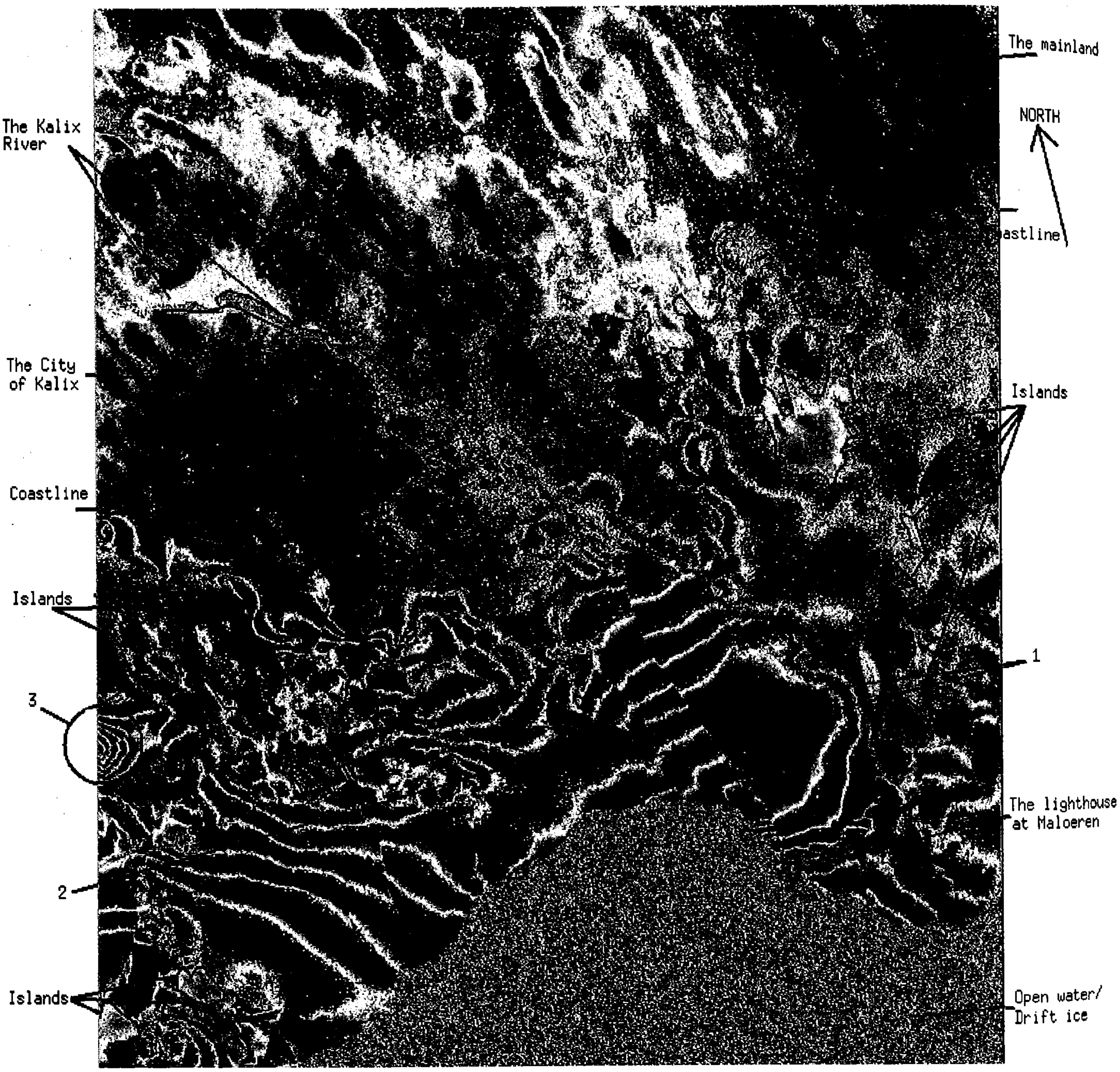

Figure 4. Interferogram no. 2, 24 and 30 March 1992. Red to red means 30 meters in height or 28 mm in movements.

According to figure 1 we have

$$h = H - R\cos\theta \tag{1}$$

where $H$ is the ground-to-satellite height, $h$ is the height of the ridge relative to surrounding level ice and $R$ is the average satellite-to-ridge distance. To determine the height, $h$, it is necessary to know all other parameters in equation 1. The problem is that we do not know $H$ and $\theta$ accurately enough to perform absolute measurements. However, by differentiating equation 1, it is possible to determine relative heights within the scene (Hagberg, 1994)

$$dh = -\cos\theta dR + R\sin\theta d\theta \tag{2}$$

We are only interested in the differential parallel baseline, $dB_p$ , and since $dB_p = B_n d\theta$ (see figure 4) and $d\theta$ is known from equation 2, we may derive a linearised expression for phase variations between pixels in an interferogram

$$\Delta\varphi = \frac{4\pi B_n}{\lambda R\tan\theta}\Delta R + \frac{4\pi B_n}{\lambda R\sin\theta}\Delta h + \Phi_{noise} + n \times 2\pi \tag{3}$$

where the operator $\Delta$ means the difference between two pixels in the interferogram, $B_n$ is the baseline normal to the line of sight, $\Phi_{noise}$ is the phase noise due to speckle decorrelation, random changes of scatterers and thermal noise. The last term represents the phase ambiguity. There will also be an extra phase shift if objects in a scene move between image acquisitions, *c.f.* figure 5.

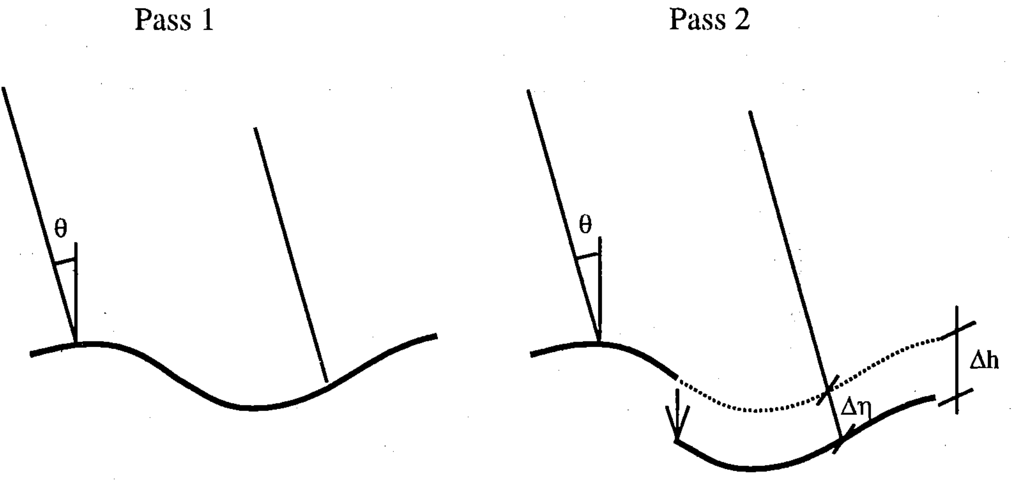
Pass 1

Pass 2

(a)

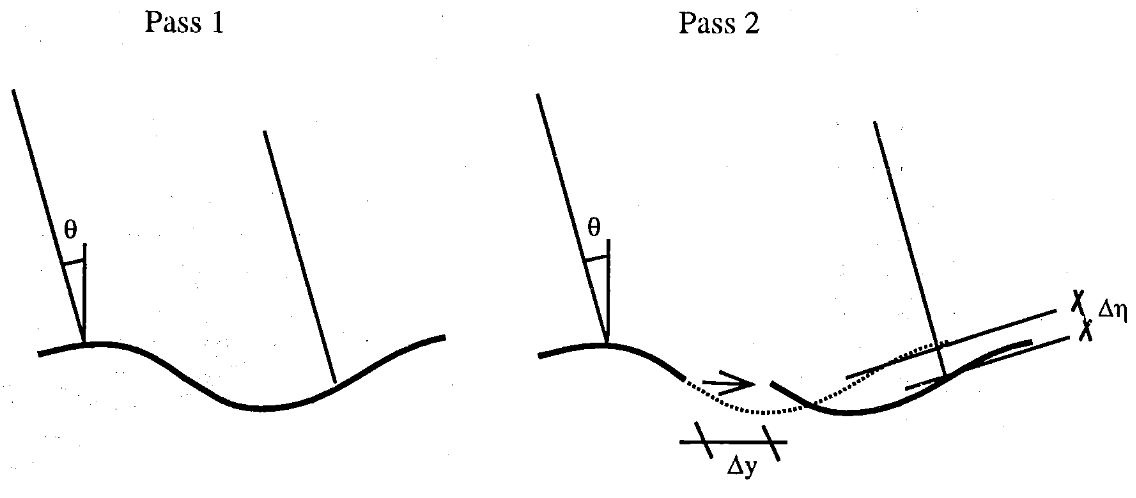

**(b)**

Figure 5. Phase shift, $\Delta\eta$, due to relative movements within the scene between image acquisitions
(a) Vertical movement
(b) Horizontal movement

Considering the extra phase shift due to relative temporal movements, equation 3 will be

$$\Delta\varphi = \frac{4\pi B_n}{\lambda R \tan\theta}\Delta R + \frac{4\pi B_n}{\lambda R \sin\theta}\Delta h + \frac{4\pi}{\lambda}\Delta\eta + \Phi_{noise} + n \times 2\pi \qquad (4)$$

The first term in equation 4 is purely a systematic effect which is easily removed by applying a correction. In the second term there is a relation between height and phase. Thus a measurement of relative heights is possible in an interferogram. The third term shows a relation between movements and phase and thus a measurement of small movements is possible.

### *4.2. Problems*

There are mainly four problems associated with interferograms (Hagberg and Ulander, 1994)

- the ambiguity of the phase that is due to modulo 2π phase registration
- second-order effects of the imaging geometry
- the ambiguity of heights and temporal changes of the scene
- the ambiguous direction of a temporal change

The phase ambiguity in an interferogram has to be removed in order to create a correct phase measurement. The phase is only registered in the interval [-π,π] (*i.e.* its principal value). A correct number of 2π must be added to the phase; the phase must be unwrapped (Goldstein *et al.* 1988). The coherence in the interferogram must be good to make it possible to unwrap the phase correctly (*i.e.* the scene must be reasonably stable between acquisitions). For example, since lakes and oceans are expected to have no coherence, they appear as noisy regions in an interferogram.

The ambiguity of height and movements of an object is total. After correction and phase unwrapping equation 4 reduces to

$$\Delta\varphi = \frac{4\pi B_n}{\lambda R \sin\theta}\Delta h + \frac{4\pi}{\lambda}\Delta\eta = k_1\Delta h + k_2\Delta\eta \qquad (5)$$

The ratio $k_1/k_2$ comes to $B_n/(R\sin\theta)$. In other words, the phase could be made more or less sensitive to heights compared to temporal changes by using different baselines. Note that, with a baseline of 100 meters, the phase in ERS-1 SAR interferograms is roughly over 1,000 times more sensitive to temporal movements of an object than of its height.

## 5. Phase shifts over ice ridge

From SAR measurements alone, it is impossible to know whether the phase shift over the long ice ridge (marked '2' in the interferograms) originates from the height of the ice ridge or the relative movements of the surrounding area. The following measurements rely on the assumption that the phase shift over the ridge originates from either the ridge height or the ridge's relative movements. One may then derive the heights or the movements of the area (according to equation 5). A part of the ridge, sitting on some breakers, have been selected and perpendicular profiles have been extracted. Those profiles have been examined for the phase shift.

### *5.1. Measurements*

The following figures are derived from measurements over the ridge (from the level ice north of the ridge to the level ice south of the ridge, *i.e.* across the ridge) in interferogram no. 1. If the phase shift originates solely from the height of the ridge, the height is displayed on the left-hand side of the diagrams. If the phase originates solely from relative movements, the movement is displayed on the right-hand side of the diagrams. The level ice at the north part of the ridge is set as a reference.

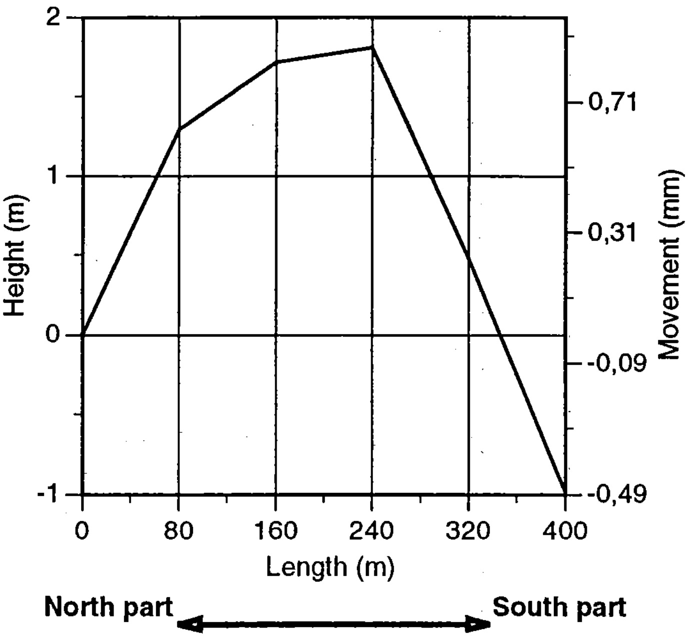

Figure 6. Measurements from interferogram #1

The same procedure is carried out with interferogram no. 2 and the results are found in figure 7.

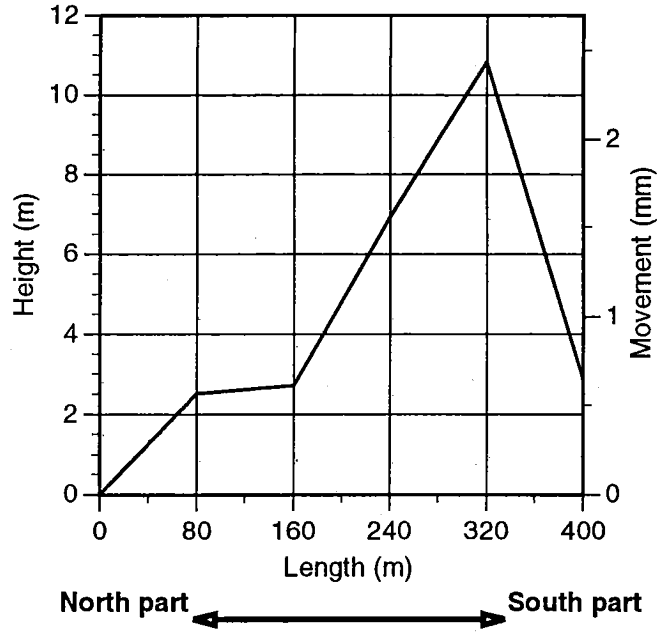

Figure 7. Measurements from interferogram #2

### 5.2. Discussion

According to figures 6 and 7, very small relative movements of the ridge give rise to substantial phase variations. Since the relative movement, $\Delta\eta$, does not depend on the baseline, this phase shift will be constant for different baselines. If one has a larger baseline (meaning $B_n$ in equation 4), the phase will be more sensitive to heights of the surface. Interferograms with longer baselines would probably show better agreement between surface height and phase. Of course, with no time period between image acquisitions, phase variations due to movements will disappear.

Nevertheless, the measurements from interferogram no. 1 could actually display the ridge height. The proposed heights are not unlikely. Unfortunately, there is no ground truth available. Other ridges were measured during BEERS-92, but those do not appear in the interferograms. With no ground truth available, it is impossible to say whether the measurements are significant for the ridge heights. Measurements from interferogram no.2 presumably show movements, it is not very likely to have 10 meters high ridges in the Bay of Bothnia.

## 6. Phase shifts along ice floe

The ice floe divided by the two icebreaker tracks (marked '1' in the interferograms) is clearly distinguished by the interferometric fringes. Assuming that this ice floe is flat the interferometric fringes are totally induced by a motion between the image acquisitions. Normally, there are small hills and ridges in an ice pack, but with our baselines these contributions to phase shifts along the ice floe compared to the motion of it, are negligible.

As the movement direction is ambiguous (it could be vertical and/or horizontal) we will try to determine what direction it is and possibly rule out factors or determine the factor behind the movements. The northern part of the ice floe seems to stable with the surrounding ice and the southern part has moved. The southern part could have moved up or down or it could have been stretched out or compressed (like a steel spring would) or possibly a mix of the two movements.

### *6.1. Vertical movement*

If the movement is solely vertical, it is possible to derive the movement by using equation 4. One explanation of a vertical movement may be a change in sea water level during the period assuming that this floe is more affected by sea water level changes than the surrounding ice pack. A comparison between the sea water level from Kalix (about 15 km north of the floe) and an assumed vertical movement is found in table 1. The 24 March is set as the sea water level reference and upward movement is set positive.

Table 1. Comparison between sea water level and vertical movements

| **Date** | **Kalix sea water level (cm)** | **Assumed vertical position of the ice pack (cm)** | |
|---|---|---|---|
| | | Interferogram 1, 27-30 March | Interferogram 2, 24-30 March |
| 24 March 1992 | 0 | - | 0 |
| 27 March 1992 | + 29 | 0 | - |
| 30 March 1992 | + 2 | + 18 | + 18 |

Comparing measurements from interferogram no.1 and the sea water level, the sea water level has sunk 27 cm between the two dates and the ice floe has risen 18 cm, it is not likely that the phase shift is caused by this event. However, comparing interferogram no.2 and the sea water level, the interferogram suggests a movement of 18 cm but the sea water level has barely changed. Thus the phase shift cannot be solely dependant of the sea water level.

### *6.2. Horizontal movement*

It is also possible to derive a horizontal movement along the ice floe, assuming that the floe has only moved horizontally. Possible factors for compressing or stretching the ice floe may be winds, sea currents, water from the outlet of Kalix river *etc.* A table comparing winds and assumed vertical movement is shown in table 2. Southbound movement is set positive.

Table 2. Comparison between wind and horizontal movements

| **Date** | **Wind speed and direction** | **Assumed horizontal position of the ice pack (cm)** | |
|---|---|---|---|
| | | Interferogram 1, 27-30 March | Interferogram 2, 24-30 March |
| 24 March 1992 | NW 4 m/s | | 0 |
| 25 March 1992 | SW 6 m/s | | |
| 26 March 1992 | SE 7 m/s | | |
| 27 March 1992 | SE 5 m/s | 0 | |
| 28 March 1992 | N 7 m/s | | |
| 29 March 1992 | N 7 m/s | | |
| 30 March 1992 | N 5 m/s | + 94 | + 94 |

Considering the available data, it is in this case harder to rule out or include the wind factor. Both interferograms suggest a movement of 94 cm to the south, but over slightly different periods. Considering only the wind statistics, the ice should have moved north between 24 and 27 March and south between 27 and 30 March. Including the geography of the place, the ice would probably only be affected by southerly winds as there is open water only to the south for the wind to pitch up any waves and currents. Thus the ice floe should have only moved when affected by southerly winds, *i.e.* between 24 and 27 March. These assumptions do not, however, comply with the derived movements from the interferograms. These measurements suggest a movement only between 27 and 30 March. On the other hand, a southbound movement during these days comply well with the northerly winds.

There may also be other factors behind horizontal movements. Water from the Kalix river may have pushed the ice floe outwards to the open sea. If that is the case though, the movements should have been constant in time. Icebreakers may have actually pushed the ice when using the icebreaker track. This may explain why both interferograms suggest the same movement; an icebreaker may have used one of the tracks between 27 and 30 March.

### 6.3. Discussion

In both cases of vertical and horizontal movements, it is peculiar that only this chunk of ice has moved and not the surrounding ice pack. Probably, the surrounding ice pack is more stable due to its size. Considering the above comparisons it is possible to rule out the sea water level as a cause for these movements and state that the wind has little effect on these movements. We therefore propose that these movements are caused by icebreakers, sea currents at the ice edge and sea currents under the ice pack.

## 7. Conclusions

InSAR makes it possible to produce maps of the fast ice displacement on the cm-scale over large areas. Such information should be of value for investigating models of ice deformation and ice dynamics. Unfortunately, there is an ambiguity between horizontal and vertical movements. The ambiguity may to some extent be solved by using interferograms from both ascending and descending orbits.

This study has also shown that there are additional information in the interferograms compared to the intensity images. A number of new features have been recognised. Ice ridge heights for example should be of great value for ice-breakers and merchant vessels. The problem is that interferograms from a repeat-pass configuration simply are not up to date, they are at least 3 days old. Icebreaker captains are of course mainly interested in the present ice situation, not a situation some days old. Interferograms with a shorter time lag would certainly be more interesting. Another problem for a repeat-pass system is the ambiguities between displacements and ridge height. A system without the time lag, for example an air-borne system with two antennas or a tethered satellite system (Zebker *et al.* 1992), would make it possible to produce unambiguous maps of the ice ridge heights in real time.

## Acknowledgements

We would like to acknowledge Dr. Lars M.H. Ulander at CUT for fruitful discussions and insights and for his review of the manuscript. Bertil Håkansson, SMHI, is acknowledged for supplying the meteorological data.

## References

GABRIEL A.K., GOLDSTEIN R.M., and ZEBKER H.A., 1989, Mapping small elevation changes over large areas: Differential radar interferometry, Journal of Geophysical Research, 94(B7), pp. 9183-9191

GOLDSTEIN R.M., ENGELHARDT H., KAMB B., and FROLICH R.M., 1993, Satellite Radar Interferometry for Monitoring Ice Sheet Motion: Application to an Antarctic Ice Stream, Science, 262, pp. 1525-1530

GOLDSTEIN R.M., ZEBKER H.A., and WERNER C.L., 1988, Satellite radar interferometry: Two-dimensional phase unwrapping, Radio Science, 23, pp. 713-720

GRAHAM L.C., 1974, Synthetic interferometer radar for topographic mapping, Proceedings of the IEEE, 62, pp. 763-768

HAGBERG J.O., 1994, Repeat-pass Satellite SAR Interferometry, Technical report no. 170L, Department of Radio and Space Science, Chalmers University of Technology, Gothenburg, Sweden

HAGBERG J.O., and ULANDER L.M.H., 1994, ASAR External Calibration and Validation Study, Technical Note no. 2, Internal report RSG 1994:1, Department of Radio and Space Science, Chalmers University of Technology, Gothenburg, Sweden

LI F.K., and GOLDSTEIN R.M., 1990, Studies of multibaseline spaceborne interferometric synthetic aperture radars, IEEE Transactions on Geoscience and Remote Sensing, 28(1), pp. 88-96

MASSONNET D., ROSSI M., CARMONA C., ADRAGNA F., PELTZER G., FEIGL K., and RABAUTE T., 1993, The displacement field of the Landers earthquake mapped by radar interferometry, Nature, 364(6433), pp. 138-142

PRATI C., and ROCCA F., 1990, Limits to the resolution of elevation maps from stereo SAR images, International Journal of Remote Sensing, no. 11, pp. 2215-2235

RIGNOT E.J.M., and van ZYL J.J., 1993, Change detection techniques for ERS-1 SAR data, IEEE Transactions on Geoscience and Remote Sensing, 31(4), pp. 896-90

ZEBKER H.A., and GOLDSTEIN R.M., 1986, Topographic mapping from interferometric synthetic aperture radar observations, Journal of Geophysical Research, 91(B5), pp. 4993-4999

ZEBKER H. A., MADSEN S.N., MARTIN J., WHEELER K.B., MILLER T., LOU Y., ALBERTI G., VETRELLA S., and CUCCI A., 1992, The TOPSAR interferometric radar topographic mapping instrument, IEEE Transactions on Geoscience and Remote Sensing, 30(5), pp. 933-940